

Integration of a Continuum-Based Finite Element Tire Modeling Framework in Multibody Dynamics Algorithms

BY

MOHIL D. PATEL

B.Sc., University of Illinois at Chicago, 2014

THESIS

Submitted as partial fulfillment of the requirements
for the degree of Doctor of Philosophy in Mechanical Engineering
in the Graduate College of the
University of Illinois at Chicago, 2018

Chicago, Illinois

Defense Committee:

Dr. Ahmed A. Shabana, Chair and Advisor, Mechanical and Industrial Engineering
Dr. Craig Foster, Civil and Materials Engineering
Dr. Sheng-Wei Chi, Civil and Materials Engineering
Dr. Eduard Karpov, Civil and Materials Engineering
Dr. Ali Afshari, Gamma Technologies Inc.

This thesis is dedicated to my family.

ACKNOWLEDGMENTS

I would like to first express my deepest gratitude to my advisor Dr. Ahmed A. Shabana for his invaluable advice, support, guidance, patience and never-ending encouragement throughout my graduate studies at the University of Illinois at Chicago. His vital insights on my work and the many conversations we had on flexible multibody dynamics helped me gain a unique perspective on academic research and the field of flexible multibody dynamics. I would also like to thank the members of my thesis committee: Dr. Craig Foster, Dr. Sheng-Wei Chi, Dr. Eduard Karpov and Dr. Ali Afshari for their participation on my thesis committee and their helpful insights on my work.

I would like to thank Dr. Carmine Pappalardo, Dr. Grzegorz Orzechowski, Dr. Qiang Tian, Dr. Gang He and Dr. Gengxiang Wang for their collaboration on my research, and the many interesting conversations on a variety of topics. I would particularly like to thank Dr. Carmine Pappalardo and Dr. Grzegorz Orzechowski for their deep technical insights on the absolute nodal coordinate formulation and multibody dynamics theory. I would also like to thank my friends and colleagues in the Dynamic Simulation Laboratory: Dr. Ashraf Hamed, Shubhankar Kulkarni, Dr. Ulysses Contreras, Dr. Zuqing Yu, Dr. Antonio Recuero, Dr. Liang Wang, Emanuele Grossi, Brian Tinsley, Brynne Nicolsen and Dr. Michael Wallin for their help and again interesting conversations during the quick coffee breaks.

I would like to thank my family for their continuous support during my graduate studies. I would particularly like to thank my grandparents and my aunt for their never-ending love and support towards a good education. Finally, I would like to thank my parents, Mita and Divyesh Patel, without whose support, love, encouragement and guidance I would not be where I am today.

CONTRIBUTIONS OF AUTHORS

Chapter 2 represents a published paper (Patel, M., Orzechowski, G., Tian, Q., and Shabana A.A., 2016, “A New Multibody System Approach for Tire Modeling using ANCF Finite Elements,” *Proceedings of Institution of Mechanical Engineers Part K: Journal of Multibody Dynamics*, 230(1), pp. 69-84.) in which I am the first author. Dr. Grzegorz Orzechowski assisted with the tire modeling aspects of this paper and assisted in proofreading the paper. Dr. Qiang Tian assisted in the composite modeling section of this paper and with proofreading the paper. My advisor Dr. Ahmed A. Shabana supervised the research for this paper and assisted greatly with writing the manuscript. I contributed to the modeling of the tire and vehicle numerical example, writing of the manuscript and generation of the figures. **Chapter 3** represents a published paper (He, G., Patel, M., and Shabana, A.A., 2017, “Integration of Localized Surface Geometry in Fully Parameterized ANCF Finite Elements,” *Computer Methods in Applied Mechanics and Engineering*, 313, pp. 966-985.) for which I am the second author. I collaborated with Dr. Gang He in writing the code for the simulations presented in the paper, which includes all the finite element examples. I co-wrote the paper with Dr. Gang He and assisted with creating the figures as well. My advisor Dr. Ahmed A. Shabana assisted with reviewing the paper and supervising the research. **Chapter 4** represents a paper (Patel, M., and Shabana, A.A., 2017, “Locking Alleviation in the Large Displacement Analysis of Beam Elements: The Strain Split Method,” submitted to *Acta Mechanica*) submitted to a journal where I am the first author. My advisor Dr. Ahmed A. Shabana supervised the research and assisted with writing the paper. **Chapter 5** represents a paper (Patel, M., Pappalardo, C.M., Wang, G., and Shabana, A.A., 2017, “Integration of Geometry and Small and Large Deformation Analysis for Vehicle Modelling: Chassis, and Airless and Pneumatic Tire Flexibility,” submitted to *International Journal of Vehicle Performance*) submitted to a journal where I am first author

and was responsible for the writing of the paper and the technical material shown. Dr. Carmine Pappalardo assisted with the writing of the paper and numerical examples regarding the ANCF structural discontinuities. Dr. Gengxiang Wang assisted with reviewing the paper and creating the off-road wheeled vehicle model. Dr. Ahmed A. Shabana reviewed the paper and supervised the research.

TABLE OF CONTENTS

1. INTRODUCTION	1
1.1 Tire Modeling.....	2
1.2 Localized Surface Geometry in FEs.....	5
1.3 Locking in ANCF FEs.....	8
1.4 Vehicle Modeling: Small and Large Deformation and Structural Discontinuities	9
1.5 Scope and Organization of the Thesis	14
2. ANCF TIRE MODELING	19
2.1 ANCF Tire Geometry.....	20
2.2 Air Pressure and Contact Forces	23
2.2.1 Air Pressure Force	23
2.2.2 Tire/Ground Contact Force	25
2.2.3 Spin Velocity	27
2.3 ANCF Reference Node	29
2.3.1 Preprocessor Reference Node/Element Node Constraints	29
2.3.2 Preprocessor Reference Node Inertia	31
2.3.3 ANCF-RN Rigidity Constraints	32
2.4 Composite Tires	32
2.5 Numerical Results	35
2.5.1 ANCF Fully Parameterized Plate Element Tire Assembly	35
2.5.2 Bulldozer Vehicle Model	36
2.5.3 Simulation Results.....	40
2.6 Concluding Remarks	45
3. LOCALIZED SURFACE GEOMETRY IN ANCF FINITE ELEMENTS	47
3.1 Localized Surface Geometry Modeling Methods	48
3.2 ANCF Geometry	51
3.3 Integration of Localized Surface	52
3.3.1 The Definition of Localized Surface	52
3.3.2 Localized Geometry and ANCF Elements	54
3.4 Numerical Integration Method	58
3.4.1 Global Domain and Subdomain Integration Method	58

TABLE OF CONTENTS (continued)

3.4.2 Comparison of the Two Integration Methods	61
3.5 ANCF Governing Equations	63
3.6 Numerical Results	64
3.6.1 Plate Contact Example	65
3.6.2 Cantilever Plate Validation	70
3.6.3 Tire Contact Example.....	74
3.7 Concluding Remarks	79
4. ANCF LOCKING ALLEVIATION: STRAIN SPLIT METHOD	81
4.1 Locking Alleviation in Classical FEs	82
4.2 Locking Alleviation in ANCF Elements	87
4.3 ANCF FEs	90
4.3.1 ANCF Kinematics	91
4.3.2 General Continuum Mechanics Approach	92
4.3.3 Higher-Order Planar Beam Element	93
4.3.4 Plane Stress and Plane Strain Assumptions	94
4.4 ANCF Strain Split Method.....	96
4.4.1 Strain Split Method (SSM).....	96
4.4.2 SSM Generalization	99
4.4.3 SSM Objectivity and Initially Curved Geometry.....	101
4.5 Other Locking Solution Approaches.....	102
4.5.1 Enhanced Assumed Strain (EAS) and Method of Incompatible Modes	102
4.5.1.1 EAS Strain Interpolation	105
4.5.2 Elastic Line Approach	106
4.5.3 Enhanced Continuum Mechanics Approach	107
4.6 Numerical Examples	108
4.6.1 Slender Beam: Small Deformation.....	109
4.6.2 Thick Beam: Large Deformation	109
4.6.3 Initially Curved Beam: Large Deformation	112
4.6.4 Dynamic Analysis: Pendulum Problem	115
4.6.5 Three-Dimensional Dynamic Analysis: Cantilever Beam	117

TABLE OF CONTENTS (continued)

4.7 Concluding Remarks	119
5. VEHICLE MODELING: STRUCTURAL DISCONTINUITY, SMALL AND LARGE DEFORMATION	121
5.1 Small and Large Deformation Analysis	122
5.1.1 FE/FFR Formulation	122
5.1.2 ANCF Finite Elements	126
5.2 FFR and ANCF Modeling of Structural Discontinuities.....	128
5.2.1 FE/FFR Formulation	129
5.2.2 ANCF Finite Elements	130
5.3 MBS Equations of Motion	136
5.4 Numerical Results and Discussion	138
5.4.1 L-shaped Beam and Y-shaped Plate Pendulums	138
5.4.2 Wheeled Vehicle Model.....	142
5.4.2.1 MBS Vehicle Model.....	143
5.4.2.2 Flexible Subsystems: Chassis and Tires.....	146
5.4.2.3 Comparative Study	152
5.5 Concluding Remarks	160
6. CONCLUSIONS AND FUTURE WORK	162
6.1 Conclusions	162
6.2 Future Work	166
APPENDIX A	167
APPENDIX B	169
APPENDIX C	171
CITED LITERATURES	173
VITA.....	194

LIST OF TABLES

TABLE 1. TREAD CLASSIFICATION FOR COMMERCIAL TIRES	6
TABLE 2. INERTIA PROPERTIES OF VEHICLE REFERENCE NODES.....	37
TABLE 3. INITIAL GLOBAL POSITIONS OF VEHICLE REFERENCE NODES	37
TABLE 4. ANCF PLATE ELEMENT TIRE GEOMETRIC PROPERTIES	39
TABLE 5. ANCF PLATE ELEMENT TIRE MATERIAL PROPERTIES.....	39
TABLE 6. SIMULATION PARAMETERS	40
TABLE 7. MATERIAL PROPERTIES USED IN THE PLATE CONTACT EXAMPLE.....	66
TABLE 8. CONTACT PARAMETERS USED IN THE PLATE CONTACT EXAMPLE.....	66
TABLE 9. MATERIAL PROPERTIES USED IN THE CANTILEVER PLATE EXAMPLE ..	71
TABLE 10. COMPARISON OF THE CANTILEVER PLATE TIP VERTICAL POSITION WITH AND WITHOUT LOCALIZED GEOMETRY.....	72
TABLE 11. MATERIAL PROPERTIES USED IN THE TIRE EXAMPLE	75
TABLE 12. CONTACT PARAMETERS USED IN THE TIRE EXAMPLE	78
TABLE 13. EFFECT OF USING PLANE STRESS AND PLANE STRAIN.....	96
TABLE 14. LOCKING ALLEVIATION TECHNIQUE ABBREVIATIONS.....	108
TABLE 15. SMALL DEFORMATION OF CANTILEVER BEAM STATIC EXAMPLE: TIP VERTICAL DISPLACEMENT.....	109
TABLE 16. LARGE DEFORMATION OF CANTILEVER BEAM STATIC EXAMPLE: TIP VERTICAL DISPLACEMENT.....	111
TABLE 17. LARGE DEFORMATION OF CURVED CANTILEVER BEAM STATIC EXAMPLE: TIP X DISPLACEMENT	113
TABLE 18. VEHICLE INERTIA PROPERTIES	144
TABLE 19. IDEAL JOINTS USED IN VEHICLE MODEL	144
TABLE 20. COMPLIANT JOINT ELEMENTS USED IN VEHICLE MODEL	145
TABLE 21. CHASSIS FREQUENCIES	147

LIST OF FIGURES

Figure 1. One ANCF-mesh-four-wheel assembly	4
Figure 2. Structural discontinuities in a truck chassis	9
Figure 3. Pneumatic off-road tire (upper figure) and airless off-road tire (lower figure).....	10
Figure 4. Wheeled bulldozer model.....	14
Figure 5. Initially curved ANCF structures	21
Figure 6. Air pressure	24
Figure 7. Contact forces.....	26
Figure 8. ANCF tire assembly	30
Figure 9. Composite laminated tire cross section	33
Figure 10. All ANCF vehicle model.....	37
Figure 11. ANCF fully parameterized plate element tire cross section and mid-surface representation	38
Figure 12. Chassis reference node longitudinal displacement.....	41
Figure 13. Chassis reference node vertical displacement	42
Figure 14. First component of \mathbf{r}_x gradient of front right rim reference node	43
Figure 15. Chassis longitudinal speed	43
Figure 16. Contact patch of noncomposite material vehicle tire in static (non-rolling) condition	44
Figure 17. Contact patch of noncomposite material vehicle tire in rolling condition	44
Figure 18. Analytical tire contact force distribution.....	45
Figure 19. Integration of localized geometry with ANCF geometry.....	55
Figure 20. Mapping between the localized geometry parameters and ANCF element coordinates	57
Figure 21. Distribution of integration points using the global domain and subdomain methods	60
Figure 22. Comparison of global domain and subdomain integration method.....	62
Figure 23. One-plate contact example	67
Figure 24. Vertical displacement using different numbers of integration points	68
Figure 25. Vertical displacement using different numbers of subdomains	68
Figure 26. 2×2 ANCF plate element mesh with localized geometry	70
Figure 27. Cantilever plate reference configuration and cross section.....	71
Figure 28. Convergence of classical FE code solution for plate structure with local geometry...	73

LIST OF FIGURES (continued)

Figure 29. Convergence of ANCF solution for plate structure with local geometry.....	73
Figure 30. Difference between ANCF solution and classical FE solution	74
Figure 31. ANCF tire geometry	75
Figure 32. Tire tread with four grooves	76
Figure 33. Value of $ \mathbf{J} $ at the middle point on the bottom of the tire tread surface	77
Figure 34. Position convergence of ANCF solution for tire contact example.....	77
Figure 35. Slender cantilever beam problem	95
Figure 36. Thick cantilever beam problem	110
Figure 37. Curved cantilever beam problem.....	112
Figure 38. Comparison of beam tip vertical displacement for different formulations in case of plane stress	115
Figure 39. Comparison of beam tip vertical displacement between general continuum mechanics and strain split method with plane strain assumption.....	116
Figure 40. Graphical representation of the pendulum motion in case of plane strain	117
Figure 41. Three-dimensional cantilever beam dynamic analysis.....	118
Figure 42. Comparison of cantilever beam tip horizontal position for different models	119
Figure 43. Coordinate systems involved in FE-FFR formulation.....	123
Figure 44. FE-FFR structural discontinuity	129
Figure 45. ANCF structural discontinuity	132
Figure 46. L-shaped beam pendulum with structural discontinuity	139
Figure 47. L-shaped beam tip vertical position: ANCF and rigid body model comparison.....	140
Figure 48. ANCF L-shaped beam engineering shear strain and cosine of angle at structural discontinuity	140
Figure 49. Y-shaped plate/shell pendulum model	141
Figure 50. Y-shaped plate/shell pendulum tip vertical position: ANCF and rigid body model comparison	142
Figure 51. Off-road wheeled vehicle model	143
Figure 52. Front left suspension close-up	145
Figure 53. FFR chassis mesh	146
Figure 54. FFR chassis first five mode shapes and frequencies	148

LIST OF FIGURES (continued)

Figure 55. ANCF pneumatic tire	149
Figure 56. ANCF airless tire.....	150
Figure 57. Distributed radial damping model.....	151
Figure 58. Durability vehicle simulation test track.....	153
Figure 59. Chassis longitudinal velocity.....	153
Figure 60. Chassis longitudinal displacement	154
Figure 61. Chassis vertical displacement.....	154
Figure 62. Front left spindle vertical displacement	156
Figure 63. Airless tire hitting second bump with ε_{yy} strain contours	156
Figure 64. Pneumatic tire hitting second bump with ε_{yy} strain contours.....	157
Figure 65. FFR chassis total deformation instance during dynamic simulation.....	157
Figure 66. Vertical deformation at chassis point P with respect to BCS	158
Figure 67. Vertical deformation at chassis point P with respect to BCS after applying low-pass filter	159
Figure 68. Axial stress at chassis point P with respect to BCS.....	159
Figure 69. Axial stress at chassis point P with respect to BCS after applying low-pass filter ...	160

SUMMARY

Flexible *multibody systems* (MBS) are systems of interconnected rigid and flexible bodies and are typically characterized by large reference translations and rotations. Examples of such systems include automotive vehicles, trains, aircrafts and musculoskeletal systems. The flexible bodies found in MBS models can be characterized by small and large deformation. The MBS dynamics literature consists of various methods of formulating the governing equations of motion, describing the MBS models and incorporating component flexibility. In case of flexible MBS models, the fidelity, accuracy and efficiency of the model will depend on the formulation and numerical methods used by the MBS software, which keep evolving and improving over time. The goal of this thesis is to develop a new computational framework for the modeling and integration of *finite element* (FE) tires in MBS dynamics algorithms. Historically tire modeling techniques used in MBS computer programs have consisted of curve-fitted analytical formulations, discrete/compliant-type elastic tire models and co-simulated classical FE models. This thesis proposes a new method of FE-based tire modeling that utilizes the *absolute nodal coordinate formulation* (ANCF) elements and can be systematically implemented in non-incremental MBS dynamics algorithms. The advantages of such a type of tire modeling are two-fold: the distributed inertia and elasticity of the tire can be successfully represented, and the model can exploit the existing MBS dynamics algorithms for obtaining efficient and reliable solutions. Along with the overall structural modeling aspects of tires, a new approach for the inclusion of surface geometry within ANCF FEs is developed, with tire tread details being a good example of such type of geometry. This thesis also discusses locking phenomena in fully parameterized ANCF beam and plate/shell elements and proposes a new locking alleviation technique. Finally, this thesis will demonstrate the feasibility of developing new and detailed vehicle models that include a large

SUMMARY (continued)

number of interconnected rigid and flexible bodies that could have structural discontinuities and are subjected to small and large deformation.

In the new computational multibody system framework proposed in this thesis for developing accurate tire models, ANCF FEs are used to create the geometry and perform the FE/MBS analysis. The computational procedure used in this thesis allows for modeling composite tires and for using a continuum-based air pressure and contact tire force models. The ANCF tire mesh, which allows for high spinning speed, has a constant inertia matrix and zero Coriolis and centrifugal forces. The concept of the ANCF reference node, is used to develop linear connectivity conditions between the tire mesh and rim, thereby allowing for imposing these linear conditions at a preprocessing stage. Using this approach, the dependent variables are eliminated at a preprocessing stage before the start of the simulation. The ANCF reference node, which is not associated with a particular FE, is used to define the inertia of the rigid rims. The inertia coefficients associated with the rim reference nodes are first developed in terms of the ANCF position and gradient coordinates. The rigidity of each rim reference node is enforced during the dynamic analysis using six nonlinear algebraic constraint equations that are combined with the dynamic differential equations of motion using the technique of Lagrange multipliers. It is shown in this thesis that the concept of the ANCF reference node can be used to develop a complete vehicle model using one ANCF mesh in which the redundant variables are systematically eliminated at a preprocessing stage, and consequently, the number of differential and algebraic equations that need to be solved is significantly reduced.

In order to better capture the tire surface geometric details, this thesis introduces a new method for the integration of localized surface geometry within fully parameterized ANCF FEs.

SUMMARY (continued)

The localized surface geometry details can be described on ANCF element surfaces without the need for mesh refinement. The localized surface is represented using a standard computational geometry method, *Non-uniform rational B-spline* (NURBS), which can describe both conic surface and freeform surface efficiently and accurately. The basic idea of the integration of localized surface geometry with ANCF elements lies in the inclusion of such detail in the element mass matrix and forces. The integration can be implemented by overlapping the localized surface geometry on the original ANCF element or by directly trimming the ANCF element domain to fit the required shape. During the integration process, a mapping between ANCF local coordinates and NURBS localized geometric parameters is used for a consistent implementation of the overlapping and trimming methods. Additionally, two numerical integration methods are compared for the rate of convergence. The results show that the proposed subdomain integration method is better, since it is optimized for dealing with complex geometry. The proposed subdomain method can be used with any fully parameterized ANCF element. In order to analyze the accuracy of the proposed method, a cantilever plate example with localized surface geometry is used, and the simulation results with the proposed method are compared with the simulation results obtained using a commercial FE code. Two other examples that include contact with ground and localized surface geometry are also provided. These examples are a simple plate structure with surface geometry and a tire with tread details. The incompressible hyperelastic Mooney–Rivlin material model is used to describe the material used in the tire tread. It is shown through the tire contact patch that the proposed method can successfully capture the effect of the tread grooves. The rate of convergence and volumetric locking of fully parameterized ANCF elements are also discussed in this thesis.

SUMMARY (continued)

As it is the case with conventional FEs, fully parameterized ANCF FEs can experience the phenomenon of locking as well. This thesis proposes a new locking alleviation technique for ANCF beam and plate/shell elements based on a strain split approach. The thesis also surveys classical FE and ANCF locking alleviation techniques discussed in the literature. Because ANCF beam elements, which allow for the cross section stretch, fully capture the Poisson effect, Poisson locking is an issue when such beam elements are considered. The two-dimensional fully-parameterized ANCF beam element is primarily used in the locking analysis because such an element can serve as a good surrogate model for three-dimensional ANCF beams and plates/shells as far as membrane, bending and transverse shearing behavior is concerned. In addition to proposing the *strain split method* (SSM) for ANCF locking alleviation, this thesis also assesses the ANCF FE performance in the cases of higher-order interpolation, enhanced assumed strain method, elastic line method, and the enhanced continuum mechanics approach; and demonstrates the design of the enhanced strain interpolation function by using the shape functions of higher-order ANCF elements. Additionally, a new higher-order ANCF two-dimensional beam element is proposed in order to compare its performance with other FEs that require the use of other locking alleviation techniques proposed and reviewed in the thesis. Finally, several numerical examples are shown to demonstrate the effectiveness of the locking alleviation methods applied to ANCF elements. The purpose of the work on locking in this thesis is to show that dealing with locking in fully-parameterized ANCF elements is feasible and that several methods exist to effectively improve the ANCF element performance without sacrificing important ANCF element properties and features including position vector gradient continuity. Because of the use of ANCF position vector gradients as nodal coordinates, complex stress-free initially-curved geometries can be

SUMMARY (continued)

systematically obtained. Such initially-curved geometries require special attention when attempting to solve locking problems, as will be discussed in this thesis.

Finally, this thesis demonstrates an approach for developing new and detailed vehicle models that include flexible components with complex geometries, including chassis, and airless and pneumatic tires with distributed inertia and flexibility. The methodology used is based on successful integration of geometry, and small and large deformation analysis using a mechanics-based approach. The *floating frame of reference* (FFR) formulation is used to model the small deformations, whereas ANCF is used for the large deformation analysis. Both formulations are designed to correctly capture complex geometries including structural discontinuities. To this end, a new ANCF-preprocessing approach based on linear constraints that allows for systematically eliminating dependent variables and significantly reducing the component model dimension is proposed. One of the contributions of this thesis is the development of the first ANCF airless tire model which is integrated in a three-dimensional MBS algorithm designed for solving the differential/algebraic equations of detailed vehicle models. On the other hand, relatively stiff components with complex geometries, such as the vehicle chassis, are modeled using the FE/FFR formulation which creates a local linear problem that can be exploited to eliminate high frequency and insignificant deformation modes. Numerical examples that include a simple ANCF pendulum with structural discontinuities and a detailed off-road vehicle model consisting of flexible tires and chassis are presented. Three different tire types are considered in this study; a brush-type tire, a pneumatic FE/ANCF tire, and an airless FE/ANCF tire. The numerical results are obtained using the general-purpose MBS computer program **SIGMA/SAMS** (Systematic Integration of Geometric Modeling and Analysis for the Simulation of Articulated Mechanical Systems).

CHAPTER 1

INTRODUCTION

Multibody system (MBS) dynamics computer programs have become an important part of product development and analysis in several industries, and thus require continuous evolution in order to provide users with better modeling fidelity and solution accuracy. As MBS dynamics computer programs evolved over time, they saw the incorporation of finite element (FE) based modeling methods for the coupled analysis of rigid and deformable bodies. The incorporation of small deformation behavior was achieved through the floating frame of reference (FFR) formulation while the absolute nodal coordinate formulation (ANCF) helped develop fully coupled flexible MBS models capable of undergoing large deformation. With the advent of high performance computing, the fidelity and solution times of MBS models have improved as well. The constant evolution of MBS dynamics has not only led to more user friendly, efficient and accurate MBS codes, but also to better engineered products. One such product is the tire. Modeling tires in MBS computer programs is of importance to the automotive, aerospace, construction and agricultural machinery industries. In order to do so the MBS dynamics computer programs must be capable of capturing the correct geometry, material, and joint conditions, all of which may be highly nonlinear in nature. Capturing the geometric and material nonlinearities is of importance when modeling tires in MBS algorithms and computer programs, since tire modeling fidelity can significantly impact the stability, NVH (noise-vibration-harshness) and/or durability analysis of wheeled vehicles. The methods proposed in this thesis help simplify the process of integration of FE tire models in MBS algorithms and computer programs. Furthermore, this thesis also contributes to the integration of geometry within FE models, thus helping improve their fidelity while keeping their computational cost relatively low. This thesis contributes to the successful integration of

computer-aided design and analysis (I-CAD-A) and demonstrates how geometry and analysis models can be unified. Another subject that this thesis addresses is locking in ANCF FEs. Locking is a phenomenon that adversely affects the FE solution and must be dealt with for the sake of solution accuracy. Several methods on FE locking alleviation exist in the vast FE literature. This thesis reviews many of these methods used in the classical FE and ANCF literature and proposes a new method of locking alleviation for ANCF beam and plate/shell elements.

1.1 Tire Modeling

Tires are widely used in many automotive, aerospace, and construction machine applications. The stability and performance of these systems as well as their safe operation depend on the tire design and reliability. While the importance of tires for the safe operation of many systems is recognized, many tire modeling techniques do not correctly capture the tire distributed inertia and elasticity. Tire modeling and virtual prototyping techniques mainly employ three main techniques (Alvarez et al., 2005; Canudas-de-Wit et al., 2003; Clover and Bernard, 1998; Deur et al., 2004; Deur et al., 2005; Gim and Nikravesh, 1990; Gipser, 2005; Gruber et al., 2012; Kim et al., 2008; Koishi et al., 1998; Lee et al., 1997; Lugner et al., 2005; Pacejka, 2002; Sugiyama and Suda, 2009; Zegelaar et al., 2008). These techniques are the analytical approach, the discrete element approach, and the continuum-based FE approach, each of which has its advantages and disadvantages. A detailed review of tire modeling can be found in the work of Lugner et al. (2005) and Pacejka (2002). Analytical tire models, on the other hand, are based on experimentally acquired data which are curve fitted to match the vehicle dynamic response (Gim and Nikravesh, 1990; Kim et al., 2008). The discrete element models, which employ simplifying assumptions, do not capture important tire deformation modes and do not account for the distributed inertia and elasticity of the tires.

Most existing FE tire models, on the other hand, are not practical for efficient implementation in MBS algorithms and require the use of thousands of degrees of freedom (Lee et al., 1997). Additionally, these existing FE tire models employ elements that do not ensure the continuity of the rotation field at the element interfaces and nodal points, and these models require the use of co-simulation techniques when used with MBS algorithms. Because of the high dimensionality and limitations of existing tire models, the integration of FE tire models with computational MBS algorithms is still at a level that precludes full exploitation of the powerful computational MBS algorithms in developing more detailed vehicle models that include significant details. This thesis aims at addressing this deficiency in the literature by proposing a new approach for developing continuum-based tire models that have distributed inertia and elasticity.

In order to address the complexity and high dimensionality of existing FE tire models, ANCF FEs are used in this thesis. While ANCF FEs allow for accurately describing the spinning motion and account for the forces resulting from high speed reference rotations, these elements lead to a constant mass matrix, a feature that can be exploited to develop efficient tire models that can be integrated with MBS algorithms (Shabana, 2012). Furthermore, ANCF FEs allow for describing arbitrary geometry including the tire curved geometry using a relatively small number of FEs as previously demonstrated in the literature in other application areas including belt drives and track chains (Dufva et al., 2007; Maqueda et al., 2010). These elements also allow for describing the contact surface geometry by employing spline functions that can be potentially used to define complex tread shapes. Both ANCF beams and plate/shell elements can be effectively used in developing new tire models. New constrained dynamics concepts must be introduced in order to develop efficient tire assembly models. ANCF FEs allow for developing an efficient tire assembly model that can be systematically integrated with MBS algorithms. The flexible tire belt

structure and the rigid rim are modeled as one FE mesh, thereby allowing for the tire assembly at a preprocessing stage. The interface between the flexible belt and rigid rim is represented using linear algebraic equations which are used to eliminate dependent variables at a preprocessing stage before the start of the simulation. This can be achieved because the use of the ANCF absolute positions and gradients as nodal coordinates allows defining joints, including rigid joints, using linear constraint equations. An ANCF preprocessor can also be developed such that the joints can be defined at arbitrary points that are not necessarily nodal points (Hamed et al., 2015). The rigid rim can be defined using the concept of the ANCF reference node which is not associated with any of the tire mesh FEs (Shabana, 2015A; Shabana, 2015B). The concept of the reference node allows for developing a detailed tire assembly model as the one shown in Figure 1 using one ANCF mesh. In this assembly model, each tire has its own spin rotation degree of freedom (Shabana, 2015B). The ANCF reference node has a set of nodal coordinates that include absolute position vector and three gradient vectors when fully parameterized ANCF FEs are used.

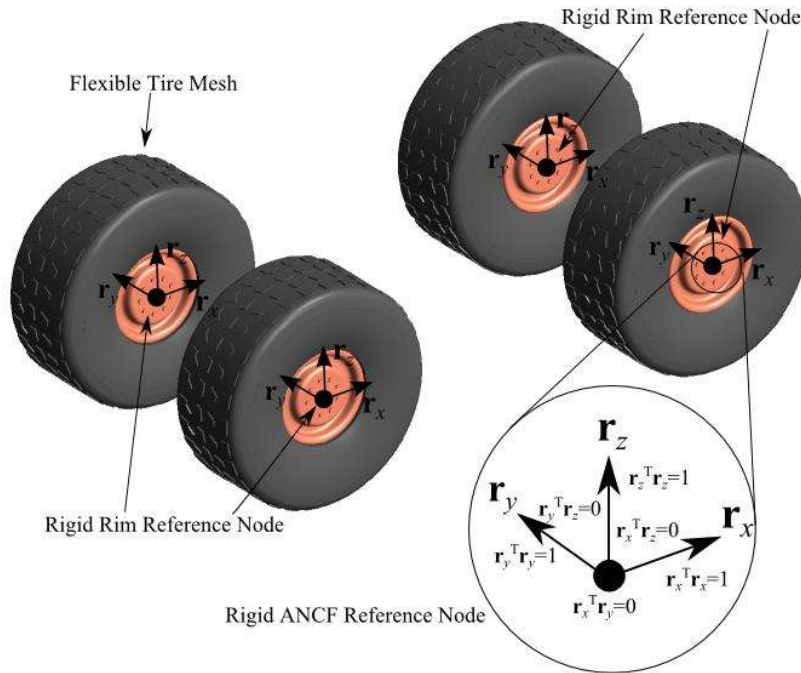





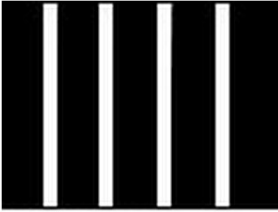

Figure 1. One ANCF-mesh-four-wheel assembly

If gradient deficient plate FEs are used, the rim reference node has a set of coordinates that include absolute position vector and two gradient vectors. Using the rim reference node and linear interpolation, the inertia coefficients associated with the position and gradient coordinates of the rim reference node can be systematically developed. In the assembled tire model proposed in this thesis, it is necessary to define the rim inertia associated with the gradient coordinates of the rim node in order to obtain a non-singular inertia matrix for the tire mesh. Because of the fact that this positive definite inertia matrix is constant, a Cholesky transformation can be used to obtain an identity generalized inertia matrix associated with the ANCF Cholesky coordinates (Shabana, 2012). A set of nonlinear algebraic constraint equations is imposed on the reference node gradient vectors during the dynamic simulation in order to ensure the rigidity of the rim. These equations are solved simultaneously with the tire dynamic equations.

1.2 Localized Surface Geometry in FEs

Because detailed localized surface geometry is found in many structural and mechanical system applications, considering the effect of such geometry during the FE or flexible MBS analysis is important. An example of localized geometry that affects the behavior of a system is the tread details in a tire. Table 1 shows a classification of the different kinds of tread details that are specific to the application type of the tire they are designed for. In some cases, simplification of the tire model by ignoring such details may be a reasonable assumption, however in certain analyses like hydroplaning situations ignoring the tread details can lead to incorrect results. Hence, including localized geometry in the FE or flexible MBS analysis is essential in certain simulation scenarios. When classical FE methods are used with MBS dynamics codes, difficulties are encountered in achieving the correct solution for problems involving large deformation and rotation due to the

Table 1. Tread classification for commercial tires [<https://www.yokohamaotr.com/otr/tires-101/otr-technology/tread-designs>]

<i>Type</i>	<i>Pattern</i>	<i>Properties</i>
Rock		<ul style="list-style-type: none"> • Application: Off-the-road vehicles (OTR) • Excellent cut resistance • Large ground contact area
Traction		<ul style="list-style-type: none"> • Application: High traction vehicle (OTR, truck) • Directional tread pattern • Excellent traction
Block/Lug		<ul style="list-style-type: none"> • Application: Trucks, OTR vehicles • Wide tread and rounded shoulders • Low contact pressure • Good on soft and muddy terrains • Excellent traction
Rib		<ul style="list-style-type: none"> • Application: Automotive, trucks • Grooves running parallel to direction of motion • High directional stability • Excellent fuel economy
Smooth		<ul style="list-style-type: none"> • Application: Underground mines, construction • High wear and cut resistance • Used for compaction and leveling • Narrow groove on edge used to measure tread wear

incremental-rotation assumptions used in existing FE formulations (Neto et al., 2004; Shabana, 1997; Das et al., 2010). The ANCF method which uses absolute positions and gradients as nodal coordinates can not only capture correct rigid body motion and large deformation but also has the advantages of a constant inertia matrix and zero Coriolis and centrifugal forces, and can describe a freeform surface's geometry accurately (Sanborn and Shabana, 2009; Lan and Shabana, 2010). Due to the fact that a non-incremental solution procedure can be used, ANCF elements can be easily implemented in general purpose MBS algorithms. Although ANCF has many advantages in

the simulation of very flexible bodies, the representation of localized surface geometry, such as holes, grooves and protrusions which can play significant roles in the overall dynamics of the structure, without mesh refinement remains a challenge (Cho et al., 2004; Gipser, 2005; Lugner et al., 2005; Pacejka, 2006). Depending on the goal of the simulation, ignoring such details could potentially lead to incorrect solutions (Cho et al., 2004).

Capturing detailed localized geometry is a challenging research topic in the Computer Aided Design (CAD) field as well (Li and Ke, 2000; Schmidt et al., 2012). In the CAD field, the main methods for representing complex shapes include trimming, sewing and Boolean operations, wherein small surface patches or small solids are used to represent complex geometric shapes; an approach that can be computationally quite expensive and may cause problems such as geometric error or numerical instabilities (Li and Ke, 2000). In order to circumvent such processes in the Computer Aided Engineering (CAE) field, the FE models are often simplified by simply removing local geometric features from the overall body before meshing or subjected to mesh refinement until the desired geometry details are captured (Cho et al., 2004; Ito et al., 2009; Kagan et al., 2003). Nonetheless as previously mentioned, ignoring some of these geometric details may not be acceptable in certain analysis scenarios. On the other hand, refining the mesh may cause the mesh data to increase exponentially and prolong the computation time greatly. Sometimes a very fine mesh can make the analysis almost impossible because of the limitations on the computer memory and processing capabilities. Several researchers have recently focused their investigations on new meshing methods or elements that enable local refinement (Kagan et al., 2003; Kleiss et al., 2012) by making use of hierarchical B-splines and NURBS (Bornemann and Cirak, 2013), T-splines (Uhm and Youn, 2009) and PHT splines (Wang et al., 2011). Such methods are effective both in reducing the mesh size and obtaining accurate results (Cho et al., 2004). These methods however

are complicated to implement, and their effectiveness depends on the given geometry being analyzed. Furthermore, such methods that are dependent on a rigid recurrence scheme could pose several problems when used with ANCF elements (Gantoi et al., 2013).

1.3 Locking in ANCF FEs

ANCF was proposed as a new FE formulation designed for correctly and efficiently capturing large deformation and rotation effects in a non-incremental solution framework (Shabana, 1997). Over the past two decades, a significant amount of research has been conducted on ANCF elements and its applications. ANCF element technology includes several different types of beam, plate/shell and solid elements based on standard polynomial basis functions (Von Dombrowski, 1997; Omar and Shabana, 2001; Mikkola and Shabana, 2003; Shabana, 2013; Olshevskiy et al., 2014), rational basis functions (Sanborn and Shabana, 2009; Pappalardo et al. 2016A) and with rotations as degrees of freedom instead of gradient vectors (Zheng and Shabana, 2017; Pappalardo et al., 2016B). ANCF elements have been used in a diverse range of applications like tracked vehicles, tires, satellites and pantograph-catenary systems (Hamed et al., 2015; Patel et al., 2016; Liu et al., 2011; Kulkarni et al., 2017). However, like classical FEs, ANCF elements can suffer from the locking phenomenon. ANCF locking has been studied by several authors in the past and solutions have been proposed. Detailed reviews on ANCF formulation and elements can be found in the work of Gerstmayr et al. (2013) and Nachbagauer (2014). Some types of locking that ANCF elements can suffer from include shear, volumetric and Poisson locking. Of these, Poisson locking particularly affects ANCF beam and plate/shell elements due to the different orders of interpolation in the longitudinal/in-plane and thickness direction. This thesis proposes a new locking alleviation technique for dealing with Poisson locking in ANCF beam and plate/shell elements and reviews

and compares several other locking alleviation techniques used with such structural ANCF elements.

1.4 Vehicle Modeling: Small and Large Deformation and Structural Discontinuities

This thesis is also concerned with the development of new detailed MBS small- and large-deformation vehicle models consisting of components with complex geometries including structural discontinuities. Despite the fact that computational rigid MBS algorithms have been widely used in the analysis of vehicle systems since the 1980s (Orlandea, 1973; Haug et al., 1981), incorporating component flexibility is necessary in order to develop high fidelity vehicle models that can be effectively used in accurate and reliable durability investigations. The *finite element floating frame of reference* (FE/FFR) formulation, introduced in the early 1980's for the small-deformation analysis of MBS applications with structural discontinuities (Shabana, 2013), leads to accurate representation of the nonlinear inertia forces and coupling between the reference and elastic displacements. An example of a vehicle component with structural discontinuities is the chassis depicted in Figure 2 which shows slope discontinuities at several locations in which beam structures are connected.

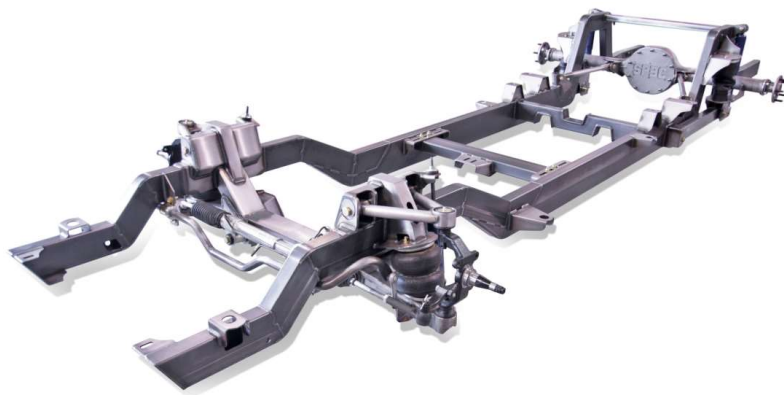


Figure 2. Structural discontinuities in a truck chassis (<http://roadstershop.com/product/full-chassis/1967-72-c10-truck-spec-chassis/>)

Because in the FFR formulation, the FE deformation is described in the body coordinate system and the large rotation and translation of the flexible body are described using the local body coordinate system which serves as the body reference, the FE/FFR formulation allows using non-isoparametric elements with large-rotation non-incremental MBS solution procedures.



Figure 3. Pneumatic off-road tire (upper figure) and airless off-road tire (lower figure)

(Upper figure: <http://www.nittotire.com/light-truck-tires/trail-grappler-mud-terrain-light-truck-tire/>; lower figure: <http://croctyres.com.au/wp-content/uploads/2015/12/image10.jpg/>)

The analysis of the large deformation, on the other hand, can be accomplished using ANCF (Patel et al., 2016; Recuero et al., 2016B; Shabana, 2012). ANCF elements employ gradient vectors instead of infinitesimal rotations as nodal coordinates, allowing for exact description of rigid body motion even in the case of beam, plate, and shell elements. Fully parameterized ANCF elements, in particular, can be used to systematically describe structural discontinuities of components made of relatively softer materials such as tires. Figure 3 depicts two different types of tires that will be considered in this thesis. The first is a pneumatic tire which has smooth nominal geometry, while the second is an airless tire which has slope discontinuities. The fact that there is no distinction between plate and shell structures when ANCF elements are used allows for developing complex geometry models by proper selection of the nodal coordinates in the reference configuration.

MBS dynamics, widely used in the analysis of wheeled vehicles (Blundell and Harty, 2004), provides significant insight on the design and performance of the vehicle before a working prototype can be manufactured. While the FE/FFR formulation was introduced more than three decades ago, long before ANCF elements were introduced, there exists a large number of vehicle applications in which the use of the small-deformation FE/FFR formulation can contribute to developing accurate and efficient computer models, particularly when combined with an ANCF large-deformation approach. Efficient modeling of vehicle systems that include stiff chassis and more flexible tires will require efficient implementation of both methods in computational MBS algorithms. The two methods, however, employ two fundamentally different approaches for the treatment of structural discontinuities. In the FE/FFR approach, in which infinitesimal rotations are used as nodal coordinates, a conventional vector coordinate transformation is used; while in the ANCF approach, in which gradients are used as nodal coordinates, a gradient transformation

must be used to account for the effect of structural discontinuities. In the FFR approach, an intermediate element coordinate system must be introduced, while the ANCF approach does not require the use of such an intermediate coordinate system for the treatment of structural discontinuities because of the use of the position vector gradients.

Several vehicle components like the chassis shown in Figure 2 are typically modeled using the FE/FFR approach since a small-deformation assumption can be made. The FE/FFR formulation was used to study the nonlinear dynamics of a vehicle traversing over an obstacle with the goal of examining the chassis deformation by Shabana (1985). The FFR three-dimensional beam element was used to model the chassis of a dune buggy subjected to external excitation through a half-sine function based road bump (Agrawal and Shabana, 1986). Ambrosio and Goncalves (2001) compared the results of the rigid and flexible chassis models of a detailed sport vehicle undergoing various maneuver tests. Sampo (2011) studied the dynamics of a formula student vehicle by considering the chassis flexibility. Shiiba et al. (2012) investigated the effect of using several non-modal model order reduction techniques on the flexible chassis of a detailed racing vehicle model with specific emphasis on ride characteristics. Carpinelli et al. (2012) compared rigid and flexible body models for the prediction of ride and handling characteristics of a commercial sedan vehicle. Goncalves and Ambrosio (2003) optimized the suspension spring and damper coefficients of a wheeled vehicle that included a flexible chassis.

Another deformable vehicle component whose behavior has significant effect on the vehicle performance is the tire whose behavior is characterized by large rotation and deformation. Several tire models have been proposed over the past two decades for use with MBS vehicle models that include formula-based curve-fitted, discrete mass-spring-damper-based, and FE-based models. The formula-based tire models are typically used for vehicle dynamics simulations where

the analysis is concerned with low-frequency tire and vehicle dynamics. The *Magic Formula* tire model proposed by Pacejka (2002) is an example of a widely used formula-based tire model. The discrete mass-spring-damper models yield better fidelity and are typically used in ride quality and durability simulations. Several commercial MBS software have implemented the discrete mass-spring-damper-based FTire model proposed by Gipser (2005). The FE-based tire models can capture a larger spectrum of frequency response and are also used for NVH (noise-vibration-harshness) and durability analyses where the tire high frequency response and stress is studied as well (Koishi et al., 1998). While there is a very large number of investigations on the FE modeling of tires, there is a relatively small number of investigations that couple FE tires and MBS vehicle models without the use of co-simulation techniques. A new ANCF method of tire-rim assembly was recently proposed (Shabana, 2015B), and was used by Patel et al. (2016) to develop a new tire model in which the tire was modeled using ANCF plate/shell elements and the rim was modeled using the ANCF reference node. Recuero et al. (2016B) demonstrated the use of ANCF elements in the simulation of the tire/soil interaction, whereas Pappalardo et al. used the rational ANCF elements (2016A) and the so-called consistent rotation-based formulation (ANCF/CRBF) elements (2016B) to model the tire. Yamashita et al. (2016) modeled the tire using the bilinear ANCF shell element and demonstrated braking and cornering scenarios with the tire model. Sugiyama and Suda (2009) modeled the tire as a ring-type structure using planar curved ANCF beam elements and compared its vibration modes with analytical and experimental results. Recuero et al. (2017) examined the tire-soil interaction using a co-simulated rigid body vehicle model, FE tire model that utilized bilinear shell elements, and DEM (discrete element method) soil model.

1.5 Scope and Organization of the Thesis

Chapter 2 was published in the *Proceedings of the Institution of Mechanical Engineers, Part K: Journal of Multi-body Dynamics* and is used in this thesis based on the author reuse rights as shown in Appendix A (Patel et al., 2016). Chapter 2 is focused on making the following specific new contributions regarding tire modeling in MBS models. It is shown for the first time how ANCF tire models can be integrated with computational MBS algorithms by using new concepts recently introduced. The concept of the ANCF reference node is used to develop a tire assembly in which a vehicle model, including the tires, can be represented using one ANCF mesh in which the linear connectivity conditions are used to eliminate redundant variables at a preprocessing stage. Example of such vehicle models that will be considered in this chapter is shown in Figure 4.

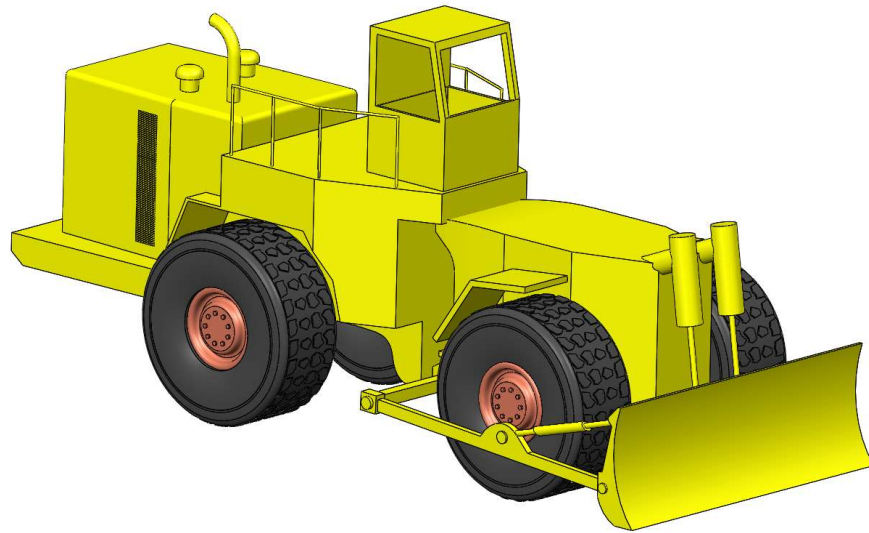


Figure 4. Wheeled bulldozer model

Integration of high fidelity FE tire models with MBS algorithms using existing solution procedures requires the use of co-simulation techniques in which two different computer codes, FE and MBS codes, are used. This chapter shows how FE vehicle models that include tires with distributed

inertia and elasticity can be developed without the need for using co-simulation techniques. In this chapter, only one MBS computer code is used in the analysis of the new vehicle models. In the developed ANCF vehicle mesh, the reference node inertia matrix must be correctly formulated in order to avoid singularities. It is shown in this chapter how the optimum sparse matrix structure of the dynamic equations of motion can be preserved by introducing a minimum set of nonlinear algebraic equations that ensure the rigidity of the rims, axles, and possibly the chassis of the vehicle. Chapter 2 also presents a continuum-based air pressure model that allows for accounting for the change of the inner surface area of the tire. In this continuum-based air pressure model, Nanson's formula is used to define the area in the current deformed configuration in terms of the area in the reference configuration. This new continuum-based air pressure model can be used as alternative to the discrete spring models often used in the literature to model the tire air pressure. General and more accurate tire models require the use of composite materials. It is shown in this chapter how an ANCF composite tire model can be systematically developed and integrated with MBS algorithms. To this end, fully parameterized ANCF plate elements are used. The results obtained using the composite and non-composite tire models are compared. The result of this chapter will allow developing new efficient detailed tire models which can be integrated with MBS algorithms. This, in turn, will allow for exploiting the powerful MBS techniques in the analysis of new vehicle models that include significant details that cannot be captured using existing analysis and simulation methods.

Chapter 3 was published in *Computer Methods in Applied Mechanics and Engineering* and is used in this thesis based on the author reuse rights as shown in Appendix A (He et al., 2017). Chapter 3 proposes a new method for the implementation of localized geometry into ANCF FE surfaces. The proposed method can be used with any fully parameterized ANCF element. This

chapter reviews the three levels of including localized surface geometry in FE methods, briefly introduces the concepts and methodologies used in the definition of fully parameterized ANCF elements, describes two methods of integrating localized surface geometry with ANCF elements, compares the results obtained using the global domain integration method and subdomain integration method and briefly describes the governing equations of motion and the contact method used in the numerical examples presented in this chapter. Chapter 3 also presents three numerical examples and compares the results obtained using the approach described in this chapter with the results obtained using a commercial FE code in order to demonstrate the effectiveness of the proposed approach.

The aim of **Chapter 4** (Patel and Shabana, 2017; submitted to *Acta Mechanica*) is multi-fold; however, the overall focus of the chapter is on locking alleviation techniques in ANCF. Two-dimensional ANCF beam elements are primarily used in this chapter to demonstrate the effectiveness of the locking alleviation techniques proposed and discussed in this chapter since they can be considered as a good surrogate to understand and quantify the membrane, bending and transverse shear related response of three-dimensional beam and plate/shell elements. The contents of this chapter are as follows: Locking alleviation techniques in the classical FE literature are reviewed and discussed in order to emphasize the fact that locking is a commonly occurring phenomenon in most FEs and can be dealt with in the case of fully-parameterized ANCF elements by identifying the cause of the locking and studying previous contributions in this area. Existing ANCF locking alleviation techniques are briefly reviewed and ANCF element kinematics and the general continuum mechanics approach are briefly discussed. A new two-dimensional higher-order beam element is proposed, followed by a short discussion on the effect of constitutive model assumptions on the planar ANCF beam element. A new locking alleviation technique called the

strain split method (SSM) is proposed for two-dimensional beam elements, and is generalized for three-dimensional beam and plate/shell elements. The enhanced continuum mechanics approach and the elastic line approach are briefly reviewed. The enhanced assumed strain approach is also reviewed and a method of incorporating higher-order ANCF shape functions in lower-order beams through enhanced strains is demonstrated. Finally, this chapter compares the locking alleviation techniques proposed and discussed in it using five numerical examples that include three static and two dynamic examples.

Chapter 5 (Patel et al., 2017; submitted to *International Journal of Vehicle Performance*) focuses on developing a computational framework based on the integration of geometry and small- and large-deformation analysis for the nonlinear dynamics of detailed vehicle models that consist of rigid and flexible bodies. The proposed approach captures accurately structural discontinuities that characterize the chassis (as the one shown in Figure 2) and airless tires (shown in Figure 3). In this geometry-based approach, the chassis and tires are modeled as flexible bodies using the small-deformation FFR and large-deformation ANCF elements, respectively. Specifically, the main contents of this chapter can be summarized as follows: The first ANCF airless tire model with distributed inertia and elasticity is developed in this chapter and integrated with computational MBS algorithms without the need for using co-simulation techniques. The FE model accurately captures the structural discontinuities that characterize this tire type. An approach for vehicle assembly based on the integration of rigid body, small-deformation FFR, and large-deformation ANCF algorithms is proposed for developing new and detailed vehicle models. Stiff components such as the chassis are modeled using FFR elements, while more flexible components such as the tires are modeled using ANCF elements. A new method for the treatment of structural discontinuities using ANCF elements is proposed. In the new approach, linear algebraic constraint

equations are formulated at a preprocessing stage, thereby allowing for systematically reducing the model dimension by eliminating dependent variables before the start of the dynamic simulation. A damping model for ANCF pneumatic tires is introduced which accounts for the energy dissipation in the tire material as well as due to the pressurized air in a tire model. New **high-mobility multi-purpose wheeled vehicle (HMMWV)** models are developed in this chapter as well. In one model, airless tires are used, while in a second model pneumatic tires are used. Both tires models are described using ANCF elements. In the vehicle models developed, the chassis is modeled using FFR elements, and a component-mode synthesis method is used to eliminate insignificant high frequency modes. Using the HMMWV model, the chapter presents a comparative study based on three different vehicle models. The first model is the vehicle with brush-type tires, the second is a vehicle with pneumatic tires, and the third is a vehicle with airless tires. The results obtained using these three different models are compared.

Chapter 6 consists of a summary of the conclusions regarding the approaches proposed and numerical examples discussed in Chapters 2 to 5. Chapter 6 also briefly discusses potential future work with regards to the methods proposed in this thesis.

CHAPTER 2

ANCF TIRE MODELING

This chapter (published as Patel et al., 2016) introduces a new computational multibody system (MBS) framework for developing accurate tire models using the finite element (FE) absolute nodal coordinate formulation (ANCF). ANCF plate/shell FEs are used to create the geometry and perform the FE/MBS analysis of the tires. It is important to note that in ANCF there is no difference between plate and shell elements due to the use of position vector gradients which help with shaping the element to the required geometry. The computational procedure used in this study allows for modeling composite tires and for using a continuum-based air pressure and contact tire force models. The ANCF tire mesh, which allows for high spinning speed, has a constant inertia matrix and zero Coriolis and centrifugal forces. The concept of the ANCF reference node, introduced recently, is used to develop linear connectivity conditions between the tire and rim, thereby allowing for imposing these linear conditions at a preprocessing stage. Using this approach, the dependent variables are eliminated at a preprocessing stage before the start of the simulation. The reference node, which is not associated with a particular FE, is used to define the inertia of the rigid rims. The inertia coefficients associated with the rim reference nodes are first developed in terms of the ANCF position and gradient coordinates. The rigidity of each rim is enforced during the dynamic analysis using six nonlinear algebraic constraint equations that are combined with the dynamic differential equations of motion using the technique of Lagrange multipliers. It is shown in this chapter that the concept of the ANCF reference node can be used to develop a complete vehicle model using one ANCF mesh in which the redundant variables are systematically eliminated at a preprocessing stage, and consequently, the number of differential and algebraic equations that need to be solved is significantly reduced. The use of the new

approach proposed in this chapter is demonstrated using a vehicle model described by one ANCF mesh.

2.1 ANCF Tire Geometry

ANCF FEs will be used in this chapter for creating the geometry and performing the analysis of the tire system. These elements can be used as the basis for a successful integration of computer aided design and analysis (ICADA). The ANCF position field can be written as $\mathbf{r}(\mathbf{x}, t) = \mathbf{S}(\mathbf{x}) \mathbf{e}(t)$, where \mathbf{r} is the global position vector, $\mathbf{x} = [x \ y \ z]^T$ is the vector of the element spatial coordinates, t is time, $\mathbf{S} = \mathbf{S}(\mathbf{x})$ is the element shape function matrix, and $\mathbf{e}(t)$ is the vector of the element nodal coordinates that include absolute position and gradient coordinates (Shabana, 2012). The vector of ANCF nodal coordinates $\mathbf{e}(t)$ can be written as $\mathbf{e}(t) = \mathbf{e}_o + \mathbf{e}_d(t)$, where \mathbf{e}_o is the vector of nodal coordinates in the reference configuration, and \mathbf{e}_d is the vector of nodal displacements. Using this partitioning, the assumed displacement field can be written as $\mathbf{r}(\mathbf{x}, t) = \mathbf{S}(\mathbf{x}) \mathbf{e}(t) = \mathbf{S}(\mathbf{x}) (\mathbf{e}_o + \mathbf{e}_d(t))$. This description is consistent with the general continuum mechanics description $\mathbf{r}(\mathbf{X}, t) = \mathbf{X} + \mathbf{u}(\mathbf{X}, t)$, where \mathbf{X} is the absolute position vector of an arbitrary point in the reference configuration, and \mathbf{u} is the displacement vector. This can be made clearer if one writes $\mathbf{X} = \mathbf{S} \mathbf{e}_o$ and $\mathbf{u} = \mathbf{S} \mathbf{e}_d$. By appropriate choice of the vector \mathbf{e}_o , initially curved structures can be defined in a straight forward manner using ANCF FEs (Shabana, 2015B). The relationship between the volume of the curved structure V_o in the initial configuration to the volume of the straight structure V (Figure 5) is defined as $dV_o = J_o dV$, where $J_o = |\mathbf{J}_o|$ is the determinant of the matrix of position vector gradients $\mathbf{J}_o = \partial \mathbf{X} / \partial \mathbf{x} = \partial (\mathbf{S} \mathbf{e}_o) / \partial \mathbf{x}$, which is constant.

Therefore, integration with respect to the domain V_o can be converted to integration with respect to the straight element domain V by using the relation $dV_o = J_o dV$. This allows for using the original element dimensions to carry out the integrations associated with the initially curved configuration.

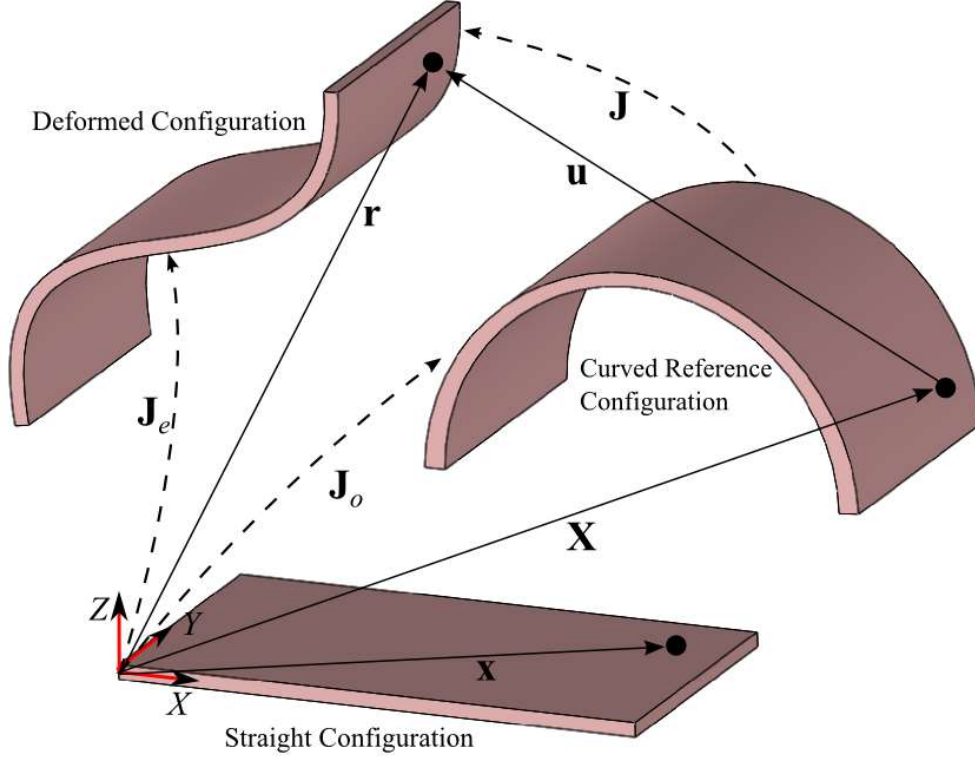


Figure 5. Initially curved ANCF structures

The Lagrangian strain tensor $\boldsymbol{\varepsilon}$ is defined as $\boldsymbol{\varepsilon} = (\mathbf{J}^T \mathbf{J} - \mathbf{I})/2$. This tensor can be defined using the ANCF description as

$$\mathbf{J} = \frac{\partial \mathbf{r}}{\partial \mathbf{X}} = \left(\frac{\partial \mathbf{r}}{\partial \mathbf{x}} \right) \left(\frac{\partial \mathbf{x}}{\partial \mathbf{X}} \right) = \left(\frac{\partial (\mathbf{S} \mathbf{e})}{\partial \mathbf{x}} \right) \mathbf{J}_o^{-1} = \mathbf{J}_e \mathbf{J}_o^{-1} \quad (1)$$

where $\mathbf{J}_e = \partial(\mathbf{S} \mathbf{e})/\partial \mathbf{x}$. Therefore, the Lagrangian strain tensor can be written as

$$\boldsymbol{\varepsilon} = \frac{1}{2}(\mathbf{J}^T \mathbf{J} - \mathbf{I}) = \frac{1}{2}(\mathbf{J}_o^{-1T} (\mathbf{J}_e^T \mathbf{J}_e) \mathbf{J}_o^{-1} - \mathbf{I}) \quad (2)$$

The relationship between the volume in the current deformed configuration v and the volume in the curved reference configuration V_o can be written as $dv = JdV_o$, where $J = |\mathbf{J}|$ is the determinant of the matrix of position gradients \mathbf{J} . It follows that $dv = JdV_o = |\mathbf{J}_e| |\mathbf{J}_o^{-1}| dV_o$. Using the relationship $dV_o = J_o dV$, one has $dv = |\mathbf{J}_e| dV$ (Shabana, 2012). The procedure described in this section to model the initial curvature was used in the literature in the analysis of belt drives and rubber chains (Dufva et al., 2007; Maqueda et al., 2010).

Several ANCF beam and plate FEs can be used to develop efficient tire models that have distributed inertia and elasticity. Fully parameterized ANCF FEs allow for capturing important tire details using a spline function parametric relationship that converts a volume to a surface with arbitrary shape. In this chapter, fully parameterized ANCF plate elements are used. The superscript i will be used to refer to the tire number, while the superscript j will refer to the element number. When ANCF fully parameterized elements are used, the global position vector \mathbf{r}^{ij} of an arbitrary point on the element j of a tire i can be defined using the element shape function matrix \mathbf{S}^{ij} and the vector of nodal coordinates \mathbf{e}^{ij} as $\mathbf{r}^{ij} = \mathbf{S}^{ij}(x, y, z) \mathbf{e}^{ij}(t)$, where t is time, and x , y , and z are the local element coordinates. As previously mentioned, the vector of nodal coordinates \mathbf{e}^{ij} consists of absolute position and gradient coordinates. A node of a fully parameterized element in the three-dimensional analysis can have twelve coordinates that define the global position vector of the node and the three gradient vectors $\mathbf{r}_x^{ij} = \partial \mathbf{r}^{ij} / \partial x$, $\mathbf{r}_y^{ij} = \partial \mathbf{r}^{ij} / \partial y$, and $\mathbf{r}_z^{ij} = \partial \mathbf{r}^{ij} / \partial z$ (Shabana, 2012; Dufva et al., 2007; Maqueda et al., 2010; Gantoi et al., 2013). The representation

$\mathbf{r}^{ij} = \mathbf{S}^{ij}(x, y, z)\mathbf{e}^{ij}(t)$ describes a volume since three parameters (coordinate lines) x , y , and z are used for this fully parameterized element.

While this chapter will be mainly concerned with the contributions outlined in Section 1.5 of Chapter 1, it is important to point out that the ANCF representation allows for systematically converting volume geometry to surface geometry (Gantoi et al., 2013). This can be accomplished by eliminating one of the independent parameters by writing this parameter in terms of the other two. For example, the use of the functional relationship $z = f(y)$ converts the ANCF volume geometry to surface geometry by writing $\mathbf{r}^{ij} = \mathbf{S}^{ij}(x, y, f(y))\mathbf{e}^{ij}(t)$, where $f(y)$ is a known function that can be used to define the surface shape. A more general two-parameter function relationship such as $z = f(x, y)$ can also be used. Spline function representations can be used to define the parametric relationship.

2.2 Air Pressure and Contact Forces

In this section, a continuum-based air pressure tire force model is introduced. This pressure force model can be used instead of the discrete spring models often used in the literature to model the tire air pressure. The formulation of the tire/ground contact force used in this chapter is also explained in this section.

2.2.1 Air Pressure Force

Air pressure tire forces require integration over areas as shown in Figure 6. One approach to consider the effect of the air pressure in tire applications is to write an expression for the tire pressure acting on the surface of the element j of the tire i as $p_i = p_t(\mathbf{e}^{ij}, t)$, where \mathbf{e}^{ij} is the

vector of ANCF tire coordinates. The pressure is assumed to apply in a direction normal to the surface defined by the unit normal \mathbf{n}^{ij} . One can therefore define the pressure vector $\mathbf{p}_t = \mathbf{p}_t(\mathbf{e}^{ij}, t) = p_t \mathbf{n}^{ij}$. The position vector of the material points on the surface can be written as $\mathbf{r}^{ij} = \mathbf{r}^{ij}(\alpha_1, \alpha_2)$, where α_1 and α_2 are the parameters that define the surface. Using ANCF description, one can, without any loss of generality, select α_1 and α_2 such that $\alpha_1 = x$ and $\alpha_2 = y$. A unit normal to the surface \mathbf{n}^{ij} can be defined as $\mathbf{n}^{ij} = \mathbf{r}_{\alpha_1}^{ij} \times \mathbf{r}_{\alpha_2}^{ij} / \|\mathbf{r}_{\alpha_1}^{ij} \times \mathbf{r}_{\alpha_2}^{ij}\|$.

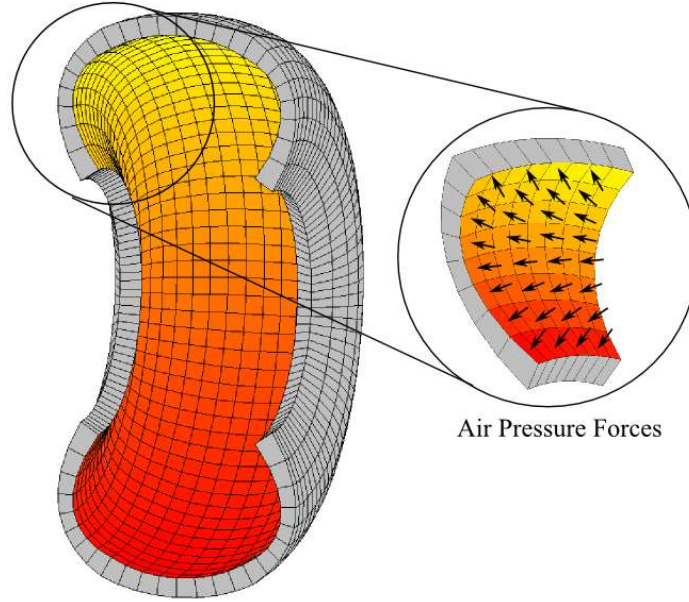


Figure 6. Air pressure

The virtual work of the pressure force can then be written as $\delta W_p^{ij} = \int_s \mathbf{p}_t^T \delta \mathbf{r}^{ij} ds^{ij}$, where s^{ij} is the area in the current configuration. Using Nanson's formula, one can write ds^{ij} in terms of the area defined in the reference configuration as $ds^{ij} = \left(J^{ij} / \sqrt{\mathbf{n}^{ijT} \mathbf{J}^{ij} \mathbf{J}^{ijT} \mathbf{n}^{ij}} \right) dS_o^{ij}$, where J^{ij} is the determinant of the matrix of position vector gradients \mathbf{J}^{ij} , and S_o^{ij} is the area in the reference configuration. It follows that the virtual work of the tire pressure forces can be written as

$\delta W_p^{ij} = \int_{S_o^{ij}} \left(J^{ij} p_t \mathbf{n}^{ij} / \sqrt{\mathbf{n}^{ijT} \mathbf{J}^{ij} \mathbf{J}^{ijT} \mathbf{n}^{ij}} \right)^T \delta \mathbf{r}^{ij} dS_o^{ij}$. One can also define S_o^{ij} in terms of S^{ij} that defines the area in the straight configuration.

Using the ANCF description $\mathbf{r}^{ij} = \mathbf{S}^{ij}(\mathbf{x}) \mathbf{e}^{ij}$, one can write the virtual work of the pressure force as $\delta W_p^{ij} = \left(\int_{S_o^{ij}} \left(J^{ij} p_t \mathbf{n}^{ij} / \sqrt{\mathbf{n}^{ijT} \mathbf{J}^{ij} \mathbf{J}^{ijT} \mathbf{n}^{ij}} \right)^T \mathbf{S}^{ij}(\mathbf{x}) dS_o^{ij} \right) \delta \mathbf{e}^{ij}$. This equation can be written as

$\delta W_p^{ij} = \mathbf{Q}_p^{ijT} \delta \mathbf{e}^{ij}$, where the vector of generalized pressure forces is defined as

$\mathbf{Q}_p^{ij} = \int_{S_o^{ij}} \mathbf{S}^{ijT} \left(J^{ij} p_t \mathbf{n}^{ij} / \sqrt{\mathbf{n}^{ijT} \mathbf{J}^{ij} \mathbf{J}^{ijT} \mathbf{n}^{ij}} \right) dS_o^{ij}$. This vector, which has dimension equal to the

dimension of the vector of generalized coordinates of the FE, can be evaluated using numerical

integration methods. In the case of small deformation, $J^{ij} / \sqrt{\mathbf{n}^{ijT} \mathbf{J}^{ij} \mathbf{J}^{ijT} \mathbf{n}^{ij}} \approx 1$, and the expression

of the vector of generalized pressure force reduces to $\mathbf{Q}_p^{ij} = \int_{S_o^{ij}} \mathbf{S}^{ijT} (p_t \mathbf{n}^{ij}) dS_o^{ij}$.

2.2.2 Tire/Ground Contact Force

A simple contact model is employed in this chapter for the tire/ground contact. The model is based on a penalty approach and coulomb friction and is similar to the model used for belt drives by Dufva et al. (2007). A grid of contact points is generated on each plate element and the normal and tangential contact forces are applied at these points as shown in Figure 7. Each point is detected for ground penetration and for its relative velocity with respect to the ground in order to apply the corresponding normal and tangential forces. The contact forces are treated as point forces in this chapter where the normal component is defined as $\mathbf{f}_n^{ij} = (k_p d + c_p \dot{d}) \mathbf{n}$, where \mathbf{f}_n^{ij} is the normal component of the contact force, k_p is the ground stiffness coefficient, c_p is the ground damping

coefficient, d is the penetration, \dot{d} is the rate of penetration, and \mathbf{n} is the unit normal to the ground surface.

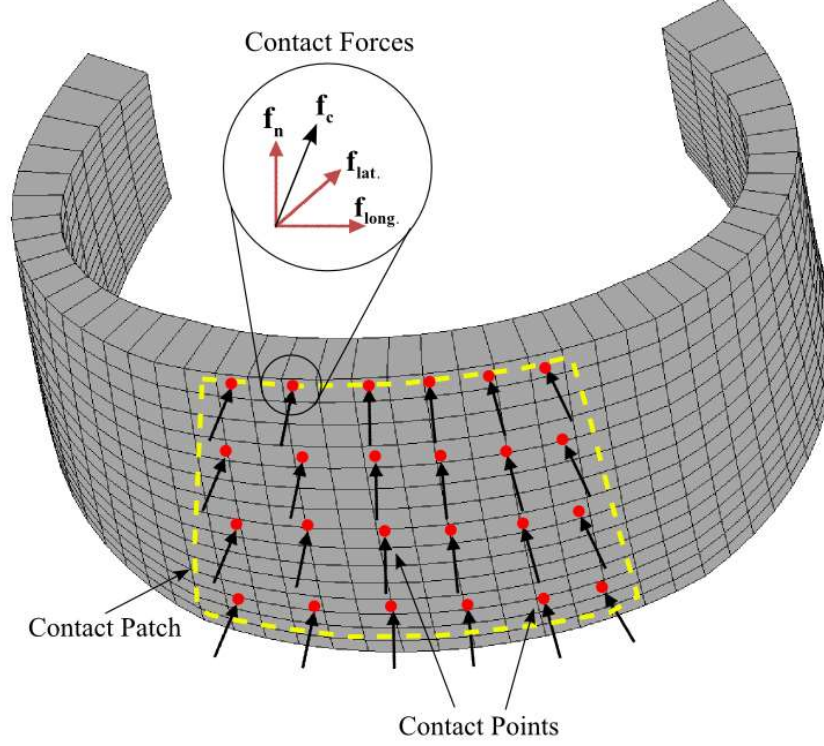


Figure 7. Contact forces

The ground surface can be described by surface functions that can be possibly generated through experimentally recorded ground surface data. Using these data and curve fitting, the unit normal to the surface can be determined and used in the formulation of the contact force. The penetration d is calculated as $d = (\mathbf{r}_p^{ij} - \mathbf{r}_p^g) \cdot \mathbf{n}$, where \mathbf{r}_p^{ij} is the global position of the contact point on the tire and \mathbf{r}_p^g is the global position of the corresponding contact point on the ground surface. The velocity vector at the contact point on the element can be written as $\dot{\mathbf{r}}_p^{ij}(\mathbf{x}, t) = \mathbf{S}^{ij}(\mathbf{x})\dot{\mathbf{e}}^{ij}(t)$, and the tangential velocity which is used to define the direction of the friction forces is given as $\mathbf{v}_{tP}^{ij} = \dot{\mathbf{r}}_p^{ij} - (\dot{\mathbf{r}}_p^{ij} \cdot \mathbf{n})\mathbf{n}$. The direction of the friction force is based on the direction of the corresponding tangential velocity

of the contact point, and is thus defined using the unit vector $\mathbf{t}^{ij} = \mathbf{v}_{tp}^{ij} / \|\mathbf{v}_{tp}^{ij}\|$. The friction force is then defined as follows:

$$\mathbf{f}_t^{ij} = \begin{cases} -\mu \|\mathbf{f}_n^{ij}\| \mathbf{t}^{ij} & \|\mathbf{v}_{tp}^{ij}\| > v_s \\ -\mu \|\mathbf{f}_n^{ij}\| \mathbf{t}^{ij} \sin \frac{\pi\gamma}{2} & \|\mathbf{v}_{tp}^{ij}\| \leq v_s \end{cases} \quad (3)$$

where $\gamma = \|\mathbf{v}_{tp}^{ij}\| / v_s$, and v_s is a problem dependent slip velocity. The second expression of the friction force that is used when the magnitude of \mathbf{v}_{tp}^{ij} is less than v_s helps smooth the transition of the friction force when it changes directions, thus avoiding a discontinuity in the friction force function which improves the computational efficiency of the model. Finally, the vector of contact forces is given by $\mathbf{f}_c^{ij} = \mathbf{f}_n^{ij} + \mathbf{f}_t^{ij}$. The expression for the vector of generalized contact forces can be obtained by using the virtual work of the contact forces and is given by $\mathbf{Q}_c^{ij} = \mathbf{S}^{ijT}(\mathbf{x}) \mathbf{f}_c^{ij}$. Depending on the dimensions of the tire model considered, the number of contact points can be varied in order to yield more efficient simulations. Additionally, since the tire is pressurized, and Gauss integration is used to obtain the pressure distribution on its inner surface, the contact forces can be evaluated at the Gauss integration points mapped on the tire outer surface for ease of implementation.

2.2.3 Spin Velocity

While the simple contact force model discussed in the preceding subsection is used for simplicity, other ANCF contact force models can be used as well. Some of the tire contact forces require extracting kinematic variables that define the tire rotations at the contact point. For instance, some of the creep force models include a spin moment that is function of the angular velocity at the contact point. In order to evaluate the spin angular velocity at an arbitrary point, one needs to

evaluate the velocity gradient tensor \mathbf{L} , which can be written as $\mathbf{L} = \partial \dot{\mathbf{r}} / \partial \mathbf{r} = (\partial \dot{\mathbf{r}} / \partial \mathbf{X})(\partial \mathbf{X} / \partial \mathbf{r}) = \dot{\mathbf{J}}\mathbf{J}^{-1}$, where superscripts that refer to the tire and element numbers are dropped for the simplicity of the notation, and $\mathbf{X} = [X \ Y \ Z]^T = \mathbf{S}\mathbf{e}_o$. The velocity gradient tensor can be written as $\mathbf{L} = \mathbf{D} + \mathbf{W}$, where $\mathbf{D} = (1/2)(\mathbf{L} + \mathbf{L}^T)$ is the symmetric rate of deformation tensor and $\mathbf{W} = (1/2)(\mathbf{L} - \mathbf{L}^T)$ is the skew-symmetric spin tensor. Using ANCF FEs, the velocity gradient tensor can be written in terms of the gradient vectors at an arbitrary point as (Recuero et al., 2016A)

$$\mathbf{L} = \dot{\mathbf{J}}\mathbf{J}^{-1} = \begin{bmatrix} \dot{\mathbf{r}}_X & \dot{\mathbf{r}}_Y & \dot{\mathbf{r}}_Z \end{bmatrix} \begin{bmatrix} \mathbf{J}_{R1}^{-1} \\ \mathbf{J}_{R2}^{-1} \\ \mathbf{J}_{R3}^{-1} \end{bmatrix} = \dot{\mathbf{r}}_X \otimes \mathbf{J}_{R1}^{-1} + \dot{\mathbf{r}}_Y \otimes \mathbf{J}_{R2}^{-1} + \dot{\mathbf{r}}_Z \otimes \mathbf{J}_{R3}^{-1} \quad (4)$$

where \mathbf{J}_{Ri}^{-1} denotes the i^{th} row of the inverse of the matrix of position vector gradients, and \otimes denotes outer (dyadic) product of two vectors. The spin tensor can be obtained from the velocity gradient tensor as

$$\mathbf{W} = \tilde{\boldsymbol{\omega}} = \frac{1}{2} \left(\dot{\mathbf{r}}_X \otimes \mathbf{J}_{R1}^{-1} + \dot{\mathbf{r}}_Y \otimes \mathbf{J}_{R2}^{-1} + \dot{\mathbf{r}}_Z \otimes \mathbf{J}_{R3}^{-1} - \mathbf{J}_{R1}^{-1} \otimes \dot{\mathbf{r}}_X - \mathbf{J}_{R2}^{-1} \otimes \dot{\mathbf{r}}_Y - \mathbf{J}_{R3}^{-1} \otimes \dot{\mathbf{r}}_Z \right) \quad (5)$$

where $\tilde{\boldsymbol{\omega}}$ is the skew symmetric matrix associated with the angular velocity vector $\boldsymbol{\omega}$. Using this equation, one can show that the angular velocity vector can be written in terms of the ANCF gradients as (Recuero et al., 2016A)

$$\boldsymbol{\omega} = \frac{1}{2} \left(\mathbf{J}_{R1}^{-1} \times \dot{\mathbf{r}}_X + \mathbf{J}_{R2}^{-1} \times \dot{\mathbf{r}}_Y + \mathbf{J}_{R3}^{-1} \times \dot{\mathbf{r}}_Z \right) \quad (6)$$

This expression of the angular velocity vector at an arbitrary point takes into account the effect of the rigid body motion and the elastic deformation of the tire.

2.3 ANCF Reference Node

The concept of the ANCF reference node (ANCF-RN) can be used to define bodies which are not associated with FEs. Using this concept, one can develop an ANCF mesh which has a constant inertia matrix. Such a mesh allows also for eliminating at a preprocessing stage the linear algebraic equations that define linear constraint conditions between the element nodes and the ANCF reference nodes. The ANCF reference nodes also allow for defining rigid bodies as components of the ANCF mesh. These rigid bodies can represent the tire rims, axles, and/or the chassis of the vehicle model.

2.3.1 Preprocessor Reference Node/Element Node Constraints

The ANCF-RN can have a number of coordinates equal to the number of coordinates used for the element nodes (Shabana, 2015A; Shabana, 2015B). In this section, superscript i refers to the subsystem, superscript r refers to the reference node, and superscript k refers to the flexible body node at the interface. If \mathbf{J}^{ir} is the matrix of the reference node position vector gradients and \mathbf{J}^{ik} is the matrix of the k^{th} node position vector gradients, then one has $\mathbf{J}^{ik} = \mathbf{J}^{ir} \mathbf{J}^{ikr}$, where \mathbf{J}^{ikr} is a constant matrix that defines the orientation of the gradient vectors of node k with respect to the reference node. It is also important to point out that an assumption is made in the development presented in this section that the reference node, which is not an element node, will be represented by a rigid triad, that is, the ANCF-RN gradient vectors will remain orthogonal unit vectors (Shabana, 2015A; Shabana, 2015B).

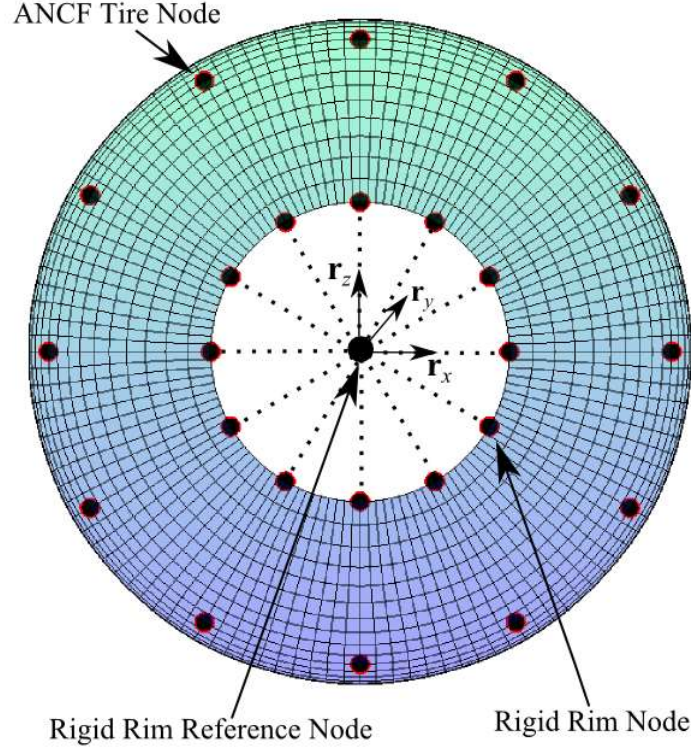


Figure 8. ANCF tire assembly (•••• Relative position and gradient vector constraints)

In order to connect a flexible tire to a rim or an axle defined by a reference node as shown in Figure 8, the following linear algebraic constraint equations are imposed at a preprocessing stage:

$$\left. \begin{aligned} \mathbf{r}^{ik} - \mathbf{r}^{ir} &= x^{ik} \mathbf{r}_x^{ir} + y^{ik} \mathbf{r}_y^{ir} + z^{ik} \mathbf{r}_z^{ir}, \\ \begin{bmatrix} \mathbf{r}_x^{ik} & \mathbf{r}_y^{ik} & \mathbf{r}_z^{ik} \end{bmatrix} &= \begin{bmatrix} \mathbf{r}_x^{ir} & \mathbf{r}_y^{ir} & \mathbf{r}_z^{ir} \end{bmatrix} \mathbf{J}^{ikr}, \quad k = 1, \dots, m_r \end{aligned} \right\} \quad (7)$$

In this equation, the parameters x, y , and z used for the reference node gradients can be assumed to coincide with the mesh parameters X, Y , and Z , \mathbf{r}^{ik} is the global position of node k on the flexible body/rigid body interface, \mathbf{r}^{ir} is the global position of the reference node, m_r is the number of nodes at the interface, and x^{ik}, y^{ik} , and z^{ik} are the coordinates of node k with respect to the reference node in the initial reference configuration. Since rigidity conditions will be applied to the reference node during the dynamic simulation, the right hand side of the first equation in

Eq. 7, $x^{ik}\mathbf{r}_x^{ir} + y^{ik}\mathbf{r}_y^{ir} + z^{ik}\mathbf{r}_z^{ir}$, will ensure a constant length between the two points since it is defined by three constant coordinates along three orthogonal unit vectors.

2.3.2 Preprocessor Reference Node Inertia

Because the reference node is not an element node, the inertia associated with the ANCF-RN position and gradient coordinates must be properly defined to ensure having a positive definite inertia matrix. A linear interpolation can be used as the basis for the definition of the reference node inertia. Such an interpolation leads to exact description of the inertia if the reference node is used to represent a rigid body and the ANCF-RN gradient vectors remain orthogonal unit vectors at the initial configuration as well as during the dynamic simulation. If the tire rim, for example, is treated as a rigid body, the location of an arbitrary point on the rim can be written as (Shabana, 2015A; Shabana, 2015B)

$$\mathbf{r}^{ira}(x, y, z) = \mathbf{r}^{ir} + \begin{bmatrix} \mathbf{r}_x^{ir} & \mathbf{r}_y^{ir} & \mathbf{r}_z^{ir} \end{bmatrix} \begin{bmatrix} x \\ y \\ z \end{bmatrix} \quad (8)$$

In this equation, x, y , and z are the coordinates that define the position vector of an arbitrary point on the rigid rim with respect to the reference node. A virtual change in this position vector leads to $\delta\mathbf{r}^{ira}(x, y, z) = \delta\mathbf{r}^{ir} + x\delta\mathbf{r}_x^{ir} + y\delta\mathbf{r}_y^{ir} + z\delta\mathbf{r}_z^{ir}$, and the virtual work of the rim inertia forces can be written as $\delta W_i^{ir} = \int_{V^{ir}} \rho^{ir} \mathbf{r}^{iraT} \delta\mathbf{r}^{ira} dV^{ir}$, where V^{ir} and ρ^{ir} are, respectively, the volume and mass density of the rim. The virtual work of the rim inertia forces can be written as $\delta W_i^{ir} = \mathbf{Q}^{irT} \delta\mathbf{e}^{ir}$, where $\mathbf{Q}^{ir} = \mathbf{M}^{ir} \mathbf{e}^{ir}$, where \mathbf{M}^{ir} is the reference node symmetric and constant mass matrix. One can show that the elements of this mass matrix can be expressed in terms of the mass moments of inertia, while the other elements define moments of mass. The dimension of the inertia matrix \mathbf{M}^{ir}

is equal to the number of the ANCF-RN coordinates. For use with the fully parameterized plate element considered in this chapter, the dimension of \mathbf{M}^{ir} is 12×12 . Because \mathbf{M}^{ir} is constant, it can be evaluated at a preprocessing stage and used with the inertia matrices of the FEs that define the flexible tire to construct the tire mesh inertia matrix that can be used to develop the Cholesky transformation used to define an identity generalized inertia matrix (Shabana, 2012).

2.3.3 ANCF-RN Rigidity Constraints

An ANCF-RN rigid body can be defined by imposing six nonlinear algebraic constraint equations that can be introduced to the dynamic formulation using the technique of Lagrange multipliers. Using this approach, an identity generalized mass matrix for the ANCF mesh can still be used, leading to an optimum sparse matrix structure for the dynamic equations of motion. The ANCF-RN rigidity constraint equations must be satisfied at the position, velocity, and acceleration levels. These six nonlinear constraint equations, which can be written mathematically as $\|\mathbf{r}_x^{ir}\| = 1, \|\mathbf{r}_y^{ir}\| = 1, \|\mathbf{r}_z^{ir}\| = 1$, and $\mathbf{r}_x^{ir} \cdot \mathbf{r}_y^{ir} = 0, \mathbf{r}_x^{ir} \cdot \mathbf{r}_z^{ir} = 0, \mathbf{r}_y^{ir} \cdot \mathbf{r}_z^{ir} = 0$, ensure the rim rigidity. Using this approach, multi-wheel assembly, as the one shown in Figure 1 (Chapter 1), can be described using one ANCF mesh. Using this concept, a vehicle model that has several rigid rims, axles, and rigid chassis can be represented using one ANCF mesh.

2.4 Composite Tires

Modern tires are complicated composite structures generally made of wide ranges of composite materials, such as rubber, synthetic fabric with high tensile strength and steel. The tread is a type of rubber composite manufactured to provide traction and reduce wear and tear under different ground conditions. The belt layer and ply are also made from fibrous composite materials with

continuous steel fibers embedded in rubber. For this reason, the tire material needs to be modeled using anisotropic and nonlinear constitutive laws, and the belt and ply layers in the FE models need to be defined independently.

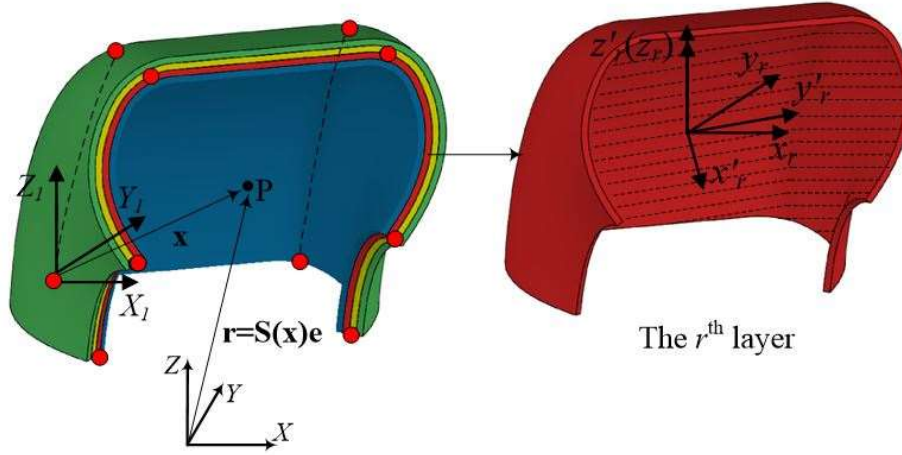


Figure 9. Composite laminated tire cross section

As shown in Figure 9, composite laminated tire structures can be meshed by the composite laminated ANCF plate elements. The element layers are assumed to be bonded together, and the bonds are assumed to be infinitesimally thin and perfect so that there is no relative motion between the laminae. For the tire r^{th} layer of orthotropic material, the constitutive equations can be written in the primed coordinate system x'_r, y'_r, z'_r as (Liu et al., 2011)

$$\begin{bmatrix} \bar{\sigma}_{11} \\ \bar{\sigma}_{22} \\ \bar{\sigma}_{33} \\ \bar{\sigma}_{23} \\ \bar{\sigma}_{13} \\ \bar{\sigma}_{12} \end{bmatrix}_r = \begin{bmatrix} \bar{C}_{11} & \bar{C}_{12} & \bar{C}_{13} & 0 & 0 & 0 \\ \bar{C}_{21} & \bar{C}_{22} & \bar{C}_{23} & 0 & 0 & 0 \\ \bar{C}_{31} & \bar{C}_{32} & \bar{C}_{33} & 0 & 0 & 0 \\ 0 & 0 & 0 & \bar{C}_{44} & 0 & 0 \\ 0 & 0 & 0 & 0 & \bar{C}_{55} & 0 \\ 0 & 0 & 0 & 0 & 0 & \bar{C}_{66} \end{bmatrix} \begin{bmatrix} \bar{\epsilon}_{11} \\ \bar{\epsilon}_{22} \\ \bar{\epsilon}_{33} \\ 2\bar{\epsilon}_{23} \\ 2\bar{\epsilon}_{13} \\ 2\bar{\epsilon}_{12} \end{bmatrix}_r \quad (9)$$

where $(\bar{\sigma}_{ij})_r$ and $(\bar{\varepsilon}_{ij})_r$ are, respectively, the components of the stress and strain vectors $\bar{\sigma}_r$ and $\bar{\varepsilon}_r$ of the r^{th} layer, and \bar{C}_{ij} are the constants that define the matrix of elastic coefficients $\bar{\mathbf{C}}_r$ which has nine independent parameters that are required to model the material anisotropy (Kollar and Springer, 2003). The matrix of the elastic coefficients can be defined in the unprimed coordinate system using the transformation relation $\mathbf{C}_r = \hat{\mathbf{T}}_{\sigma r} \bar{\mathbf{C}}_r \hat{\mathbf{T}}_{\varepsilon r}^{-1}$, where the transformation matrices $\hat{\mathbf{T}}_{\sigma r}$ and $\hat{\mathbf{T}}_{\varepsilon r}$ are the matrices required to transform the stress and strain vectors defined in Eq. 9, that is, $\sigma_r = \hat{\mathbf{T}}_{\sigma r} \bar{\sigma}_r$ and $\varepsilon_r = \hat{\mathbf{T}}_{\varepsilon r} \bar{\varepsilon}_r$. The transformation matrices $\hat{\mathbf{T}}_{\sigma r}$ and $\hat{\mathbf{T}}_{\varepsilon r}$ are functions of the rotation angles between the unprimed and primed systems as shown in Figure 9. More discussion on the form of these transformation matrices can be found in the work of Liu et al. (2011).

Using this ANCF composite laminated plate element, the continuity of the nodal position vector will be satisfied automatically. In addition, it is assumed that the element deformation is elastic in each layer, and the failure behavior of the laminate is not considered. In Figure 9, XYZ represents the global coordinate system, and \mathbf{x} is the local position vector of an arbitrary point P on the FE, which is defined in the element coordinate system $X_1Y_1Z_1$. As shown by Liu et al. (2011), the elastic forces of the r^{th} layer of the composite plate of the tire can be obtained using the following expression of the virtual work:

$$\delta W_{sr} = -\frac{1}{2} \int_{V_r} (\mathbf{D}_r : \varepsilon_r) : (\mathbf{J}^T \delta \mathbf{J} + (\delta \mathbf{J}^T) \mathbf{J}) dV_r \quad (10)$$

where \mathbf{D}_r is the fourth-order tensor of the elastic coefficients, \mathbf{J} is the matrix of position vector gradients, and V_r is the volume of layer r in the reference configuration. The virtual change in the matrix of position vector gradients $\delta \mathbf{J}$ can be expressed in terms of the virtual changes in the

ANCF plate element coordinates. The reader can find the detailed description of an efficient implementation of the elastic forces in the work by Liu et al. (2011). The integral in the preceding equation is evaluated numerically. The domain of integration for each ANCF FE must be divided into several subdomains. The number of subdomains can be the number of the element layers. In the integration process, the tensor of the elastic coefficients \mathbf{D}_r and the coordinate transformation matrices will assume values that depend on the specific layer.

2.5 Numerical Results

This section provides a numerical example that demonstrates the use of the ANCF reference node to develop a vehicle model described by one FE mesh only. This example also shows how tire models used in MBS applications can be developed using a small number of ANCF FEs that describe the geometry and spinning motion accurately.

2.5.1 ANCF Fully Parameterized Plate Element Tire Assembly

One of the goals of this chapter is to develop a tire assembly meshed with ANCF fully parameterized plate elements and the ANCF-RN. The plate elements are used to create the three dimensional tire mesh while the ANCF-RN is used to describe the rigid rim inertia as shown in Figure 1 (Chapter 1). As described previously in this chapter, the reference node is connected to the corresponding rim nodes on the plate elements at a preprocessing stage, thereby allowing for reducing the MBS problem dimension and the number of degrees of freedom required in the dynamic simulation. As shown in Figure 1 (Chapter 1), six independent gradient vector constraints are imposed on the reference node in order to define a rigid triad that has six degrees of freedom; three translations and three rotations. Figure 8 shows the assembly of the tire and the rim in one

unified mesh which is obtained by imposing relative position and gradient vector constraints between the rim reference node and the tire ANCF plate nodes that lie on the rim circumference. These constraints between the reference node and flexible tire nodes can be applied at a preprocessing stage in order to reduce the problem dimensionality. The high order of interpolation of the ANCF fully parameterized plate element and the use of gradient vectors as nodal coordinates allow for modeling highly curved structures like a tire in a straightforward manner, as demonstrated in this chapter. Thus, the number of elements required to accurately mesh the curved tire geometry can be reduced significantly.

2.5.2 Bulldozer Vehicle Model

In order to demonstrate the implementation of the procedures and concepts introduced in this chapter, the vehicle model shown in Figure 4 (Chapter 1) is used. This vehicle is mainly used in mining and construction industries (Caterpillar, 2013). Typically, wheeled bulldozers like the model considered in this numerical study do not have any suspension, so the wheels are directly attached to the chassis. Additionally, in order to steer, the chassis of the vehicle is divided into two distinct pieces that are connected by a central revolute joint; each piece having a set of wheels. For simplicity and since the vehicle model developed in this chapter is made to move only in the forward or longitudinal direction, the chassis is considered as a single entity and is modeled using one reference node. Nonetheless, as demonstrated in the literature, a revolute joint can be introduced at a preprocessing stage allowing for the systematic elimination of the dependent variables using the resulting linear algebraic equations of the ANCF revolute joints. Along with the chassis, the vehicle model has two axles that serve as the connection points for the four wheels. Each axle is modeled using two reference nodes, one at each end of the axle. The rim reference nodes are attached to the axle reference nodes at a preprocessing stage leading to a vehicle model

that is completely described by one ANCF FE mesh. Figure 10 shows the constraints applied between different reference nodes. The inertia properties of the vehicle model are provided in Table 2 and the initial configuration of the vehicle is described in Table 3.

Table 2. Inertia properties of vehicle reference nodes

Component Reference Node	Mass (kg)	Principal Moments of Inertia ($\text{kg} \cdot \text{m}^2$) (I_{xx} , I_{yy} , I_{zz})
Chassis	45000	20000, 20000, 20000
Axle	150	100, 10, 100
Rim	750	300, 350, 300

Table 3. Initial global positions of vehicle reference nodes (COM: center of mass)

Component Reference Node	Number of Reference Nodes	Initial Position (x,y,z) (m)
Chassis (COM)	1	3.28298145, 0, 1.314
Axle	4	5.9409629, ± 1.665382 , 1.314 0.625, ± 1.665382 , 1.314
Rim	4	5.9409629, ± 1.665382 , 1.314 0.625, ± 1.665382 , 1.314

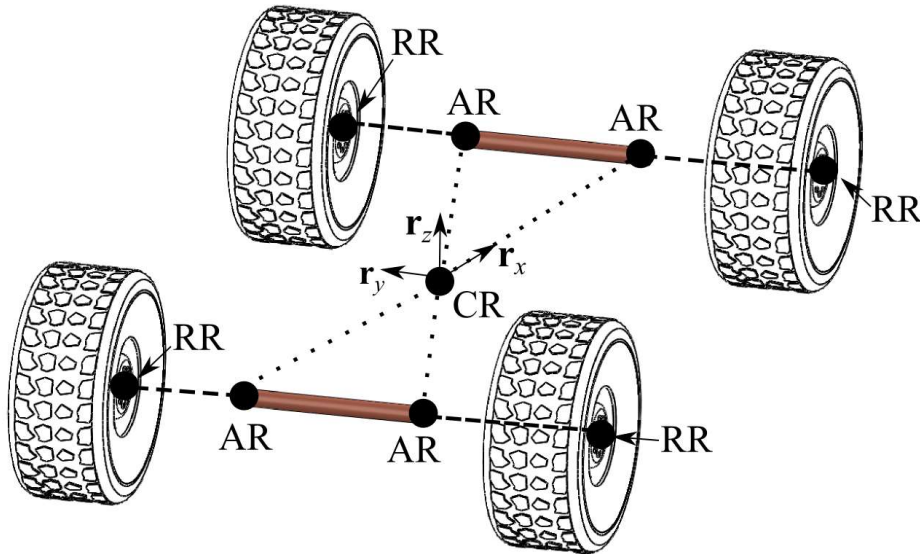


Figure 10. All ANCF vehicle model (CR: Chassis reference node; AR: Axle reference node; RR:

Rim reference node; •••• Rigid joint; ----- Revolute joint)

The overall dimensions of the tire used in this vehicle model are based on 45/65 R45 L-4 I STAR tire manufactured by Michelin. Figure 11 shows the cross section of the ANCF tire used in this chapter. This ANCF tire mesh consists of three curved plate elements in its cross section and a total of thirty-six plate elements for one tire. Since the emphasis of this chapter is to demonstrate the application of the ANCF-RN in the development of a tire assembly and a vehicle model, a linear elastic material model is used for the tire for simplicity.

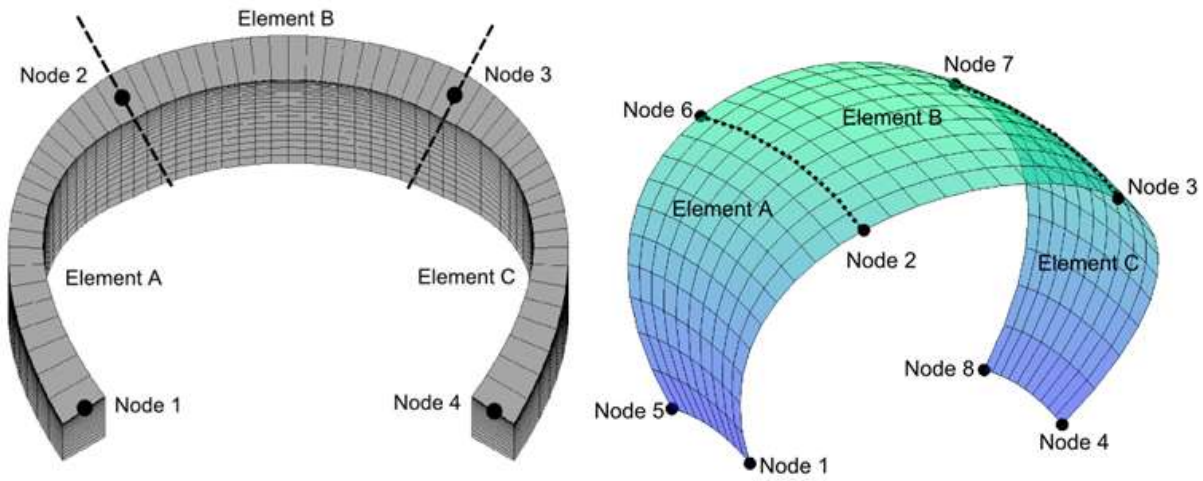


Figure 11. ANCF fully parameterized plate element tire cross section and mid-surface representation

Two vehicle models are considered in this chapter, one with single material tires which will be referred to as the non-composite tire model henceforth, and one with composite tires. The geometric and material properties of the non-composite (single material) tires used in this chapter are provided in Table 4 and 5, respectively. The geometric properties of the composite tires are the same as that of the non-composite tires provided in Table 4 whereas the elastic moduli of different layers of the composite tires used in this chapter are given in Table 5 which correspond to that of the belt, cap-ply, and carcass (Yang, 2011). The belt, cap-ply, and carcass make up most of the elastic parts of the tire cross section and therefore have a very dominant effect on the overall

stiffness of the tire structure in comparison to its relatively less stiff rubber components. Finally, this vehicle model is described by 9 ANCF-RNs (4 for the tires, 4 for the axles, and 1 for the chassis), 144 ANCF fully parameterized plate elements, 408 constraint equations describing the tire-rim-vehicle assembly that are eliminated at a preprocessing stage, 26 gradient vector constraints that ensure the rigidity of the reference nodes and a total of 2412 nodal coordinates. Because of the dependency established among the vehicle reference node coordinates at the preprocessing stage, the number of gradient vector constraints required to be enforced during the dynamic analysis is reduced from 54 to only 26.

Table 4. ANCF plate element tire geometric properties

Tire Property	Value
Size Specification	45/65 R45
Rim Diameter (m)	1.143
Overall Diameter (m)	2.628
Element Dimensions (m) (L, W, T)	1.114, 0.299, 0.100
Density (kg/m ³)	1500
No. of ANCF Plate Elements Per Tire	36

Table 5. ANCF plate element tire material properties

Non-composite (single material)	
Density (kg/m ³)	1500
Modulus of Elasticity (GPa)	2.0
Modulus of Rigidity (GPa)	1.0
Composite (multi material)	
Density (kg/m ³)	1500
Cap-Ply Modulus of Elasticity (GPa)	4.18
Belt Modulus of Elasticity (GPa)	11.3
Carcass Modulus of Elasticity (GPa)	2.05

2.5.3 Simulation Results

Two different dynamic simulation vehicle models are considered in this section. In the first model, the tires are assumed to be made of non-composite material, while in the second model a composite material constitutive law is used for the tires in order to demonstrate the generality of the implementation. The goal of these simulations is to demonstrate the effectiveness of using the ANCF-RN in developing new FE vehicle and tire models. In these simulations, vehicle static equilibrium positions are first achieved by allowing the vehicle system to settle at the beginning of the dynamic simulation. After reaching the vehicle static equilibrium position, a forward force is applied to the chassis reference node in order to induce free rolling of the tires between 0.3s and 1.5s. To compare the results, the same contact and tire pressure parameters are used for both models, these parameters are provided in Table 6. A 10×10 grid of integration points is created on the tire plate elements in order to evaluate the pressure and contact forces whereas a $7 \times 7 \times 3$ grid of integration points is used to calculate the elastic forces of the plate elements. The results of both simulations are shown in Figures 12-17. Figure 12 shows the longitudinal or forward displacement of the chassis whereas Figure 13 shows the chassis vertical displacement. Because this vehicle model does not have a suspension and no damping is used, the chassis vertical displacement shows oscillations.

Table 6. Simulation parameters

Parameter	Value
Ground Stiffness (MN/m)	22.5
Ground Damping (MN.s/m)	0.3
Friction Coefficient μ	0.85
Slip Velocity (m/s)	0.01
Tire Pressure (kPa)	400

The results presented in Figure 13 also show a difference in the vertical behavior of the composite and non-composite tire vehicle models. The composite tire vehicle model has smaller vertical displacement than the non-composite vehicle model due to its higher stiffness which leads to smaller tire deformation. In order to show that ANCF plate elements used in this study can capture the tire spinning motion, Figure 14 shows the time evolution of the first component of the gradient vector \mathbf{r}_x of the reference node that represents the front right rim. This value oscillates between 1 and -1, which demonstrates that the large tire rotation is indeed captured.

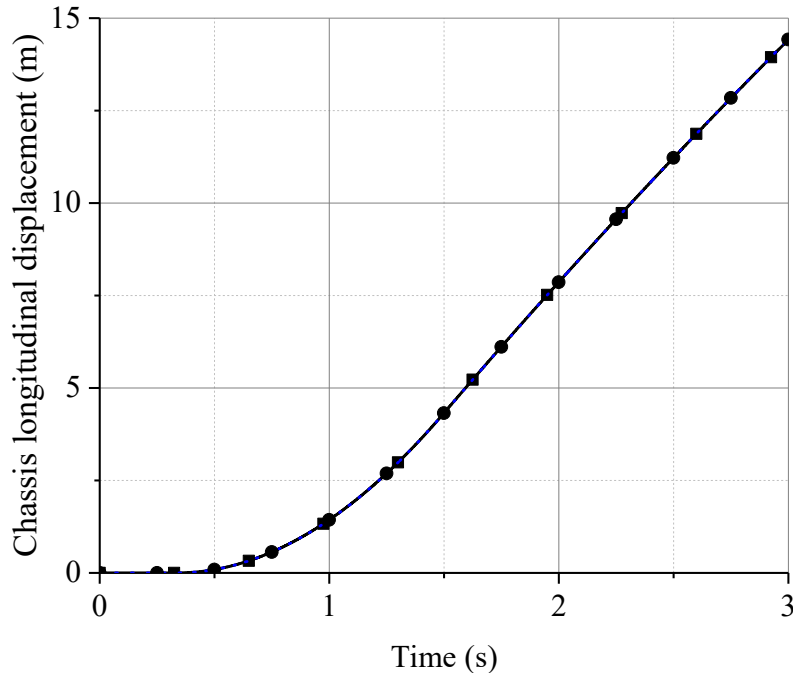


Figure 12. Chassis reference node longitudinal displacement (—■— Noncomposite;
 - -●- - Composite)

The numerical results presented in Figure 15, which show the longitudinal velocity of the chassis, clearly demonstrate the effect of the application of the forward force between 0.3s and 1.5s when the vehicle is accelerating, and the deceleration of the vehicle after 1.5s due to the presence of the friction force generated by the tire/ground interaction. Figure 16 shows the shape of the contact

patch and the normal force distribution of the non-composite front right tire when the vehicle is not moving whereas Figure 17 shows the shape of the contact patch and the normal force distribution of the same tire when the vehicle is accelerating. As expected and can be seen from the results presented in Figure 17, the location of the maximum normal force in the contact patch of an accelerating tire is found to be slightly displaced in the direction of motion when compared to that of the static case.

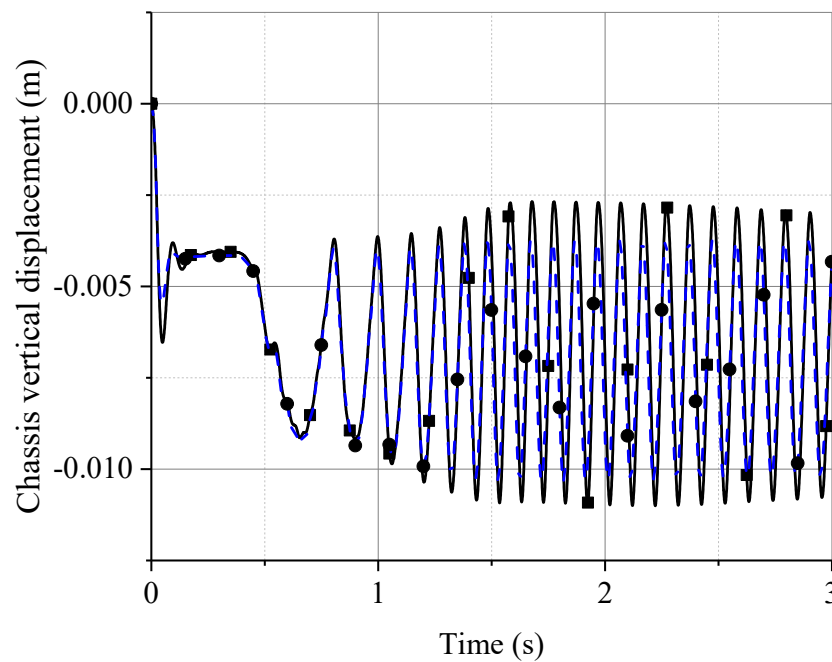


Figure 13. Chassis reference node vertical displacement (—■— Noncomposite;
- - -●- - Composite)

This behavior is consistent with tire mechanics as can be seen in Figure 18 that shows the analytical contact force distribution of a static tire and a rolling tire (Blundell and Harty, 2004). Furthermore, the normal force distribution of the front right tire when the vehicle is static is also consistent with the analytical description shown in Figure 18, with both being symmetric in the longitudinal direction and the maximum value being in the center of the contact patch.

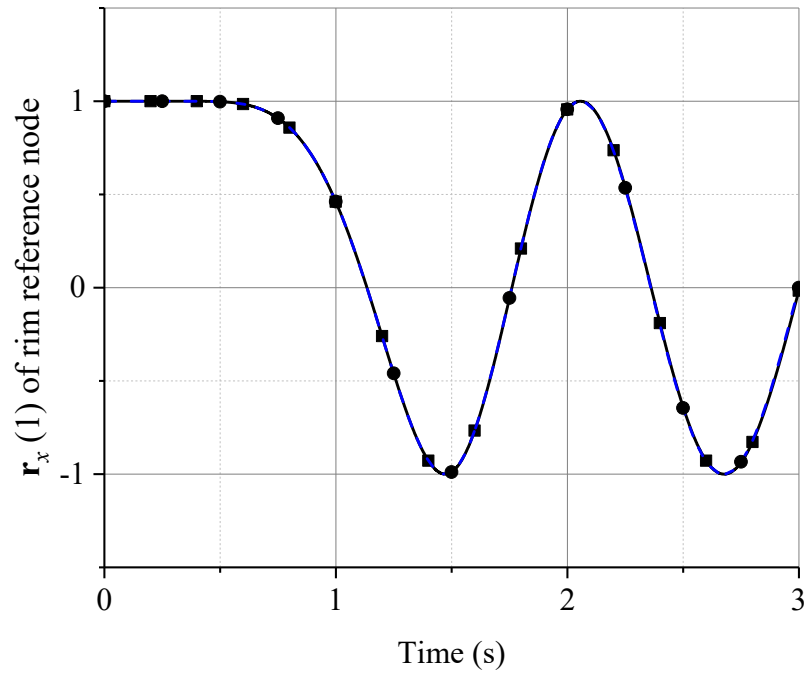


Figure 14. First component of \mathbf{r}_x gradient of front right rim reference node (—■— Noncomposite; - -●- - Composite)

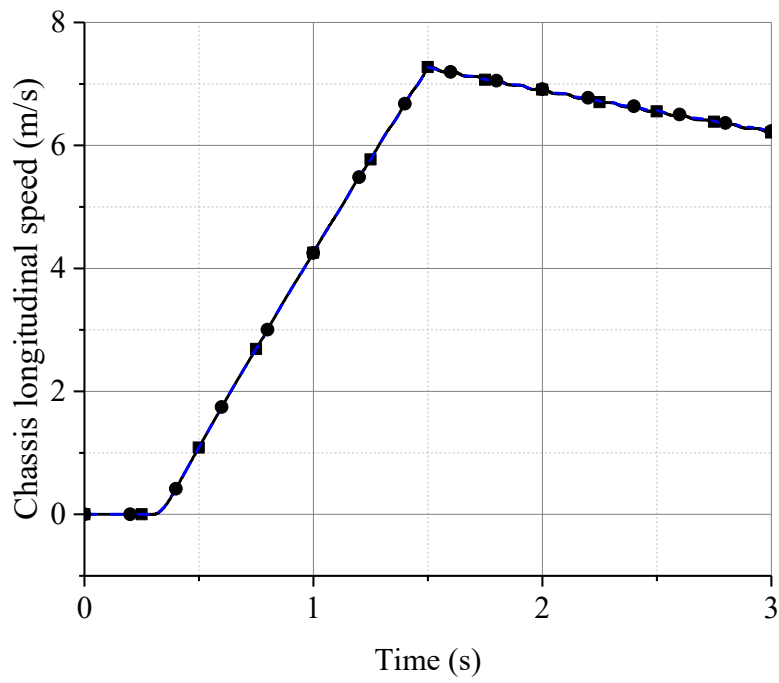


Figure 15. Chassis longitudinal speed (—■— Noncomposite; - -●- - Composite)

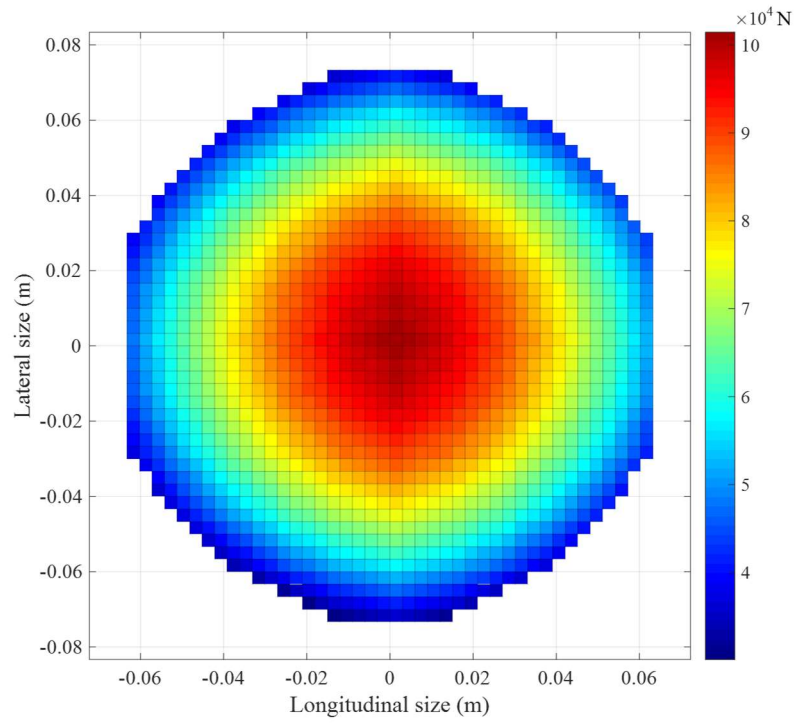


Figure 16. Contact patch of noncomposite material vehicle tire in static (non-rolling) condition

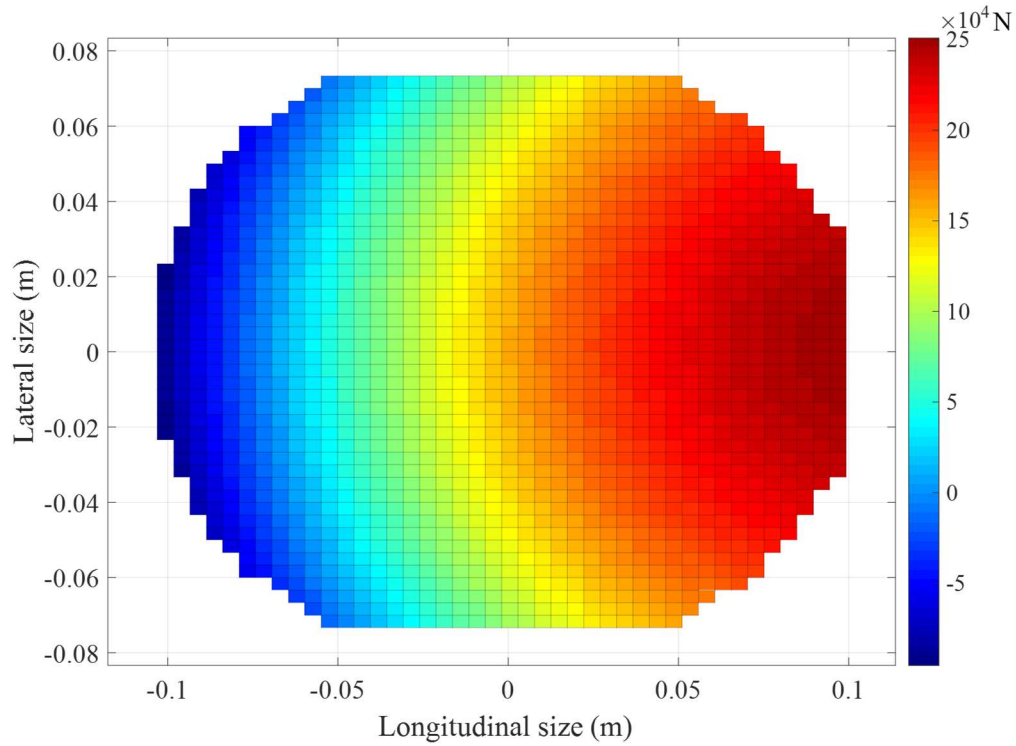


Figure 17. Contact patch of noncomposite material vehicle tire in rolling condition

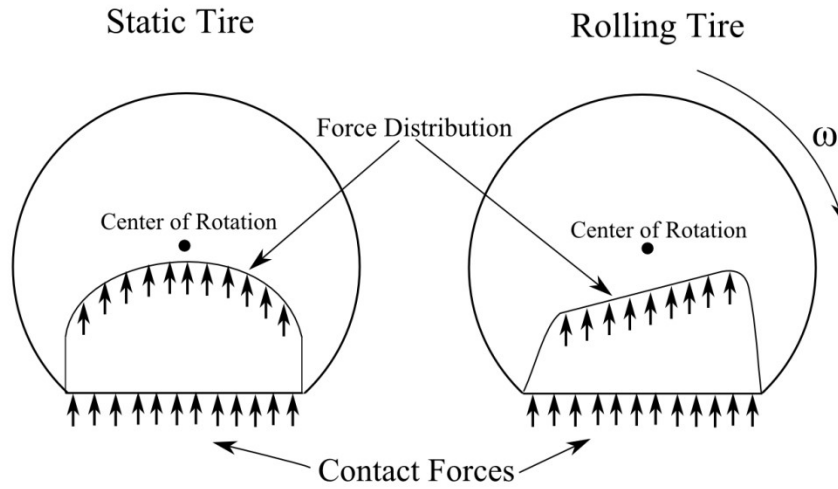


Figure 18. Analytical tire contact force distribution (Blundell and Harty, 2004)

2.6 Concluding Remarks

In this chapter, a new computational procedure for modeling tire and vehicle systems is presented. The chapter demonstrates the integration of ANCF tire models with computational MBS algorithms by using the new concept of the ANCF reference node. This concept is used to develop a tire assembly in which a vehicle model, including the tires, can be represented using one ANCF mesh in which the linear connectivity conditions are used to eliminate redundant variables at a preprocessing stage. The computational approach used in this chapter allows for developing detailed FE vehicle models that include tires with distributed inertia and elasticity without the need for using co-simulation techniques, only one MBS simulation environment is required. The optimum sparse matrix structure of the dynamic equations of motion is preserved by introducing a minimum set of nonlinear algebraic equations that ensure the rigidity of the rims, axles, and possibly the chassis of the vehicle. A continuum-based air pressure tire model that allows for

accounting for the change of the inner surface area of the tire due to the contact forces is proposed. In this continuum-based air pressure model, Nanson's formula is used to define the area in the current deformed configuration in terms of the area in the reference configuration. This continuum-based air pressure model can be used as an alternative to the discrete spring models often used in the literature to model the tire pressure forces. Because general and more accurate tire models require the use of composite materials, it is shown how an ANCF composite tire model can be systematically developed and integrated with MBS algorithms. To this end, fully parameterized ANCF plate elements are used. Numerical results are presented in this chapter in order to demonstrate the implementation of the proposed computational MBS approach.

CHAPTER 3

LOCALIZED SURFACE GEOMETRY IN ANCF FINITE ELEMENTS

This chapter (published as He et al., 2017) introduces a new method for the integration of localized surface geometry with fully parameterized absolute nodal coordinate formulation (ANCF) finite elements. In this chapter, ANCF finite elements are used to create the global geometry and perform the finite element (FE)/multibody system (MBS) analysis of deformable bodies. The localized surface geometry details can be described on ANCF element surfaces without the need for mesh refinement. The localized surface is represented using a standard computational geometry method, Non-uniform rational B-spline (NURBS), which can describe both conic surface and freeform surface efficiently and accurately. The basic idea of the integration of localized surface geometry with ANCF elements lies in the inclusion of such detail in the element mass matrix and forces. The integration can be implemented by overlapping the localized surface geometry on the original ANCF element or by directly trimming the ANCF element domain to fit the required shape. During the integration process, a mapping between ANCF local coordinates and NURBS localized geometric parameters is used for a consistent implementation of the overlapping and trimming methods. Additionally, two numerical integration methods are compared for the rate of convergence. The results show that the proposed subdomain integration method is better, since it is optimized for dealing with complex geometry. The proposed subdomain method can be used with any fully parameterized ANCF element. In order to analyze the accuracy of the proposed method, a cantilever plate example with localized surface geometry is used, and the simulation results with the proposed method are compared with the simulation results obtained using a commercial FE code. Two other examples that include contact with ground and localized surface geometry are also provided. These examples are a simple plate structure with surface geometry

and a tire with tread details. The incompressible hyperelastic Mooney-Rivlin material model is used to describe the material used in the tire tread. It is shown through the tire contact patch that the proposed method can successfully capture the effect of the tread grooves. The ANCF tire model is also used to demonstrate that convergence of the position level results can be achieved.

3.1 Localized Surface Geometry Modeling Methods

There are three different levels in the FE analysis at which the local surface geometry can be implemented in the model. For level one, the geometry details are included while building the CAD model, for level two, these details are included while generating the FE mesh, and for level three, the details are included during the numerical integration process of the FE problem. Thus, the localized surface geometry modeling approach can be classified as the geometric shape design level (Kagan et al., 2003; Bouclier et al., 2016; Chemin et al., 2015), mesh level and numerical integration level (Wang, 2000; Nicolas and Fouquet, 2013).

In the CAD field, the techniques used to represent the localized geometry mainly include local and global refinement methods, trimming and the merging methods (Piegl and Tiller, 1997; Schmidt et. al, 2012). Global refinement is the simplest refinement technique in geometric design (Li and Ke, 2000). For example, the most useful method when B-spline and NURBS are used is to insert knots where the local feature exists (Kagan et al., 2003; Yu and Shabana, 2015). However, the patches near the local geometric feature must be refined simultaneously to ensure conformity, and this may introduce many undesired control points. The disadvantage of this approach is that it leads to rapidly growing computing and storage requirements. Trimmed NURBS surface has become one of the most effective and widely used methods in current CAD systems for modeling complex surfaces because it provides a promising alternative for representing NURBS domains of

arbitrarily complex topology (Schmidt et al., 2012). The trimmed NURBS surface approach makes adding localized surface geometry convenient and easy. One disadvantage of the trimmed NURBS surface method is that it can lead to difficulties during mesh generation, by often making the mesh irregular and overly fine, which may lead to highly deformed elements in the reference configuration, error in the FE solution due to a distorted mesh, and a higher computational cost in case of an overly fine mesh. In order to improve the flexibility of splines and enable local refinement, several new splines have been developed recently, including hierarchical B-splines and NURBS (Bornemann and Cirak, 2013; Bouclier et al., 2016), LRB-splines and T-splines (Uhm and Youn, 2009; Wang et al., 2011; Schillinger et al., 2012). T-splines have attracted considerable attention in both the computational geometry and analysis communities since they can also represent trimmed multi-patch geometries. PHT-splines which are based on T-splines have been used in the framework of isogeometric analysis (Bouclier et al., 2016). Forsey and Bartels (1988) introduced the concepts of hierarchical B-splines, which provide the capability for local refinement of surfaces and multi-resolution surface editing. Since this method is not restricted to the underlying B-spline mathematics, it is applicable to any parametric tensor product or triangular representation. There are several methods in the CAD field for localized surface geometry modeling, but it is difficult to use them in conjunction with ANCF since they are very complicated to implement and might lead to issues regarding the continuity and conformity between elements which is an important aspect of the ANCF method.

Methods for the inclusion of localized geometry at the mesh level also consist of global refinement and local refinement. There are several major approaches that allow adaptive refinement in the FE analyses including the h-refinement, p-refinement and r-refinement (Chemin et al., 2015; Wang, 2000). H-refinement is considered a non-local refinement method because more

than one element is refined at the same time. The algorithm for h-refinement is simple and it is easy to apply to complicated domains. There are similar refinement techniques based on a hierarchical split of the standard finite element which allow localized surface geometry modeling (Wang, 2000; Nicolas and Fouquet, 2013). However, most adaptive mesh refinement methods are approximations of the original mesh to within a given tolerance, and therefore, conformance of the elements can be difficult to achieve. Furthermore, as finer meshes are being developed in order to capture fine geometry details, the computing and storage requirements and the number of degrees of freedom of the mesh increase. Since the ANCF method employs higher order displacement polynomials in order to achieve gradient continuity, conformance in some elements, and more detailed deformation shapes, ANCF elements normally have more degrees of freedom as compared to the classical FEs which can lead to long simulation time.

In the FE method, the inertia and elastic force coefficients in the weak form of the equilibrium equations are evaluated using numerical integration methods. Hence the influence of a local geometric shape can also be considered by adjusting the integration domain or the distribution of integration points when calculating these inertia and force coefficients which are required in order to obtain the solution of the FE problem. The detailed localized surface can be described by a curve or surface which is then used to adjust the integration points. In this case, the original mesh does not need to be refined to the size factor of the geometric feature to be captured. Integration point level methods include the subdomain method and the adaptive integration method. In the adaptive integration method, the mesh or the geometric domain area can be divided into several smaller domains that use different integration methods depending on the accuracy requirements or shape representation (Bouclier et al., 2016; Schillinger et al., 2012). Recently, a large number of investigations have been focused on virtual domains and meshless methods which

can be considered as numerical methods developed for inclusion of details and features that cannot be easily captured using the traditional FE shape functions (Schillinger et al., 2012). When ANCF elements are used, it is more practical to use the integration point level method to model localized surface geometry because this method does not require any kind of mesh refinement and it is easy to implement.

3.2 ANCF Geometry

In MBS applications, the method used to create the model geometry as well as to analyze the FE mesh developed using this geometry must ensure the consistency and accuracy of the results. ANCF has shown its versatility in dealing with complex geometry such as tires, leaf springs, tank cars etc. (Patel et al., 2016; Yu et al., 2016). This section briefly reviews the ANCF equations that will be used in other sections of this chapter.

Flexible bodies that undergo large deformation do not always have uniform dimensions throughout the body. For example, the geometric shape and transverse deformation in the thickness cannot always be ignored. Considering this modeling complexity, fully parameterized ANCF elements are good choices for the analysis of large deformation problems. Amongst the collection of fully parameterized ANCF elements, the conforming plate element, which ensures gradient continuity on the element edges, is selected for the development presented in this chapter (Mikkola and Shabana, 2003). As described in Chapter 2, the global position vector of an arbitrary point on an ANCF plate element j on body i can be defined using the element generalized coordinates \mathbf{e}^{ij} and the element shape function matrix \mathbf{S}^{ij} as $\mathbf{r}^{ij}(x, y, z, t) = \mathbf{S}^{ij}(x, y, z)\mathbf{e}^{ij}(t)$, where t is time, and (x, y, z) are the element local coordinates. The vector of nodal coordinates \mathbf{e}^{ij} can be written as

$\mathbf{e}^{ij}(t) = [\mathbf{e}_1^{ijT} \quad \mathbf{e}_2^{ijT} \quad \mathbf{e}_3^{ijT} \quad \mathbf{e}_4^{ijT}]^T$, where the subscript refers to the node number. The generalized coordinates at a given node k include absolute position and three gradient vector coordinates, which can be written as $\mathbf{e}_k^{ij} = [(\mathbf{r}_k^{ij})^T \quad (\partial \mathbf{r}_k^{ij} / \partial x)^T \quad (\partial \mathbf{r}_k^{ij} / \partial y)^T \quad (\partial \mathbf{r}_k^{ij} / \partial z)^T]^T$ for $k = 1, 2, 3, 4$. When fully parameterized ANCF elements are used to represent the flexible bodies, the parameter z can be expressed as a function of x and y , allowing the thickness of the element to vary with the other two local coordinates. Using this concept, the position vector of an arbitrary point on the element can be defined as $\mathbf{r}^{ij}(x, y, z, t) = \mathbf{S}^{ij}(x, y, f(x, y))\mathbf{e}^{ij}(t)$, this equation is obtained by simply substituting the local coordinate z using a function $f(x, y)$ (Gantoi et al., 2013). Using this simple method, any given localized surface geometry can be described in the ANCF element without the need for further mesh refinement. By writing one parameter, z , in terms of the other two parameters, x and y , a surface with an arbitrary shape can be defined using the function relationship $z = f(x, y)$. The function $f(x, y)$ can be used to represent complex geometry and can also be defined analytically or numerically.

3.3 Integration of Localized Surface

This section introduces the integration of localized surface geometry with the global ANCF surface geometry. The concept of NURBS which is used to describe localized surface geometry is also briefly introduced.

3.3.1 The Definition of Localized Surface

In this chapter, the localized surface geometry to be integrated with the fully parameterized ANCF elements is defined using the NURBS representation, which is a generalized version of the B-

spline method and has become a standard geometric modeling method in CAD and computer graphics industries. Unlike general Lagrange polynomials, NURBS can describe a circle and sphere exactly and will be briefly reviewed in this section. Let $\mathbf{U} = (u_1, u_2, \dots, u_{n+p+1})$, called the knot vector, be a non-decreasing sequence of parameter values, where p is the degree of the NURBS curve, n is the number of control points, and u_i is the knot value and the set of all knot values makes up the knot vector \mathbf{U} . The i -th B-spline basis function of degree p , denoted by $N_{i,p}(u)$ is defined as (Piegl and Tiller, 1997)

$$\left. \begin{aligned} N_{i,0}(u) &= \begin{cases} 1 & u_i \leq u < u_{i+1} \\ 0 & \text{otherwise} \end{cases} \\ N_{i,p}(u) &= \frac{u - u_i}{u_{i+p} - u_i} N_{i,p-1}(u) + \frac{u_{i+p+1} - u}{u_{i+p+1} - u_{i+1}} N_{i+1,p-1}(u) \end{aligned} \right\} \quad (11)$$

B-spline curves are defined as follows:

$$\mathbf{c}(u) = \sum_{i=0}^n N_{i,p}(u) \mathbf{P}_i \quad (12)$$

where \mathbf{P} is the vector of control points of the B-spline curve. NURBS curve, which is the weighted and rational form of B-spline, can be expressed as follows (Piegl and Tiller, 1997):

$$\mathbf{c}(u) = \frac{\sum_{i=0}^n N_{i,p}(u) w_i \mathbf{P}_i}{\sum_{i=0}^n N_{i,p}(u) w_i} \quad (13)$$

where w_i is the weight of i -th control point. A NURBS surface of degree p in the direction u and degree q in direction v is represented as follows (Piegl and Tiller, 1997):

$$\mathbf{p}(u, v) = \frac{\sum_{i=0}^n \sum_{j=0}^m N_{i,p}(u) N_{j,q}(v) w_{ij} \mathbf{P}_{ij}}{\sum_{i=0}^n \sum_{j=0}^m N_{i,p}(u) N_{j,q}(v) w_{ij}} \quad (14)$$

where the size of control points matrix \mathbf{P}_{ij} and weights w_{ij} is $n \times m$.

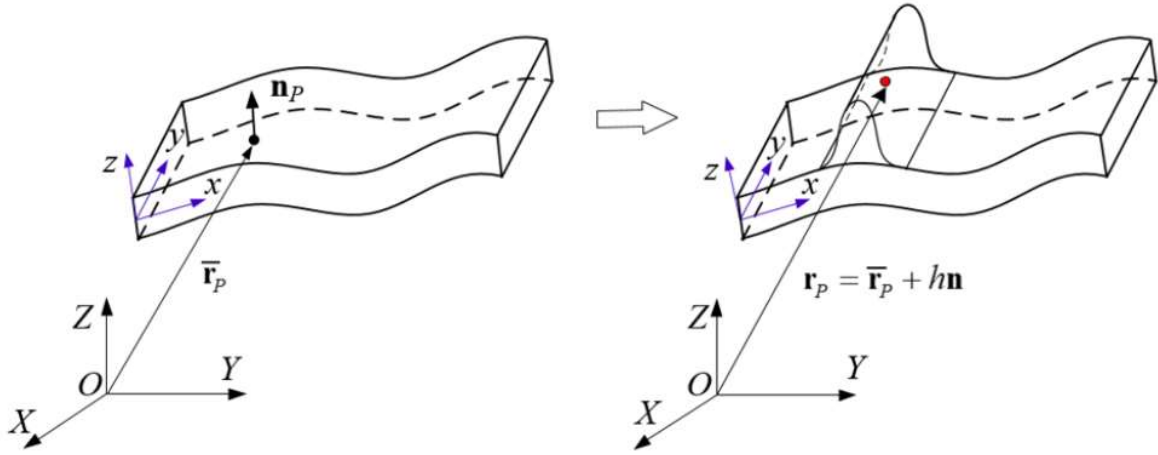
3.3.2 Localized Geometry and ANCF Elements

In this section, two methods for integrating the localized geometry with ANCF elements are described. The global geometry of the structure is represented by the ANCF shape functions and the element nodal coordinates, whereas the shape of localized geometry is described using the NURBS representation. As mentioned earlier the basic ANCF geometry that the localized geometry is superimposed on can be defined as $\bar{\mathbf{r}}(x, y, z, t) = \mathbf{S}(x, y, z) \mathbf{e}(t)$. In this section, \mathbf{r} refers to the ANCF element geometry that accounts for the local geometry features, whereas $\bar{\mathbf{r}}$ refers to the ANCF geometry without localized geometry modifications. When a local feature such as a protrusion is added in an element domain Ω_l , its shape can be defined by overlapping a height value on the basic element shape along a direction normal to the surface. Accordingly, the modified position field with the groove in the element can be denoted as

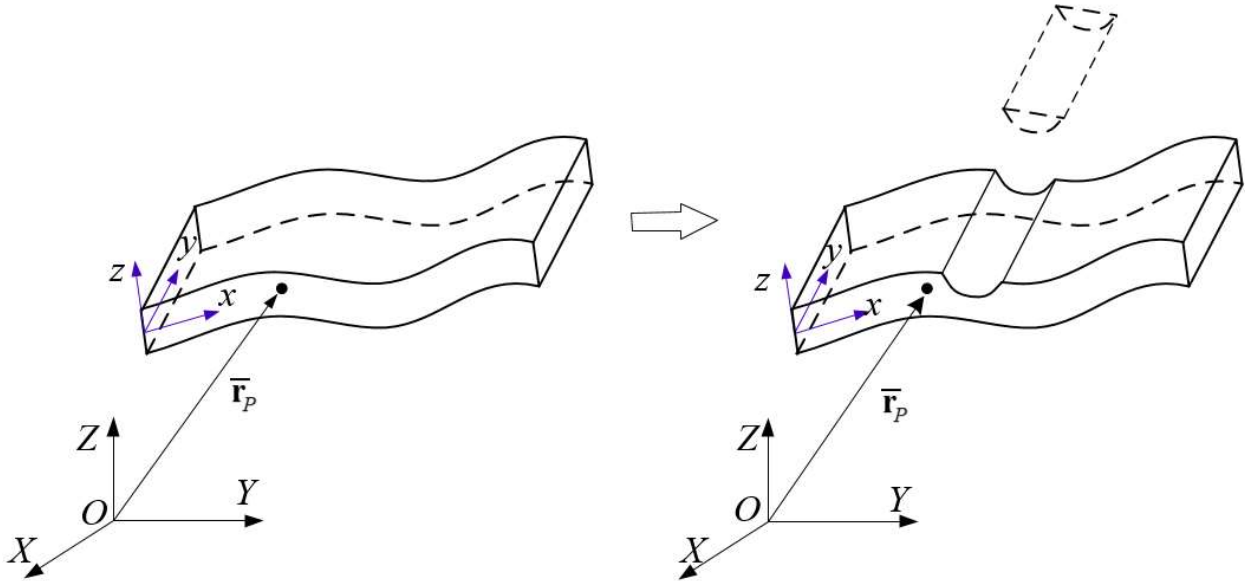
$$\mathbf{r}(x, y, z, t) = \begin{cases} \bar{\mathbf{r}}(x, y, z, t) & (x, y) \notin \Omega_l \\ \bar{\mathbf{r}}(x, y, z, t) + h(x, y) \mathbf{n} & (x, y) \in \Omega_l \end{cases} \quad (15)$$

where \mathbf{n} is the normal to the basic ANCF surface calculated as $\mathbf{n} = (\bar{\mathbf{r}}_x \times \bar{\mathbf{r}}_y) / |\bar{\mathbf{r}}_x \times \bar{\mathbf{r}}_y|$, $h(x, y)$ is the thickness of the localized geometry, which may be represented by a NURBS curve or surface, and Ω_l is the domain on which localized geometry is defined. As shown in Figure 19(a), if the height is set to a positive value, a protrusion can be defined in the ANCF element. This method

can also be used to define other localized geometries by defining different NURBS curves and surfaces.



(a) Overlapping method



(b) Domain trimming method

Figure 19. Integration of localized geometry with ANCF geometry

Another method that is quite useful in defining localized surface geometry, especially when dealing with features like a groove, can be implemented by trimming a given ANCF domain with

a boundary curve described by NURBS as is illustrated in Figure 19(b). This method can be more general than the overlapping method particularly when multiple curves or surfaces are used to define the boundary. However, for the fully parameterized ANCF elements considered in this chapter, the focus is on the simple situation of a single type of localized geometry, so only one NURBS curve or NURBS surface is used to define the trimming boundary. The easiest way to implement this method is to augment the original thickness domain of the element from $z_0 \in [-0.5, 0.5]$ to either $z \in [z_{min}, 0.5]$ or $z \in [-0.5, z_{max}]$ where the upper and lower surface of the element can be locally defined by the dimensionless coordinates z_{max} and z_{min} respectively which may be controlled by a function $f(x, y)$, and $[,]$ refers to a closed interval.

Since during the numerical integration process (x, y, z) are the local coordinates in the element straight configuration and the parameters of NURBS are commonly based on the arc length of the curve or the isoparametric curves, a mapping, $(x, y) \rightarrow (u, v)$, is required between the ANCF local coordinates and NURBS localized geometric parameters, which is shown in Figure 20. For example, if the localized geometry is defined on the top surface of the ANCF element, the domain of this geometry can be defined along the element longitudinal and lateral directions as $x \in [0, 1]$ and $y \in [y_a, y_b]$ respectively. However, the range of the function defining the geometry may only vary with y . For such geometry and for the overlapping and the trimming methods described in this section, the mapping process between ANCF and NURBS can be summarized as follows:

- Step 1:** If $y \in [y_a, y_b]$, $\bar{y} = (y - y_a) / (y_b - y_a)$, GOTO Step 2; ELSE GOTO Step 5.2
- Step 2:** Initialize $\bar{u}_0 = \bar{y}$

- Step 3:** Carry out Newton iteration: $\bar{u}_{k+1} = \bar{u}_k - (\mathbf{B}^T \mathbf{c}(\bar{u}_k) - y) / \mathbf{B}^T \mathbf{c}'(\bar{u}_k)$, where
- $$\mathbf{B} = [0 \quad 1 \quad 0]^T$$
- Step 4:** If $|\bar{u}_{k+1} - \bar{u}_k| > \varepsilon$, where ε is a specified tolerance, GOTO Step 3, ELSE GOTO Step 5.1
- Step 5.1:** $(x, y, z_{\max}) = \mathbf{c}(\bar{u}_{k+1})$; GOTO Step 6
- Step 5.2:** $(x, y, z_{\max}) = (x, y, 0.5)$; GOTO Step 6
- Step 6:** Calculate numerical integration points and weights in vertical domain $[-0.5, z_{\max}]$
- Step 7:** Calculate actual element global coordinates by either overlapping or domain trimming method

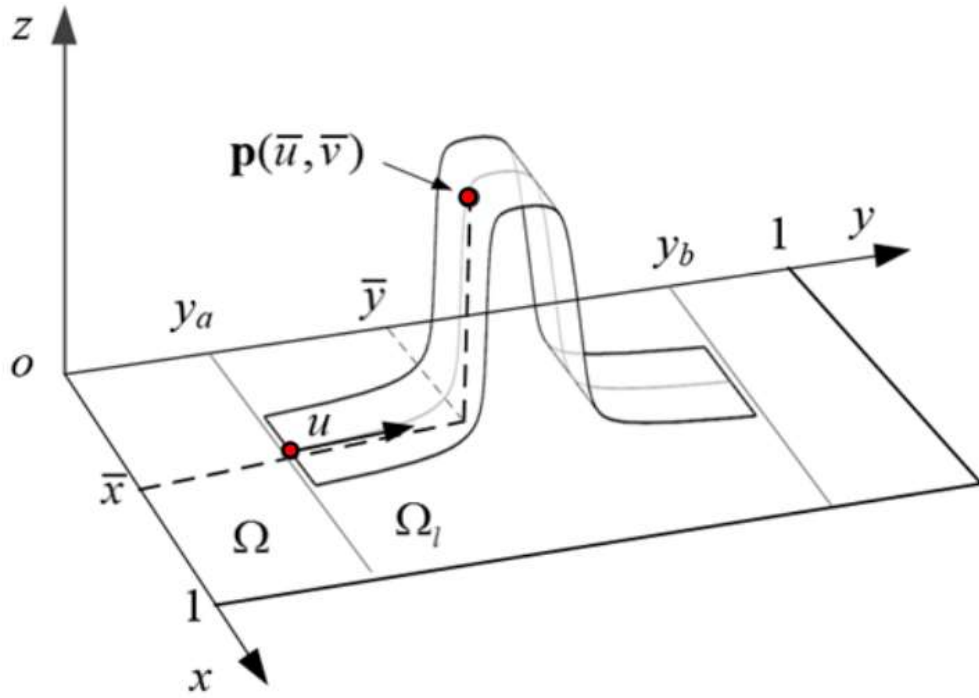


Figure 20. Mapping between the localized geometry parameters and ANCF element coordinates

Using the procedure described in this section, the mapping between the NURBS parameters and the ANCF local coordinates can be achieved, and the localized geometry can be superimposed on the ANCF surface.

3.4 Numerical Integration Method

The basic idea of the FE method is to approximate the governing differential equations of the flexible body by mesh discretization and numerical integration. Mesh refinement is currently the only way to define detailed geometry using ANCF elements. A very fine mesh of ANCF elements without parallel computation could lead to long simulation run times. Since the computational implementation of the FE method as well as the new concepts proposed in this chapter heavily rely on numerical integration, this section will discuss the numerical integration method used and its accuracy.

3.4.1 Global Domain and Subdomain Integration Method

The number and distribution of the integration points has a significant influence on the simulation accuracy. The Gauss integration method is the standard method used in the FE analysis since it is the most accurate numerical integration method for a given number of integration points. Therefore, the Gauss integration method is used in this chapter as well. In order to integrate the localized geometry in this chapter, two methods: the global domain and the subdomain methods are used and compared.

In the global domain integration method, there is only one integration domain Ω_g for every element, and an integration point can be identified by its coordinates in the element as

$\mathbf{q}_i = (x_i, y_i, z_i) = (x_i, y_i, f(x_i, y_i))$. A function $\varphi(x_i, y_i, z_i)$ can be numerically integrated using the global domain method as

$$\Gamma_g = \sum_{i=1}^{n_g} \varphi(x_i, y_i, z_i) w_i = \sum_{i=1}^{n_g} \varphi(x_i, y_i, f(x_i, y_i)) w_i \quad (16)$$

where n_g is the total number of integration points, and w_i is the weight corresponding to the i^{th} integration point. The weights are usually dependent on the orthonormal functions used in the integration scheme and the number of integration points in each direction.

In the subdomain integration method, on the other hand, the whole domain Ω of an element is divided into n_d subdomains $\Omega_1, \Omega_2, \dots, \Omega_{n_d}$ where this set of subdomains satisfies $\Omega = \Omega_1 \cup \Omega_2 \cup \dots \cup \Omega_{n_d}$ and $\Omega_k \cap \Omega_l = \emptyset$ when $k \neq l$. There are \bar{n}_i integration points in each subdomain Ω_j , and the function $\varphi(x_i, y_i, z_i)$ can be numerically integrated on Ω using the subdomain method as

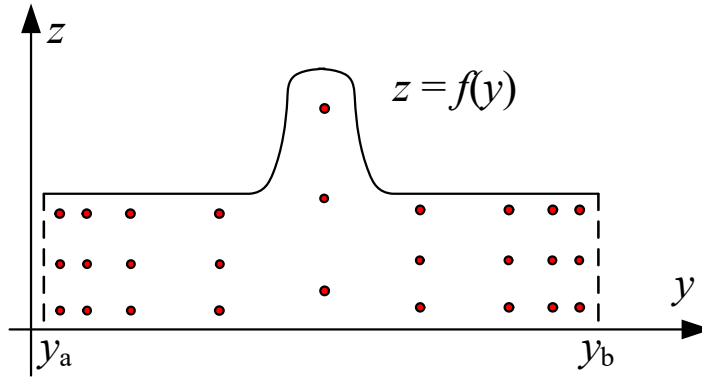
$$\Gamma_l = \sum_{j=1}^{n_d} \sum_{i=1}^{\bar{n}_i} \varphi(\bar{x}_{ji}, \bar{y}_{ji}, f(\bar{x}_{ji}, \bar{y}_{ji})) \bar{w}_{ji} \quad (17)$$

where \bar{w}_{ji} is the integration weight related to the corresponding integration point defined by

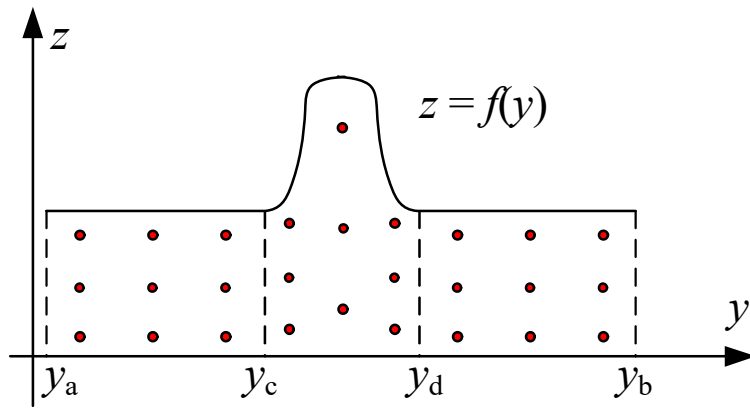
$$\bar{\mathbf{q}}_{ji} = (\bar{x}_{ji}, \bar{y}_{ji}, \bar{z}_{ji}) = (\bar{x}_{ji}, \bar{y}_{ji}, f(\bar{x}_{ji}, \bar{y}_{ji})).$$

Figure 21 shows the distribution of integration points generated by the two integration methods in the same integration domain that includes localized geometry. One major difference between the two methods is that the subdomain method allows for much more flexibility and control of integration points in the domain that is being integrated since the regular single domain or global domain integration is constrained by the abscissa of the integration points which are the

roots of the Legendre polynomial, whereas with the subdomain integration the subdomains can be adjusted based on the configuration of the local geometry. As can be seen in Figure 21, the global domain integration method leads to 3 integration points capturing the localized geometry, whereas the use of the subdomain method would lead to 9 integration points capturing the effect of the localized geometry and leading to more accurate results.



(a) Global domain method



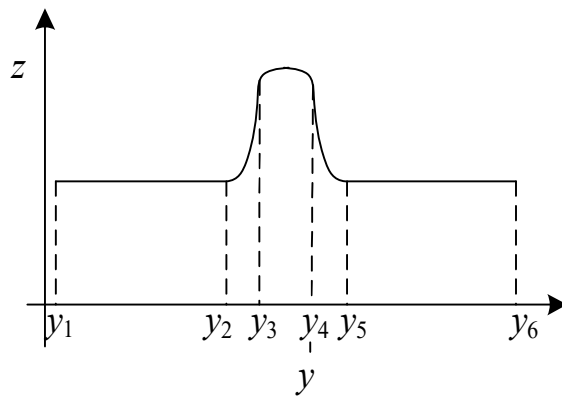
(b) Subdomain method

Figure 21. Distribution of integration points using the global domain and subdomain methods

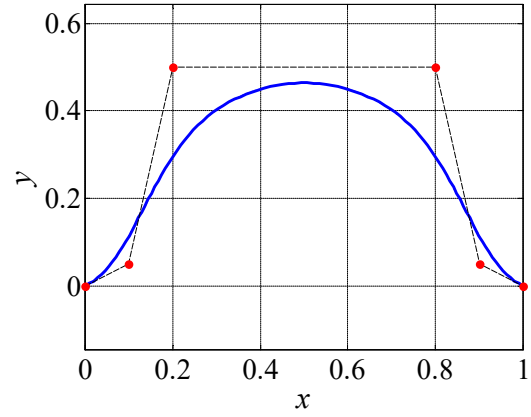
3.4.2 Comparison of the Two Integration Methods

Figure 22 compares the two integration methods described previously in this section. Figure 22(a) shows the discretization of the element in the y direction using the subdomain method. The element thickness is varied using the function $z = f(y)$ defined on the domain $[y_1, y_6]$, wherein the local geometry feature of interest is located in the middle of the given domain. The whole domain is divided into five subdomains, of which subdomains $[y_2, y_3]$, $[y_3, y_4]$ and $[y_4, y_5]$ are used to define the local feature. Figure 22(b) shows the detailed localized geometry shape, which is represented by a NURBS curve and its control points, which are also shown in the figure. In order to compare between the global and subdomain integration methods, the norm of the mass matrix is evaluated for a plate element with the localized geometry information given in Figure 22(a) and 22(b) superimposed on its lower surface. Figure 22(c) shows the results of the norm of the mass matrix evaluated using the two numerical integration methods. The mass matrix of ANCF elements is defined as $\mathbf{M} = \int_V \rho \mathbf{S}^T \mathbf{S} J_o dV$, where ρ is the mass density, V is the volume in the straight configuration, and J_o is the determinant of the matrix of position vector gradients that define the curved geometry in the reference configuration. In this example, the density ρ is assumed to be $1500 \text{ kg} / \text{m}^3$, the length and width both are taken to be 1m, and the thickness is 0.05m. As can be seen in Figure 22(c), while using the subdomain integration method, increasing the number of integration points to more than 3 in every subdomain leads to faster convergence in the norm of the mass matrix. However, when using the global domain integration method, even increasing the number of integration points to more than 40 does not lead to satisfactory convergence of the norm of the mass matrix. These results show that local and more dense

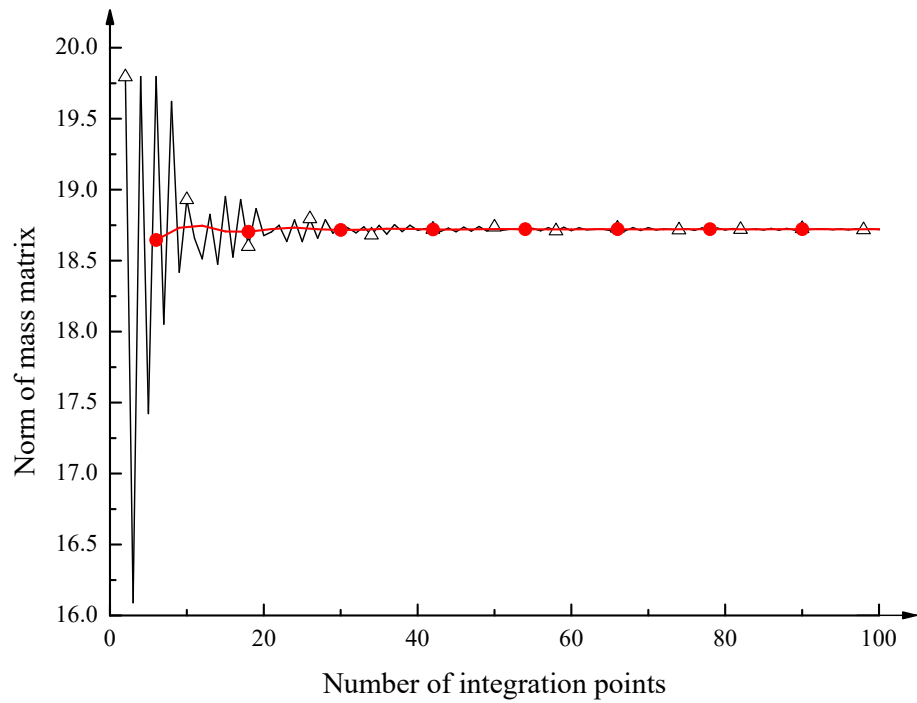
distribution of the integration point mesh using the subdomain method is a better choice considering the balance between solution accuracy and computational cost.



(a) Division of subdomain



(b) Localized geometry (● Control point)



(c) Comparison of mass matrix norm using the two integration methods

(—△— Global domain —●— Subdomain)

Figure 22. Comparison of global domain and subdomain integration method

3.5 ANCF Governing Equations

In this chapter, the dynamic equations of motion are formulated using ANCF elements. This formulation leads to a constant mass matrix and nonlinear elastic force vector. Regardless of the complexity of the geometry superimposed on the ANCF elements, the mass matrix remains constant and the Coriolis and centrifugal forces are identically zero vectors. Using the expressions of the kinetic energy, strain energy and the virtual work of external forces, the dynamic equations of the ANCF element can be defined in the form $\mathbf{M}\ddot{\mathbf{e}} + \mathbf{Q}_k = \mathbf{Q}_e$, where \mathbf{M} is the mass matrix, \mathbf{e} is the vector of nodal coordinates, \mathbf{Q}_k is the vector of elastic forces, and \mathbf{Q}_e is the vector of generalized external forces including the gravity force and contact force \mathbf{Q}_c . Using the continuum mechanics approach, the virtual work of the elastic forces of fully parameterized elements can be written as $\delta W_k = - \int_V \boldsymbol{\sigma}_{P2} : \delta \boldsymbol{\varepsilon} dV$ where $\boldsymbol{\sigma}_{P2}$ is the second Piola-Kirchhoff stress tensor conjugate to $\boldsymbol{\varepsilon}$ which is the Green-Lagrange strain tensor defined as $\boldsymbol{\varepsilon} = \frac{1}{2}(\mathbf{J}^T \mathbf{J} - \mathbf{I})$, where \mathbf{J} is the matrix of position vector gradients. In case of a curved reference configuration $\mathbf{J} = \frac{\partial \mathbf{r}}{\partial \mathbf{X}} = \left(\frac{\partial \mathbf{r}}{\partial \mathbf{x}} \right) \left(\frac{\partial \mathbf{x}}{\partial \mathbf{X}} \right) = \mathbf{J}_e \mathbf{J}_o^{-1}$ where \mathbf{r} and \mathbf{X} are, respectively, the position vector of a material point in the current configuration and reference configuration, and $\mathbf{x} = [x \ y \ z]^T$ is the vector of element spatial coordinates. For generality, $\boldsymbol{\sigma}_{P2}$ can be derived from the strain energy function as $\boldsymbol{\sigma}_{P2} = 2\partial U / \partial \mathbf{C}_r$, where U is the strain energy potential function, and \mathbf{C}_r is the right Cauchy-Green deformation tensor defined as $\mathbf{C}_r = \mathbf{J}^T \mathbf{J}$ (Ogden, 1984; Shabana, 2012). In the case of the hyperelastic nearly incompressible Mooney-Rivlin material model used in one of the examples in this chapter, $U = \mu_{10}(\bar{I}_1 - 3) + \mu_{01}(\bar{I}_2 - 3) + \frac{1}{2}k(J - 1)^2$ where μ_{10} , μ_{01} are material coefficients,

\bar{I}_1, \bar{I}_2 are the invariants of the deviatoric part of the \mathbf{C}_r tensor, k is the penalty term and $J = |\mathbf{J}|$ (Ogden, 1984; Shabana, 2012; Orzechowski and Fraczek, 2015).

Similar to the contact model described in Chapter 2, a simple contact model based on a penalty approach and coulomb friction is used in this chapter as well. The contact forces are treated as point forces where the normal component is defined as $\mathbf{f}_n = (k_p d + c_p \dot{d}) \mathbf{n}$, where \mathbf{f}_n is the normal component of the contact force, k_p is the ground stiffness coefficient, c_p is the ground damping coefficient, d and \dot{d} are the penetration and the rate of penetration respectively, and \mathbf{n} is the unit normal to the ground surface at the contact point. The penetration is calculated as $d = (\mathbf{r}_p - \mathbf{r}_p^g) \cdot \mathbf{n}$, where \mathbf{r}_p is the global position of the contact point on the flexible body, and \mathbf{r}_p^g is the global position of the corresponding contact point on the ground (Patel et al., 2016). For the tangential contact forces, each contact point is detected for its relative velocity with respect to the ground in order to apply the tangential force that depends on the coefficient of friction μ . The expression for the generalized contact forces associated with the ANCF generalized nodal coordinates can be obtained by using the virtual work of the contact forces and is given by $\mathbf{Q}_c = \mathbf{S}(\mathbf{x})^T \mathbf{f}_c$, where $\mathbf{f}_c = \mathbf{f}_n + \mathbf{f}_t$, where subscripts n and t refer to normal and tangential directions, respectively.

3.6 Numerical Results

Three numerical examples are presented in this section to demonstrate the method of adding localized surface geometry. In the first example, a plate-like structure with localized geometry meshed with ANCF plate elements is used in the simulation of contact with a ground. Different numbers of subdomains and integration points are used to compare their influence on the accuracy

of the results. In the second example, the deformation of a cantilever plate with grooves under a concentrated force at a corner of the free end is simulated and the results are compared with the results obtained using a commercial FE code (ANSYS, 2013). In the third example, ANCF plate elements with a nearly incompressible Mooney-Rivlin rubber material are used to model a tire with tread details, and the convergence of this model is demonstrated by refining the tire mesh.

3.6.1 Plate Contact Example

In this example, localized surface geometry is overlapped on the ANCF elements and the structure is allowed to free fall and contact with a ground. The length and width of the plate element are both 1m and the thickness is 0.05m. The localized geometry that is defined between $[0.4, 0.6]$ of the non-dimensional y coordinate of the element is shown in Figure 23(a). The material and contact properties are given in Table 7 and 8, respectively. There is one integration domain in the vertical and longitudinal directions of the element with 3 and 7 integration points, respectively, whereas the integration domain in lateral direction is divided into several subdomains according to the shape of the localized geometry, and the number of integration points in the lateral subdomains is varied from 2 to 5 in order to examine the effectiveness of the subdomain integration scheme. Figure 23(b) shows the contact patch of one ANCF plate element with localized surface geometry.

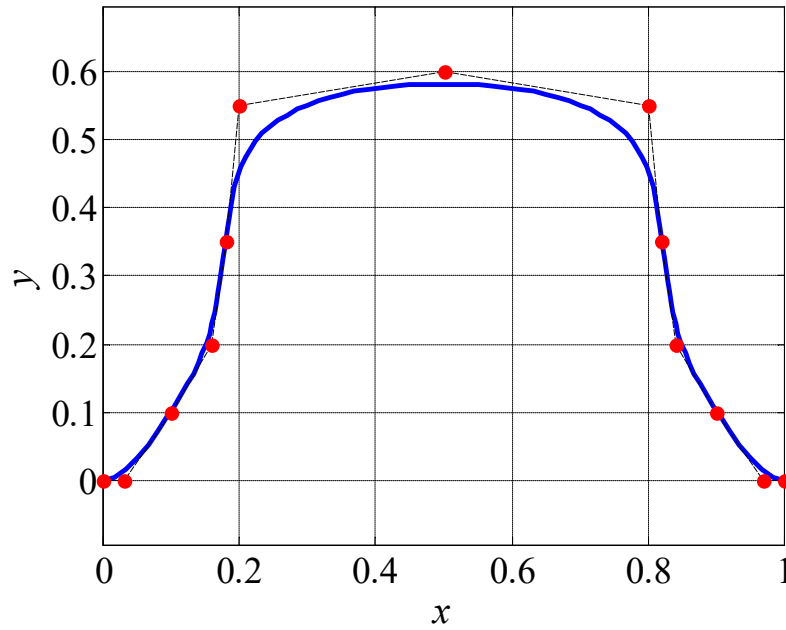
In order to analyze the effect of the subdomain division and number of integration points per subdomain, the vertical position of a contact point on the plate lower surface is shown. First the influence of the number of integration points per subdomain is analyzed by dividing the element lateral domain into 3 subdomains. As shown in Figure 24, as the number of integration points per subdomain is increased from 2 to 5, the solution converges.

Table 7. Material properties used in the plate contact example

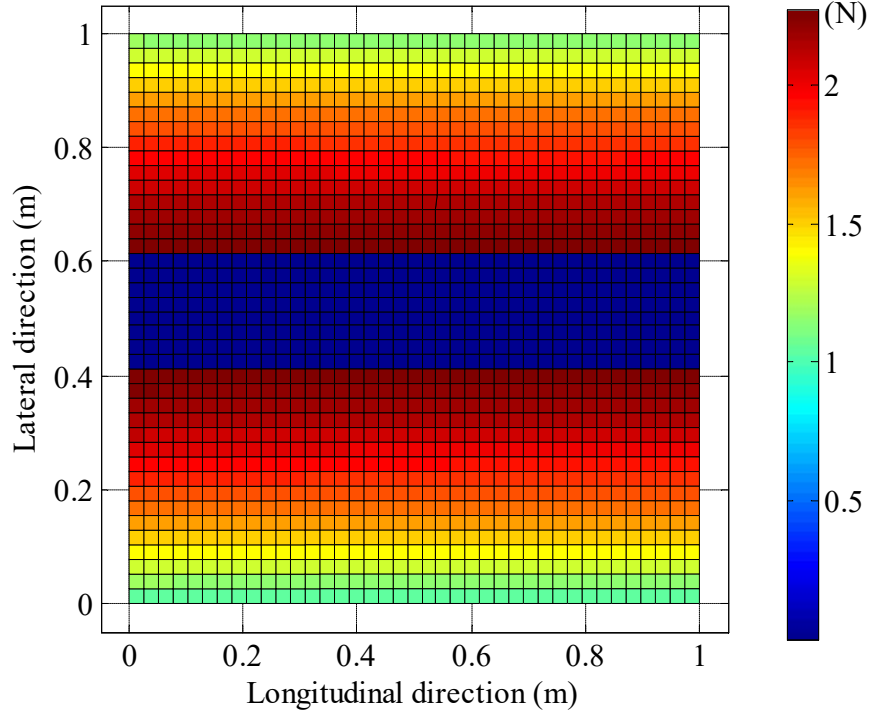
Linear Elastic	
Density (kg/m ³)	7860
Modulus of Elasticity (MPa)	0.2
Modulus of Rigidity (MPa)	0.1

Table 8. Contact parameters used in the plate contact example

Parameter	Value
Ground Stiffness (N/m)	8500
Ground Damping (N·s/m)	20.0
Friction Coefficient μ	0.75



(a) The definition of localized geometry
(● Control point)



(b) Contact force at $t=1.0s$

Figure 23. One-plate contact example

However, it can be seen from the enlarged drawing in Figure 24 that 3 integration points per subdomain are sufficient for obtaining a converged solution when compared against the extra computational cost of 5 integration points per subdomain. The effect of the number of subdomains per element is investigated using the same example. It can be seen from Figure 25 that increasing the number of subdomains from 2 to 4, with 3 integration points per subdomain yields converged results as well. Furthermore, it can be seen from the enlarged plot in Figure 25 that 3 subdomains lead to sufficiently converged results. The number of integration points per subdomain and the number of subdomains per element may have to differ for more complicated geometry; however, this example shows that the subdomain method is a viable and relatively computationally efficient method for including localized geometry details in an ANCF mesh without further mesh discretization.

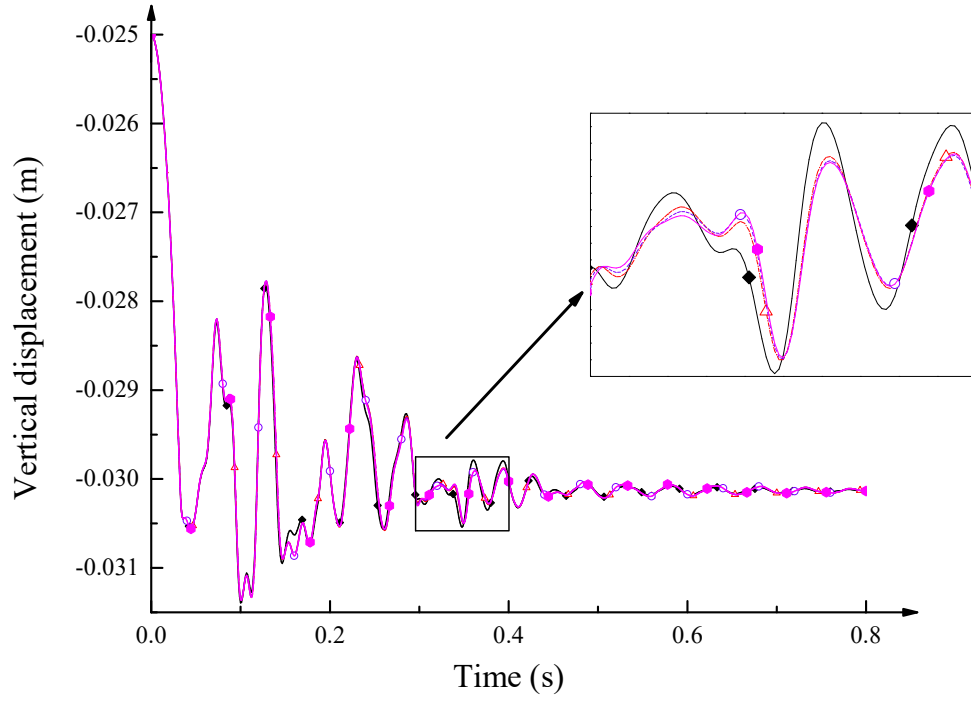


Figure 24. Vertical displacement using different numbers of integration points

(—◆— 2 points - -△- - 3 points - -○- - 4 points —●— 5 points)

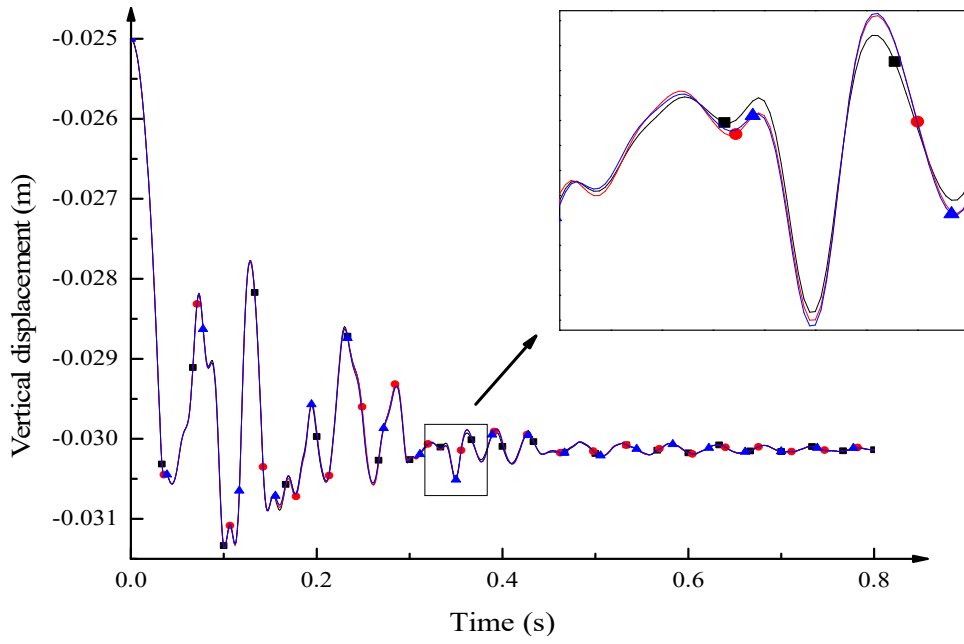
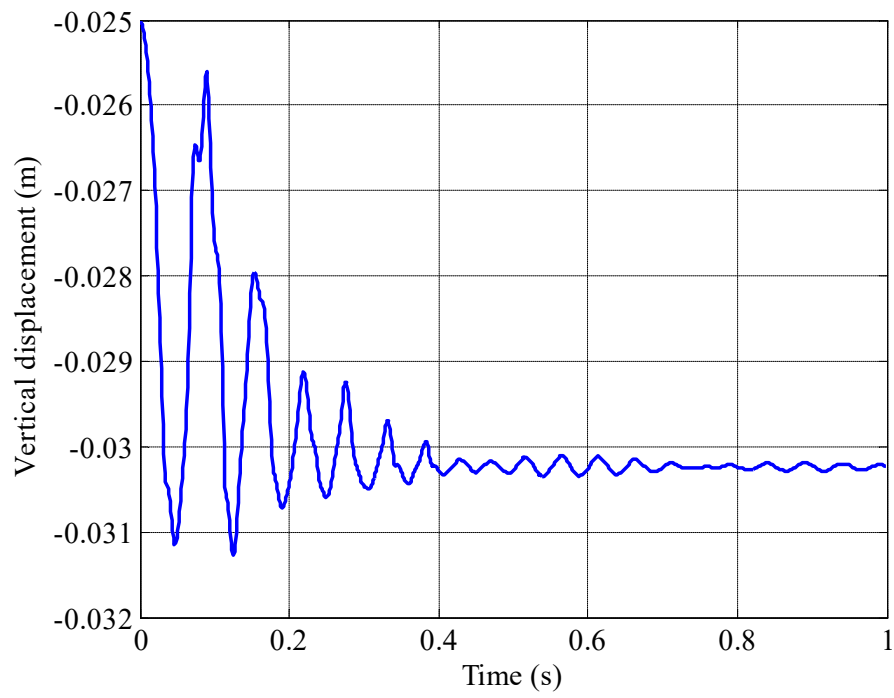
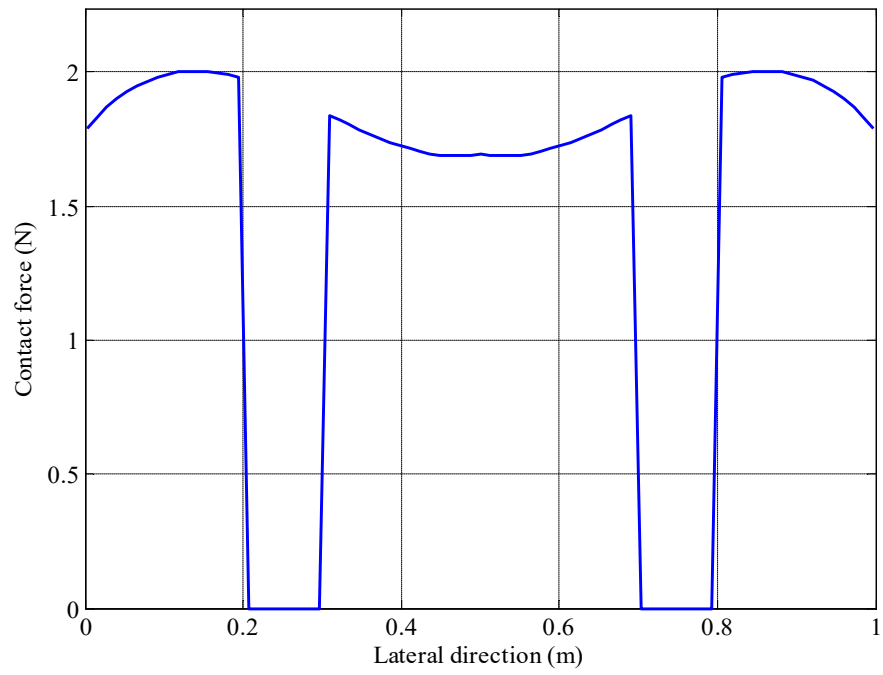


Figure 25. Vertical displacement using different numbers of subdomains

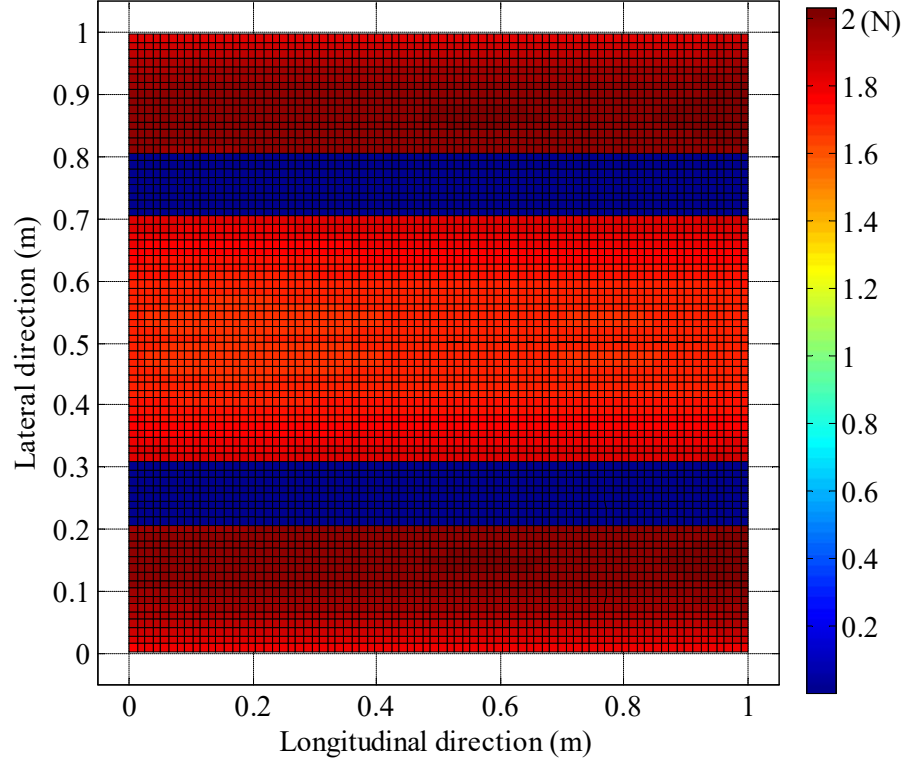
(—■— 2 subdomains —●— 3 subdomains —▲— 4 subdomains)



(a) Vertical displacement of contact point



(b) Contact force distribution at the structure mid-section at $t = 1.0s$



(c) Contact force at $t = 1.0s$

Figure 26. 2×2 ANCF plate element mesh with localized geometry

Figures 26(a), (b) and (c) show the results of the aforementioned contact example with a 2×2 mesh of ANCF plate elements with two grooves representing the localized surface geometry. The groove localized geometry shape, overall structure dimensions and the material properties are the same as one element mesh. Figure 26(a) shows the time evolution of the vertical position of the center point at the plate lower surface. Figures 26(b) and 26(c) show the contact force distribution at $t = 1s$, which clearly shows the effect of the grooves is captured in the contact force distribution.

3.6.2 Cantilever Plate Validation

In order to show that the method proposed in this chapter is able to capture the effect of the local surface geometry, a validation example in the form of a cantilever plate with a tip force at its free end is provided. The ANCF results are compared with those obtained from a commercial FE code

(ANSYS, 2013). The conforming fully parameterized plate element is used for the ANCF mesh whereas SOLID186 element which has a quadratic displacement field is used in the commercial FE code. Figure 27 shows the reference configuration of the cantilever plate. The material model is assumed to be linear elastic and the material properties are given in Table 9. The overall length, width, and thickness of the structure is taken to be $1 \times 1 \times 0.05$ m . Each ANCF element in its lateral direction is divided into 3 subdomains with 3 integration points per subdomain in order to account for the localized geometry. The loading function at point P which is the tip of the free end shown in Figure 27 is a linear function of time and reaches its maximum value of -50 N at $t = 1$ s .

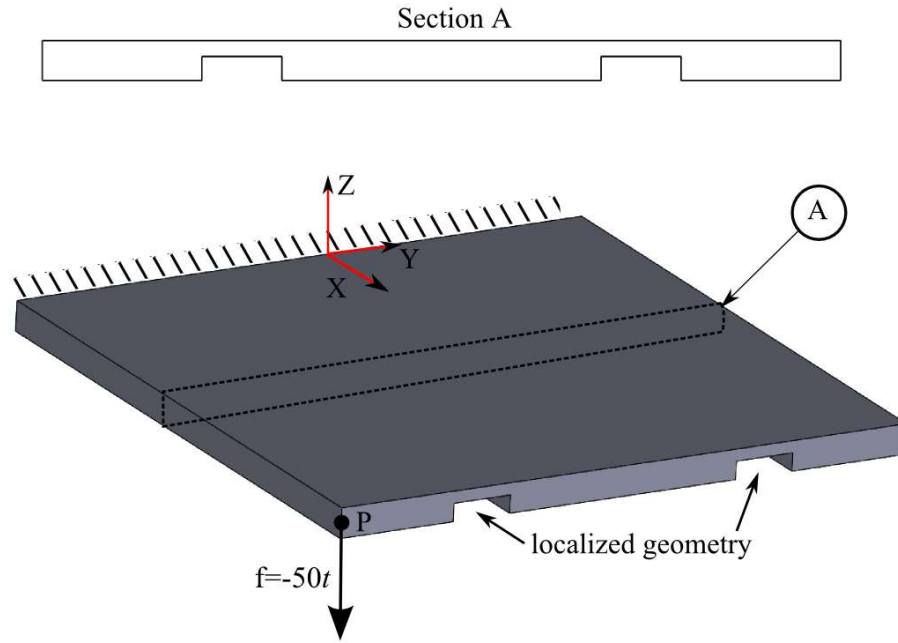


Figure 27. Cantilever plate reference configuration and cross section

Table 9. Material properties used in the cantilever plate example

Linear Elastic	
Density (kg/m^3)	2000
Modulus of Elasticity (MPa)	2.0
Modulus of Rigidity (MPa)	1.0

Table 10. Comparison of the cantilever plate tip vertical position with and without localized geometry

Mesh		With Local Geometry (m)	Without Local Geometry (m)
ANCF	2×2	-0.4098	-0.3763
	3×3	-0.4649	-0.4332
	4×4	-0.5030	-0.4654
	5×5	-0.5232	-0.4774
	6×6	-0.5335	-0.4853
	8×8	-0.5412	-0.4928
	12×12	-0.5469	-0.4966
	16×16	-0.5511	-0.4981
Classical FE converged mesh		-0.5669	-0.5022

Figures 28 and 29 show the convergence of the classical FE mesh and ANCF mesh for the given geometry, respectively, and Figure 30 shows the error in the ANCF results against the converged classical FE solution. There is a small difference in the converged solutions of classical FE method and ANCF. This difference can be attributed to the way how each method accounts for the localized geometry in a different manner, however when compared to the total deformation of the structure, the difference in the vertical displacement of the tip point P is approximately 2.79%. Furthermore, Table 10 compares the ANCF solution for the same cantilever plate problem with and without the localized geometry details against a converged classical FE solution. Table 10 gives the vertical position of the tip point P shown in Figure 27 at $t=1s$. Accounting for the localized geometry has a softening effect on the structure since removing material in the longitudinal and lateral directions of the structure will reduce its bending stiffness as can be seen from the ANCF and classical FE solutions with and without the local geometry. Thus, the method proposed in this chapter can successfully capture the effect of the localized geometry in a given ANCF mesh.

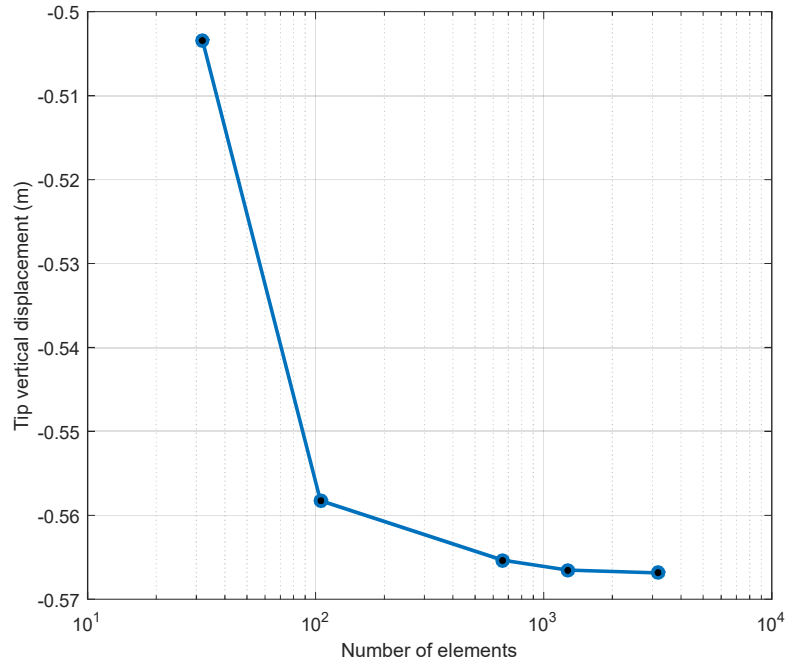


Figure 28. Convergence of classical FE code solution for plate structure with local geometry

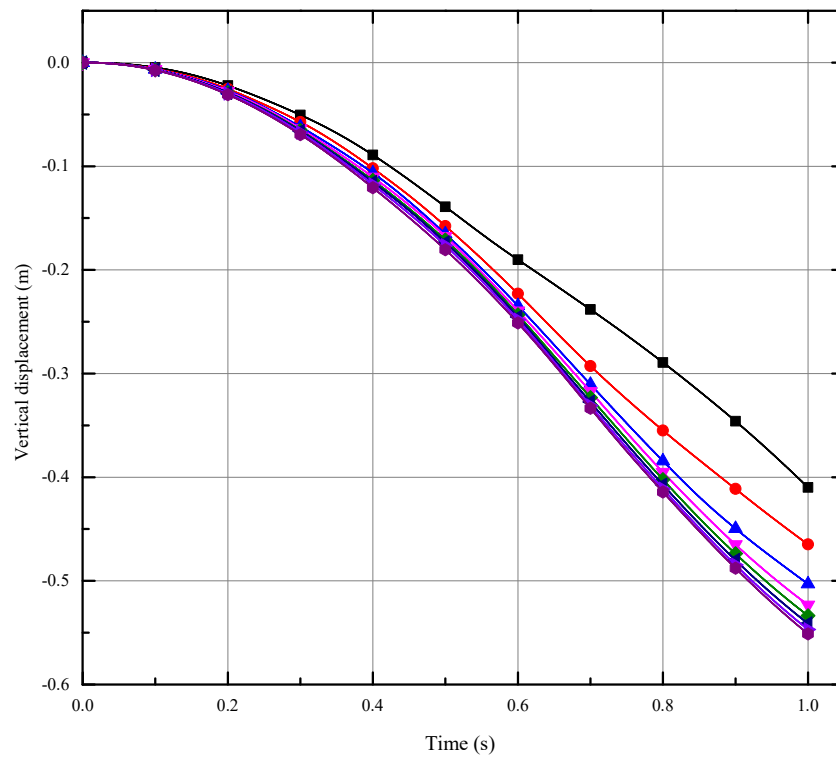


Figure 29. Convergence of ANCF solution for plate structure with local geometry

(—■— 2X2 —●— 3X3 —▲— 4X4 —▼— 5X5 —◆— 6X6 —◀— 8X8 —▶— 12X12 —●— 16X16)

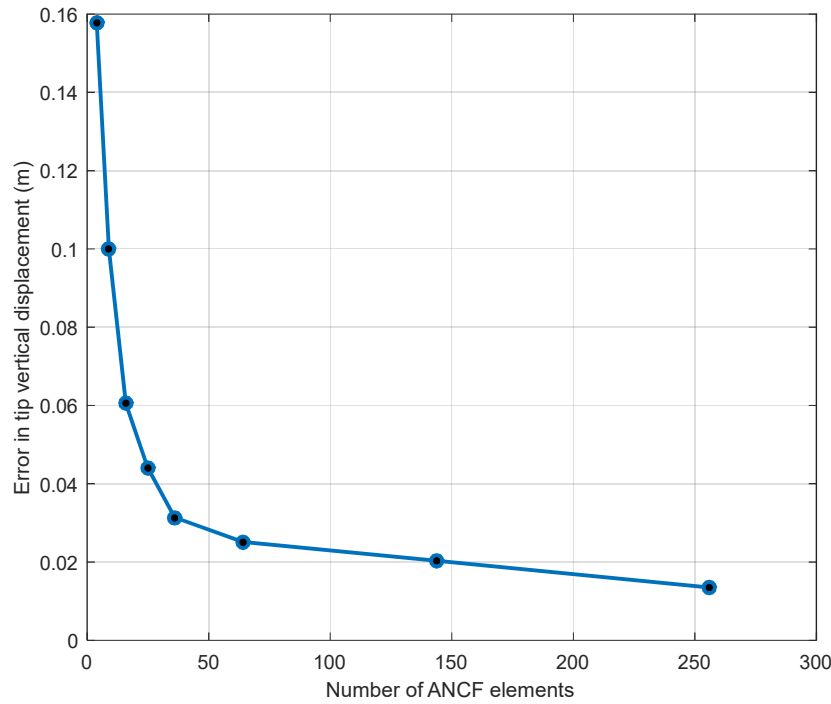


Figure 30. Difference between ANCF solution and classical FE solution

3.6.3 Tire Contact Example

In this numerical example, a tire meshed with 240 ANCF plate elements is dropped on ground and the resulting contact patch is examined. NURBS is used to create the tire tread details, which are the grooves in the tire. This type of detail in the tire surface geometry is known as the rib type tread as shown in Table 1 (Chapter 1). The tire is based on the 45/65 R45 tire size and a nearly incompressible hyperelastic Mooney-Rivlin material is used to represent the rubber in the tread. Figure 31 shows the overall shape and cross section of the tire without any tread details. The material and contact parameters used for this example can be found in Tables 11 and 12 respectively. The NURBS method using parameter mapping is used to superimpose the localized tread geometry on the outer surface of the tire. Figure 32(a) shows the control points and the shape of the NURBS curve used for representing the grooves in the tire, whereas the contact patch from

the tire-ground contact is shown in Figure 32(b). Figure 32(b) clearly shows that the contact force is zero in the groove regions of the tire and the tire is supported on the rib regions that are in contact with the ground. Figure 33 shows the determinant of the Jacobian (matrix of position vector gradients) at the center point of the tire tread lower surface, clearly illustrating that the material stays nearly incompressible during the large deformation of the tire. This example clearly shows the effectiveness of the subdomain method in capturing the localized surface geometry in the case of tires in contact with ground using the ANCF framework.

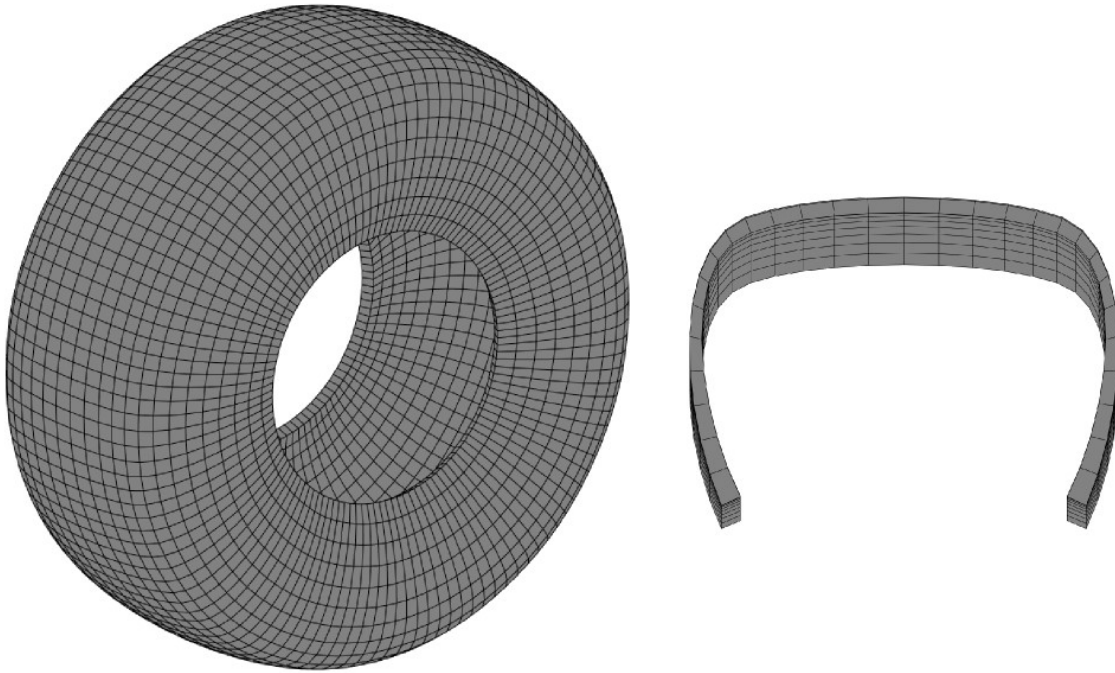
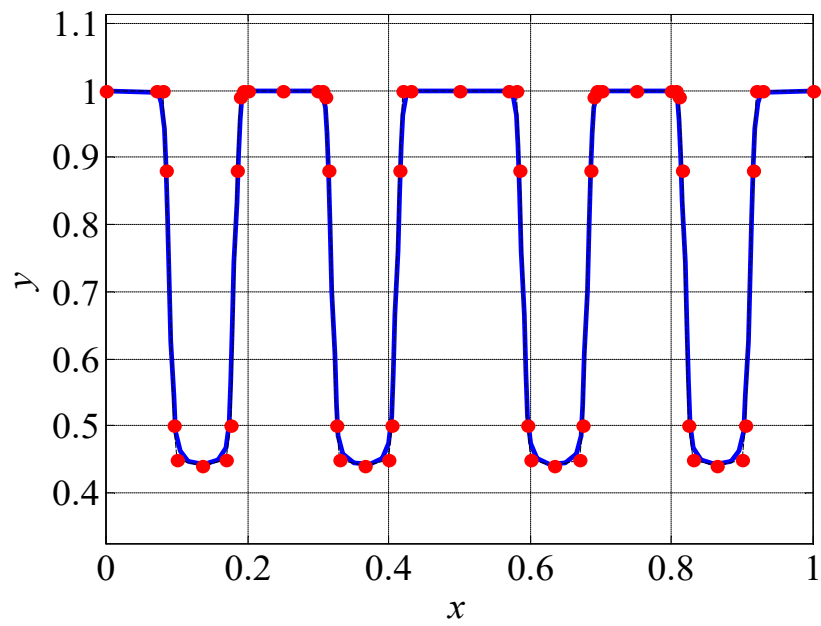


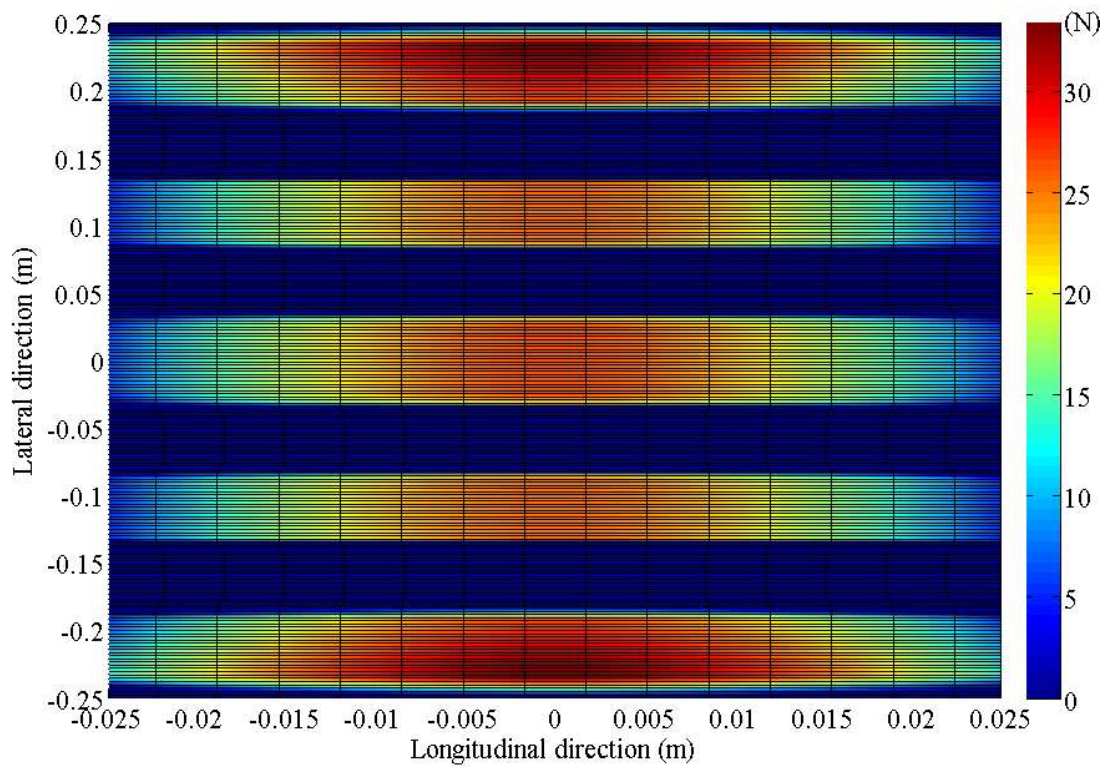
Figure 31. ANCF tire geometry

Table 11. Material properties used in the tire example

Mooney-Rivlin	
Density (kg/m^3)	1500
Coefficient μ_{10} (MPa)	2.5
Coefficient μ_{01} (MPa)	2.0
Penalty coefficient k	1.33×10^8



(a) Localized surface geometry of the tire tread
(● Control point)



(b) Tire tread contact patch

Figure 32. Tire tread with four grooves

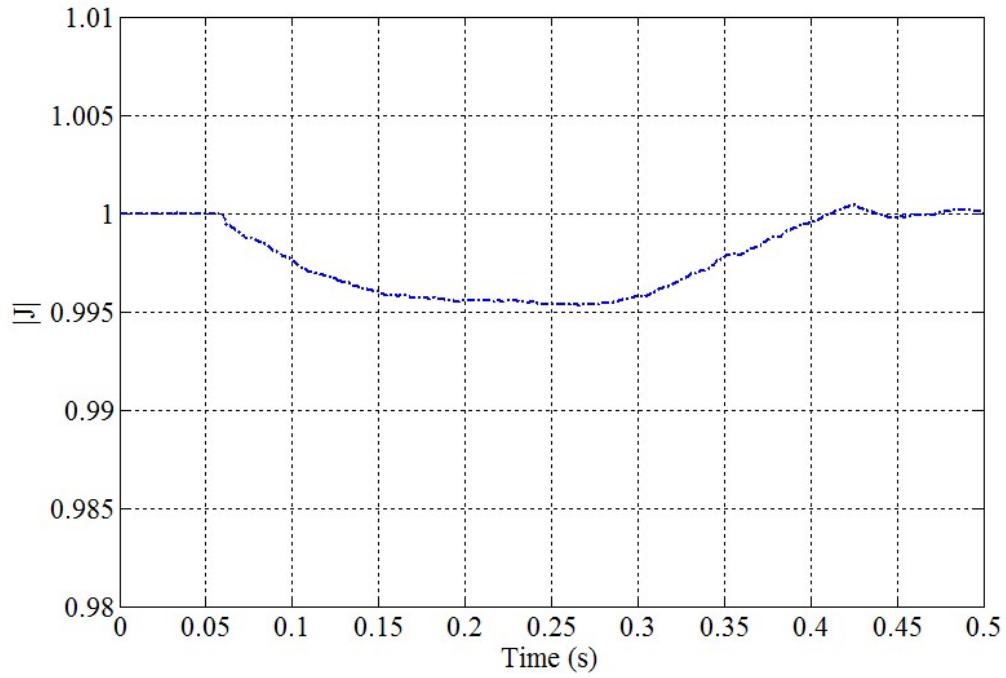


Figure 33. Value of $|\mathbf{J}|$ at the middle point on the bottom of the tire tread surface

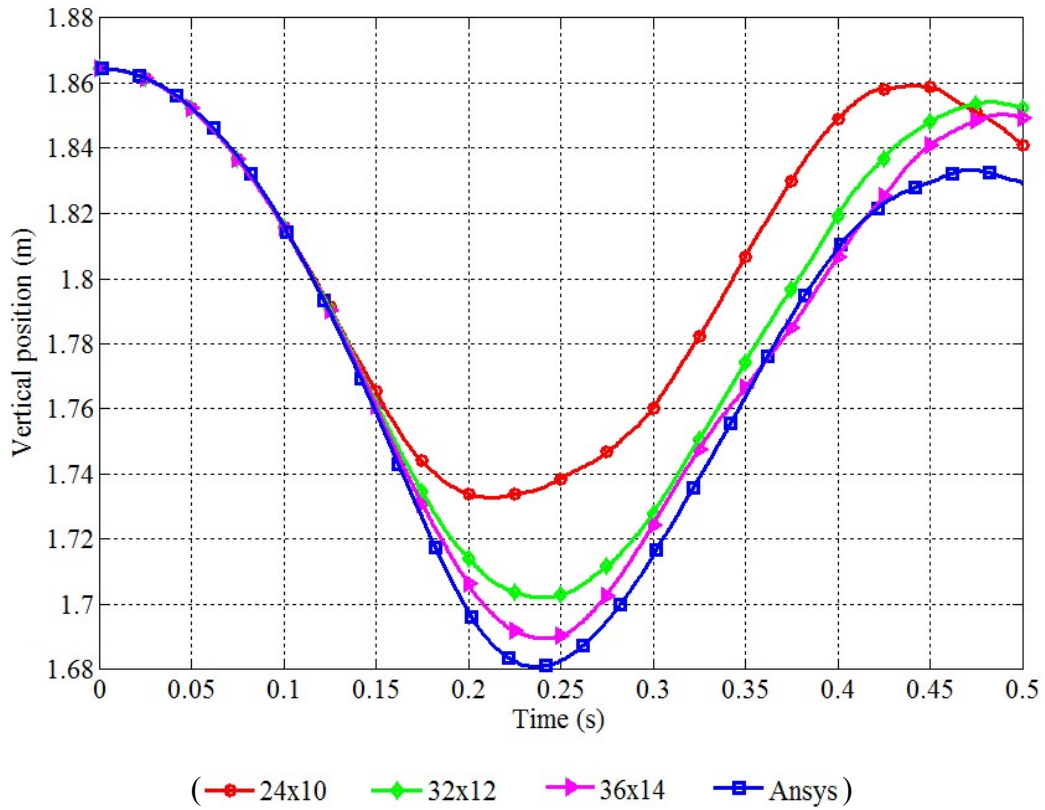


Figure 34. Position convergence of ANCF solution for tire contact example

Table 12. Contact parameters used in the tire example

Parameter	Value
Ground Stiffness (kN/m)	70
Ground Damping (N.s/m)	160
Friction Coefficient μ	0.75

Furthermore, in order to demonstrate the convergence of the model, the tire mesh is refined and the convergence of the model against results acquired from a commercial FE code is shown in Figure 34 through the evolution of the vertical position of node 1 on the tire mesh. The mesh code provided in Figure 34 follows an $n \times m$ format where n refers to the number of elements in the tire radial direction, whereas m refers to the number of elements in the tire lateral direction. The commercial FE code mesh consisted of 22,631 quadratic tetrahedral elements in order to be able to correctly capture the localized geometry on the surface of the tire. The material and contact parameters used for this convergence analysis are provided in Tables 11 and 12 respectively. For the ANCF results, selectively reduced integration was used on the volumetric term of the Mooney Rivlin material model, whereas full integration was used on the deviatoric terms. The small difference between the converged ANCF result and the commercial FE code results can be attributed to the presence of some shear locking in the model since the deviatoric term of the Mooney Rivlin model used full integration in the x and y element directions. The reason for this is the usage of subdomain integration in the element lateral direction which adds more integration points in that domain in order to capture the localized geometry. Reduced integration with subdomain integration would lead to 1 integration point in every subdomain which might lead to spurious modes, potential hourglassing in the elements and a very crude approximation of the localized geometry. The study of reduced integration with subdomain integration requires more investigation and can be considered as a topic of research in the future. These results also lead to

the conclusion that special attention must be paid to the tire mesh discretization as well as element locking phenomena in order to have a good ANCF model that yields accurate results. Further validation is required to ensure the correlation with a physical model; however, this study also shows that the continuum-based fully parameterized plate element can achieve convergence with mesh refinement and locking alleviation techniques.

3.7 Concluding Remarks

In this chapter, a method for the integration of localized surface geometry with fully parameterized ANCF elements is proposed. ANCF FEs are used to create the global geometry and perform the FE/MBS analysis of the bodies. The surface geometry details can be added without refining the mesh to the scale of the detailed features. The localized surface may be represented by NURBS and can accurately describe complex geometric shapes such as a conic surface and freeform surface. The basic idea lies in the integration of the localized surface with the global surface by augmenting the geometry during the numerical integration process. Two methods for including the localized geometry in the ANCF elements are proposed. The overlapping method simply changes the thickness of the element using a function that is dependent on the lateral and longitudinal coordinates of the element. The domain trimming method takes advantage of the powerful NURBS geometry as a tool to trim the domain of original ANCF element according to the shape of the localized geometry. While using NURBS to define the localized geometry, a mapping between ANCF local coordinates and NURBS localized geometric parameters is used in both geometric integration methods. Furthermore, a comparison of two numerical integration methods, the global domain and the subdomain methods is presented in this chapter. The results show that the subdomain method is better suited for integrating complex geometry in ANCF elements since it

has more flexibility in the distribution of the Gauss integration points. Using the subdomain method, any kind of geometry can be superimposed in the case of fully parameterized ANCF elements without the need for further mesh refinement during dynamic simulations. A cantilever plate example with localized surface geometry is provided to validate the proposed method by comparing the simulation results obtained with the proposed methods against a commercial FE code. A model of a flexible ANCF plate contacting with rigid ground is used to study the effect of the number of subdomains and the number of integration points per subdomain used in accounting for the localized geometry. Finally, a tire model meshed with ANCF plate elements and described by a hyperelastic incompressible Mooney-Rivlin material with four grooves integrated as localized surface geometry is considered. The results from the tire simulation that capture the effect of the grooves in the tire contact patch show the effectiveness of the proposed methods whereas the convergence study performed with the tire model helps support the basis of the proposed concepts by demonstrating that the model can achieve convergence with mesh refinement and reduced integration techniques which help alleviate locking. In summary, the proposed method does a good job of capturing surface geometry without significantly increasing the computational cost that comes from mesh refinement. Future studies can be focused on eliminating the limitations of the method that include the fact that very localized deformations of the more intricate geometry cannot be easily captured since the element deformation field is still governed by its basis functions, and that the method will be challenging to use with very complex three-dimensional changes in the structure's geometry. Studying the effects of reduced integration within the subdomain integration scheme can also be considered as a topic of future investigations.

CHAPTER 4

ANCF LOCKING ALLEVIATION: STRAIN SPLIT METHOD

This chapter (Patel and Shabana, 2017) proposes a new locking alleviation technique for absolute nodal coordinate formulation (ANCF) beam and plate elements based on a strain split approach. The chapter also surveys classical finite elements (FEs) and ANCF locking alleviation techniques discussed in the literature. Because ANCF beam elements, which allow for the cross section stretch, fully capture the Poisson effect, Poisson locking is an issue when such beam elements are considered. The two-dimensional fully-parameterized ANCF beam element is primarily used in this chapter because such an element can serve as a good surrogate model for three-dimensional ANCF beams and plates as far as membrane, bending and transverse shearing behavior is concerned. In addition to proposing the *strain split method* (SSM) for ANCF locking alleviation, this chapter assesses the ANCF FE performance in the cases of higher-order interpolation, enhanced assumed strain method, elastic line method, and the enhanced continuum mechanics approach; and demonstrates the design of the enhanced strain interpolation function by using the shape functions of higher-order ANCF elements. Additionally, a new higher-order ANCF two-dimensional beam element is proposed in order to compare its performance with other FEs that require the use of other locking alleviation techniques proposed and reviewed in the chapter. Finally, several numerical examples are shown to demonstrate the effectiveness of the locking alleviation methods applied to ANCF elements. The purpose of this chapter, apart from proposing a new locking alleviation technique, a new higher-order beam element, and comparing several existing locking alleviation techniques, is to show that dealing with locking in fully-parameterized ANCF elements is feasible and that several methods exist to effectively improve the ANCF element performance without sacrificing important ANCF element properties and features

including position vector gradient continuity. Because of the use of ANCF position vector gradients as nodal coordinates, complex stress-free initially-curved geometries can be systematically obtained. Such initially-curved geometries require special attention when attempting to solve locking problems, as will be discussed in this chapter.

4.1 Locking Alleviation in Classical FEs

Because many classical FEs suffer from locking problems, locking has been thoroughly investigated by the FE community and numerous techniques have been proposed over the years for effectively eliminating its effect on the element solution. Some of the locking mechanisms that affect classical FEs include shear, Poisson, curvature thickness, membrane and volumetric locking. A significant amount of literature exists for locking alleviation techniques in case of commonly used elements like the classical beam, shell, and hexahedral elements. These techniques typically include improvement of element kinematics, modification of constitutive models, usage of mixed formulations or a specifically tailored numerical fix for the locking problem at hand. This section will review some of the general locking alleviation techniques used in the classical FE theory and locking alleviation methods specifically designed for classical beams. Due to the immense amount of literature available on the topic of FE locking, only a tiny fraction of it pertaining to specific locking alleviation techniques will be presented in this section.

One of the most widely used techniques to alleviate locking is *reduced integration* and two of the earliest investigations on this topic are by Zienkiewicz et al. (1971, 1974) where the performances of the shell element, isoparametric quadrilateral element, and the beam element are improved. Reduced and *selective integration* was applied to plate elements by Hughes et al. (1978) to alleviate shear locking in the thin regime. Malkus and Hughes (1978) demonstrated the

equivalence of certain mixed formulations and the displacement formulation using reduced integration, and showed that reduced integrated elements can match the performance of their mixed formulation counterpart. Hughes et al. (1977) used reduced integration to significantly improve the behavior of a bilinear plate element in bending applications. Noor and Peters (1981) used reduced and selective integration for curved beams and discussed the equivalence and ‘near equivalence’ of mixed and displacement based beam models by comparing their stiffness matrices.

The *B-bar* and the *F-bar methods* have been popular strategies for dealing with volumetric locking. The B-bar method is a generalized extension of selectively reduced integration where the strain displacement matrix is split into deviatoric and dilatational parts and the dilatational part is modified to help alleviate volumetric locking (Hughes, 1987). The F-bar approach is similar to the B-bar approach, but also applicable in the nonlinear regime. In the simplified F-bar approach, the deformation gradient is scaled using its determinant at the integration point and at the centroid of the element (de Souza Neto et al., 2008).

Mixed methods have been extensively used in FE literature for tackling issues like incompressibility, excessive bending stiffness, and shear locking. Sussman and Bathe (1987) used a mixed displacement and pressure formulation to alleviate volumetric locking in the incompressible regime. Pian (1985) proposed a mixed element based on the Hellinger-Reissner variational principle and consistently assumed stress and displacement fields to improve the bending behavior of beams and plates. Liu et al. (1988) proposed the so called flexurally super-convergent elements which are based on the Veubeke-Hu-Washizu variational principle, showing good accuracy in coarse meshes. Dorfi and Busby (1994) proposed a mixed curved composite beam element that showed good convergence for displacements and stresses. Kim and Kim (1998) proposed a mixed-hybrid curved beam element with nodeless degrees of freedom that is free of

locking and can accurately predict stresses as well. Taylor et al. (2003) proposed a mixed FE method for beam and frame problems that is locking free and has properties similar to the flexibility method. A popular locking alleviation technique that has its variational basis in mixed methods is the *enhanced assumed strain method* that was proposed by Simo and Rifai (1990) and is a generalization of the method of *incompatible modes* that was proposed by Bazeley et al. (1965) and studied by Wilson et al. (1973) and Taylor et al. (1976) for rectangular elements. The enhanced strain method was extended to geometrically nonlinear problems by Simo and Armero (1992). Furthermore, it was demonstrated that the method of incompatible modes is a special case of the enhanced strain approach (Simo and Rifai, 1990). The enhanced strain approach was used by Simo et al. (1993) to improve the performance of tri-linear brick elements in the nearly incompressible regime. Even though the enhanced strain technique can significantly improve the element behavior in incompressible and bending deformations, the element might exhibit hour-glassing in case of large strain compression (Wriggers and Reese, 1996). Andelfinger and Ramm (1993) developed two- and three-dimensional plate and shell elements using the enhanced strain approach and showed their equivalence to the assumed stress elements based on the Hellinger-Reissner approach (Pian and Sumihara, 1984). Stolarski and Chen (1995) improved the bending behavior of the two-dimensional isoparametric quadrilateral element by studying the deformation modes of the element and enhancing the strains based on physical considerations. Schwarze and Reese (2009) applied reduced integration and the enhanced strain approach to the eight-node solid-shell element and demonstrated that the element can satisfy exactly the membrane and bending patch tests. Bischoff and Romero (2007) proposed a generalized method of incompatible modes which is based on a pure displacement formulation, yet its elements are equivalent to the mixed formulation based enhanced strain elements.

There is also a significant amount of work done on understanding locking in the FE literature. A seminal work on understanding locking was carried out by Babuska and Suri (1992A) who provided quantification for the FE tendency to exhibit locking and investigated the element robustness as certain parameters of the model approached limiting values. As a specific case of a limiting parameter, Babuska and Suri (1992B) investigated locking onset in two-dimensional elements as the Poisson ratio approached 0.5 and studied the robustness of h and p FE refinements. Armero (2000) investigated the material instabilities of enhanced strain elements under plane strain finite deformation and expanded on locking quantification in the finite deformation range. Bathe (2001) and Gilewski and Sitek (2011) used a numerical *inf-sup test* to quantify the convergence properties of shell elements under bending deformation. According to Bathe (2001), satisfaction of ellipticity, consistency, and inf-sup conditions typically means that the shell element will be robust and perform well in both membrane and bending dominated problems. Prathap and Bhashyam (1982) explained locking in beams as the presence of spurious constraints related to certain deformations like pure bending in case of conventional elements which might be field-inconsistent. Prathap and Babu proposed field consistent elements by using reduced integration or *field consistent strain interpolation* (1986A). Rakowski (1990, 1991) explained the phenomena of shear locking in linear and quadratic beam elements by showing that using their shape functions leads to the solution of differential equations that are different from those arising from beam theory. Stolarski and Belytschko (1983) studied shear and membrane locking in curved C^0 beam elements and demonstrated that shear and membrane locking are interrelated, reduced integration weakens the flexural-membrane coupling that exists in curved elements and that mixed curved elements could also suffer from membrane and shear locking.

Another method for tackling locking is improving the element itself. There is a significant amount of literature on beam elements where the improved element targets specific locking mechanisms. Heyliger and Reddy (1988) proposed a higher-order shear deformable beam element specifically for bending and vibration problems that can correctly account for the parabolic shear stress distribution in the cross-section, thus eliminating the need for shear correction coefficient. Lee and Sin (1994) made use of curvatures as degrees of freedom in order to alleviate locking in curved beam structures and accurately represent their bending energy. The rotations and radial and tangential displacements can be retrieved from relationships between the curvature derivatives and beam strain measures in the Lee and Sin element. Yunhua (1998) used the field consistence approach to explain shear and membrane locking in low order beam elements and consequently used the field consistence approach to improve element performance. Friedman and Kosmatka (1993) developed a locking free two-node shear deformable beam element by using cubic and quadratic polynomials for transverse and rotational degrees of freedom, respectively, and having them satisfy Timoshenko's beam differential equations. Raveendranath et al. (1999) proposed a shear deformable curved beam element that produces no spurious constraints in thin regimes, hence showing excellent performance for thin curved beam structures. A detailed review on shear deformable beam theory and beam elements associated with it can be found in the work of Reddy (1997) and Reddy et al. (1997). Furthermore, shear and membrane locking free beam elements can be found in the works of Prathap and Babu (1986B), Reddy (1997) and Choi and Lim (1995).

Some other methods to alleviate locking include *stress projection methods* and *stiffness scaling methods*. Belytschko et al. (1985) used the mode decomposition method to remove shear and membrane locking in beam elements. The mode decomposition method which is a special case of stress projection methods essentially projects the nodal displacements on a subspace of

displacements such that certain modes of deformation like inextensional bending can be correctly captured. Stolarski and Belytschko (1986A, 1986B) demonstrated the equivalence of the mode decomposition method and mixed FEs based on the Hellinger-Reissner principle. Carpenter et al. (1986) utilized shear scaling factors to alleviate shear locking in C^0 beam elements by splitting the stiffness matrix into bending and shear parts and modifying the shear part using a shear scaling factor that is computed using the element material and dimensional parameters. The shear scaling factor method was also used by Tessler and Hughes (1983) to accurately represent the transverse shear energy in case of plate elements. Furthermore, they demonstrated that the modified stiffness matrices remain well conditioned for almost the entire range of length-to-thickness ratios. It must be noted that shear scaling is different from shear correction factor. Shear correction factor that was proposed by Timoshenko (1921) and discussed in detail by Dong et al. (2010) is a standard technique used in all lower-order beam elements in order to capture a good approximation of the shear energy within the element.

4.2 Locking Alleviation in ANCF Elements

Like classical FEs, ANCF elements are not, in general, locking free. The locking mechanisms affecting classical FEs also affect ANCF elements, i.e. shear, Poisson, curvature thickness, and volumetric locking. While this section will review some of the investigations on the quantification and alleviation of locking in ANCF elements with emphasis on beams; for a detailed review on ANCF elements and their locking mechanisms, the reader may also refer to Gerstmayr et al. (2013) and Nachbagauer (2014).

Sopanen and Mikkola (2003) studied the fully-parameterized ANCF three-dimensional beam element for bending, shear and torsional deformations using three different elastic force

formulations and concluded that the element does not suffer from significant shear locking and that modifying the constitutive model for the beam element based on continuum mechanics approach can improve its performance. Schwab and Meijaard (2005) compared the modal properties of the ANCF three-dimensional beam element with the classical beam element by improving the ANCF beam bending deformation through the elastic line approach and shear deformation through independent shear stress and strain fields introduced via the Hellinger-Reissner and the Veubeke-Hu-Washizu principles, respectively. Gerstmayr and Matikainen (2006) developed a higher-order beam element that is of fifth order in the longitudinal direction and linear in the cross-section and demonstrated improvement in the prediction of axial and shear stress when compared to solution from a commercial FE code. Garcia-Vallejo et al. (2007) explained the phenomena of curvature thickness locking and shear locking in the two-dimensional ANCF beam element by studying the kinematics of the element. Furthermore, they proposed a quadratic beam element that has good bending characteristics. Dufva et al. (2005) used a mixed displacement and shear strain interpolation to alleviate the two-dimensional ANCF beam element of shear locking by considering a linear distribution of the shear deformation along the longitudinal axis and improving its bending behavior by neglecting the Poisson coupling between the longitudinal and transverse normal strains. Gerstmayr and Irschik (2008) studied the axial and bending deformation of ANCF beams in detail using the elastic line approach and proposed modifications to the strain measures in order to improve element accuracy in bending deformation. Hussein et al. (2007) used the elastic line approach without Poisson coupling and a Hellinger-Reissner based independent shear stress interpolation in the dynamic analysis of stiff and thin beams. Gerstmayr et al. (2008) improved the performance of the original two-dimensional ANCF beam element by forming the elastic forces using two distinct and separate methods, the first is the enhanced continuum

mechanics approach which is like selectively reduced integration and the second is based on the Reissner or Simo-Vu Quoc beam theory. In order to deal with volumetric locking in case of nearly incompressible materials, Orzechowski and Fraczek (2015) resorted to selectively reduced integration and the generalized F-bar approach in the three-dimensional ANCF beam element. In the past decade, several ANCF beam elements with specific locking alleviation strategies have been proposed. Kerkkanen et al. (2005) proposed a two-dimensional linear ANCF beam element and used selectively reduced integration on the shear energy in order to avoid shear locking. Sugiyama and Suda (2007) introduced a fully-parameterized curved beam element that used independent shear stress and transverse normal strain interpolations. Sugiyama et al. (2010) proposed a curved gradient deficient ANCF beam element with normal strain and curvature measures described with respect to the curved reference configuration such that tangential and radial deformations can be correctly captured. Matikainen et al. (2010) improved the original ANCF beam element by introducing a trapezoidal deformation mode in the cross-section kinematics, thus alleviating it of Poisson locking. Nachbagauer et al. (2011, 2013A) proposed two- and three-dimensional linear and quadratic beam elements that used structural mechanics approach and enhanced continuum mechanics formulation to alleviate locking. Shen et al. (2014) proposed a higher-order three-dimensional ANCF beam element that had quadratic interpolation for the cross-section deformation. The higher-order element effectively eliminated Poisson locking and could capture the warping effect in beams. This higher-order beam element was further analyzed by Orzechowski and Shabana (2016) in case of buckling, torsional deformation and different cross-sectional geometries. Ebel et al. (2016A) developed and analyzed several higher-order beam elements that can completely avoid Poisson locking due to improved cross-sectional deformation and showed the efficacy of the elements via the Princeton beam experiment. Hurskainen et al.

(2017) developed a hybrid ANCF beam element with an independently interpolated shear deformation field, and demonstrated good convergence for bending problems. Mohamed and Liu (2014) developed a gradient deficient beam element that uses a combination of plane strain and elastic line approach, thus exhibiting less locking than the pure continuum mechanics approach. Locking alleviation techniques similar to those used with ANCF beam elements have also been proposed for ANCF plate/shell elements. Dmitrochenko et al. (2009) extended the work of Hussein et al. (2007) to three-dimensional beam and plate elements. Mikkola and Matikainen (2006) extended the mixed interpolation approach to three-dimensional plate elements and demonstrated its superior performance in bending scenarios compared to the original element. Ebel et al. (2016B) developed higher-order plate elements that alleviate shear and Poisson locking by making use of higher-order interpolation in the cross-section. Yamashita et al. (2015) proposed a bilinear ANCF shell element and improved its membrane and bending behavior by using the assumed natural strain and the enhanced assumed strain approach. In case of membrane dominated problems, Sanborn et al. (2011) identified the issue of curve induced distortion and membrane locking that occurs in thin plate elements and proposed a method known as *flat mapped extension modeling* to modify the axial strain by systematically excluding the effect of the curvature. Valkeapää et al. (2015) used an elastic middle surface approach which is analogous to the elastic line approach along with assumed natural strain and the enhanced assumed strain methods in order to alleviate locking in the ANCF shell element.

4.3 ANCF FEs

This section briefly describes the nonlinear absolute nodal coordinate formulation (ANCF) and the continuum mechanics approach for formulating the elastic forces. This brief review presents some

of the basic equations that will be used repeatedly and/or referred to in the chapter. One of the contributions of this chapter is to introduce a new higher-order beam element which will be used as the basis for comparison with lower-order ANCF elements. In addition to introducing this element in this section, the effect of the constitutive model selection on the behavior of the planar ANCF beam elements is also discussed.

In addition to using global nodal position vectors, ANCF has the distinguished feature of using the position vector gradients as nodal coordinates. The position vector gradients are tangents to the element coordinate lines, and therefore, their transformation when the elements are assembled differ from the conventional coordinate transformation used in the classical FE literature. Furthermore, ANCF beams differ from their classical FE counterparts which do not allow for the cross-section deformations. Because of the use of the transverse gradient vectors as degrees of freedom, ANCF elements allow for the stretch of the cross-section. For this reason, Poisson effect is fully captured when ANCF elements are used, and as a consequence, ANCF beam elements may experience Poisson locking which is not observed when conventional beam elements are used, as will be discussed in this chapter. The use of the gradient vectors allows for obtaining complex geometries including initially curved geometries that require special attention when attempting to solve the locking problem, as will be discussed in this chapter.

4.3.1 ANCF Kinematics

In ANCF, the global position vector of an arbitrary point on the flexible body can be written as $\mathbf{r}(\mathbf{x}, t) = \mathbf{S}(\mathbf{x})\mathbf{e}(t)$, where $\mathbf{S}(\mathbf{x})$ is the matrix of shape functions and $\mathbf{e}(t)$ is the vector of nodal position and gradient vectors that are defined in the global coordinate system. Depending on the element, $\mathbf{e}(t)$ can also consist of curvature vectors. The ANCF formulation leads to a constant mass matrix and zero Coriolis and centrifugal forces. Furthermore, in order to avoid

computationally expensive matrix inversion or LU decomposition, Cholesky decomposition can be applied to obtain an identity generalized mass matrix associated with the ANCF Cholesky coordinates. Over the past two decades several researchers have proposed a wide range of ANCF elements. These elements include several beam, plate/shell, hexahedral and tetrahedral elements (Shabana, 2012). For ANCF elements, no distinction is made between plate and shell elements since initially curved structures can be systematically obtained using appropriate vector of nodal coordinates in the reference configuration. The constant ANCF element mass matrix can be written as $\mathbf{M} = \int_{V_0} \rho \mathbf{S}^T \mathbf{S} dV_0$, where ρ and V_0 are respectively, the mass density and volume in the reference configuration. The ANCF generalized external force vector due to a given force \mathbf{f}_e can simply be written as $\mathbf{Q}_e = \mathbf{S}(\mathbf{x})^T \mathbf{f}_e$.

4.3.2 General Continuum Mechanics Approach

The general continuum mechanics approach can be used to formulate the elastic forces of the ANCF elements. Using the Green-Lagrange strain and second Piola-Kirchhoff stress tensors which are defined with respect to the reference configuration, the virtual work of the elastic forces can be written as $\delta W_k = - \int_{V_0} \boldsymbol{\sigma}_{p2} : \delta \boldsymbol{\varepsilon} dV_0$ where $\boldsymbol{\sigma}_{p2}$ is the second Piola-Kirchhoff stress tensor and $\boldsymbol{\varepsilon}$ is the Green-Lagrange strain tensor. This general approach allows for incorporating any type of material and geometric nonlinearities in the FE analysis. The stress tensor $\boldsymbol{\sigma}_{p2}$ can be defined as $\boldsymbol{\sigma}_{p2} = 2(\partial U / \partial \mathbf{C}_r)$, where U is the strain energy potential function that is typically written in terms of the invariants of the right Cauchy deformation tensor \mathbf{C}_r , defined as $\mathbf{C}_r = \mathbf{J}^T \mathbf{J}$. (Bonet and Wood, 1997; Ogden, 1984; Shabana, 2012). Alternatively, the elastic forces can be derived directly from the strain energy potential as $\mathbf{Q}_k = (\partial U / \partial \mathbf{e})$ where \mathbf{e} is the vector of nodal coordinates.

4.3.3 Higher-Order Planar Beam Element

One method for dealing with some locking types is using higher-order elements that have richer displacement interpolations that can capture certain important deformation modes in the element, including pure bending. The use of such higher-order elements has the advantage of being able to accurately capture complex geometries that cannot be captured with low-order elements that fail to satisfy some continuity conditions for beam-like structures where curvatures have significant effects. The ANCF two-dimensional shear deformable beam element proposed by Omar and Shabana (2001) can be considered to be a higher-order element considering the fact that there are other ANCF beam elements proposed by Nachbagauer et al. (2011) in the literature that are of lower-order. Omar and Shabana element is cubic in the longitudinal direction and linear in the transverse direction, whereas the elements proposed by Nachbagauer et al. (2011) are linear in the transverse direction and linear and quadratic in the longitudinal directions. All these elements, however, suffer from severe locking when used with the general continuum mechanics approach and a non-zero Poisson ratio. One must resort to using specialized elastic force formulations like the enhanced continuum mechanics approach and the Reissner-Simo-Vu-Quoc structural mechanics-based approach in order to achieve good performance from these elements. One of the main reason for the poor performance of these elements with the general continuum mechanics approach is the linear interpolation considered in the transverse direction. As explained by Shen et al. (2014) and Orzechowski and Shabana (2016), the use of Hooke's law in this case leads to a stiff behavior in the element response to non-uniform strain distribution like bending. One approach explored in previous investigations is refining the displacement polynomial of the lower-order elements to be quadratic in the transverse directions to allow the element to deform in a way that correctly captures the Poisson coupling effect within the element. A new higher-order element

is hence proposed here in order to explore the efficacy of this approach in the two-dimensional analysis and to later compare the use of the higher-order element approach with other locking alleviation approaches. The higher-order element, which is quadratic in the beam transverse direction, has the following interpolating polynomial:

$$\mathbf{r} = \begin{bmatrix} a_0 + a_1x + a_2y + a_3xy + a_4x^2 + a_5y^2 + a_6xy^2 + a_7x^3 \\ b_0 + b_1x + b_2y + b_3xy + b_4x^2 + b_5y^2 + b_6xy^2 + b_7x^3 \end{bmatrix} \quad (18)$$

The vector of nodal coordinates of a node i for the new higher-order element is given as $\mathbf{e}^i = [\mathbf{r}^{iT} \quad \mathbf{r}_x^{iT} \quad \mathbf{r}_y^{iT} \quad \mathbf{r}_{yy}^{iT}]^T$, where \mathbf{r} is the global position vector, $\mathbf{r}_\alpha = \partial \mathbf{r} / \partial \alpha$ is a gradient vector where $\alpha = x, y$, and $\mathbf{r}_{yy} = \partial^2 \mathbf{r} / \partial y^2$ is a curvature vector. The vectors \mathbf{r} , \mathbf{r}_α , \mathbf{r}_{yy} are two-dimensional vectors. The shape functions for the element based on the polynomials of Eq. 18 are provided in Appendix B.1. As can be noticed from the displacement polynomial and the shape functions, the element is quadratic in the y coordinate and hence the normal transverse strain will no longer be constant in the y direction, allowing reducing the Poisson locking effect specifically in bending situations. This element can be considered as a special (two-dimensional) case of the three-dimensional higher-order element proposed by Shen et al. (2014) and analyzed by Orzechowski and Shabana (2016). Even though the shape functions of this two-dimensional element can be considered as a subset of the set of the three-dimensional higher-order element shape functions, its performance, as will be demonstrated in the next section, is dependent on the constitutive model and on plane stress or plane strain used in the case of linear materials.

4.3.4 Plane Stress and Plane Strain Assumptions

The use of the appropriate constitutive model is important in the two-dimensional analysis of ANCF beams. The two available linear constitutive models are the plane strain and the plane stress models. Plane strain assumes the strain components $\varepsilon_{zz} = \varepsilon_{xz} = \varepsilon_{yz} = 0$, whereas plane stress

assumes the stress components $\sigma_{zz} = \sigma_{xz} = \sigma_{yz} = 0$ (Bonet and Wood, 1997; Ogden, 1984; Shabana, 2012). Even though several previous ANCF investigations suggest that the analyst may choose either of the two assumptions, the effect of these assumptions on ANCF element performance has not been previously investigated. This chapter also examines the effect of plane strain versus plane stress assumption on the ANCF two-dimensional beam elements using the general continuum mechanics approach. Since in case of a beam, typically the thickness of the structure is not larger than the length, plane stress is recommended as the appropriate assumption. The effect of the constitutive model can be demonstrated through a simple example of a beam undergoing small deformation. Two types of elements are considered in this case, the original two-dimensional beam element that was proposed by Omar and Shabana (2001) and the higher-order element proposed in this chapter. A cantilever beam problem is considered with material properties $E = 2 \times 10^{11} \text{ Pa}$, $\nu = 0.3$, beam length of 1m, height of 0.01m and thickness of 0.01m. The cantilever beam, shown in Figure 35, is subjected to a vertical tip load of -10N. The results for plane strain and plane stress static analysis on the two element types are shown in Table 13. Since this is a thin beam, the classical Euler-Bernoulli beam theory predicts the analytical vertical tip deformation to be -0.02m.

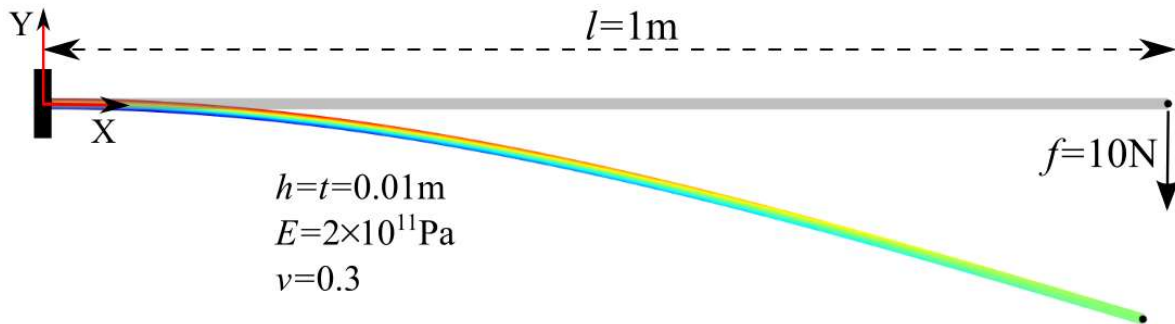


Figure 35. Slender cantilever beam problem (deformation with respect to undeformed state is magnified for graphical purposes)

Table 13. Effect of using plane stress and plane strain (Om-Sh: Omar and Shabana beam)

Number of Elements	Plane Strain		Plane Stress	
	Om-Sh (m)	Higher-Order (m)	Om-Sh (m)	Higher-Order (m)
5	-0.014690096	-0.017941054	-0.017979431	-0.019726994
10	-0.014817360	-0.018138433	-0.018148212	-0.019936221
20	-0.014845969	-0.018181342	-0.018183872	-0.019979401
50	-0.014853811	-0.018193062	-0.018193509	-0.019991023

As can be seen from Table 13, the plane stress assumption leads to accurate results with the higher-order beam element and some under-prediction of deformation with the Omar and Shabana element. The plane strain assumption on the other hand results in significant under-prediction of deformation in both beam models as they cannot achieve the analytical solution. This simple analysis demonstrates that the constitutive model also affects the element performance and such a constitutive model must be carefully selected in case of two-dimensional ANCF beam analysis.

4.4 ANCF Strain Split Method

In this section, the ANCF strain split method (SSM) for solving the ANCF beam and plate locking problems is proposed and discussed. The basic differences between this method and some specific locking solution methods proposed in the literature will also be discussed in this chapter.

4.4.1 Strain Split Method (SSM)

A new method is proposed in this chapter in order to address the locking problem in ANCF beams and plates/shells. Specifically, this approach targets the Poisson locking present in ANCF beam and plate/shell elements. The basic idea is to analyze the element kinematics and then decouple the higher-order terms found in the axial strain and the transverse strain through an additive decomposition of the Green-Lagrange strain tensor and the constitutive law. According to the analysis performed by Sugiyama et al. (2006), the two-dimensional shear deformable beam element position field and gradients can be written, respectively, as

$$\mathbf{r} = \mathbf{r}^c + y\mathbf{r}_y, \quad \mathbf{r}_x = \mathbf{r}_x^c + y\mathbf{r}_{yx}, \quad \mathbf{r}_y = \mathbf{r}_y \quad (19)$$

where c corresponds to the centerline. Accordingly, the matrix of position vector gradients can be written as $\mathbf{J} = \begin{bmatrix} \mathbf{r}_x & \mathbf{r}_y \end{bmatrix} = \begin{bmatrix} \mathbf{r}_x^c + y\mathbf{r}_{yx} & \mathbf{r}_y \end{bmatrix}$. The matrix of position vector gradients can be additively decomposed as

$$\mathbf{J} = \begin{bmatrix} \mathbf{r}_x^c & \mathbf{r}_y \end{bmatrix} + \begin{bmatrix} y\mathbf{r}_{yx} & \mathbf{0} \end{bmatrix} = \mathbf{J}^c + \mathbf{J}^k \quad (20)$$

where $\mathbf{J}^c = \begin{bmatrix} \mathbf{r}_x^c & \mathbf{r}_y \end{bmatrix}$ is associated with the centerline, and $\mathbf{J}^k = \begin{bmatrix} y\mathbf{r}_{yx} & \mathbf{0} \end{bmatrix}$ is associated with the curvature and shear deformation of the element. Thus, the Green-Lagrange strain and the right Cauchy deformation tensor can be written, respectively, as

$$\left. \begin{aligned} \boldsymbol{\varepsilon} &= \frac{1}{2} [\mathbf{J}^T \mathbf{J} - \mathbf{I}] = \frac{1}{2} [\mathbf{C}_r - \mathbf{I}] \\ \mathbf{C}_r &= \mathbf{J}^{cT} \mathbf{J}^c + \mathbf{J}^{cT} \mathbf{J}^k + \mathbf{J}^{kT} \mathbf{J}^c + \mathbf{J}^{kT} \mathbf{J}^k \end{aligned} \right\} \quad (21)$$

where each matrix that appears in the \mathbf{C}_r expression can be written as

$$\left. \begin{aligned} \mathbf{J}^{cT} \mathbf{J}^c &= \begin{bmatrix} \mathbf{r}_x^{cT} \mathbf{r}_x^c & \mathbf{r}_x^{cT} \mathbf{r}_y \\ \mathbf{r}_y^T \mathbf{r}_x^c & \mathbf{r}_y^T \mathbf{r}_y \end{bmatrix}, & \mathbf{J}^{cT} \mathbf{J}^k &= \begin{bmatrix} y\mathbf{r}_x^{cT} \mathbf{r}_{yx} & 0 \\ y\mathbf{r}_y^T \mathbf{r}_{yx} & 0 \end{bmatrix}, \\ \mathbf{J}^{kT} \mathbf{J}^c &= \begin{bmatrix} y\mathbf{r}_{yx}^T \mathbf{r}_x^c & y\mathbf{r}_{yx}^T \mathbf{r}_y \\ 0 & 0 \end{bmatrix}, & \mathbf{J}^{kT} \mathbf{J}^k &= \begin{bmatrix} y^2 \mathbf{r}_{yx}^T \mathbf{r}_{yx} & 0 \\ 0 & 0 \end{bmatrix} \end{aligned} \right\} \quad (22)$$

Accordingly, the strain tensor can be written as

$$\boldsymbol{\varepsilon} = \begin{bmatrix} \varepsilon_{11} & \varepsilon_{12} \\ \varepsilon_{21} & \varepsilon_{22} \end{bmatrix} = \frac{1}{2} \left(\begin{bmatrix} \mathbf{r}_x^{cT} \mathbf{r}_x^c + 2y\mathbf{r}_x^{cT} \mathbf{r}_{yx} + y^2 \mathbf{r}_{yx}^T \mathbf{r}_{yx} & \mathbf{r}_x^{cT} \mathbf{r}_y + y\mathbf{r}_{yx}^T \mathbf{r}_y \\ \mathbf{r}_y^T \mathbf{r}_x^c + y\mathbf{r}_y^T \mathbf{r}_{yx} & \mathbf{r}_y^T \mathbf{r}_y \end{bmatrix} - \begin{bmatrix} 1 & 0 \\ 0 & 1 \end{bmatrix} \right) \quad (23)$$

The strain tensor can be split into two parts, one associated with the beam centerline and the other part associated with the higher-order terms that contribute to cross-section deformation, bending, and curvature definition as $\boldsymbol{\varepsilon} = \boldsymbol{\varepsilon}^c + \boldsymbol{\varepsilon}^k$ where

$$\left. \begin{aligned} \boldsymbol{\varepsilon}^c &= \frac{1}{2}(\mathbf{J}^{cT} \mathbf{J}^c - \mathbf{I}) = \frac{1}{2} \left(\begin{bmatrix} \mathbf{r}_x^{cT} \mathbf{r}_x^c & \mathbf{r}_x^{cT} \mathbf{r}_y^c \\ \mathbf{r}_y^{cT} \mathbf{r}_x^c & \mathbf{r}_y^{cT} \mathbf{r}_y^c \end{bmatrix} - \begin{bmatrix} 1 & 0 \\ 0 & 1 \end{bmatrix} \right) \\ \boldsymbol{\varepsilon}^k &= \frac{1}{2}(\mathbf{J}^{cT} \mathbf{J}^k + \mathbf{J}^{kT} \mathbf{J}^c + \mathbf{J}^{kT} \mathbf{J}^k) = \frac{1}{2} \begin{bmatrix} 2\mathbf{y} \mathbf{r}_x^{cT} \mathbf{r}_{yx} + \mathbf{y}^2 \mathbf{r}_{yx}^T \mathbf{r}_{yx} & \mathbf{y} \mathbf{r}_{yx}^T \mathbf{r}_y \\ \mathbf{y} \mathbf{r}_y^T \mathbf{r}_{yx} & 0 \end{bmatrix} \end{aligned} \right\} \quad (24)$$

In order to alleviate locking, Poisson coupling can be used only in the lower-order terms of the normal strains that are contained in the expression of $\boldsymbol{\varepsilon}^c$. Thus, the second Piola-Kirchhoff stress can be written in Voigt form as $\boldsymbol{\sigma}_v = \mathbf{E}^c \boldsymbol{\varepsilon}_v^c + \mathbf{E}^k \boldsymbol{\varepsilon}_v^k$, where the strains are also in Voigt form. With an assumption of plane strain the matrices of elastic coefficients can be defined as

$$\mathbf{E}^c = \begin{bmatrix} \lambda + 2\mu & \lambda & 0 \\ \lambda & \lambda + 2\mu & 0 \\ 0 & 0 & \mu k_s \end{bmatrix}, \quad \mathbf{E}^k = \text{diag}(E, E, \mu k_s) \quad (25)$$

where λ and μ are the Lamé parameters, E is the Young's modulus, k_s is the shear correction coefficient defined as $k_s = 10(1+\nu)/(12+11\nu)$ and ν is the Poisson's ratio. This leads to uncoupling of the transverse normal strain and the higher-order terms associated with bending that are contained in the longitudinal normal strain. This type of uncoupling in the deformation modes can significantly improve the element bending behavior as will be demonstrated in the numerical results section of this chapter.

With regard to its treatment of the coupling between transverse normal and higher order strains, SSM is different from locking alleviation techniques proposed in classical FE literature like the enhanced assumed strain (Simo and Rifai, 1990) and the *free formulation* (Bergan and Nygard, 1984) that work with either element kinematics or the stiffness matrix to deal with locking. In case of the enhanced assumed strain approach, an incompatible strain field is added to the compatible strain field to improve element performance as will be discussed in Section 4.5 of this chapter. The free formulation is based on the concept of using nonconforming *higher order*

displacement field along with the so called *basic* displacement components which include the rigid body and constant strain element modes. The stiffness in the free formulation is written as the sum of the basic stiffness and the higher order stiffness (Felippa, 1989). Furthermore, the stiffness coupling between the basic element modes and higher order modes is modified to improve element convergence. It should be noted that this approach is different from the SSM approach since the SSM approach relies on the strain decomposition and different constitutive models to alleviate locking. In case of the free formulation, the same constitutive model is used in all stiffness calculations, hence the method relies purely on a kinematic enhancement approach. In the conclusion of Felippa's paper (1989) it is noted that the free formulation has to do with "freedom" from element conformity requirements which can help improve its performance. Since in the SSM approach no such requirement or assumption is exercised on the element in order to alleviate locking, SSM is fundamentally different from the free formulation as a locking alleviation technique.

4.4.2 SSM Generalization

The strain split method proposed for the two-dimensional beam element can be easily extended to the three-dimensional beam and plate/shell elements since these elements share similar features with the ANCF planar elements considered in this chapter. The behavior of the spatial beam and plate/shell elements depends on the geometry of the centerline or mid-surface and the definition of the transverse gradients. According to Sugiyama et al. (2006), in case of a three-dimensional ANCF beam element, the position field and gradients can be written as

$$\left. \begin{aligned} \mathbf{r} &= \mathbf{r}^c + y\mathbf{r}_y + z\mathbf{r}_z \\ \mathbf{r}_x &= \mathbf{r}_x^c + y\mathbf{r}_{yx} + z\mathbf{r}_{zx} \\ \mathbf{r}_y &= \mathbf{r}_y, \quad \mathbf{r}_z = \mathbf{r}_z \end{aligned} \right\} \quad (26)$$

The matrix of position vector gradients can be written as

$$\mathbf{J} = \begin{bmatrix} \mathbf{r}_x^c + y\mathbf{r}_{yx} + z\mathbf{r}_{zx} & \mathbf{r}_y & \mathbf{r}_z \end{bmatrix} = \mathbf{J}^c + \mathbf{J}^k \quad (27)$$

where $\mathbf{J}^c = \begin{bmatrix} \mathbf{r}_x^c & \mathbf{r}_y & \mathbf{r}_z \end{bmatrix}$, and $\mathbf{J}^k = \begin{bmatrix} y\mathbf{r}_{yx} + z\mathbf{r}_{zx} & \mathbf{0} & \mathbf{0} \end{bmatrix}$ Using this split of the matrix of position

vector gradients, the Green-Lagrange strain can be written as $\boldsymbol{\varepsilon} = \boldsymbol{\varepsilon}^c + \boldsymbol{\varepsilon}^k$ where

$$\boldsymbol{\varepsilon}^c = \frac{1}{2}(\mathbf{J}^{cT}\mathbf{J}^c - \mathbf{I}), \quad \boldsymbol{\varepsilon}^k = \frac{1}{2}(\mathbf{J}^{cT}\mathbf{J}^k + \mathbf{J}^{kT}\mathbf{J}^c + \mathbf{J}^{kT}\mathbf{J}^k) \quad (28)$$

and finally, the second Piola-Kirchhoff stress can be defined in Voigt form as $\boldsymbol{\sigma}_v = \mathbf{E}^c \boldsymbol{\varepsilon}_v^c + \mathbf{E}^k \boldsymbol{\varepsilon}_v^k$

where

$$\mathbf{E}^c = \begin{bmatrix} \lambda + 2\mu & \lambda & \lambda & 0 & 0 & 0 \\ \lambda & \lambda + 2\mu & \lambda & 0 & 0 & 0 \\ \lambda & \lambda & \lambda + 2\mu & 0 & 0 & 0 \\ 0 & 0 & 0 & \mu & 0 & 0 \\ 0 & 0 & 0 & 0 & \mu k_{s2} & 0 \\ 0 & 0 & 0 & 0 & 0 & \mu k_{s3} \end{bmatrix} \quad (29)$$

$$\mathbf{E}^k = \text{diag}(E, E, E, \mu, \mu k_{s2}, \mu k_{s3})$$

In case of three-dimensional ANCF plate/shell elements, the position field and gradients can be described using the element mid-surface and transverse gradient vector as

$$\left. \begin{aligned} \mathbf{r} &= \mathbf{r}^m + z\mathbf{r}_z, & \mathbf{r}_x &= \mathbf{r}_x^m + z\mathbf{r}_{zx}, \\ \mathbf{r}_y &= \mathbf{r}_y^m + z\mathbf{r}_{zy}, & \mathbf{r}_z &= \mathbf{r}_z \end{aligned} \right\} \quad (30)$$

Accordingly, the matrix of position vector gradients and its additive split can be defined as

$$\mathbf{J} = \begin{bmatrix} \mathbf{r}_x^m + z\mathbf{r}_{zx} & \mathbf{r}_y^m + z\mathbf{r}_{zy} & \mathbf{r}_z \end{bmatrix} = \mathbf{J}^m + \mathbf{J}^k \quad (31)$$

In this equation, $\mathbf{J}^m = \begin{bmatrix} \mathbf{r}_x^m & \mathbf{r}_y^m & \mathbf{r}_z \end{bmatrix}$, and $\mathbf{J}^k = \begin{bmatrix} z\mathbf{r}_{zx} & z\mathbf{r}_{zy} & \mathbf{0} \end{bmatrix}$. The derivation for the plate/shell

element strains and stresses follows the same procedure as discussed for the beam element.

4.4.3 SSM Objectivity and Initially Curved Geometry

In the case of initially curved stress-free geometry, the Green-Lagrange strain tensor can be written as $\boldsymbol{\varepsilon} = (\mathbf{J}^T \mathbf{J} - \mathbf{I})/2$, where $\mathbf{J} = \mathbf{J}_e \mathbf{J}_0^{-1}$, $\mathbf{J}_e = \partial \mathbf{r} / \partial \mathbf{x}$, $\mathbf{J}_0 = \partial \mathbf{X} / \partial \mathbf{x}$, \mathbf{x} is the element spatial coordinates in the straight configuration, $\mathbf{X} = \mathbf{S}(\mathbf{x}) \mathbf{e}_0$ is the element parameters in the stress-free reference configuration, and \mathbf{e}_0 is the vector of the ANCF element coordinates in the reference configuration. Therefore, the Green-Lagrange strain tensor can be written as $\boldsymbol{\varepsilon} = (\mathbf{J}_0^{-T} \mathbf{J}_e^T \mathbf{J}_e \mathbf{J}_0^{-1} - \mathbf{I})/2$. One can write the strain tensor in terms of the covariant strain tensor $\tilde{\boldsymbol{\varepsilon}}$ as

$$\boldsymbol{\varepsilon} = \mathbf{J}_0^{-T} \left(\frac{1}{2} (\mathbf{J}_e^T \mathbf{J}_e - \mathbf{J}_0^T \mathbf{J}_0) \right) \mathbf{J}_0^{-1} = \mathbf{J}_0^{-T} (\tilde{\boldsymbol{\varepsilon}}) \mathbf{J}_0^{-1} \quad (32)$$

In this equation, $\tilde{\boldsymbol{\varepsilon}} = (\mathbf{J}_e^T \mathbf{J}_e - \mathbf{J}_0^T \mathbf{J}_0)/2$. The matrix of position vector gradients in the current and reference configurations can be split into centerline and higher-order parts, respectively, as $\mathbf{J}_e = \mathbf{J}_e^c + \mathbf{J}_e^k$, and $\mathbf{J}_0 = \mathbf{J}_0^c + \mathbf{J}_0^k$. Using this split, the covariant strain tensor can be written as

$$\tilde{\boldsymbol{\varepsilon}} = \frac{1}{2} \left((\mathbf{J}_e^c + \mathbf{J}_e^k)^T (\mathbf{J}_e^c + \mathbf{J}_e^k) - (\mathbf{J}_0^c + \mathbf{J}_0^k)^T (\mathbf{J}_0^c + \mathbf{J}_0^k) \right) \quad (33)$$

Thus $\tilde{\boldsymbol{\varepsilon}}$ can be split as the sum of two parts as $\tilde{\boldsymbol{\varepsilon}} = \tilde{\boldsymbol{\varepsilon}}^c + \tilde{\boldsymbol{\varepsilon}}^k$, where

$$\left. \begin{aligned} \tilde{\boldsymbol{\varepsilon}}^c &= \frac{1}{2} (\mathbf{J}_e^{cT} \mathbf{J}_e^c - \mathbf{J}_0^{cT} \mathbf{J}_0^c) \\ \tilde{\boldsymbol{\varepsilon}}^k &= \frac{1}{2} (\mathbf{J}_e^{cT} \mathbf{J}_e^k + \mathbf{J}_e^{kT} \mathbf{J}_e^c + \mathbf{J}_e^{kT} \mathbf{J}_e^k - \mathbf{J}_0^{cT} \mathbf{J}_0^k - \mathbf{J}_0^{kT} \mathbf{J}_0^c - \mathbf{J}_0^{kT} \mathbf{J}_0^k) \end{aligned} \right\} \quad (34)$$

Finally, a push forward operation can be applied on the covariant strains to obtain $\boldsymbol{\varepsilon}^c$ and $\boldsymbol{\varepsilon}^k$ as

$\boldsymbol{\varepsilon} = \mathbf{J}_0^{-T} (\tilde{\boldsymbol{\varepsilon}}^c + \tilde{\boldsymbol{\varepsilon}}^k) \mathbf{J}_0^{-1}$, which can be written as

$$\boldsymbol{\varepsilon} = \boldsymbol{\varepsilon}^c + \boldsymbol{\varepsilon}^k = \mathbf{J}_0^{-T} (\tilde{\boldsymbol{\varepsilon}}^c) \mathbf{J}_0^{-1} + \mathbf{J}_0^{-T} (\tilde{\boldsymbol{\varepsilon}}^k) \mathbf{J}_0^{-1} \quad (35)$$

Using this SSM procedure, curved structures can be easily analyzed. This method is also applicable to straight structures as well because in straight structures, \mathbf{J}_0 is an identity matrix and \mathbf{J}_0^k is a null matrix.

In order to demonstrate that the strains remain objective, consider a rotation applied to \mathbf{J}_e such that $\mathbf{J}_e^* = \mathbf{R}\mathbf{J}_e$, where \mathbf{R} is a proper orthogonal rotation matrix. Consequently, \mathbf{J}_e^* can be written as $\mathbf{J}_e^* = \mathbf{R}(\mathbf{J}_e^c + \mathbf{J}_e^k)$ and the covariant strains as

$$\left. \begin{aligned} \tilde{\boldsymbol{\epsilon}}^{c*} &= \frac{1}{2}(\mathbf{J}_e^{cT} \mathbf{R}^T \mathbf{R} \mathbf{J}_e^c - \mathbf{J}_0^{cT} \mathbf{J}_0^c) = \frac{1}{2}(\mathbf{J}_e^{cT} \mathbf{J}_e^c - \mathbf{J}_0^{cT} \mathbf{J}_0^c) = \tilde{\boldsymbol{\epsilon}}^c \\ \tilde{\boldsymbol{\epsilon}}^{k*} &= \frac{1}{2}(\mathbf{J}_e^{cT} \mathbf{R}^T \mathbf{R} \mathbf{J}_e^k + \mathbf{J}_e^{kT} \mathbf{R}^T \mathbf{R} \mathbf{J}_e^c + \mathbf{J}_e^{kT} \mathbf{R}^T \mathbf{R} \mathbf{J}_e^k - \mathbf{J}_0^{cT} \mathbf{J}_0^k - \mathbf{J}_0^{kT} \mathbf{J}_0^c - \mathbf{J}_0^{kT} \mathbf{J}_0^k) \\ \tilde{\boldsymbol{\epsilon}}^{k*} &= \frac{1}{2}(\mathbf{J}_e^{cT} \mathbf{J}_e^k + \mathbf{J}_e^{kT} \mathbf{J}_e^c + \mathbf{J}_e^{kT} \mathbf{J}_e^k - \mathbf{J}_0^{cT} \mathbf{J}_0^k - \mathbf{J}_0^{kT} \mathbf{J}_0^c - \mathbf{J}_0^{kT} \mathbf{J}_0^k) = \tilde{\boldsymbol{\epsilon}}^k \end{aligned} \right\} \quad (36)$$

That is, the strain split method does not affect the strain objectivity.

4.5 Other Locking Solution Approaches

This section briefly discusses the enhanced assumed strain, elastic line, and enhanced continuum mechanics approaches used in the numerical investigation performed in this chapter to compare with the SSM results. The brief description of these methods, which are well documented in literature, will shed light on the differences between different locking solution techniques. Furthermore, an enhanced strain approach based on using higher-order ANCF element shape functions with lower-order ANCF elements is demonstrated.

4.5.1 Enhanced Assumed Strain (EAS) and Method of Incompatible Modes

The method of incompatible modes was introduced by Bazeley et al. (1965) and studied by Taylor et al. (1976) in order to improve the bending behavior of the classical quadrilateral element. The enhanced assumed strain approach proposed by Simo and Rifai (1990) is a generalization of the

method of incompatible modes. In fact, Simo and Rifai (1990) demonstrated that the method of incompatible modes is a special case of the enhanced assumed strain approach. In the enhanced strain approach, the incompatible strain field is defined using certain carefully designed interpolations by ensuring that the set of interpolating polynomials meet a list of conditions that are required for convergence and stability of the element. The basic idea is the enhancement of the element strain field by enriching its strain components so that its performance improves in non-uniform strain conditions. One disadvantage of this approach is the requirement of adding more variables to every element. Consider the Veubeke-Hu-Washizu energy functional in the reference configuration (Bischoff and Ramm, 1997):

$$\Pi_{VHW}(\mathbf{r}, \boldsymbol{\varepsilon}, \boldsymbol{\sigma}_{P2}) = \int_{V_0} U(\boldsymbol{\varepsilon}) dV_0 + \int_{V_0} \boldsymbol{\sigma}_{P2} : \left(\frac{1}{2}(\mathbf{J}^T \mathbf{J} - \mathbf{I}) - \boldsymbol{\varepsilon} \right) dV_0 - U_{ext} \quad (37)$$

where $\boldsymbol{\sigma}_{P2}$ is the second Piola-Kirchhoff stress tensor, $\boldsymbol{\varepsilon}$ is the Lagrangian strain tensor, and U and U_{ext} are, respectively, the internal and external potential energy functions. The strain field is enhanced as $\boldsymbol{\varepsilon} = \boldsymbol{\varepsilon}^{com} + \boldsymbol{\varepsilon}^{enh}$, where $\boldsymbol{\varepsilon}^{com}$ is the compatible strain field obtained from the Green-Lagrange strain tensor, and $\boldsymbol{\varepsilon}^{enh}$ is the enhanced strain field that is element-wise discontinuous. Substituting the enhanced strain in the Veubeke-Hu-Washizu functional and making a design choice for the enhanced strain field such that $\int_{V_0} \boldsymbol{\sigma}_{P2} : \boldsymbol{\varepsilon}^{enh} dV_0 = 0$ leads to

$$\Pi_{VHW}(\mathbf{r}, \boldsymbol{\varepsilon}^{enh}) = \int_{V_0} U(\boldsymbol{\varepsilon}^{com} + \boldsymbol{\varepsilon}^{enh}) dV_0 - U_{ext} \quad (38)$$

The position and enhanced strain fields can be discretized as $\mathbf{r} = \mathbf{S}(\boldsymbol{\xi})\mathbf{e}$ and $\boldsymbol{\varepsilon}^{enh} = \mathbf{M}_s(\boldsymbol{\xi})\mathbf{a}$, where \mathbf{M}_s is a shape function matrix, \mathbf{a} is a vector of additional enhanced strain variables called internal variables, $\boldsymbol{\xi} = [\xi \quad \eta]^T$, $\xi = x/l$, $\eta = y/l$ are the dimensionless element parameters, and l is the

length of the element. Equating the variation of the Veubeke-Hu-Washizu functional to zero, leads to the following set of equations

$$\left. \begin{aligned} \mathbf{f}(\mathbf{e}, \boldsymbol{\alpha}) &= \int_{V_0} \left(\frac{\partial \boldsymbol{\epsilon}^{com}}{\partial \mathbf{e}} \right)^T \frac{\partial U}{\partial \boldsymbol{\epsilon}} dV_0 - \mathbf{Q}_{ext} = \mathbf{0} \\ \mathbf{g}(\mathbf{e}, \boldsymbol{\alpha}) &= \int_{V_0} \left(\frac{\partial \boldsymbol{\epsilon}^{enh}}{\partial \boldsymbol{\alpha}} \right)^T \frac{\partial U}{\partial \boldsymbol{\epsilon}} dV_0 = \mathbf{0} \end{aligned} \right\} \quad (39)$$

Newton's method can be used to solve the nonlinear system of equations shown in Eq. 39. After linearization, the equations used in the iterative Newton-Raphson procedure can be written in the following form:

$$\begin{bmatrix} \mathbf{K} & \mathbf{P} \\ \mathbf{S} & \mathbf{G} \end{bmatrix} \begin{bmatrix} \Delta \mathbf{e} \\ \Delta \boldsymbol{\alpha} \end{bmatrix} = - \begin{bmatrix} \mathbf{f} \\ \mathbf{g} \end{bmatrix} \quad (40)$$

where the sub-matrices in this equation are defined in Appendix B.2. Alternatively, the internal variables $\boldsymbol{\alpha}$ can be eliminated at the element level using a static condensation based on the second equation of Eq. 40, $\Delta \boldsymbol{\alpha} = -\mathbf{G}^{-1}(\mathbf{g} + \mathbf{S}\Delta \mathbf{e})$, which leads to the following system of equations

$$(\mathbf{K} - \mathbf{P}\mathbf{G}^{-1}\mathbf{S})\Delta \mathbf{e} = -\mathbf{f} + \mathbf{P}\mathbf{G}^{-1}\mathbf{g} \quad (41)$$

After applying the static condensation on the internal variables $\boldsymbol{\alpha}$, the equilibrium equations can be assembled for the entire mesh, the boundary conditions applied, and the resulting system is solved for $\Delta \mathbf{e}$. Once $\Delta \mathbf{e}$ is determined, $\boldsymbol{\alpha}$ can be updated for every element (Simo and Armero, 1992; Yamashita et al., 2015). The procedure can be generalized to the dynamic case in which the element coordinates \mathbf{e} are assumed known from the numerical integration. These element coordinates can be substituted into the equation $\mathbf{g}(\mathbf{e}, \boldsymbol{\alpha}) = \mathbf{0}$ which can be used to determine the internal variables $\boldsymbol{\alpha}$ to be used in the formulation of the strain energy and elastic forces. The

guidelines for designing and using the enhanced strain interpolation functions is briefly reviewed in Appendix B.3.

4.5.1.1 EAS Strain Interpolation

In case of the two-dimensional shear deformable element (Omar and Shabana, 2001), Poisson locking can cause poor convergence even after significant mesh refinement. One way to alleviate this type of FE locking (as was discussed in Section 4.3) is to consider a quadratic displacement interpolation in the element transverse direction that would yield a linear transverse normal strain distribution which can be sufficient to account for stiffness coupling resulting from the use of Hooke's law. Therefore, one method to achieve this type of enhancement is to consider the enhanced assumed strain interpolation to be linear in the element transverse direction. The interpolation matrix and the enhanced strain in Voigt form can be written in the parametric domain as

$$\bar{\boldsymbol{\epsilon}}^{enh} = \bar{\mathbf{M}}\boldsymbol{\alpha} = \begin{bmatrix} 0 & \eta & 0 \end{bmatrix}^T \boldsymbol{\alpha} \quad (42)$$

This leads to a linear enhancement of the transverse normal strain and it can be shown that this type of assumed strain interpolation satisfies Eq. B.3 (Appendix B) because $\int_0^1 \int_{-\frac{h}{2l}}^{\frac{h}{2l}} \eta \, d\eta d\xi = 0$.

The fact that the higher-order two-dimensional ANCF beam element proposed in the preceding section is quadratic in the element transverse direction suggests using its “higher-order” shape functions as the interpolation polynomials for the enhanced strain field in order to improve the performance of the lower-order element. Keeping this concept in mind, the enhanced strain field can be assumed to be the linearized strain tensor that uses the “higher-order” shape functions that are $s_1^{HO} = l^2 (\eta^2 - \eta^2 \xi) / 2$, $s_2^{HO} = l^2 \eta^2 \xi / 2$. It follows that the higher-order shape function matrix can be written as $\mathbf{S}^{HO} = \begin{bmatrix} s_1^{HO} \mathbf{I} & s_2^{HO} \mathbf{I} \end{bmatrix}$, and the matrix of higher-order displacement

gradients and enhanced strain tensor can be written using the element enhanced strain parameters as

$$\mathbf{J}_d^{HO} = [\mathbf{S}_x^{HO} \mathbf{a} \quad \mathbf{S}_y^{HO} \mathbf{a}], \quad \bar{\boldsymbol{\varepsilon}}^{enh} = \frac{1}{2} \left(\mathbf{J}_d^{HO} + (\mathbf{J}_d^{HO})^T \right) \quad (43)$$

Furthermore, it can be shown that the enhanced strain in Voigt form can be written as

$$\bar{\boldsymbol{\varepsilon}}^{enh} = \bar{\mathbf{M}} \mathbf{a} = \begin{bmatrix} \mathbf{S}_{x1}^{HO} \\ \mathbf{S}_{y2}^{HO} \\ (\mathbf{S}_{x2}^{HO} + \mathbf{S}_{y1}^{HO}) \end{bmatrix} \mathbf{a} \quad (44)$$

where \mathbf{S}_{ab}^{HO} corresponds to the b^{th} row of the matrix $\mathbf{S}_a^{HO} = \partial \mathbf{S}^{HO} / \partial a$, and $a = x, y$. One issue with

this type of enhanced strain interpolation is that $\int_0^1 \int_{-\frac{h}{2l}}^{\frac{h}{2l}} s_{1,\xi}^{HO} d\eta d\xi \neq 0$ and $\int_0^1 \int_{-\frac{h}{2l}}^{\frac{h}{2l}} s_{2,\xi}^{HO} d\eta d\xi \neq 0$.

This violates the condition of Eq. B.3 (Appendix B). In order to address this problem, the method of the constant correction matrix proposed by Ibrahimbegovic and Wilson (1991) is used. The matrix of interpolating functions in the physical domain is modified by adding a constant correction matrix such that $\tilde{\mathbf{M}} = \mathbf{M}_s + \mathbf{M}_c$, where the matrix $\tilde{\mathbf{M}}$ satisfies the second part of Eq. B.3 (Appendix B). The correction matrix \mathbf{M}_c can be defined using the equation

$\int_{V_0} \mathbf{M}_s dV_0 + V_0 \mathbf{M}_c = \mathbf{0}$, which leads to

$$\mathbf{M}_c = -\frac{1}{V_0} \int_{V_0} \mathbf{M}_s dV_0 \quad (45)$$

In this case, $\tilde{\mathbf{M}}$ is used as the interpolation matrix to define the enhanced strain instead of \mathbf{M}_s

which violates Eq. B.3 (Appendix B).

4.5.2 Elastic Line Approach

The ANCF elastic line approach, used by Schwab and Meijaard (2005) and Hussein et al. (2007), can be an effective method for formulating the elastic forces for thin and stiff beams. The elastic line approach strain energy can be written as $U_{tot} = U_l + U_s + U_b$, where U_l, U_s, U_b represent beam centerline (line integral) based extensional, shear and bending energies respectively. Schwab and Meijaard (2005) considered the Poisson coupling of the normal strains in their work whereas Hussein et al. (2007) did not consider this Poisson coupling. For details on the derivation of the elastic forces using the elastic line approach, the reader may refer to the publications by Schwab and Meijaard (2005) and Hussein et al. (2007). A mixed method that was employed with ANCF elements in order to reduce shear locking in conjunction with the elastic line approach was the Hellinger-Reissner principle, where the shear stress field was interpolated independently within the element (Schwab and Meijaard, 2005; Hussein et al., 2007).

4.5.3 Enhanced Continuum Mechanics Approach

As mentioned in Section 4.2, another method proposed in the ANCF literature to deal with Poisson locking is the enhanced continuum mechanics approach that was proposed by Gerstmayr et al. (2008). The roots of this method lie in the concept of classical FE selectively reduced integration. The matrix of elastic coefficients is split into two parts, one that considers Poisson coupling between the normal strains and one that does not consider this effect. While the strain split method proposed earlier in this chapter is similar to the enhanced continuum mechanics approach when considering the constitutive model split, there are some fundamental differences between the two methods. In case of the enhanced continuum mechanics approach, selectively reduced integration is used and the same strain matrix is used for the full integration and reduced integration parts, whereas in case of the strain split method, full integration is used and different strain matrices are used with two different constitutive matrices. It will be demonstrated in the numerical results

section that the strain split method can be used to obtain comparable results to those of the enhanced continuum mechanics approach without the need for using reduced integration.

4.6 Numerical Examples

In order to demonstrate and compare the effect of the locking alleviation techniques on the performance of ANCF beam elements, five numerical examples are considered: three static analysis examples and two dynamic analysis examples. The first static example is that of a slender beam subjected to small deformation. The second static example is a thick beam subjected to large deformation. The third static example is that of a curved beam subjected to large deformation. The first dynamic analysis example is a two-dimensional beam pendulum subjected to gravity loading. The second dynamic analysis example is a three-dimensional cantilever beam structure subjected to gravity loading. Because all the static examples are planar, the plane stress assumption is used in all static analyses. Table 14 provides appropriate abbreviations that will be used to refer to different locking alleviation techniques. All locking alleviation techniques in Table 14 with the exception of HOEL are used with the Omar and Shabana (referred to as Om-Sh henceforth) beam element. HOEL refers to the higher-order beam element proposed in this chapter in Section 4.3. In all the examples, the shear correction factor $k_s = 10(1 + \nu)/(12 + 11\nu)$ is used with the Om-Sh beam element and not with HOEL, unless specified otherwise.

Table 14. Locking alleviation technique abbreviations

Abbreviation	Type
GCM	General continuum mechanics
ECM	Enhanced continuum mechanics
EAS-1	Single parameter enhanced assumed strain
EAS-2	Higher-order shape function based enhanced assumed strain
SSM	Strain split method
EL-SM	Schwab-Meijaard elastic line
EL-HS	Hussein et al. elastic line
ELHR-SM	Schwab-Meijaard elastic line with Hellinger Reissner shear improvement
ELHR-HS	Hussein et al. elastic line with Hellinger Reissner shear improvement
HOEL	Higher-order beam element with GCM

4.6.1 Slender Beam: Small Deformation

A slender cantilever beam subjected to a vertical tip force is considered with the same element dimensions and material properties as that of the problem described in Section 4.3.4. As was mentioned previously, the analytical solution is known in this case from the classical Euler-Bernoulli theory and is calculated to be -0.02m. The results for the static analysis are reported in Table 15 which shows the converged beam tip vertical displacement. As can be seen from these results, the Om-Sh beam element with general continuum mechanics approach cannot converge to the correct solution due to excessive stiffness resulting from Poisson locking. All the other cases can converge to the correct solution. The enhanced continuum mechanics approach, EAS-1, EAS-2 and the strain split approach show almost identical convergence in this small deformation case. Based on the results reported in Table 15, the Hellinger-Reissner principle did not improve the convergence or the solution.

Table 15. Small deformation of cantilever beam static example: tip vertical displacement (m)

TYPE	5 elements	10 elements	20 elements	50 elements	100 elements
GCM	-0.01797943	-0.01814821	-0.01818387	-0.01819351	-0.018194876
ECM	-0.01974402	-0.01994094	-0.01998069	-0.01999130	-0.019992806
EAS-1	-0.01974404	-0.01994095	-0.01998069	-0.01999130	-0.019992806
EAS-2	-0.01974414	-0.01994097	-0.01998069	-0.01999130	-0.019992806
SSM	-0.01974403	-0.01994095	-0.01998069	-0.01999130	-0.019992806
HOEL	-0.01972699	-0.01993622	-0.01997940	-0.01999102	-0.019992674
EL-SM	-0.01974323	-0.01994464	-0.01998333	-0.01999130	-0.019991743
EL-HS	-0.01974800	-0.01994487	-0.01998334	-0.01999130	-0.019991743
ELHR-SM	-0.01973830	-0.01993950	-0.01997930	-0.01998984	-0.019991308
ELHR-HS	-0.01974306	-0.01993973	-0.01997931	-0.01998984	-0.019991308
Analytical	-0.02				

4.6.2 Thick Beam: Large Deformation

A thick beam example undergoing large deformation, shown in Figure 36, is considered. The beam structure is 2m long and has a cross section that is 0.5m high and 0.1m wide. The modulus of elasticity is assumed $E = 2.07 \times 10^{11}$ Pa, and Poisson ratio is assumed $\nu = 0.3$. A fully clamped

boundary condition is applied at the left end of the beam, whereas a vertical force of $-5 \times 10^8 \times h^3$ N is applied to the right end. For this example, the curvature degrees of freedom at the beam clamped end are also constrained in case of the higher-order beam element due to the large deformation nature of the problem and large cross-section which could lead to significant cross-section deformation at the clamped end. The results of a static analysis reported in Table 16 show the converged beam tip vertical displacement. The reference solution of -0.71342 m, obtained using a commercial FE code (ANSYS, 2013), was achieved with 10,000 quadratic quadrilateral elements.

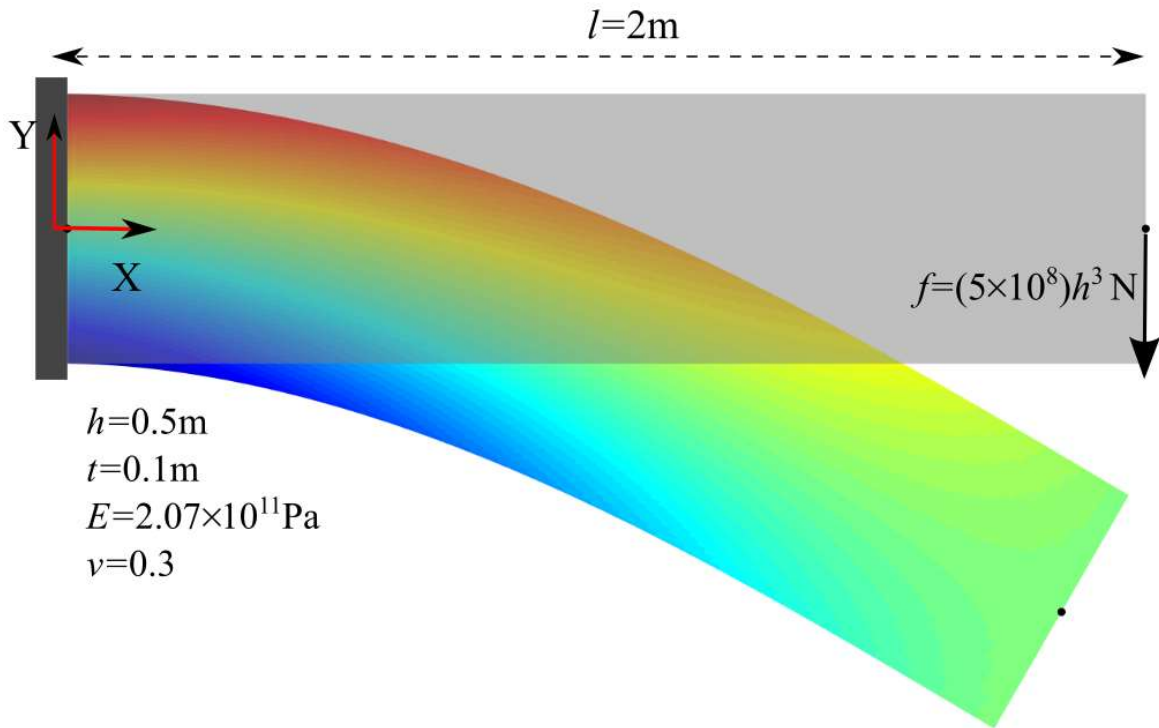


Figure 36. Thick cantilever beam problem (actual deformation shown with respect to undeformed state)

Table 16. Large deformation of cantilever beam static example: tip vertical displacement (m)

TYPE	5 elements	10 elements	20 elements	50 elements	100 elements
GCM	-0.65915558	-0.66424157	-0.66567545	-0.66620894	-0.66633102
ECM	-0.70648069	-0.71210192	-0.71364032	-0.71421138	-0.71434336
EAS-1	-0.70749271	-0.71303640	-0.71458220	-0.71516154	-0.71529576
EAS-2	-0.70914733	-0.71423843	-0.71582370	----	----
SSM	-0.70703906	-0.71261927	-0.71416020	-0.71473509	-0.71486816
HOEL	-0.69531347	-0.70527450	-0.70867124	-0.70994038	-0.71018834
EL-SM	-0.68327030	-0.68431265	-0.68437627	-0.68439711	-0.68440429
EL-HS	-0.68356363	-0.68475960	-0.68484925	-0.68487219	-0.68487886
ANSYS	-0.713420 (converged)				

As can be seen from Table 16, the general continuum mechanics approach without locking alleviation converges to the incorrect solution. The higher-order beam element, enhanced continuum mechanics approach, SSM, and the EAS-1 approach can successfully alleviate locking in this example. The EAS-2 method, however, failed to converge when more than 25 elements are used. It was observed that as the element length-to-height ratio significantly decreases, numerical instabilities similar to spurious modes or hourglassing were observed when the EAS-2 method is used with the thick beam example. Recall that EAS-2 makes use of the correction matrix along with the enhanced strain formulation. A possible explanation for this phenomenon is the ill-conditioning of the stiffness matrix caused by correction matrices as the element ratio approaches zero. Such numerical instability was not seen in the EAS-2 method in case of relatively thin beams. The critical element length-to-height ratio is found to be around 0.15 for the EAS-2 method in this specific example. It should be reported that if the height of the beam in this example was reduced to 0.1m, the numerical instability disappeared in the EAS-2 method for meshes which have more than 25 elements. A similar type of numerical instability was reported by Sussman and Bathe (2014) when using of incompatible mode elements in the case of geometrically nonlinear analyses and small strain conditions.

4.6.3 Initially Curved Beam: Large Deformation

An initially curved beam structure is subjected to large deformation in this numerical example as shown in Figure 37. The beam is clamped at one end and a constant tip force is applied in the global X direction. The value of the force is $1 \times 10^9 \times h^3$ N. The initially curved beam arc length is 1m and the arc radius is 0.6366m. The beam height and width are 0.05m each. The material properties are $E = 2.0 \times 10^{11}$ Pa, $\nu = 0.3$, and $k_s = 1$. The results from the static analysis are shown in Table 17 which shows the beam tip horizontal displacement. The reference solution of 0.17291m was obtained using a commercial FE code (ANSYS, 2013) with 1000 classical beam element mesh. The ANCF higher-order beam element, EAS-1 and EAS-2 methods can converge close to the reference solution.

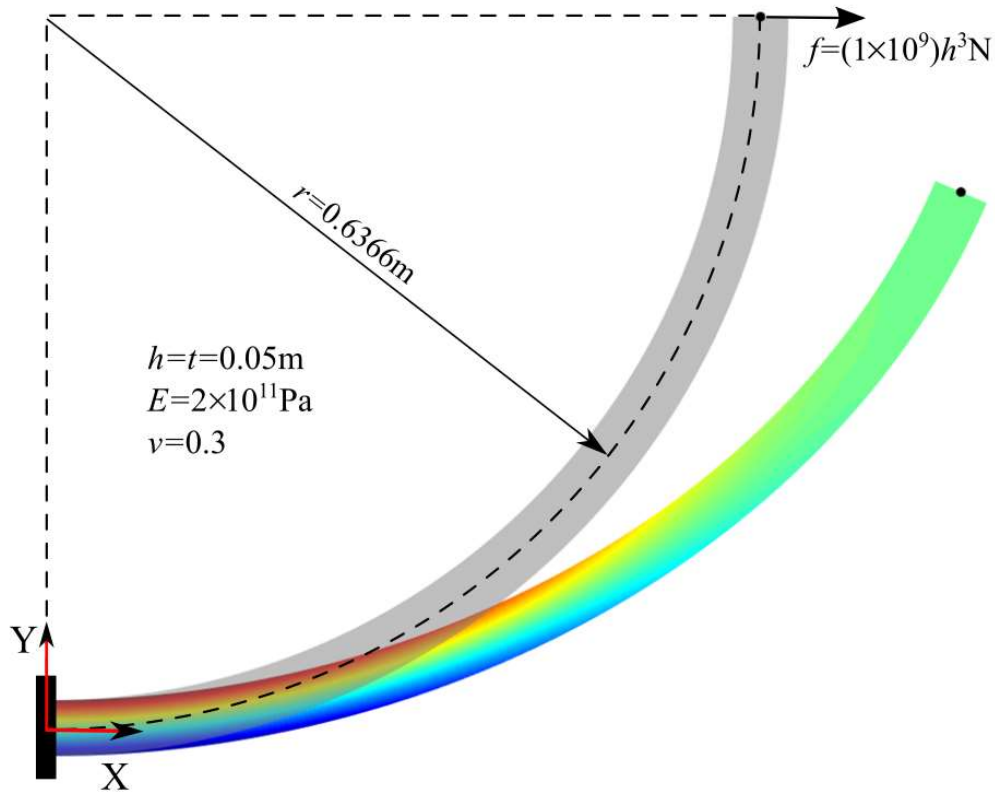


Figure 37. Curved cantilever beam problem (actual deformation shown with respect to undeformed state)

Table 17. Large deformation of curved cantilever beam static example: tip X displacement (m)

TYPE	5 elements	10 elements	20 elements	50 elements	100 elements
GCM	0.15338680	0.16172381	0.16199009	0.16196139	0.16195412
ECM	0.16989437	0.17938015	0.17974234	0.17972820	0.17972255
EAS-1	0.16295031	0.17215697	0.17250459	0.17249109	0.17248574
EAS-2	0.16311305	0.17225897	0.17263943	0.17271119	0.17273819
SSM	0.16988736	0.17937894	0.17974213	0.17972815	0.17972252
HOEL	0.16298605	0.17213835	0.17247560	0.17246368	0.17246014
ECM-L	0.16409531	0.17247265	0.17258737	0.17250808	0.17249346
SSM-L	0.16408860	0.17247216	0.17258704	0.17250726	0.17249244
ANSYS	0.17291 (converged)				

Significant locking is observed in the beam with the general continuum mechanics approach. The strain split and enhanced continuum mechanics methods slightly over-predict the deformation. The reason for this is the loss of the constitutive coupling that occurs in curved structures between higher-order longitudinal strain terms and transverse normal strain. Such a type of coupling is fully present in the general continuum mechanics approach which is used with the ANCF higher-order beam element. One remedy to avoid the over-prediction of the solution in case of the strain split method for curved structures is the consideration of coupling coefficients in the \mathbf{E}^k matrix that could represent weak coupling between the higher-order longitudinal and transverse normal strains, however, it is still not yet clear how to determine such coupling coefficients for the strain split method. For example, if the \mathbf{E}^k matrix is modified such that $\mathbf{E}^k(1,2) = \mathbf{E}^k(2,1) = E\nu$, the SSM converged solution is 0.1705m, which is an improvement compared to the solution obtained without modifying \mathbf{E}^k .

A more effective method for improving the performance of the strain split and enhanced continuum mechanics methods in case of initially curved structures is based on giving a “local” meaning to the constitutive model used in the SSM and ECM approaches. This entails the

transformation of either the constitutive coefficients into the global frame with the understanding that the constitutive coefficients are defined with respect to the element local frame or carry out strain and stress transformations between the global and element local frames (Nachbagauer et al., 2013B). Since the transformation of the constitutive coefficients is rather cumbersome, the Green-Lagrange strain tensor used in the ECM approach and the $\boldsymbol{\epsilon}^c$ and $\boldsymbol{\epsilon}^k$ strain matrices used with the SSM approach can be first transformed into the element local frame, the local stress can be evaluated within this element frame and then the resulting local stress can be transformed back into the global frame in order to evaluate the element elastic forces (Nachbagauer et al., 2013B). Using such a procedure, the SSM and ECM techniques yield accurate results for initially curved structures as can be seen in Table 17, where the results for the two approaches are labeled as SSM-L and ECM-L referring to the local interpretation of the constitutive model used. A tangent element frame can be defined in case of ANCF beam elements at the first node as $\mathbf{A} = [\mathbf{i} \quad \tilde{\mathbf{i}}]$, where $\mathbf{i} = \mathbf{r}_x / |\mathbf{r}_x|$, and $\tilde{\mathbf{i}} = [\mathbf{a}_1 \quad \mathbf{a}_2]$, $\mathbf{a}_1 = [0 \quad 1]^T$, $\mathbf{a}_2 = [-1 \quad 0]^T$. Similarly, a cross section element frame can be defined as $\mathbf{A} = [-\tilde{\mathbf{j}} \quad \mathbf{j}]$, where $\mathbf{j} = \mathbf{r}_y / |\mathbf{r}_y|$. These frames are defined using the beam reference configuration, and hence do not change with time. It was observed that using either tangent frame or cross-section frame did not make significant difference for the problem under investigation. In case of using the local interpretation for the constitutive model, the coupling coefficients in the \mathbf{E}^k matrix discussed previously are no longer required. Furthermore, the local frame is also more appropriate to use with shear correction factors used with beams. It must also be reported that the softening of the beam in case of initially curved structures discussed earlier is dependent on the beam radius of curvature, that is, less softening for a larger radius of curvature in case of SSM.

4.6.4 Dynamic Analysis: Pendulum Problem

A dynamic example is presented in order to demonstrate that the newly proposed strain split method can contribute to locking alleviation in dynamic problems as well. A beam pendulum meshed with 30 elements is considered, with a length of 1m, height of 0.25298m and a width of 0.00632m as was presented by Omar and Shabana (2001). The material properties of the pendulum are $E = 7.0 \times 10^5$ Pa, $\nu = 0.3$ and $\rho = 5540$ kg/m³. Gravity load is considered to be the external force in this problem and an assumption of plane stress was used in the analysis. The vertical displacement of the beam tip is shown as a function of time in Figure 38.

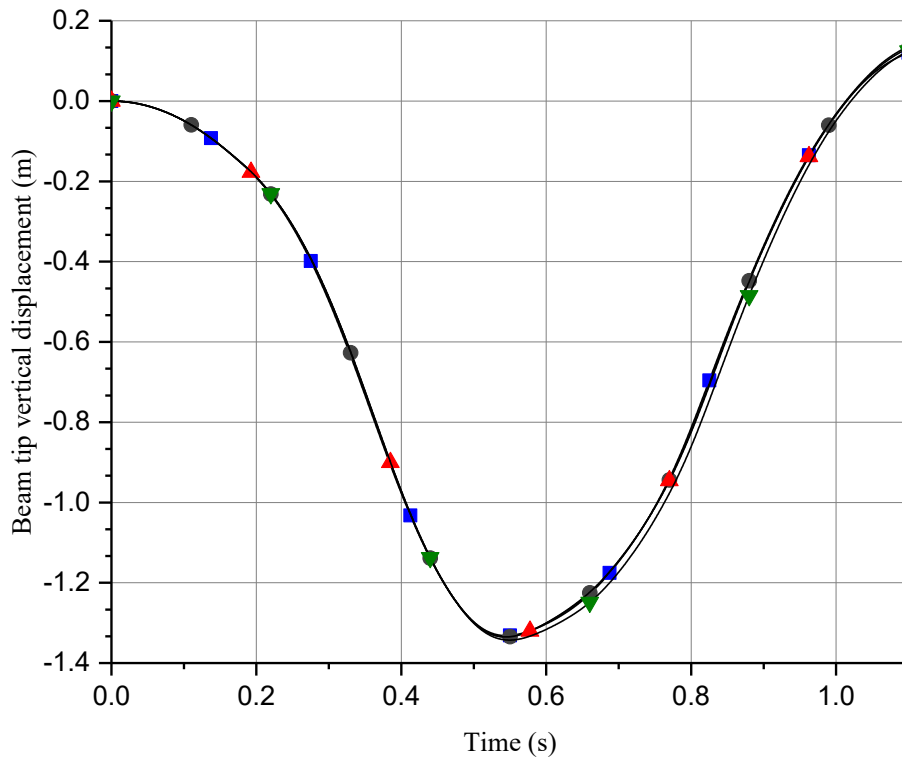


Figure 38. Comparison of beam tip vertical displacement for different formulations in case of plane stress (—■— GCM, —●— ECM, —▲— SSM, —▼— HOEL)

The Om-Sh element with general continuum mechanics approach, the strain split method, the enhanced continuum mechanics approach, and the proposed ANCF higher-order beam element are

compared in Figure 38. Results show good convergence between different models for a dynamic analysis. The deformation seen in the higher-order element model is slightly larger than the other models since this element has curvature coordinates that add additional cross-section flexibility to the element. Figure 39 shows the results of the beam tip vertical displacement obtained using the general continuum mechanics approach and the strain split method using the plane strain assumptions and the Om-Sh element.

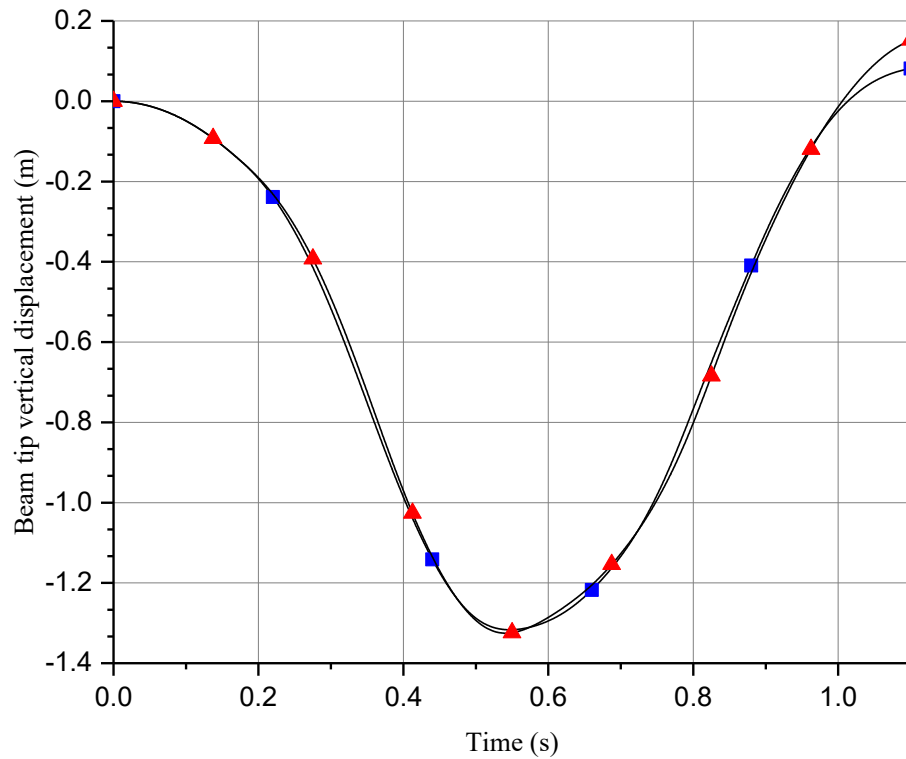


Figure 39. Comparison of beam tip vertical displacement between general continuum mechanics and strain split method with plane strain assumption (—■—GCM, —▲—SSM)

The effect of locking is more evident in case of plane strain with the general continuum mechanics approach. Figure 40 shows the beam configurations at different times during the plane strain dynamic analysis. The colored beam in Figure 40 shows the axial strain in case of the strain split

model, whereas the gray beam shows the configuration of the beam obtained using the general continuum mechanics approach.

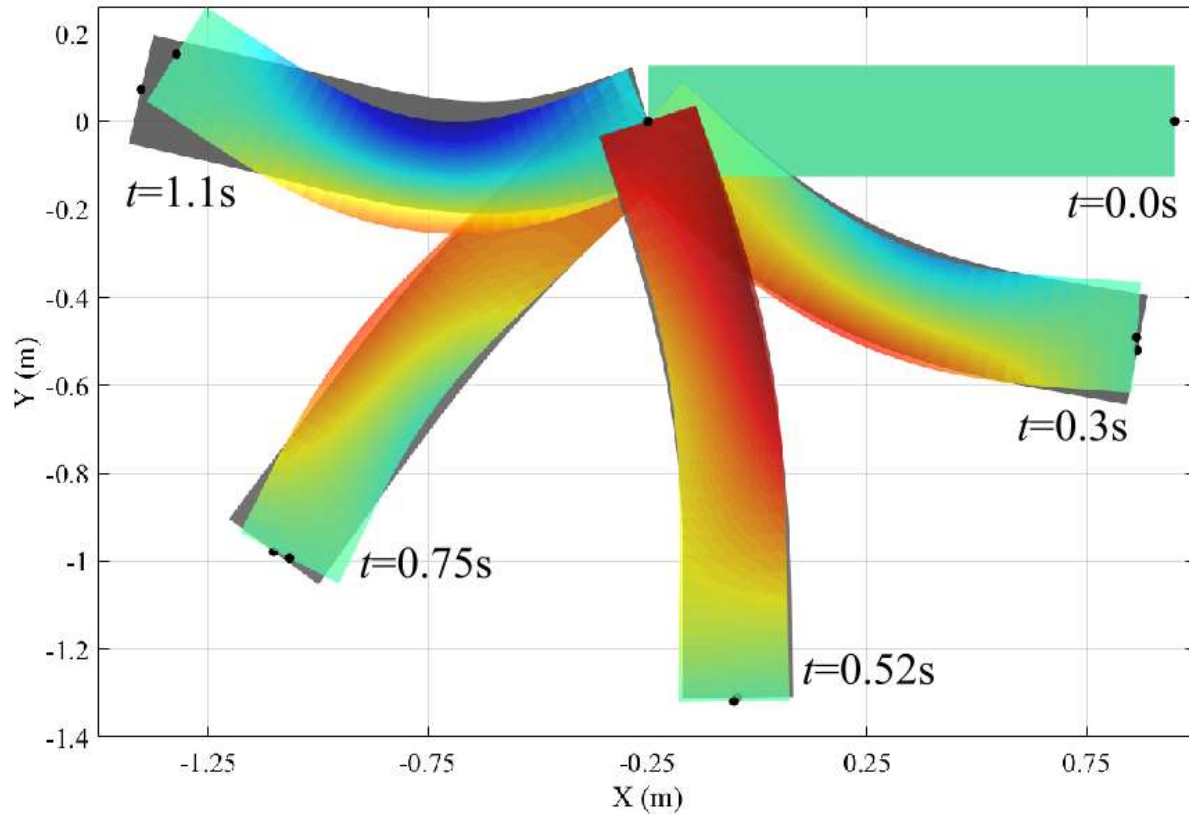


Figure 40. Graphical representation of the pendulum motion in case of plane strain (Gray: GCM; colored: SSM with axial strain contours)

4.6.5 Three-Dimensional Dynamic Analysis: Cantilever Beam

Finally, a dynamic analysis of a three-dimensional cantilever beam structure is presented. This problem is identical to the one considered by Orzechowski and Shabana (2016) where they compared the Yakoub and Shabana (2001) ANCF beam element with the Shen et al. (2014) higher-order beam element. The higher-order three-dimensional beam element does not have the locking seen in the relatively lower-order Yakoub and Shabana element. The beam structure length is 1m and the cross-section height and thickness are 0.1m and 0.07m, respectively. The material

properties considered are $E = 60 \times 10^6 \text{ Pa}$, $\nu = 0.3$, and $\rho = 7200 \text{ kg/m}^3$. Gravity loading is considered as external force. Figure 41 shows the beam reference and deformed configurations.

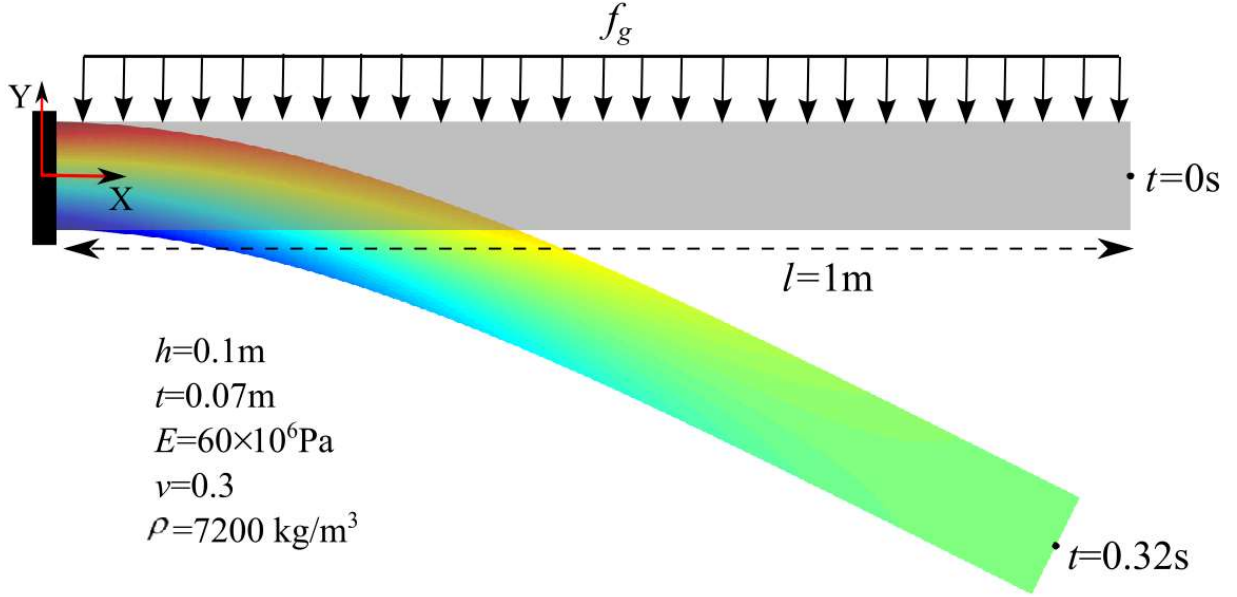


Figure 41. Three-dimensional cantilever beam dynamic analysis (Gray: beam configuration at $t=0\text{s}$; colored: beam configuration with axial strain contours at $t=0.32\text{s}$)

Figure 42 compares the Yakoub and Shabana element with the general continuum mechanics approach, strain split method, and the elastic line approach to the solution obtained from the higher-order Shen et al. (2014) element that used the general continuum mechanics approach. A mesh of 10 elements is considered for all models shown in Figure 42. It can be seen from the results presented in Figure 42 that the lower-order element with general continuum mechanics approach exhibits significant locking, whereas the other models compare well with the higher-order three-dimensional beam element. This example also demonstrates the effectiveness of the strain split method in three-dimensional beam elements. The elastic line approach gives good results in this case since the beam cross-sectional dimensions are much smaller than its length.

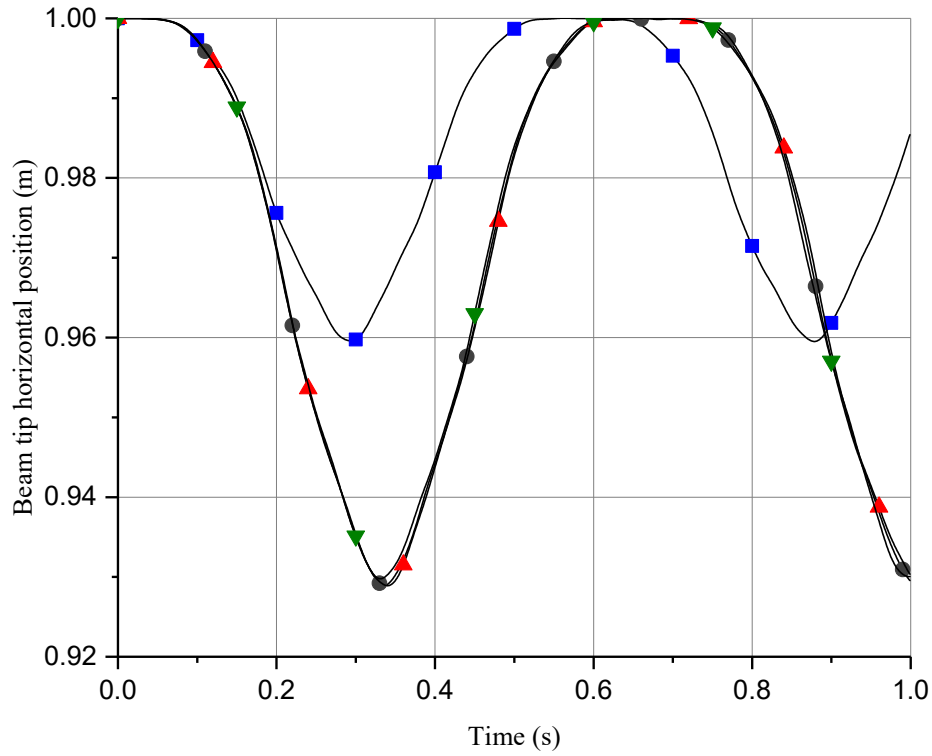


Figure 42. Comparison of cantilever beam tip horizontal position for different models (—■— Yakoub and Shabana beam with GCM, —●— Yakoub and Shabana beam with SSM, —▲— Higher-order Shen et al. beam with GCM, —▼— Yakoub and Shabana beam with elastic line approach)

4.7 Concluding Remarks

The ANCF beam element locking was the subject of this chapter which presented a literature review of classical FE and ANCF locking alleviation techniques. This literature review shows the significant contributions reported in the FE literature and clearly demonstrates that, while locking is a common problem in most FEs, it can be dealt with relatively easily and effectively. ANCF locking alleviation techniques can be broadly classified into two distinct categories: kinematics- and kinetics-based methods. Kinematics-based locking alleviation techniques alter the kinematic description of the element in order to improve its performance. Such methods include

improvement in the displacement polynomials or improvement of the strain measures. Kinetics-based methods operate at the elastic force level by modifying the stresses without directly affecting the basic element kinematics. Such methods include different formulations of the strain energy function and reduced integration. The locking alleviation techniques investigated and compared in this chapter can be categorized in the aforementioned two types. These include the new method that is proposed in this chapter to solve the ANCF beam and plate locking problems, known as the strain split method (SSM). A new higher-order two-dimensional ANCF beam element was also developed for the purpose of comparison with other locking alleviation methods. Implementation of the enhanced assumed strain method in ANCF beams using one parameter interpolation and using ANCF higher-order beam shape functions was presented and discussed. Three planar static examples that include a slender beam, a thick beam and a curved beam structure undergoing small and large deformations, one planar dynamic pendulum problem and one three-dimensional dynamic cantilever beam problem were presented, and the locking alleviation techniques were compared. The newly proposed SSM concept in curved structures was discussed and its advantages and drawbacks were discussed.

CHAPTER 5

VEHICLE MODELING: STRUCTURAL DISCONTINUITY, SMALL AND LARGE DEFORMATION

The goal of this chapter (Patel et al., 2017) is to propose an approach for developing new and detailed vehicle models that include flexible components with complex geometries, including chassis, and airless and pneumatic tires with distributed inertia and flexibility. The methodology used is based on successful integration of geometry, and small and large deformation analysis using a mechanics-based approach. The floating frame of reference (FFR) formulation is used to model the small deformations, whereas the absolute nodal coordinate formulation (ANCF) is used for the large deformation analysis. Both formulations are designed to correctly capture complex geometries including structural discontinuities. To this end, a new ANCF-preprocessing approach based on linear constraints that allows for systematically eliminating dependent variables and significantly reducing the component model dimension is proposed. One of the main contributions of this chapter is the development of the first ANCF airless tire model which is integrated in a three-dimensional multibody system (MBS) algorithm designed for solving the differential/algebraic equations of detailed vehicle models. On the other hand, relatively stiff components with complex geometries, such as the vehicle chassis, are modeled using the finite element (FE) FFR formulation which creates a local linear problem that can be exploited to eliminate high frequency and insignificant deformation modes. Numerical examples that include a simple ANCF pendulum with structural discontinuities and a detailed off-road vehicle model consisting of flexible tires and chassis are presented. Three different tire types are considered in this chapter; a brush-type tire, a pneumatic FE/ANCF tire, and an airless FE/ANCF tire. The numerical results are obtained using the general-purpose MBS computer program **SIGMA/SAMS**

(Systematic Integration of Geometric Modeling and Analysis for the Simulation of Articulated Mechanical Systems).

5.1 Small and Large Deformation Analysis

Accurate and efficient modeling of vehicle system applications requires the integration of small- and large-deformation formulations. The stresses of relatively stiff components such as rods and chassis can be efficiently modeled using a small-deformation formulation that allows for systematically eliminating insignificant deformation modes. More flexible components such as tires and belt drives, on the other hand, require the use of a large-deformation formulation. This section briefly discusses the two formulations used to describe the component flexibility in this chapter. These two fundamentally different formulations, FFR and ANCF, are integrated in one MBS computational algorithm designed for solving the differential/algebraic equations that govern the dynamics of vehicle systems. The brief presentation in this and the following sections is necessary in order to have an understanding of the fundamental differences between the two formulations in the way the coordinates are selected, and the structural discontinuities are handled. In the FE/FFR method, a conventional coordinate transformation based on orthogonal transformation matrices is used; while for ANCF elements, transformation between parameters or coordinate lines is used leading to a non-orthogonal gradient transformation.

5.1.1 FE/FFR Formulation

In the FFR formulation, the absolute position vector of an arbitrary point on body i can be written as $\mathbf{r}^i = \mathbf{R}^i + \mathbf{A}^i \bar{\mathbf{u}}^i$, where \mathbf{R}^i is the absolute position vector of body reference, \mathbf{A}^i is the rotation matrix that defines the orientation of the body reference, and $\bar{\mathbf{u}}^i$ is the local position vector of the arbitrary point. If the body is deformable, the absolute position vector can be written as

$\mathbf{r}^i = \mathbf{R}^i + \mathbf{A}^i (\bar{\mathbf{u}}_0^i + \bar{\mathbf{u}}_f^i)$, where $\bar{\mathbf{u}}_0^i$ is the local position vector of the point in the undeformed state and $\bar{\mathbf{u}}_f^i$ is the time-dependent deformation vector.

Beam elements will be used in this chapter to model the chassis in the FE/FFR formulation. The displacement field of the beam element can be written as $\mathbf{w} = \mathbf{S}\mathbf{e}$, where \mathbf{S} is the element shape function matrix and \mathbf{e} is the vector of the element nodal coordinates. The shape function matrix of the FE/FFR beam element is provided in Appendix C.1. In order to be able to correctly model structural discontinuities in the FE/FFR formulation, four coordinate systems are used: the global coordinate system (GCS), body coordinate system (BCS), intermediate coordinate system (ICS), and the element coordinate system (ECS) as shown in Figure 43.

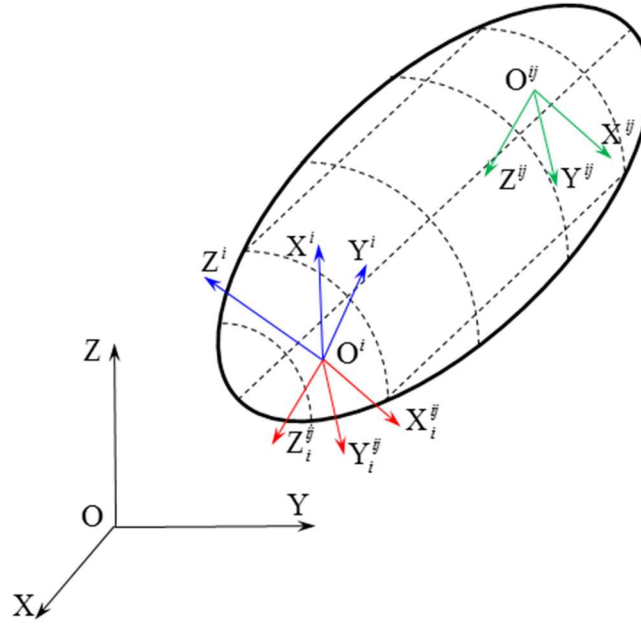


Figure 43. Coordinate systems involved in FE-FFR formulation (Black: GCS; Blue: BCS; Red: ICS; Green: ECS)

For every ECS, there exists an ICS which is initially parallel to the ECS and fixed with respect to the BCS. Using the concept of the ICS, the beam displacement field of an element j on body i can be written in the ICS as $\mathbf{w}_{ICS}^{ij} = \mathbf{S}^{ij} \mathbf{e}_{ICS}^{ij}$, where the subscript ICS refers to vectors defined in ICS. Furthermore, \mathbf{e}_{ICS}^{ij} can be written in terms of the nodal coordinates described in BCS as $\mathbf{e}_{ICS}^{ij} = \bar{\mathbf{C}}^{ij} \mathbf{q}_n^{ij}$, where \mathbf{q}_n^{ij} is the vector of nodal coordinates described in BCS, and $\bar{\mathbf{C}}^{ij}$ is a constant transformation matrix between ICS and BCS, composed of orthogonal transformation matrices. The location of the point in the BCS can be written as $\bar{\mathbf{u}}^{ij} = \mathbf{C}^{ij} \mathbf{w}_{ICS}^{ij}$ or $\bar{\mathbf{u}}^{ij} = \mathbf{C}^{ij} \mathbf{S}^{ij} \bar{\mathbf{C}}^{ij} \mathbf{q}_n^{ij}$, where \mathbf{C}^{ij} is an orthogonal transformation matrix that defines the ICS with respect to the BCS. The nodal coordinates of element j can be written in terms of the total vector of nodal coordinates of the body as $\mathbf{q}_n^{ij} = \mathbf{B}_1^{ij} \mathbf{q}_n^i$, where \mathbf{B}_1^{ij} is a Boolean matrix. Consequently, the local position vector can be written as $\bar{\mathbf{u}}^{ij} = \mathbf{C}^{ij} \mathbf{S}^{ij} \bar{\mathbf{C}}^{ij} \mathbf{B}_1^{ij} \mathbf{q}_n^i$ (Shabana, 2013). In order to define a unique displacement field by eliminating the rigid body modes of the element shape function matrix, a set of *reference conditions* must be applied. To this end, the body nodal coordinates are written as $\mathbf{q}_n^i = \mathbf{q}_0^i + \bar{\mathbf{q}}_f^i$, where \mathbf{q}_0^i is the vector of body nodal coordinates in the un-deformed configuration and $\bar{\mathbf{q}}_f^i$ is the vector of body nodal deformations which can be written as $\bar{\mathbf{q}}_f^i = \mathbf{B}_2^i \mathbf{q}_f^i$, where \mathbf{B}_2^i is the linear transformation matrix obtained using the reference conditions. Using the transformation $\bar{\mathbf{q}}_f^i = \mathbf{B}_2^i \mathbf{q}_f^i$, the local position vector $\bar{\mathbf{u}}^{ij}$ can be written as $\bar{\mathbf{u}}^{ij} = \mathbf{C}^{ij} \mathbf{S}^{ij} \bar{\mathbf{C}}^{ij} \mathbf{B}_1^{ij} (\mathbf{q}_0^i + \mathbf{B}_2^i \mathbf{q}_f^i) = \mathbf{N}^{ij} (\mathbf{q}_0^i + \mathbf{B}_2^i \mathbf{q}_f^i) = \mathbf{N}^{ij} \mathbf{q}_n^i$.

The analysis presented in this section shows that assembly of elements that have different orientations in the reference configuration requires the use of constant orthogonal transformation matrices (\mathbf{C}^{ij} and $\bar{\mathbf{C}}^{ij}$). The use of these transformations in the FE/FFR formulation is necessary

in order to have exact modeling of the rigid body dynamics. In the FE/FFR formulation, the vector of body generalized coordinates is written as $\mathbf{q}^i = [\mathbf{R}^{iT} \quad \boldsymbol{\theta}^{iT} \quad \mathbf{q}_f^{iT}]^T$, where \mathbf{R}^i and $\boldsymbol{\theta}^i$ are the body reference translation and rotational coordinates, respectively. The kinetic energy can be defined using the generalized velocities and the body mass matrix as $T^i = \frac{1}{2} \dot{\mathbf{q}}^{iT} \mathbf{M}^i \dot{\mathbf{q}}^i = \frac{1}{2} \dot{\mathbf{q}}^{iT} \left[\sum_{j=1}^{n_e} \mathbf{M}^{ij} \right] \dot{\mathbf{q}}^i$, where n_e is the number of elements, \mathbf{M}^{ij} is the mass matrix of element j , and \mathbf{M}^i is the body mass matrix which is a highly nonlinear function of the coordinates. The virtual work of the elastic forces is defined as $\delta W_s^{ij} = - \int_{V^{ij}} \delta \boldsymbol{\epsilon}^{ijT} \boldsymbol{\sigma}^{ij} dV^{ij}$, where a linear isotropic material is assumed for the stress-strain relationship. The element stiffness matrix can be written as $\mathbf{K}_{ff}^{ij} = \int_{V^{ij}} \mathbf{V}^{ijT} \mathbf{E}^{ij} \mathbf{V}^{ij} dV^{ij}$, where $\mathbf{V}^{ij} = \mathbf{D}^{ij} \mathbf{N}^{ij} \mathbf{B}_2^i$, \mathbf{E}^{ij} is the matrix of elastic coefficients, and \mathbf{D}^{ij} is the matrix that relates the strains and displacements, such that $\boldsymbol{\epsilon}^{ij} = \mathbf{D}^{ij} \bar{\mathbf{u}}_f^{ij}$. Using the transformations previously developed in this section, the element stiffness matrices can be assembled to obtain the stiffness matrix \mathbf{K}_{ff}^i which can be used to define the stiffness matrix \mathbf{K}^i associated with the total vector of coordinates of the body (Shabana, 2013). Using the mass and stiffness matrices, the FE/FFR equations of motion for an unconstrained body i can be written as

$$\mathbf{M}^i \ddot{\mathbf{q}}^i + \mathbf{K}^i \mathbf{q}^i = \mathbf{Q}_e^i + \mathbf{Q}_v^i \quad (46)$$

where \mathbf{Q}_e^i is the vector of generalized external forces, and \mathbf{Q}_v^i is the Coriolis and centrifugal quadratic velocity vector. For flexible vehicle components with complex geometry such as the chassis shown in Figure 2 (Chapter 1), the number of elastic coordinates in Eq. 46 can be very large. For this reason, coordinate reduction techniques are often used to reduce the problem dimensionality. In this chapter, the number of elastic coordinates of the chassis is reduced using

component mode synthesis methods by performing an eigenvalue analysis of the system $\mathbf{M}_{ff}^i \ddot{\mathbf{q}}_f^i + \mathbf{K}_{ff}^i \mathbf{q}_f^i = \mathbf{0}$, where \mathbf{M}_{ff}^i is the partition of the mass matrix associated with the vector of body nodal deformations. Because of the application of the reference conditions, the stiffness matrix \mathbf{K}_{ff}^i is a symmetric positive-definite matrix (Shabana, 2013). Using the eigenvalue analysis, the vector of nodal coordinates can be written as $\mathbf{q}_f^i = \bar{\mathbf{B}}_m^i \mathbf{p}_f^i$, where $\bar{\mathbf{B}}_m^i$ is the modal transformation matrix whose columns contain the eigenvectors that represent significant deformation modes, and \mathbf{p}_f^i is the vector of modal coordinates. Because insignificant high frequency mode shapes are eliminated from $\bar{\mathbf{B}}_m^i$, the number of elastic coordinates can be significantly reduced as demonstrated by the HMMWV vehicle example used in this chapter.

5.1.2 ANCF Finite Elements

Unlike the FE/FFR formulation, ANCF elements lead to highly nonlinear elastic forces and a constant mass matrix, and therefore, the Coriolis and centrifugal inertia forces are zero when these elements are used. ANCF coordinates consist of position and gradient/slope vectors that are defined in the global coordinate system. Several ANCF elements have been proposed in the literature. These ANCF elements include beam, plate/shell, solid, triangular, and tetrahedral elements that can be defined using non-rational or rational polynomials (Yakoub and Shabana, 2001; Mikkola and Shabana, 2003; Olshevskiy et al., 2014; Pappalardo et al., 2017A; Pappalardo et al., 2017B; Shabana, 2012). When ANCF elements are used, the global position vector of an arbitrary point on element j of body i can be written using the element shape functions and nodal coordinates as $\mathbf{r}^{ij} = \mathbf{S}^{ij} \mathbf{e}^{ij}$, where \mathbf{S}^{ij} is the element shape function matrix, and \mathbf{e}^{ij} is the vector of element nodal coordinates. In this chapter, both pneumatic and airless tires will be modeled using ANCF plate/shell elements whose shape functions are provided in Appendix C.2. The vector of

the four-node plate/shell element nodal coordinates \mathbf{e}^{ij} can be written as $\mathbf{e}^{ij} = [\mathbf{e}_1^{iT} \quad \mathbf{e}_2^{iT} \quad \mathbf{e}_3^{iT} \quad \mathbf{e}_4^{iT}]^T$, where the coordinates of node n can be written in the case of a fully-parameterized element as $\mathbf{e}_n^{ij} = [\mathbf{r}_n^{iT} \quad (\partial \mathbf{r}_n^{ij} / \partial x)^T \quad (\partial \mathbf{r}_n^{ij} / \partial y)^T \quad (\partial \mathbf{r}_n^{ij} / \partial z)^T]^T$, $n = 1, 2, 3, 4$, where $\mathbf{x} = [x \quad y \quad z]^T$ are element parameters. No distinction is made between ANCF plate and shell elements because an ANCF shell element has the same assumed displacement field of the ANCF plate element. The shell geometry can be systematically defined using the element nodal coordinates in the reference configuration \mathbf{e}_0^{ij} , where the subscript 0 refers to reference configuration. The use of the position vector gradients as nodal coordinates allows for obtaining complex shell geometry by a proper choice of \mathbf{e}_0^{ij} . The mass matrix of ANCF elements $\mathbf{M}^{ij} = \int_{V_0^{ij}} \rho^{ij} \mathbf{S}^{ijT} \mathbf{S}^{ij} dV_0^{ij}$ can be defined using the kinetic energy, where ρ^{ij} and V_0^{ij} are, respectively, the mass density and volume in the reference configuration. Given an external force vector \mathbf{f}_e^{ij} , the ANCF generalized force vector can be written as $\mathbf{Q}_e^{ij} = \mathbf{S}^{ijT} \mathbf{f}_e^{ij}$. For fully parameterized ANCF elements, the continuum mechanics approach can be used to formulate the elastic forces. Given an elastic energy potential function U^{ij} , the second Piola-Kirchhoff stress tensor can be written as $\boldsymbol{\sigma}_{p2}^{ij} = \partial U^{ij} / \partial \boldsymbol{\epsilon}^{ij}$, where $\boldsymbol{\epsilon}^{ij} = (\mathbf{J}^{ijT} \mathbf{J}^{ij} - \mathbf{I}) / 2$ is the Green-Lagrange strain tensor, $\mathbf{J}^{ij} = \partial \mathbf{r}^{ij} / \partial \mathbf{X}^{ij}$ is the matrix of position vector gradients, and $\mathbf{X}^{ij} = \mathbf{S}^{ij} \mathbf{e}_0^{ij}$ is the vector of the element parameters in the reference configuration. The vector of element elastic forces can be formulated based on a hyper-elastic model as $\mathbf{Q}_k^{ij} = - \int_{V_0^{ij}} (\partial \boldsymbol{\epsilon}_v^{ij} / \partial \mathbf{e}^{ij})^T \boldsymbol{\sigma}_v^{ij} dV_0^{ij}$, where the subscript v refers to Voigt (engineering) notation of the strain and stress tensors. In case of ANCF, the

equations of motion of an unconstrained ANCF body i can be written as $\mathbf{M}^i \ddot{\mathbf{e}}^i = \mathbf{Q}_k^i + \mathbf{Q}_e^i$, where \mathbf{Q}_e^i is the vector of external forces.

As previously mentioned, ANCF plate/shell elements are used in this chapter to obtain accurate initially-curved geometry description for both pneumatic and airless tires. The stress-free initially-curved geometry in the reference configuration can be achieved by writing the matrix of position vector gradients as $\mathbf{J} = \mathbf{J}_e \mathbf{J}_0^{-1}$, where $\mathbf{J}_e = \partial \mathbf{r} / \partial \mathbf{x}$, $\mathbf{J}_0 = \partial \mathbf{X} / \partial \mathbf{x}$, $\mathbf{x} = [x \ y \ z]^T$ is vector of element coordinates in the straight configuration, and $\mathbf{X} = \mathbf{S} \mathbf{e}_0$ as previously defined. With the appropriate selection of \mathbf{e}_0 , curved structures can be easily modeled using ANCF elements. Additionally, volume transformation can be written between the straight and initially-curved configuration as $dV_0 = |\mathbf{J}_0| dV$ (Bonet and Wood, 1997; Ogden, 1984; Shabana, 2012), where V and V_0 is the volume in the straight and reference configurations, respectively.

5.2 FFR and ANCF Modeling of Structural Discontinuities

Structural discontinuities appear at the locations of intersection of rigidly-connected segments which have different orientations. These discontinuities characterize vehicle system components such as the chassis shown in Figure 2 (Chapter 1) and the airless tire shown in Figure 3 (Chapter 1). In order to develop accurate computational models for these components in MBS applications, it is necessary to use approaches that account for the slope discontinuities. This section briefly describes the methods used for handling structural discontinuities in the two FE formulations used in this chapter. A new ANCF approach for the treatment of structural discontinuities is also proposed in this section. In this approach, a constant velocity transformation matrix is developed and used to eliminate the dependent variables at a preprocessing stage. The new approach offers

the flexibility and generality of combining structural discontinuity constraints with other constraints since it retains the original element coordinates before any coordinate transformation is performed.

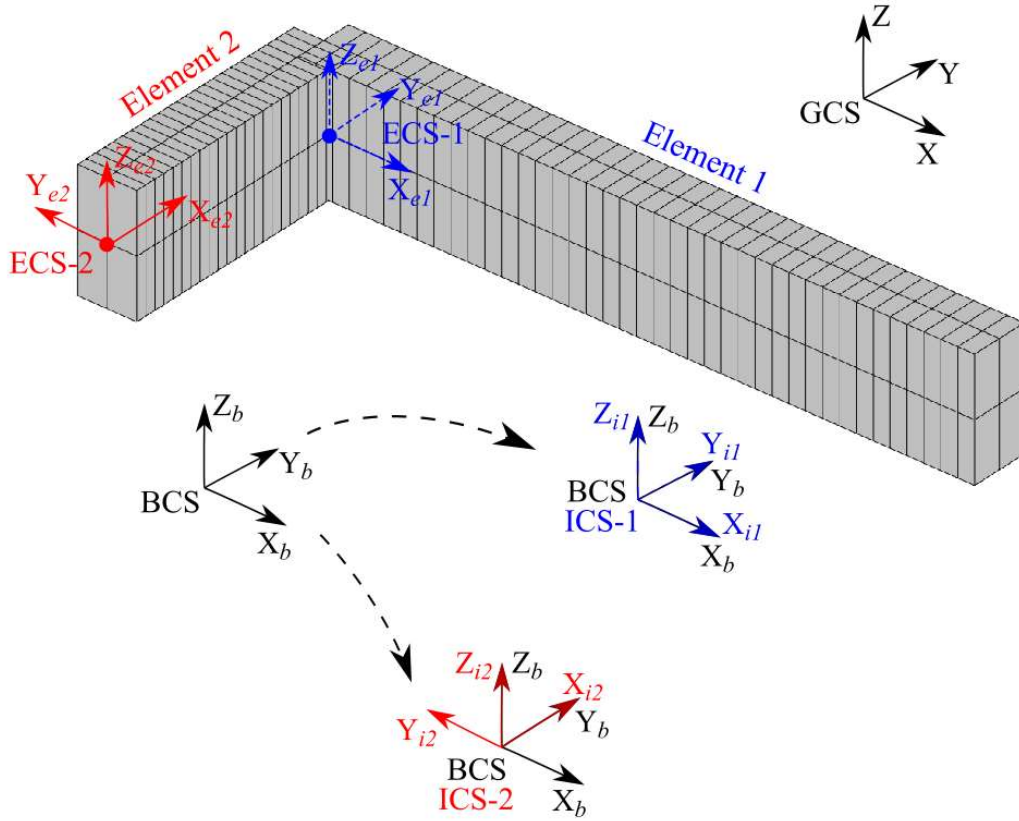


Figure 44. FE-FFR structural discontinuity (subscripts b , i and e correspond to BCS, ICS and ECS respectively)

5.2.1 FE/FFR Formulation

The element intermediate coordinate system (ICS) used in the FE/FFR formulation plays a crucial role in modeling structural discontinuities. The ICS concept is similar to that of the parallel axis theorem used in rigid body dynamics (Shabana, 2013). Consider the structure shown in Figure 44 that consists of two non-isoparametric beam elements forming an L-shaped structural discontinuity

at their intersection. For brevity, BCS, ECS and ICS in Figure 44 refer to body, element, and intermediate coordinate systems, respectively. It can be seen from Figure 44 that the orientation of ECS-1 (corresponding to element 1) is the same as that of the BCS, while the orientation of ECS-2 (corresponding to element 2) is different from that of the BCS. The shape functions of the non-isoparametric beam element used can correctly capture rigid body translation but, since this element uses infinitesimal rotations as nodal degrees of freedom, large finite rotations cannot be correctly modeled. In order to correctly capture the inertia of this structure and obtain correct rigid body kinematics, two ICSs are introduced at the BCS which are parallel to their respective ECS as shown in Figure 44. The nodal coordinates defined in the BCS corresponding to each of the two elements can be transformed into their respective ICSs using the $\bar{\mathbf{C}}^{ij}$ matrix used in Section 5.1.1. Using this transformation, the shape function matrix of the non-isoparametric beam element can be used to yield the correct position of the material points with respect to the ICS. The position of the material point obtained in the ICS can then be transformed to the BCS by using the constant transformation matrix \mathbf{C}^{ij} which is the transformation matrix that defines the ICS orientation with respect to the BCS as discussed in Section 5.1.1. Therefore, the use of the ICS concept allows modeling different types of geometric discontinuities (T-, V-, and L-sections) in the FE mesh, while correctly representing the rigid body kinematics, inertia and dynamics.

5.2.2 ANCF Finite Elements

In case of ANCF elements, handling structural discontinuities requires the use of a fundamentally different approach that involves gradient transformations that have a structure different from the orthogonal vector transformations (Shabana and Mikkola, 2003). To this end, an appropriate coordinate transformation matrix that exists between the body and element parameterizations must be used, and no intermediate coordinate systems are required because of the use of the ANCF

position vector gradients. The nodal coordinates defined with respect to the body parameterization can be transformed to coordinates with respect to the element parameterization as $\mathbf{e} = \mathbf{T}\mathbf{p}$, where \mathbf{e} and \mathbf{p} are the set of coordinates defined with respect to the element and body parameterizations, respectively, and the transformation \mathbf{T} can be written as

$$\mathbf{T} = \begin{bmatrix} \mathbf{I} & \mathbf{0} & \mathbf{0} & \mathbf{0} \\ \mathbf{0} & j_{1,1}\mathbf{I} & j_{2,1}\mathbf{I} & j_{3,1}\mathbf{I} \\ \mathbf{0} & j_{1,2}\mathbf{I} & j_{2,2}\mathbf{I} & j_{3,2}\mathbf{I} \\ \mathbf{0} & j_{1,3}\mathbf{I} & j_{2,3}\mathbf{I} & j_{3,3}\mathbf{I} \end{bmatrix} \quad (47)$$

where $j_{m,n} = \partial(\mathbf{S}_m \mathbf{e}_0) / \partial x_n$ are the components of the matrix of position vector gradients \mathbf{J}_0 defined at the reference configuration and \mathbf{S}_m is the m^{th} row of \mathbf{S} (Shabana and Mikkola, 2003).

The transformation \mathbf{T} only affects the gradient vector coordinates of the given node, not the position vector coordinates. Employing this method, the structural discontinuities can be modeled using the conventional FE assembly procedure. By doing so, the connection between two ANCF elements having a structural discontinuity at a given common node is taken into account employing a standard connectivity matrix of the FE mesh. For example, consider the structure depicted in Figure 45, which is the same as the one considered in the previous section. Without loss of generality, it is assumed that the BCS is parallel to the GCS. The structural discontinuity occurs at the shared node between the ANCF fully parameterized beam element 1 and element 2 as shown in Figure 45. It can be seen from Figure 45 that the orientation of the gradients in element 1 is the same as that of the BCS, whereas the orientation of the gradients of element 2 is rotated with respect to the shown BCS. In this case, the transformation matrix that transforms the coordinates from the body to element parameterization will be an identity matrix at the shared node for element 1. For element 2, the transformation matrix will depend on the direction cosines between the gradients at the shared node in element 2 and the BCS assuming that the set of gradient vectors at

the discontinuity node is an orthonormal set (no initial curvature). A similar procedure can be used for gradient deficient ANCF elements (Shabana and Maqueda, 2008).

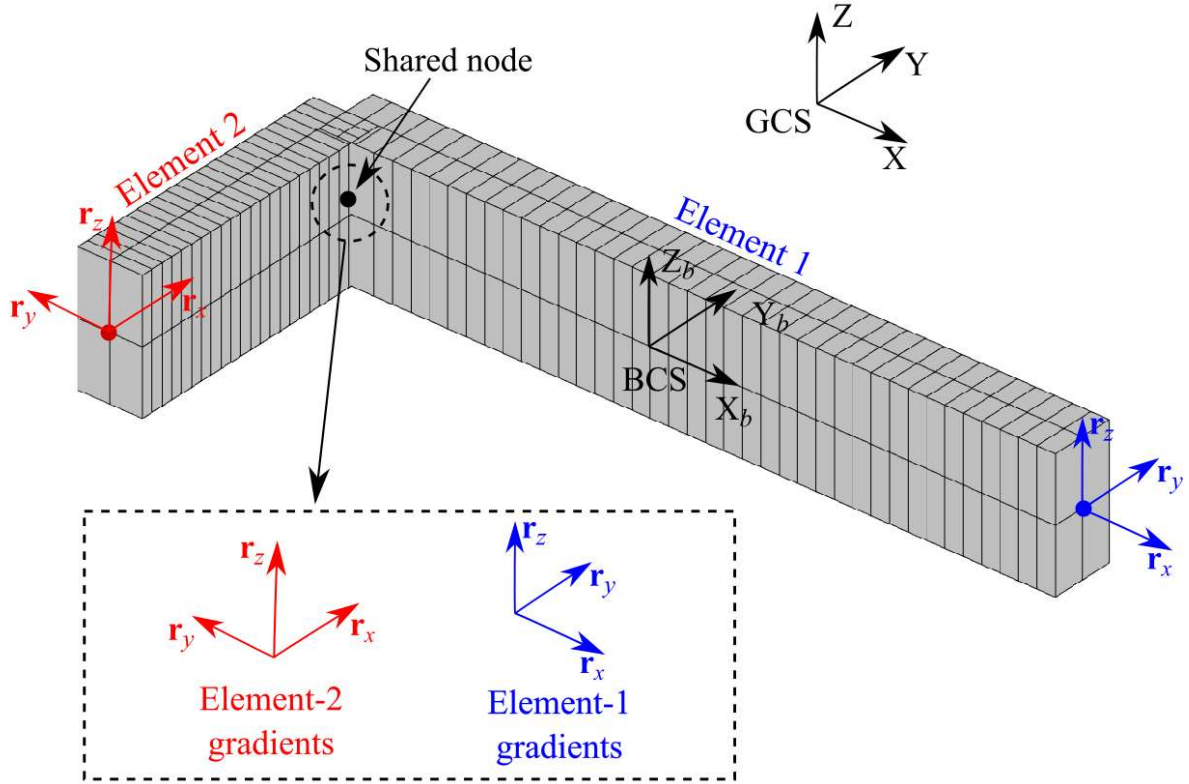


Figure 45. ANCF structural discontinuity

In this chapter, a new method for modeling structural discontinuities using ANCF elements is proposed. The proposed method generalizes the technique previously developed (Shabana and Mikkola, 2003) to structural discontinuities located at arbitrary points of an FE/ANCF mesh. Instead of directly applying the coordinate transformation $\mathbf{e} = \mathbf{T}\mathbf{p}$ to switch to the body coordinates, a constant structural discontinuity constraint Jacobian matrix is defined. This Jacobian matrix can be used to define a constant velocity transformation matrix that can be used to systematically eliminate dependent variables. This approach offers the generality and flexibility of

combining the structural discontinuity constraint equations with other constraint equations before switching to the body coordinates. By using this approach, structural discontinuities that occur at nodal locations of the FE/ANCF mesh can also be modeled, and therefore, the method previously developed in (Shabana and Mikkola, 2003) can be considered as a special case of the method proposed in this section.

In the method proposed in this section, a set of ANCF structural discontinuity algebraic constraint equations is developed. Since these algebraic constraint equations are linear, they and the associated dependent variables can be systematically eliminated at a preprocessing stage, leading to reduced order models that can be efficiently solved. In order to obtain the general set of constraint equations associated with structural discontinuities, the proposed method is composed of two steps. In the first step, two sets of coordinate lines, which represent geometric lines associated with the material fibers of the continuum body, are defined. The first set of coordinate lines referred to as $\bar{\mathbf{x}} = [\bar{x} \quad \bar{y} \quad \bar{z}]^T$ represents the element material fibers, whereas the second set of coordinate lines referred to as $\mathbf{x} = [x \quad y \quad z]^T$ represents the body material fibers. The set of coordinate lines \mathbf{x} are also referred to as *Cartesian coordinates* and serve as a unique standard for the FE mesh assembly, while the coordinate lines $\bar{\mathbf{x}}$ are simply referred to as *element coordinate lines*. Using these basic continuum mechanics concepts, the position field of a three-dimensional continuum body is defined as $\mathbf{r} = [r_1 \quad r_2 \quad r_3]^T$ and it can be written as a function of the element coordinate lines $\bar{\mathbf{x}}$ or as a function of the body coordinate lines \mathbf{x} . By using the chain rule of differentiation, one can write $(\partial \mathbf{r} / \partial \bar{\mathbf{x}}) = (\partial \mathbf{r} / \partial \mathbf{x})(\partial \mathbf{x} / \partial \bar{\mathbf{x}}) = (\partial \mathbf{r} / \partial \mathbf{x}) \mathbf{J}_b$, where \mathbf{J}_b is the Jacobian matrix that represents the transformation between the body coordinate lines and the element coordinate lines. Without loss of generality, the structural or body parameterization is defined

considering the reference configuration of the continuum body, and therefore, the Jacobian matrix of the body parametrization \mathbf{J}_b is identical to the matrix of the position vector gradients \mathbf{J}_0 defined in the body reference configuration. This tensor transformation can be rewritten in matrix form as follows:

$$\begin{bmatrix} \mathbf{r}_{\bar{x}} & \mathbf{r}_{\bar{y}} & \mathbf{r}_{\bar{z}} \end{bmatrix} = \begin{bmatrix} \mathbf{r}_x & \mathbf{r}_y & \mathbf{r}_z \end{bmatrix} \mathbf{J}_0 = \begin{bmatrix} \mathbf{r}_x & \mathbf{r}_y & \mathbf{r}_z \end{bmatrix} \begin{bmatrix} j_{11} & j_{12} & j_{13} \\ j_{21} & j_{22} & j_{23} \\ j_{31} & j_{32} & j_{33} \end{bmatrix} \quad (48)$$

where $j_{m,n}$ are the components of the matrix \mathbf{J}_0 . By adding an identity transformation for the ANCF nodal position vector, the preceding equation can be rewritten as

$$\left. \begin{aligned} \mathbf{r} &= \mathbf{r} \\ \mathbf{r}_{\bar{x}} &= j_{11}\mathbf{r}_x + j_{21}\mathbf{r}_y + j_{31}\mathbf{r}_z \\ \mathbf{r}_{\bar{y}} &= j_{12}\mathbf{r}_x + j_{22}\mathbf{r}_y + j_{32}\mathbf{r}_z \\ \mathbf{r}_{\bar{z}} &= j_{13}\mathbf{r}_x + j_{23}\mathbf{r}_y + j_{33}\mathbf{r}_z \end{aligned} \right\} \quad (49)$$

For a general node of an ANCF fully-parameterized element, the nodal coordinate vector associated with the element coordinate lines can be defined as $\mathbf{e} = [\mathbf{r}^T \quad \mathbf{r}_{\bar{x}}^T \quad \mathbf{r}_{\bar{y}}^T \quad \mathbf{r}_{\bar{z}}^T]^T$, whereas the nodal coordinate vector associated with the structural (body) parametrization can be given by $\mathbf{p} = [\mathbf{r}^T \quad \mathbf{r}_x^T \quad \mathbf{r}_y^T \quad \mathbf{r}_z^T]^T$. Therefore, as mentioned before in this section, one can write $\mathbf{e} = \mathbf{T}\mathbf{p}$, where \mathbf{T} is the transformation matrix previously defined. On the other hand, the matrix of position vector gradients defined by differentiation with respect to the body parameters can be written as $(\partial\mathbf{r}/\partial\mathbf{x}) = (\partial\mathbf{r}/\partial\bar{\mathbf{x}})(\partial\bar{\mathbf{x}}/\partial\mathbf{x}) = (\partial\mathbf{r}/\partial\bar{\mathbf{x}})\mathbf{J}_b^{-1} = (\partial\mathbf{r}/\partial\bar{\mathbf{x}})\mathbf{H}_b$, where $\mathbf{H}_b = \mathbf{J}_b^{-1}$. Assuming again that the Jacobian matrix of the body parametrization \mathbf{J}_b is identical to the matrix of the position vector gradients \mathbf{J}_0 defined in the body reference configuration, this inverse tensor transformation can be rewritten in matrix form as follows:

$$\begin{bmatrix} \mathbf{r}_x & \mathbf{r}_y & \mathbf{r}_z \end{bmatrix} = \begin{bmatrix} \mathbf{r}_{\bar{x}} & \mathbf{r}_{\bar{y}} & \mathbf{r}_{\bar{z}} \end{bmatrix} \mathbf{H}_0 = \begin{bmatrix} \mathbf{r}_{\bar{x}} & \mathbf{r}_{\bar{y}} & \mathbf{r}_{\bar{z}} \end{bmatrix} \begin{bmatrix} h_{11} & h_{12} & h_{13} \\ h_{21} & h_{22} & h_{23} \\ h_{31} & h_{32} & h_{33} \end{bmatrix} \quad (50)$$

where $h_{m,n}$ are the components of the matrix $\mathbf{H}_0 = \mathbf{J}_0^{-1}$. It follows that

$$\left. \begin{aligned} \mathbf{r}_x &= h_{11}\mathbf{r}_{\bar{x}} + h_{21}\mathbf{r}_{\bar{y}} + h_{31}\mathbf{r}_{\bar{z}} = (h_{11}\mathbf{S}_{\bar{x}} + h_{21}\mathbf{S}_{\bar{y}} + h_{31}\mathbf{S}_{\bar{z}})\mathbf{e} = \mathbf{S}_x\mathbf{T}\mathbf{p} \\ \mathbf{r}_y &= h_{12}\mathbf{r}_{\bar{x}} + h_{22}\mathbf{r}_{\bar{y}} + h_{32}\mathbf{r}_{\bar{z}} = (h_{12}\mathbf{S}_{\bar{x}} + h_{22}\mathbf{S}_{\bar{y}} + h_{32}\mathbf{S}_{\bar{z}})\mathbf{e} = \mathbf{S}_y\mathbf{T}\mathbf{p} \\ \mathbf{r}_z &= h_{13}\mathbf{r}_{\bar{x}} + h_{23}\mathbf{r}_{\bar{y}} + h_{33}\mathbf{r}_{\bar{z}} = (h_{13}\mathbf{S}_{\bar{x}} + h_{23}\mathbf{S}_{\bar{y}} + h_{33}\mathbf{S}_{\bar{z}})\mathbf{e} = \mathbf{S}_z\mathbf{T}\mathbf{p} \end{aligned} \right\} \quad (51)$$

where $\mathbf{S}_x = (h_{11}\mathbf{S}_{\bar{x}} + h_{21}\mathbf{S}_{\bar{y}} + h_{31}\mathbf{S}_{\bar{z}})$, $\mathbf{S}_y = (h_{12}\mathbf{S}_{\bar{x}} + h_{22}\mathbf{S}_{\bar{y}} + h_{32}\mathbf{S}_{\bar{z}})$, and $\mathbf{S}_z = (h_{13}\mathbf{S}_{\bar{x}} + h_{23}\mathbf{S}_{\bar{y}} + h_{33}\mathbf{S}_{\bar{z}})$.

By using these equations, one is able to write the gradient vectors of a given ANCF element as functions of the structural (body) vector of nodal coordinates. Therefore, considering two material points P^i and P^j belonging to the element i and j , respectively, one can write a set of structural discontinuity constraint equations for the connection of points P^i and P^j as follows:

$$\left. \begin{aligned} \mathbf{r}^i(P^i) - \mathbf{r}^j(P^j) &= \mathbf{0}, & \mathbf{r}_x^i(P^i) - \mathbf{r}_x^j(P^j) &= \mathbf{0}, \\ \mathbf{r}_y^i(P^i) - \mathbf{r}_y^j(P^j) &= \mathbf{0}, & \mathbf{r}_z^i(P^i) - \mathbf{r}_z^j(P^j) &= \mathbf{0} \end{aligned} \right\} \quad (52)$$

or equivalently

$$\left. \begin{aligned} \mathbf{S}^i\mathbf{T}^i\mathbf{p}^i - \mathbf{S}^j\mathbf{T}^j\mathbf{p}^j &= \mathbf{0}, & \mathbf{S}_x^i\mathbf{T}^i\mathbf{p}^i - \mathbf{S}_x^j\mathbf{T}^j\mathbf{p}^j &= \mathbf{0}, \\ \mathbf{S}_y^i\mathbf{T}^i\mathbf{p}^i - \mathbf{S}_y^j\mathbf{T}^j\mathbf{p}^j &= \mathbf{0}, & \mathbf{S}_z^i\mathbf{T}^i\mathbf{p}^i - \mathbf{S}_z^j\mathbf{T}^j\mathbf{p}^j &= \mathbf{0} \end{aligned} \right\} \quad (53)$$

Considering the vector of structural nodal coordinates $\mathbf{p}^k = \left[(\mathbf{p}^i)^T \quad (\mathbf{p}^j)^T \right]^T$ that appears in the

preceding equation, the structural discontinuity constraint Jacobian matrix can be written as

$$\mathbf{C}_{\mathbf{p}^k}^k = \begin{bmatrix} \mathbf{C}_{\mathbf{p}^i}^k & \mathbf{C}_{\mathbf{p}^j}^k \end{bmatrix} = \begin{bmatrix} \mathbf{S}^i\mathbf{T}^i & -\mathbf{S}^j\mathbf{T}^j \\ \mathbf{S}_x^i\mathbf{T}^i & -\mathbf{S}_x^j\mathbf{T}^j \\ \mathbf{S}_y^i\mathbf{T}^i & -\mathbf{S}_y^j\mathbf{T}^j \\ \mathbf{S}_z^i\mathbf{T}^i & -\mathbf{S}_z^j\mathbf{T}^j \end{bmatrix} \quad (54)$$

where \mathbf{C}^k denotes the vector of structural discontinuity constraint equations of Eq. 52 and 53 at node k . Since the structural discontinuity constraint equations are a set of linear algebraic equations grouped in the vector \mathbf{C}^k , the Jacobian matrix $\mathbf{C}_{\mathbf{p}}^k$ of this set of algebraic equations is constant, and therefore, the constraint equations and the associated dependent variables can be systematically eliminated at a preprocessing stage by developing an appropriate velocity transformation matrix. The use of the velocity transformation matrix offers the flexibility and generality of combining the structural discontinuity constraint equations with other constraint equations which are formulated in terms of the original element nodal coordinates. The basic idea of the method proposed for obtaining the structural discontinuity constraint equations is to define the gradients with respect to a unique set of coordinate lines (body coordinate lines) since in case of structural discontinuity the element gradients at a shared node that are defined with respect to two different sets of element coordinate lines cannot be simply equated.

5.3 MBS Equations of Motion

The equations of motion used in this chapter for the dynamic simulation of a vehicle system that consists of rigid, FE/FFR, and ANCF bodies are presented in this section. The differential/algebraic equations of motion are obtained using the principle of virtual work and the technique of Lagrange multipliers. The set of generalized coordinates used are $\mathbf{q} = [\mathbf{q}_r^T \quad \mathbf{q}_f^T \quad \mathbf{p}^T]^T$, where $\mathbf{q}_r = [\mathbf{q}_R^T \quad \mathbf{q}_\theta^T]^T$ are the rigid body translational and rotational coordinates collectively referred to as reference coordinates, \mathbf{q}_f represents the FE/FFR coordinates, and \mathbf{p} represents the vector of structural FE/ANCF coordinates. The equations of motion can be written as

$$\begin{bmatrix} \mathbf{M}_{rr} & \mathbf{M}_{rf} & \mathbf{0} & \mathbf{C}_{q_r}^T \\ \mathbf{M}_{fr} & \mathbf{M}_{ff} & \mathbf{0} & \mathbf{C}_{q_f}^T \\ \mathbf{0} & \mathbf{0} & \mathbf{M}_{pp} & \mathbf{C}_p^T \\ \mathbf{C}_{q_r} & \mathbf{C}_{q_f} & \mathbf{C}_p & \mathbf{0} \end{bmatrix} \begin{bmatrix} \ddot{\mathbf{q}}_r \\ \ddot{\mathbf{q}}_f \\ \ddot{\mathbf{p}} \\ \boldsymbol{\lambda} \end{bmatrix} = \begin{bmatrix} \mathbf{Q}_r + \mathbf{Q}_{v_r} \\ \mathbf{Q}_f + \mathbf{Q}_{v_f} \\ \mathbf{Q}_e \\ \mathbf{Q}_c \end{bmatrix} \quad (55)$$

where \mathbf{M}_{rr} and \mathbf{M}_{ff} are the mass matrices associated with the reference and FE/FFR deformation coordinates, respectively; \mathbf{M}_{rf} and \mathbf{M}_{fr} represent the inertia coupling between the FE/FFR reference and deformation coordinates; \mathbf{M}_{pp} is the mass matrix associated with the ANCF coordinates; \mathbf{C}_{q_r} , \mathbf{C}_{q_f} , and \mathbf{C}_p are the Jacobian matrices of the nonlinear MBS joint constraint equations associated, respectively, with the reference, FE/FFR deformation, and ANCF coordinates; $\boldsymbol{\lambda}$ is the vector of Lagrange multipliers; \mathbf{Q}_r , \mathbf{Q}_f , and \mathbf{Q}_e are the applied and elastic force vectors associated with the reference, FE/FFR deformation, and ANCF coordinates respectively; \mathbf{Q}_{v_r} and \mathbf{Q}_{v_f} are the Coriolis and centrifugal force vectors associated with the reference and FE/FFR deformation coordinates, respectively; and \mathbf{Q}_c is the quadratic velocity vector that arises from differentiating the constraint equations twice with respect to time.

For numerically solving the equations of motion, the *two-loop implicit sparse matrix numerical integration* (TLISMNI) method that utilizes the concept of coordinate partitioning and the second-order backward difference formula for time integration is used in this work (Aboubakr and Shabana, 2015). An important feature of TLISMNI is that it satisfies the constraint equations at the position, velocity, and acceleration levels. A component mode synthesis method is used for the FE/FFR model to reduce the size of the modal transformation matrix by eliminating insignificant high frequency modes. Furthermore, the concept of the *ANCF reference node* is used to model the rigid rim in the ANCF tire assembly. Using the ANCF reference node, linear constraint equations can be formulated for the tire-rim connection and the dependent variables in

the tire mesh can then be eliminated thus reducing the model dimensionality and the number of Lagrange multipliers needed in the dynamic analysis (Shabana, 2015A; Patel et al. 2016). As described in Chapter 2, the rigidity of the ANCF reference node is ensured by imposing six nonlinear constraint equations that ensure that its gradient vectors remain unit orthogonal vectors in order to define an orthonormal rigid body coordinate system.

5.4 Numerical Results and Discussion

This section presents and discusses two simple ANCF pendulum problems and a complex off-road vehicle model that includes flexible ANCF tires and FE/FFR chassis in order to demonstrate the use of the new velocity transformation-based approach introduced in Section 5.2.2 for modeling structural discontinuities in the analysis of a complex vehicle model with flexible chassis and tires without the need for co-simulation.

5.4.1 L-shaped Beam and Y-shaped Plate Pendulums

In order to demonstrate the implementation of the new ANCF approach discussed in Section 5.2.2 for modeling structural discontinuities, beam and plate pendulum models are used in this section. The beam model, which is an L-shaped pendulum model shown in Figure 46, consists of two ANCF fully parameterized beam elements that are connected at a structural discontinuity node. Three beam pendulum models are considered in this numerical example: rigid body, ANCF with modulus of elasticity $E = 2 \times 10^{12}$ Pa, and ANCF with modulus of elasticity $E = 2 \times 10^7$ Pa. The length, width, and height of the beams are 1m, 0.1m, and 0.1m, respectively. A density $\rho = 1000$ kg/m³ and Poisson's ratio $\nu = 0$ are assumed. Figure 47 shows the time evolution of the pendulum tip vertical position for the three models. As can be seen from Figure 47, the rigid body and stiff ANCF pendulum models are overlapping, whereas there is some difference in the results of the

soft ANCF pendulum model. The soft ANCF pendulum, however, follows a similar trend as that exhibited by the other two models. In order to examine the results of the new implementation, Figure 48 compares two scalar quantities and their difference at the structural discontinuity node of the ANCF model with $E = 2 \times 10^7$ Pa. These scalar quantities are $\mathbf{r}_{x1}^T \mathbf{r}_{x2}$ and $\mathbf{r}_{x1}^T \mathbf{r}_{z1}$, where the subscript $\alpha\beta$ refers to the α coordinate line on element β . The scalar quantity $\mathbf{r}_{x1}^T \mathbf{r}_{x2}$ corresponds approximately to the cosine of the angle between the two beams, whereas $\mathbf{r}_{x1}^T \mathbf{r}_{z1}$ corresponds to the engineering shear strain at the structural discontinuity node. It is shown in Figure 48 that $\mathbf{r}_{x1}^T \mathbf{r}_{x2}$ and $\mathbf{r}_{x1}^T \mathbf{r}_{z1}$ overlap and their difference is identically zero throughout the simulation.

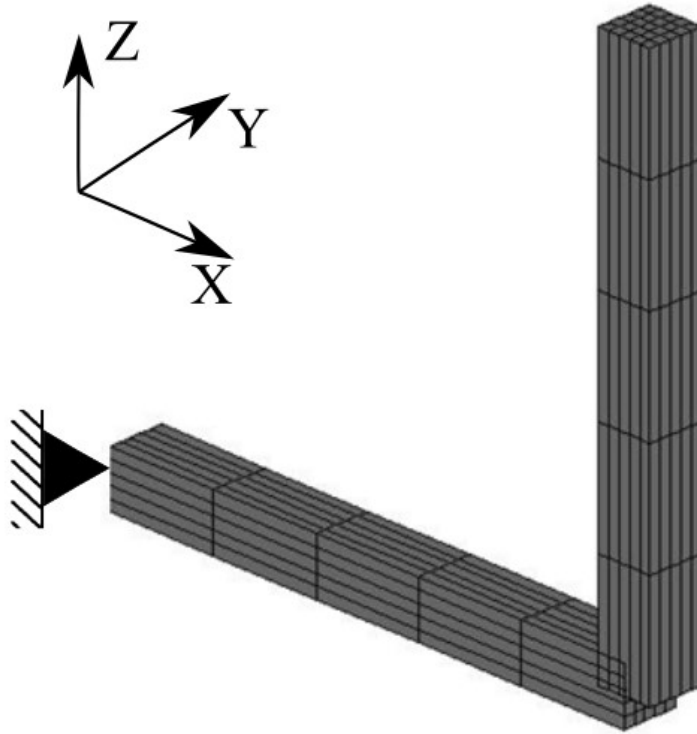


Figure 46. L-shaped beam pendulum with structural discontinuity

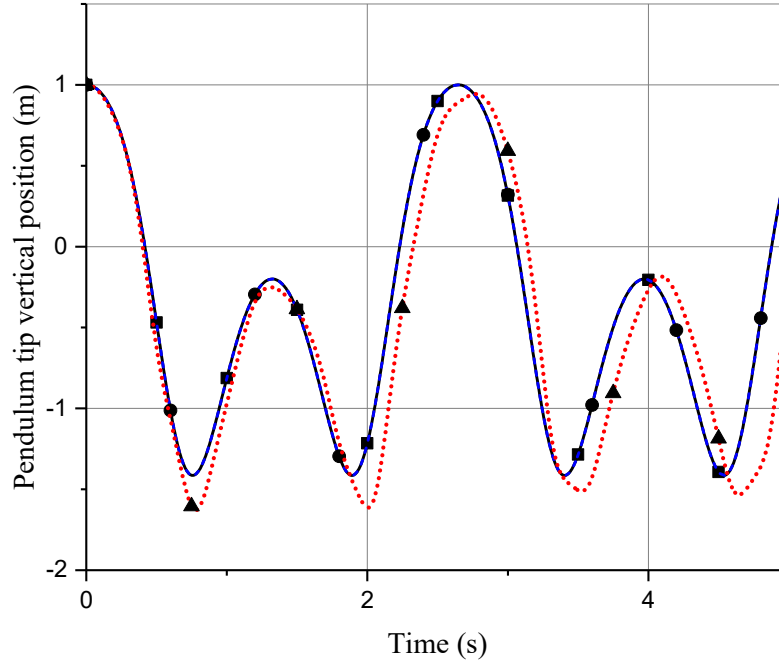


Figure 47. L-shaped beam tip vertical position: ANCF and rigid body model comparison (

—■— Rigid; - -●- - ANCF ($E = 2 \times 10^{12}$ Pa); ···▲··· ANCF ($E = 2 \times 10^7$ Pa))

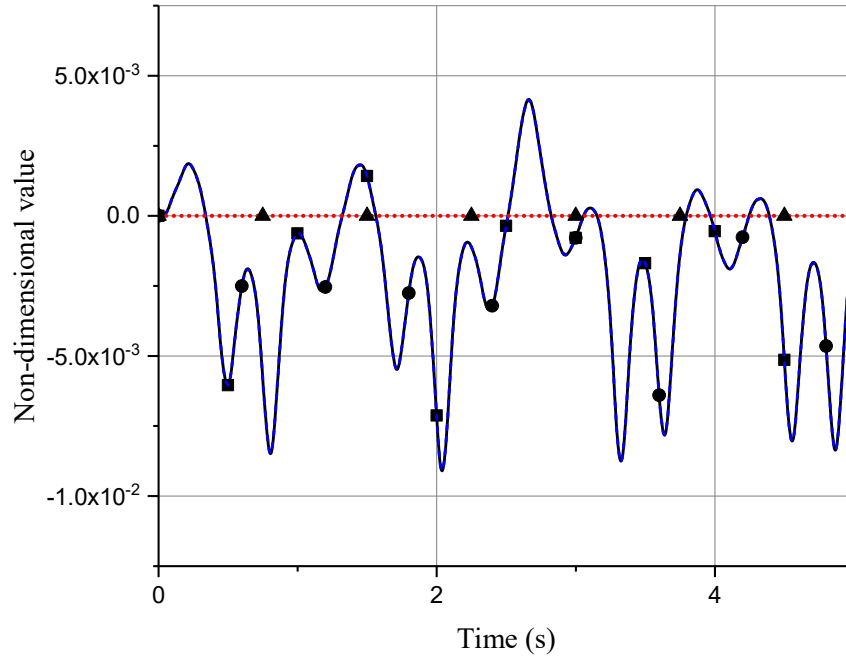


Figure 48. ANCF L-shaped beam engineering shear strain and cosine of angle at structural

discontinuity (—■— $\mathbf{r}_{x_1}^T \mathbf{r}_{x_2}$; - -●- - $\mathbf{r}_{x_1}^T \mathbf{r}_{z_1}$; ···▲··· $\mathbf{r}_{x_1}^T \mathbf{r}_{x_2} - \mathbf{r}_{x_1}^T \mathbf{r}_{z_1}$)

The plate/shell model consists of three fully parameterized ANCF plate/shell elements connecting at common structural discontinuity nodes and making a Y-shaped plate structure as shown in Figure 49. The two angled plates connect to the horizontal plate at a 45° angle measured from the horizontal plane. Figure 50 compares the right tip vertical position of the upper angled plate of a rigid body model to an ANCF model with $E = 2 \times 10^{12}$ Pa. The length, width and height of the plates are 1m, 1m, and 0.1m respectively. A density $\rho = 1000$ kg/m³ and Poisson's ratio $\nu = 0$ are used for the ANCF plate pendulum. As can be seen from Figure 50, even in this case, the rigid body and stiff ANCF pendulum models produce the same results, thus demonstrating the effectiveness of the proposed ANCF approach for modeling structural discontinuities.

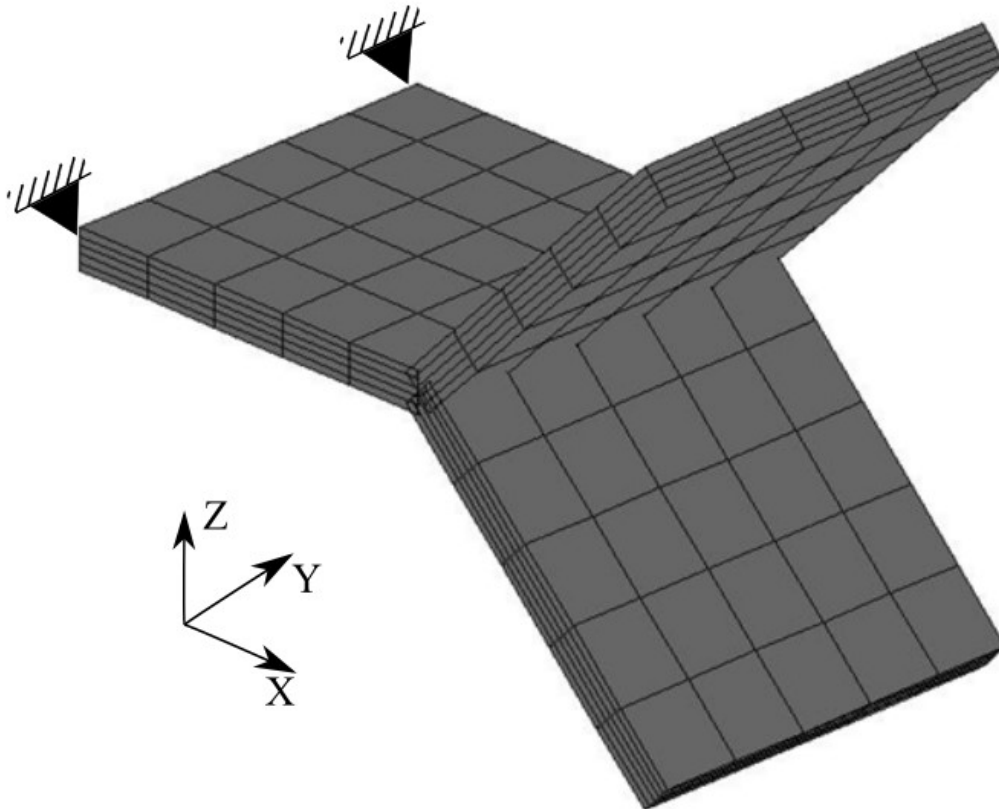


Figure 49. Y-shaped plate/shell pendulum model

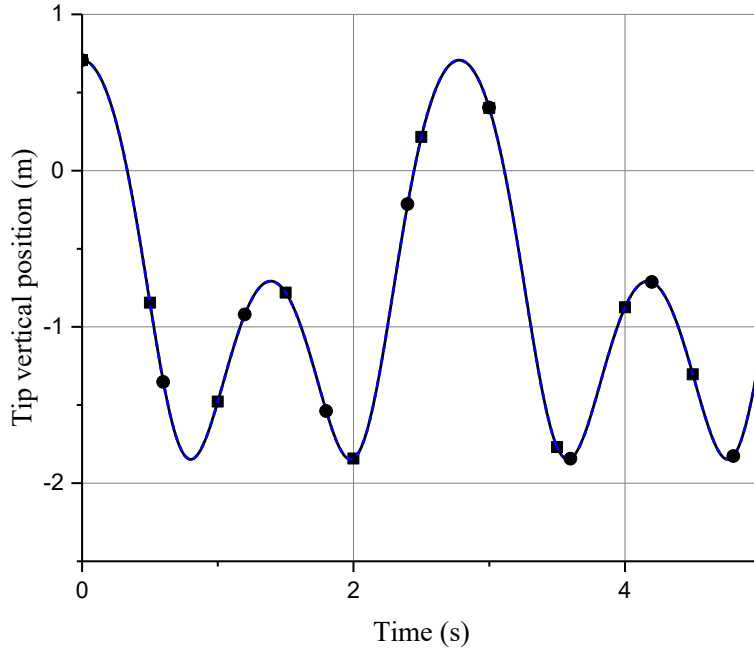


Figure 50. Y-shaped plate/shell pendulum tip vertical position: ANCF and rigid body model

comparison (—■— Rigid; - -●- - ANCF $E = 2 \times 10^{12}$ Pa)

5.4.2 Wheeled Vehicle Model

An off-road four-wheel drive vehicle model, HMMWV model shown in Figure 51, is considered as a numerical example in this section. A MBS model with a detailed suspension model was developed. The chassis and tires are considered flexible bodies in this MBS vehicle model. The chassis is modeled using the FE/FFR formulation whereas the tires are modeled using ANCF elements. Two types of flexible tires that include a pneumatic tire and an airless (non-pneumatic) tire are considered and the results obtained using these distributed inertia and elasticity tire models are compared with a rigid brush-type tire model.



Figure 51. Off-road wheeled vehicle model

5.4.2.1 MBS Vehicle Model

The vehicle model considered in this numerical example is a four-wheel drive vehicle capable of operating both on-road and off-road. The vehicle has a 190-horsepower engine, a double ‘A’ arm suspension with coil springs and double-acting shock absorbers and a recirculating ball, worm and nut based power assisted steering. The gross operating mass of the vehicle can vary; however, a good estimate of the vehicle curb mass is approximately 2500 kg. The maximum vehicle on-road speed is around 113 km/h. For simplicity, powertrain dynamics are not considered in the MBS model used in this numerical example. The steering system is modeled using a rack-pinion system. The vehicle subsystems like suspension, car-body, chassis, and tires are modeled in detail using several rigid and deformable bodies. Table 18 shows the body inertia of the vehicle components, whereas Tables 19 and 20 show the different types of ideal and compliant joints used in the model.

Table 18. Vehicle inertia properties

Components	Mass (kg)	I_{xx} (kg.m ²)	I_{yy} (kg.m ²)	I_{zz} (kg.m ²)
Chassis	708.35	156.83	1647.4	1767.3
Car body	1378.18	712.38	1952.25	2358.16
Front sub-frame	50.000	1.0000×10^{-6}	1.0000×10^{-6}	1.0000×10^{-6}
Rear sub-frame	45.359	2.9264×10^{-4}	2.9264×10^{-4}	2.9264×10^{-4}
Front left and right suspensions				
Upright	3.6382	4.0800×10^{-2}	4.2300×10^{-2}	8.3400×10^{-3}
Upper arm	5.4431	2.3300×10^{-2}	3.6100×10^{-2}	1.3200×10^{-2}
Lower arm	16.329	0.14688	0.23163	0.11852
Upper strut	5.0000	1.0000×10^{-6}	1.0000×10^{-6}	1.0000×10^{-6}
Lower strut	5.0000	1.0000×10^{-6}	1.0000×10^{-6}	1.0000×10^{-6}
Tire	68.039	1.1998	1.7558	1.1998
Tierod	0.5545	5.7854×10^{-3}	5.7854×10^{-3}	1.7745×10^{-5}
Tripot	1.9851	1.1019×10^{-3}	1.1019×10^{-3}	8.1390×10^{-4}
Drive shaft	4.2175	0.16599	0.16599	6.9283×10^{-4}
Spindle	1.1028	4.7790×10^{-4}	4.7790×10^{-4}	4.9628×10^{-4}
Rear left and right suspensions				
Upright	3.6382	4.0800×10^{-2}	4.2300×10^{-2}	8.3400×10^{-3}
Upper arm	5.9320	0.068400	0.091400	0.024000
Lower arm	16.287	0.29036	0.51811	0.23229
Upper strut	0.45359	2.9264×10^{-4}	2.9264×10^{-4}	2.9264×10^{-4}
Lower strut	0.45359	2.9264×10^{-4}	2.9264×10^{-4}	2.9264×10^{-4}
Tire	68.039	1.1998	1.7558	1.1998
Tierod	2.0412	4.2200×10^{-2}	4.2200×10^{-2}	1.9000×10^{-4}
Tripot	2.0307	1.1383×10^{-3}	1.1383×10^{-3}	8.4254×10^{-4}
Drive shaft	6.0495	0.24565	0.24565	1.4463×10^{-3}
Spindle	1.5046	7.7539×10^{-4}	7.7539×10^{-4}	9.2387×10^{-4}

Table 19. Ideal joints used in vehicle model

Joint type	Number of joints
Spherical/ball	25
Revolute/pin	16
Rigid/bracket	4
Cylindrical	8
Relative angular velocity	5
Gear	8
Rack pinion	1

Table 20. Compliant joint elements used in vehicle model

Joint type	Number of elements
Bushing	4
Bearing	16

Figure 52 shows a detailed view of the suspension system and some driveline components used in this model. Three different types of tires are used with the model, these include rigid brush-type tire, FE/ANCF pneumatic tire, and FE/ANCF airless tire. The computer implementation of the new approach proposed in this chapter in Section 5.2.2 for the treatment of the structural discontinuities was used in the analysis of the ANCF airless tire model developed in this chapter.

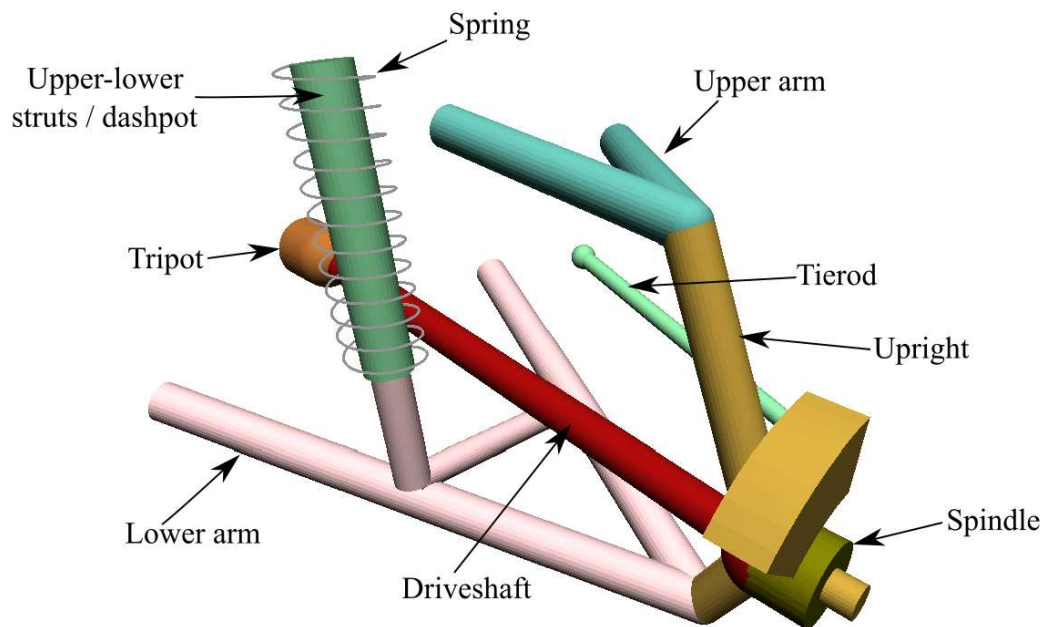


Figure 52. Front left suspension close-up

For the assembly of the vehicle model, four subsystems are considered: car body, chassis, suspension, and wheels. The wheels are connected to the spindles (suspension component), and the spindle is connected to the upright using revolute joints. A component called the subframe

connects the suspension, chassis and car body. The chassis is connected to the front and rear subframes at the NDRC locations shown in Figure 53 using bearing elements. In this chapter, NDRC is an abbreviation for **n**odal **d**isplacement **r**eference **c**onditions, which refer to the locations on the chassis where the node displacements are constrained in order to achieve a unique displacement field for the FE/FFR chassis mesh. Furthermore, the car body is also connected to the sub-frames at the same locations as that of the chassis using bearing elements. The upper and lower arms of the suspension shown in Figure 52 are connected to their respective sub-frame using revolute joints.

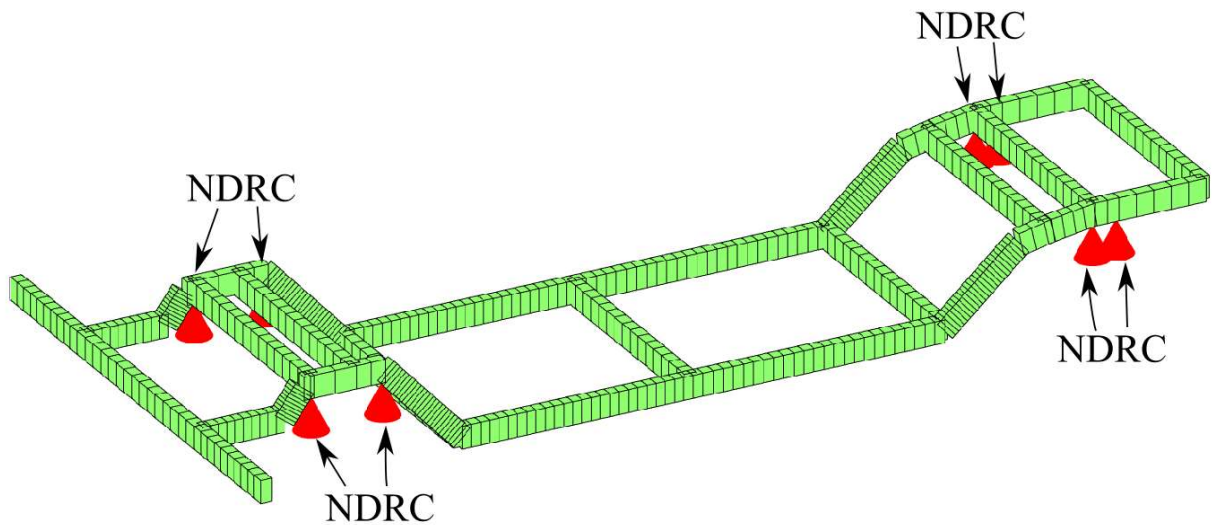


Figure 53. FFR chassis mesh (NDRC: nodal displacement reference conditions)

5.4.2.2 Flexible Subsystems: Chassis and Tires

The FE/FFR method is used to model the vehicle chassis which is meshed using 435 non-isoparametric three-dimensional beam elements with displacement and rotations as nodal coordinates. The shape function matrix for this non-isoparametric beam element is given in Appendix C.1. The material parameters considered are modulus of elasticity $E = 2.1 \times 10^{11}$ Pa, Poisson ratio $\nu = 0.33$, and mass density $\rho = 7200$ kg/m³. The cross-section is assumed to be

rectangular with width $w = 0.05$ m and height $h = 0.1$ m. The FE mesh and the applied reference conditions are shown in Figure 53. As shown in this figure, the reference conditions are selected to constrain the x , y and z nodal displacement at 8 nodes/points which represent joint locations between the vehicle suspension subsystem and chassis. The dimension of the chassis model is reduced by eliminating high-frequency modes and keeping the first 15 modes in the model. Modal damping is used in order to account for the dissipation due to structural damping. A damping ratio of 1% is used for the first 5 modes and a damping ratio of 5% is used on the remaining higher frequency modes in order to damp out insignificant high-frequency oscillations and improve the computational efficiency of the model. The first five modes of the chassis are shown in Figure 54, while Table 21 shows the frequencies associated with the 15 modes of the chassis.

Table 21. Chassis frequencies

Mode number	Frequency (Hz)
1	30.9
2	65.35
3	70.48
4	74.27
5	78.23
6	82.08
7	91.98
8	95.38
9	97.21
10	99.28
11	116.21
12	121.45
13	129.75
14	137.83
15	148.87

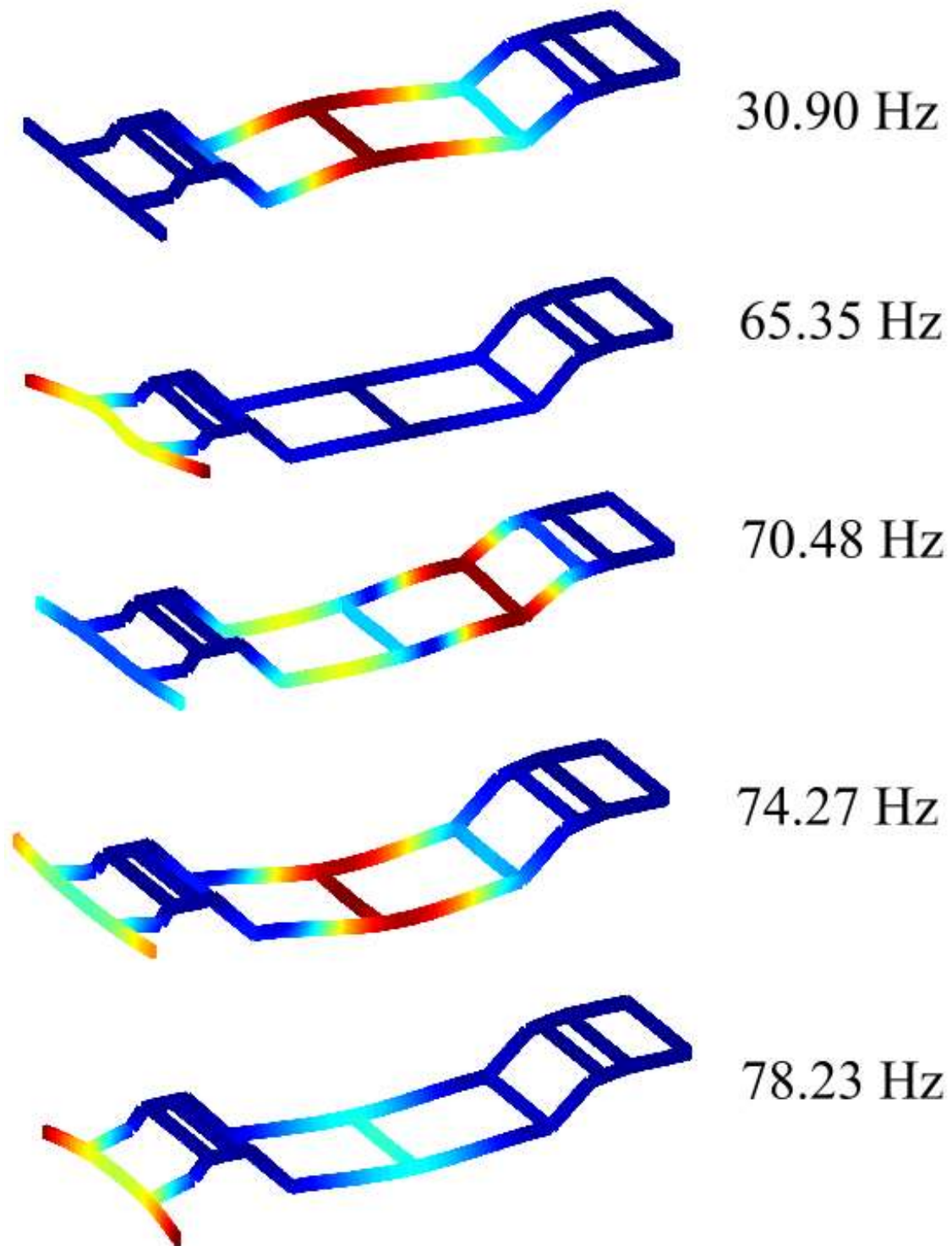


Figure 54. FFR chassis first five mode shapes and frequencies

ANCF fully-parameterized plate/shell elements, on the other hand, are used to model the pneumatic and airless tires. The 36-element pneumatic tire is shown in Figure 55, while the 25-element airless tire is shown in Figure 56. The material properties selected are $\rho = 1500 \text{ kg/m}^3$, $E = 5 \times 10^7 \text{ Pa}$, and $\nu = 0$. The air-pressure considered in the pneumatic tire is 250 kPa. The tire/ground contact penalty stiffness, damping, and coulomb friction coefficients are selected to be $k = 5 \times 10^4 \text{ N/m}$, $c = 4 \times 10^3 \text{ N.s/m}$, and $\mu = 0.8$, respectively. More details on the ANCF tire/ground contact formulation can be found in the Chapter 2.

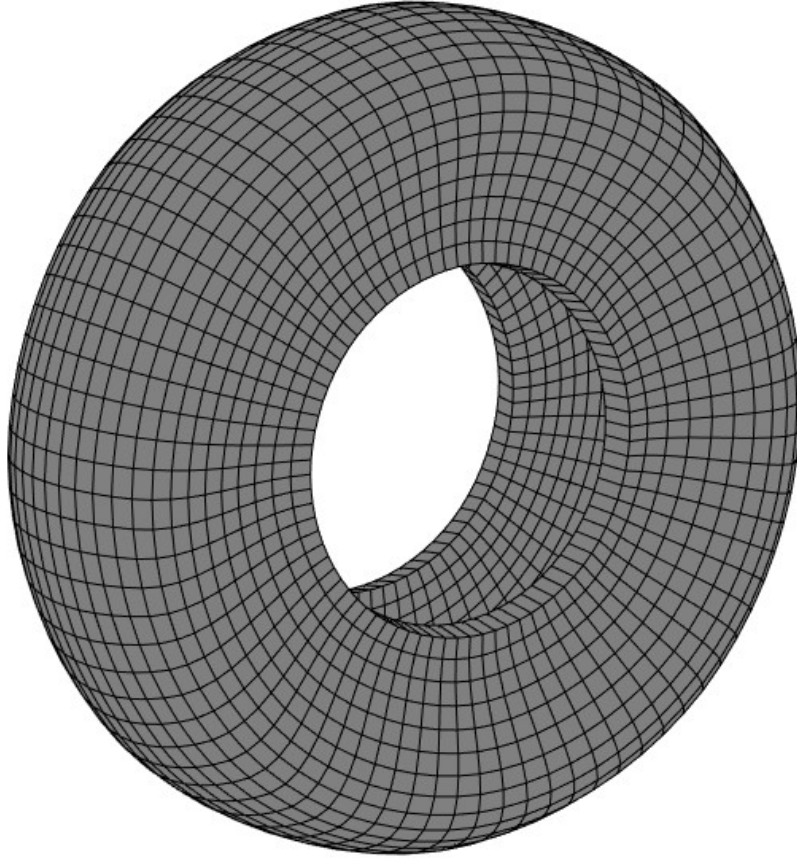


Figure 55. ANCF pneumatic tire

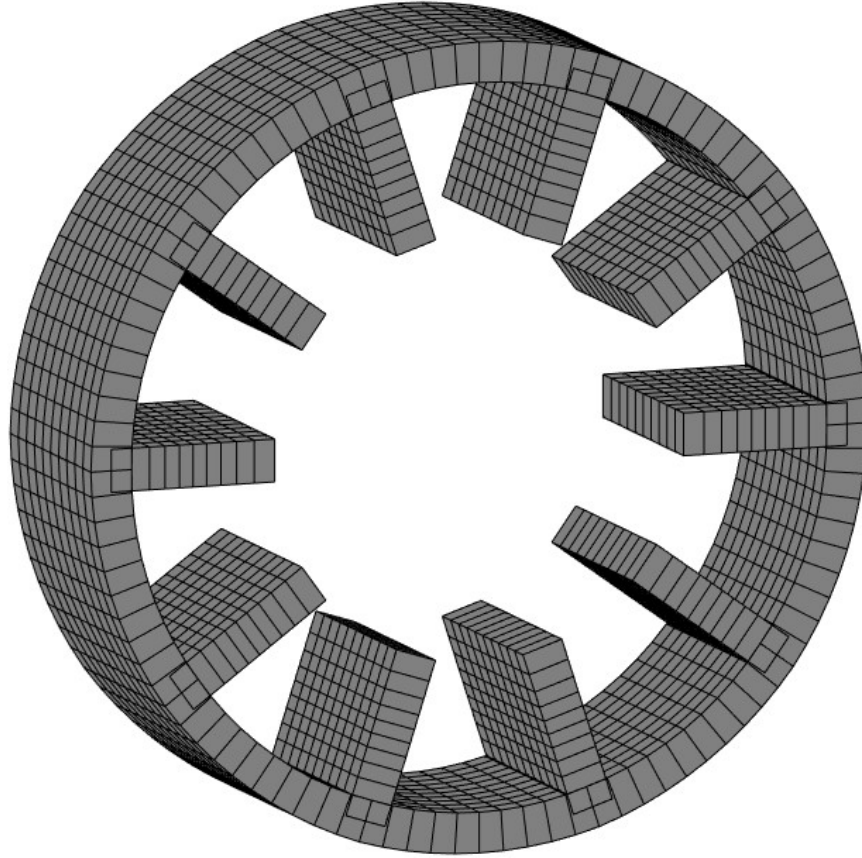


Figure 56. ANCF airless tire

Finally, a new radial damping model for the pneumatic tire is introduced wherein the relative velocity between the tire material point and the ANCF reference node that is used to model the rim is used in the formulation of the damping force as shown in Figure 57. This type of damping is introduced in the model to simulate the effect of the more realistic material damping that would occur in the tire structure. However, using this type of damping, one can relate the damping coefficient to radial damping used in several non-FE based ring type tire models which are parametrized using test data. The relative velocity between the tire material point and the ANCF reference node, \mathbf{v}_r , is calculated and its projection on the outward normal to the tire surface at that material point is used in the damping force expression. Hence, the generalized damping forces

can be written as $\mathbf{Q}_d = -\int_s \mathbf{S}^T c(\mathbf{v}_r^T \mathbf{n}) \mathbf{n} ds$, where c is a damping coefficient, \mathbf{S} is the matrix of shape functions, \mathbf{n} is the outward normal to the tire surface as shown in Figure 57, and s is the tire surface area. The generalized damping forces used in this chapter are distributed forces calculated from integration over the tire surface area.

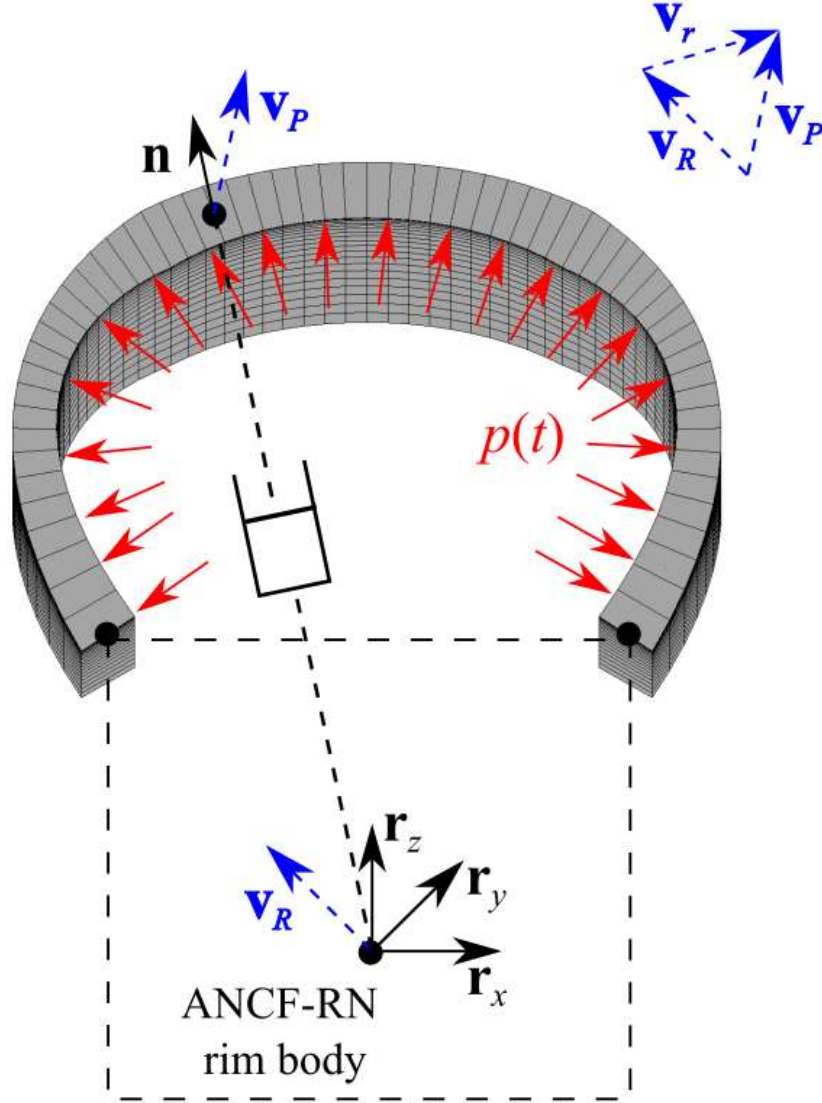


Figure 57. Distributed radial damping model (ANCF-RN: ANCF reference node)

Furthermore, this damping formulation does not affect the ability of the ANCF mesh to correctly exhibit rigid body motion since the relative velocity of the material point with respect to the ANCF rim node instead of its absolute velocity is used in the formulation of the damping force. The tire edges are clamped to the rim using linear constraints at the preprocessing stage, hence removing any rigid body motion between the tire and its respective rim reference node (Shabana, 2015A). A damping coefficient of $c = 2 \times 10^4 \text{ N.s/m}$ was used with the pneumatic tire model in the numerical model. Adding the damping to the tire model significantly improved its computational efficiency and improved the quality of the results.

5.4.2.3 Comparative Study

In order to compare the response of different tire models considered in this chapter as well as the vehicle response, the off-road wheeled vehicle model described in Section 5.4.2.1 is made to traverse several curb-like bumps. The three vehicle models used in this analysis have the same kinematic constraints and model topology. The models with the airless ANCF tire, pneumatic ANCF tire, and brush tire will be henceforth referred to as airless, pneumatic, and brush models respectively. The topology of the test track, shown in Figure 58, can be used to assess vehicle durability and the noise-vibration-harshness (NVH) response of the vehicle. The vehicle is allowed to settle initially, and then driving moments are applied to the wheels from 0.5s to 8.5s, after which the driving moments are removed, and the vehicle is allowed to decelerate. The vehicle reaches a maximum velocity of around 17 km/h during the 15s simulation. Figure 59 shows the chassis longitudinal velocity of the three vehicle models. Figure 60 shows the chassis longitudinal displacement of the three vehicle models. There are some differences in the vehicle longitudinal displacement due to the different rolling resistance coefficients of the tires that are in turn

dependent on the tire geometry and the resulting contact patch as well as the normal contact force distribution.

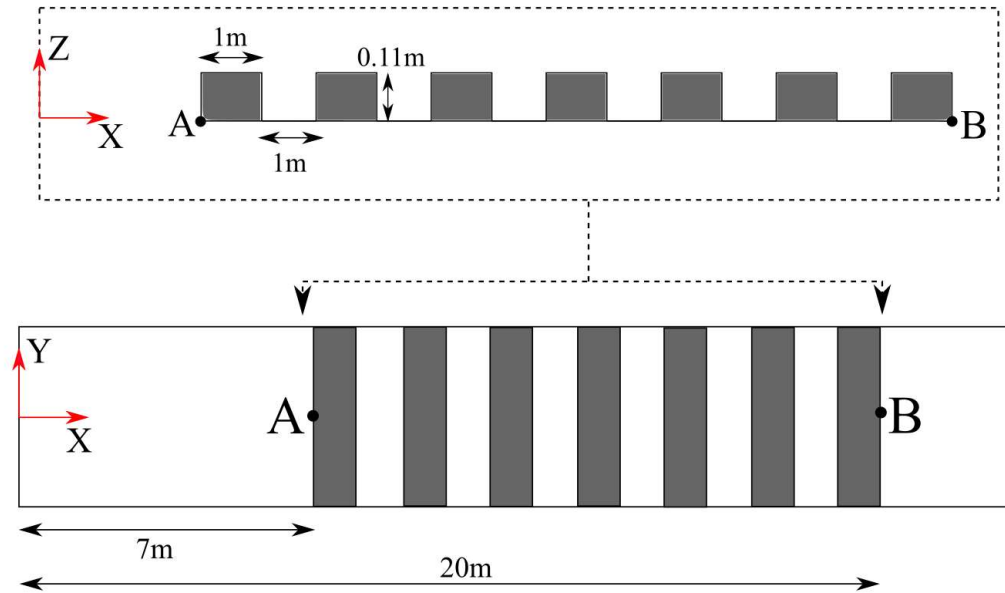


Figure 58. Durability vehicle simulation test track

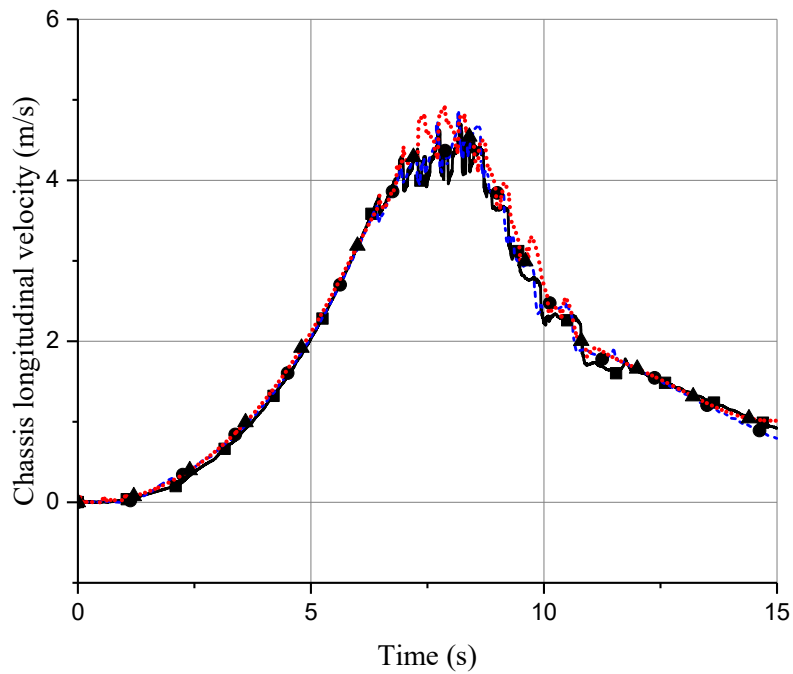


Figure 59. Chassis longitudinal velocity (—■— Airless; - - ● - - Pneumatic; ····▲···· Brush)

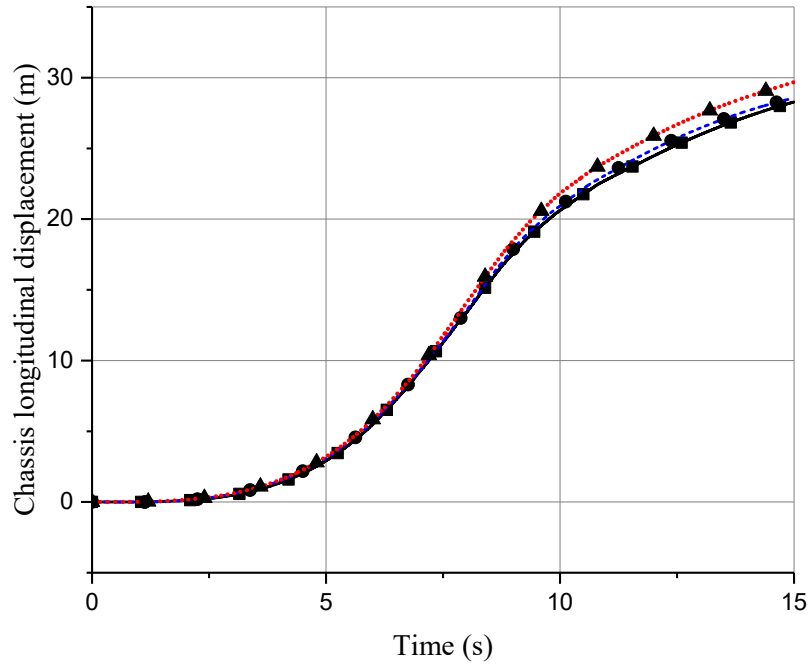


Figure 60. Chassis longitudinal displacement (—■— Airless; - -●- - Pneumatic;▲..... Brush)

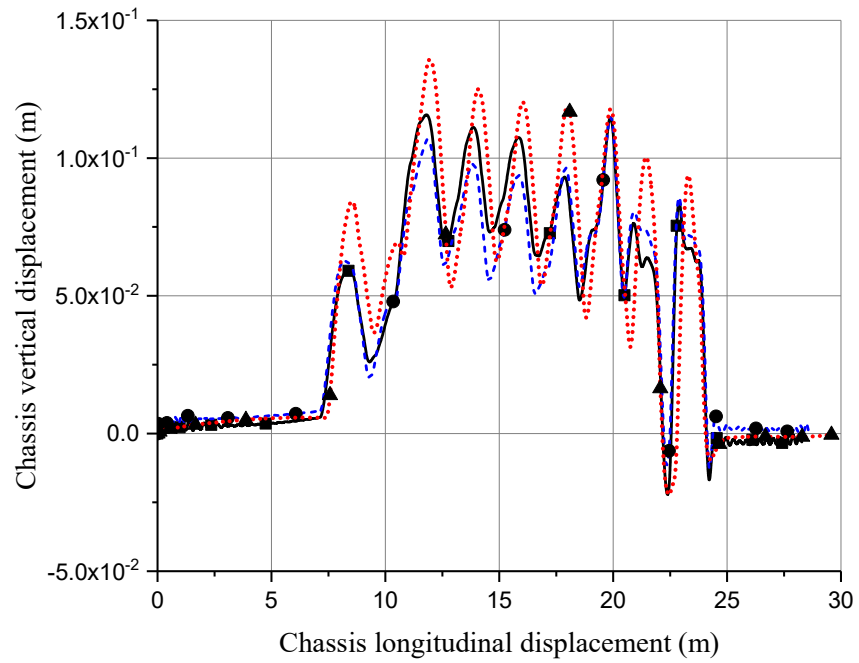


Figure 61. Chassis vertical displacement (—■— Airless; - -●- - Pneumatic;▲..... Brush)

Figure 61 shows the vertical displacement of the chassis reference. It can be noted from Figure 61 that, objectively, the vertical motion of the chassis frame of reference is quite similar for all three tire models. The chassis vertical displacement for the brush tire model is slightly larger than the FE/ANCF tire models since the brush tire model is based on a rigid tire assumption with a flexible contact patch, and leads to larger force transmission, hence slightly larger vibration amplitude of the chassis which is modeled as a sprung mass. Figure 62 shows the vertical displacement of the front left spindle as the suspension subsystem traverses the seven curb-like bumps in the test track. It can be noted from Figure 62 that the upward displacement due to a bump in case of the brush tire model occurs with a slight delay when compared to that of the FE/ANCF tire models. The reason for this phenomenon is that the brush tire model has a single contact point directly below the wheel center, hence the bump is only detected by the brush tire model when the brush tire center coincides with the start of the bump. In case of the FE/ANCF tires, since the contact detection is done for the elements near the ground while accounting for the variation in the ground geometry due to the bumps, the FE tires can detect the sudden change in ground geometry away from wheel center with much higher accuracy than the brush tire model. However, it must be noted that the brush tire model is typically used in ride quality simulations instead of NVH-type durability simulations. Figures 63 and 64 show the strains in the front right airless and pneumatic tires as they come into contact with the second bump of the test track, respectively. Along with examining the dynamic events occurring in the flexible tires, the chassis that is modeled using the FE/FFR approach can be analyzed for deformation and stress hot spots in order to improve its design or simply ensure that stresses remain within the material yield limit when the model is tested under certain external excitations and loads. Figure 65 shows the chassis total deformation for the dynamic event of the vehicle front tires passing over the second bump.

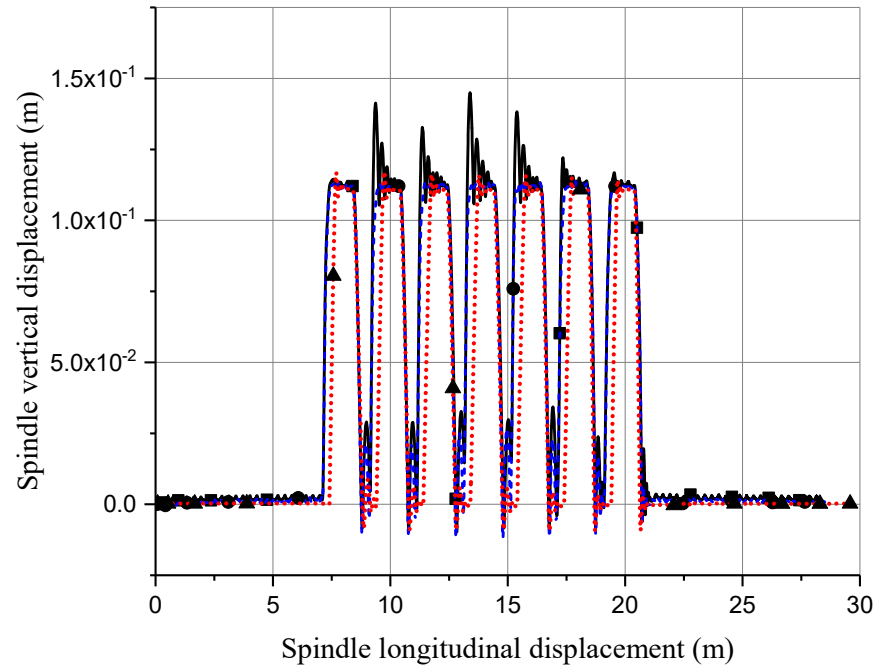


Figure 62. Front left spindle vertical displacement (—■— Airless; - - ● - - Pneumatic; . . . ▲ . . . Brush)

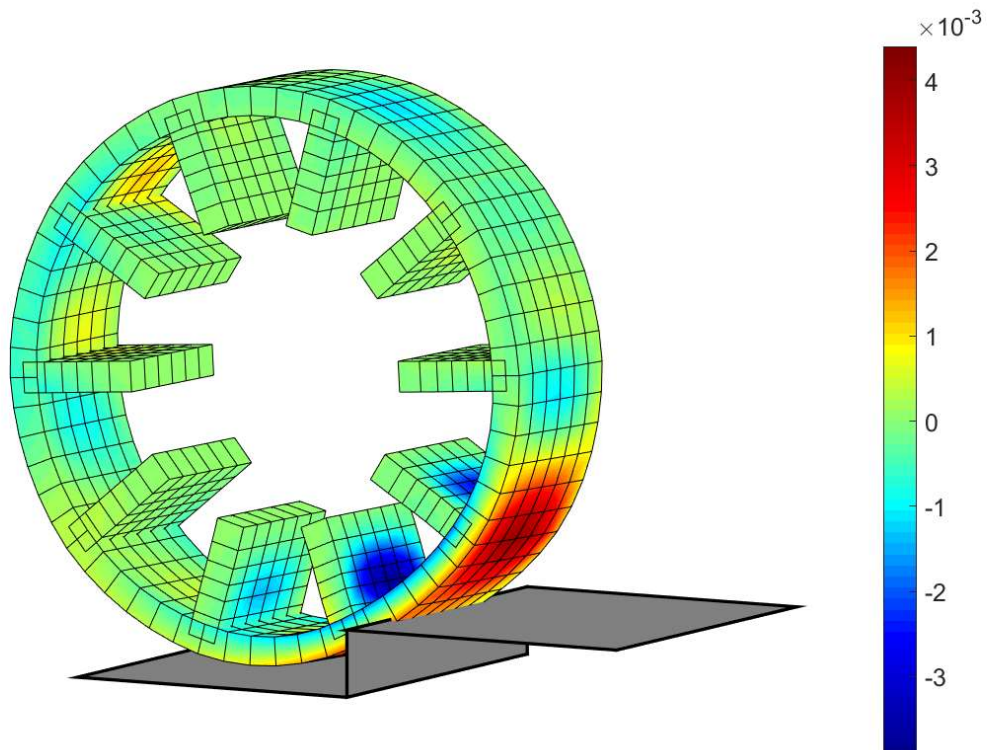


Figure 63. Airless tire hitting second bump with ϵ_{yy} strain contours

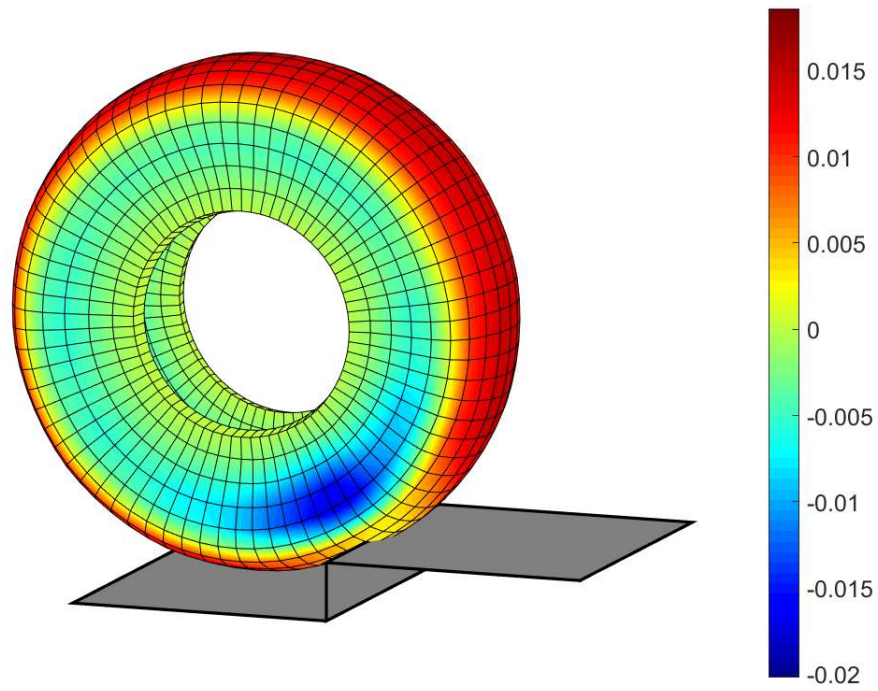


Figure 64. Pneumatic tire hitting second bump with ϵ_{yy} strain contours

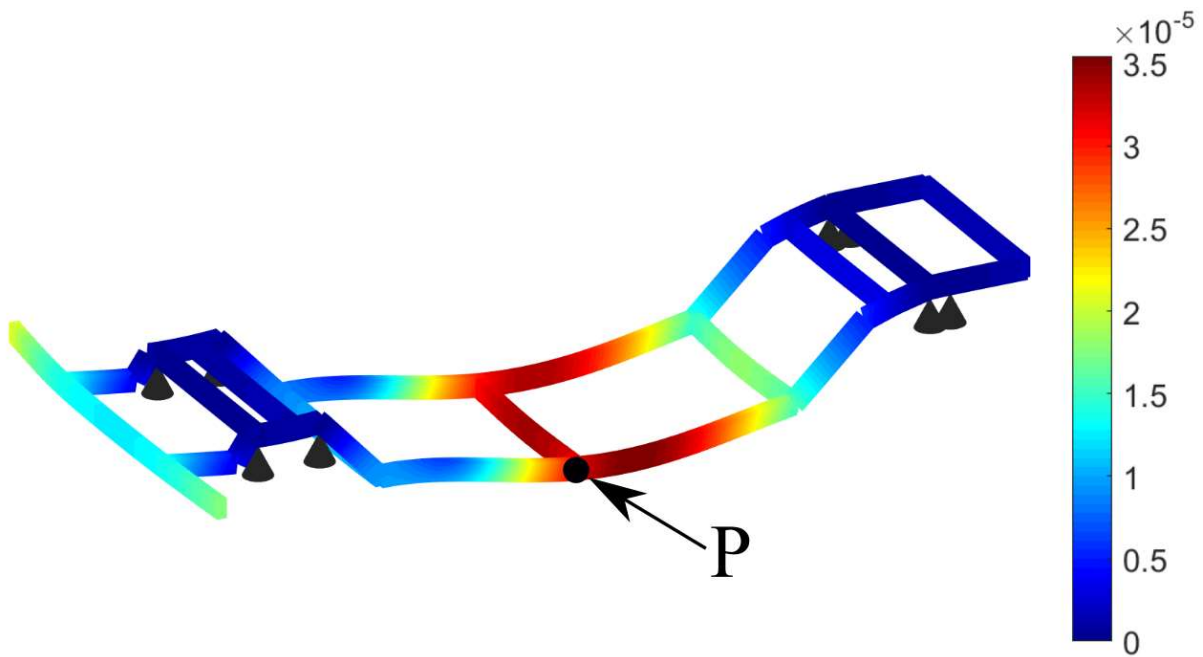


Figure 65. FFR chassis total deformation instance during dynamic simulation (with deformation contours)

Figure 66 shows the vertical deformation time history of point P shown in Figure 65. Since the deformation data shown in Figure 66 contain some high frequencies, it can be harder to correlate it with the vehicle overall motion, for this reason, Figure 67 shows the vertical deformation of chassis point P after applying a low-pass filter with a cut-off frequency of 3.33 Hz. Similar to analyzing the deformations, element stresses can also be extracted and analyzed. Figure 68 shows the axial stress at point P whereas Figure 69 shows the same result after applying the low-pass filter. It can be seen from the results of Figures 66-69 that the trend in the chassis vertical deformation and axial stress for the three types of tire models traversing the test track is quite similar. The deformation in the chassis used with brush tire model is larger than its FE/ANCF counterparts due to the reason previously mentioned, that is, the rigidity of the tire which leads to larger force transmission.

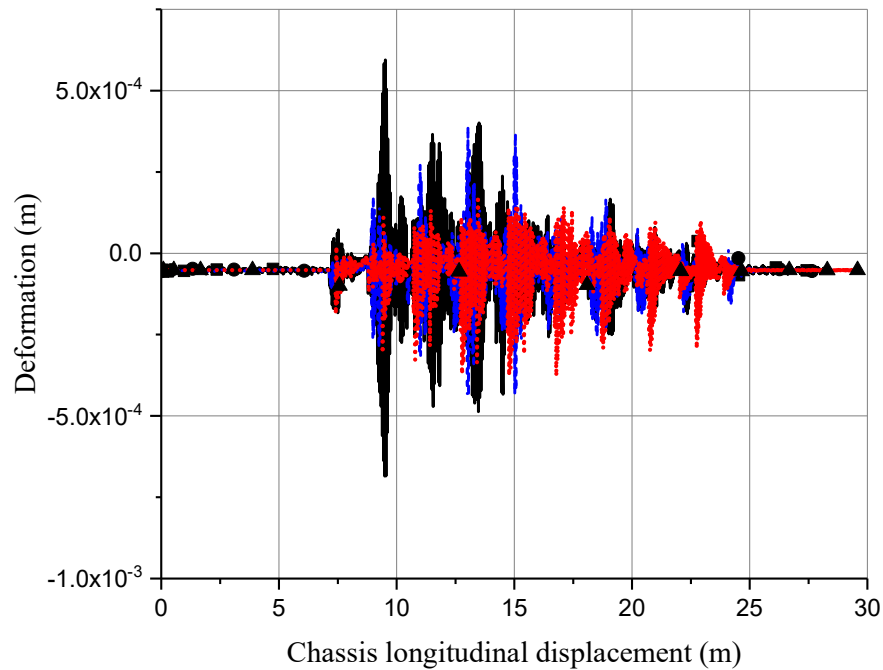


Figure 66. Vertical deformation at chassis point P with respect to BCS (—■— Airless;

---●--- Pneumatic;▲..... Brush)

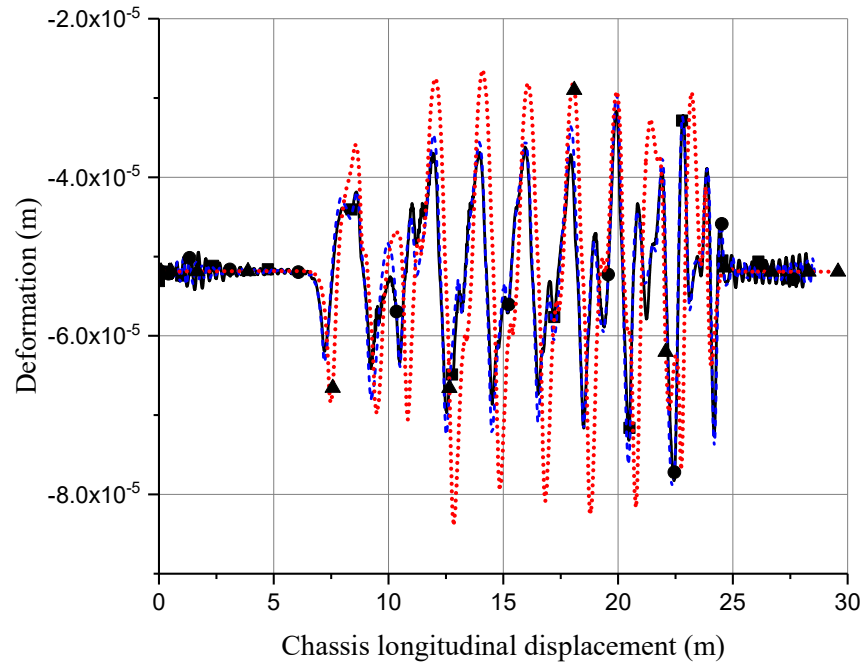


Figure 67. Vertical deformation at chassis point P with respect to BCS after applying low-pass

filter (—■— Airless; - -●- - Pneumatic; ···▲··· Brush)

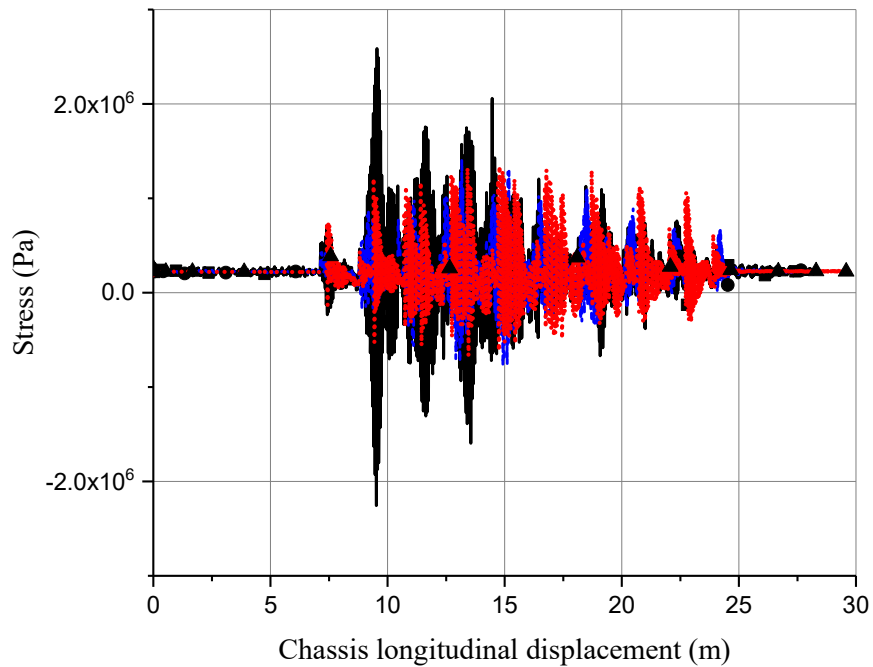


Figure 68. Axial stress at chassis point P with respect to BCS (—■— Airless; - -●- -

Pneumatic; ···▲··· Brush)

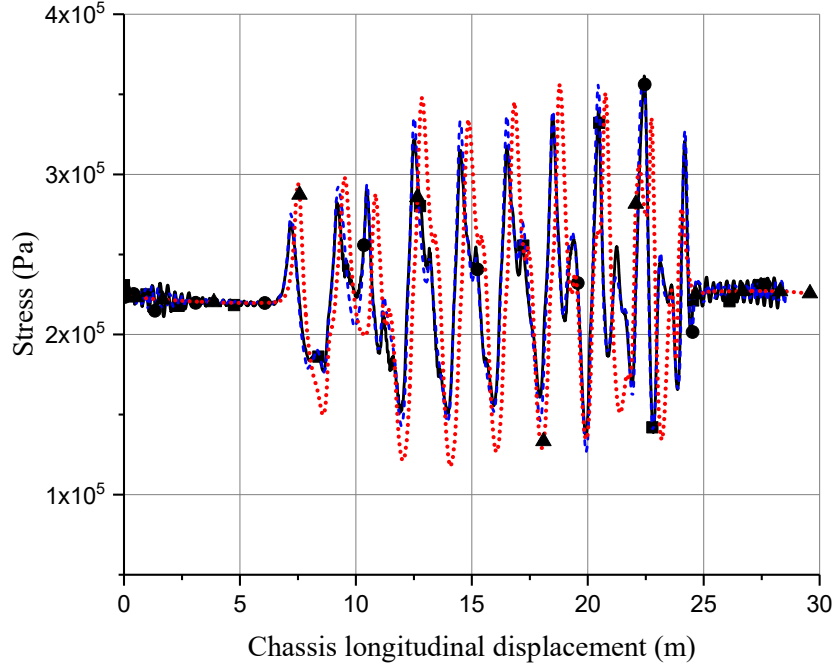


Figure 69. Axial stress at chassis point P with respect to BCS after applying low-pass filter (

—■— Airless; - -●- - Pneumatic;▲..... Brush)

5.5 Concluding Remarks

The goal of this chapter is to develop a computational framework for complex vehicle systems that consist of components with geometry characterized by structural discontinuities as in the cases of chassis and airless tires. Accurate durability analysis of such systems requires the integration of small- and large-deformation formulations. The chapter proposes a new ANCF approach for modeling structural discontinuities in which a constant velocity transformation matrix that allows combining the structural discontinuity constraint equations with other ANCF constraint equations before the application of any coordinate transformation. The ANCF linear constraint equations are used to eliminate dependent variables at a preprocessing stage. The chapter also proposes a new radial damping model for the tires and demonstrates its use in MBS vehicle system applications. The use of the new computational framework proposed in this chapter is demonstrated by

developing and performing the simulation of a detailed wheeled vehicle model that consists of rigid body, FFR, and ANCF components. The vehicle components undergoing small deformations are modeled using the FFR approach, whereas the components undergoing large deformations and finite rotations are modeled using the ANCF approach. Three types of tire models that include a rigid brush-type tire model, an ANCF airless tire model, and an ANCF pneumatic tire model are compared as the vehicle traverses a series of bumps. The airless tire is modeled for the first time using ANCF fully parameterized plate/shell elements, which is one of the main contributions of this chapter.

CHAPTER 6

CONCLUSIONS AND FUTURE WORK

6.1 Conclusions

In this thesis, a new computational procedure for modeling tire and vehicle systems is presented. The thesis demonstrates the integration of absolute nodal coordinate formulation (ANCF) tire models with computational multibody system (MBS) algorithms by using the new concept of the ANCF reference node. This concept is used to develop a tire assembly in which a vehicle model, including the tires, can be represented using one ANCF mesh in which the linear connectivity conditions are used to eliminate redundant variables at a preprocessing stage. The computational approach used in this thesis allows for developing detailed finite element (FE) vehicle models that include tires with distributed inertia and elasticity without the need for using co-simulation techniques, only one MBS simulation environment is required. The optimum sparse matrix structure of the dynamic equations of motion is preserved by introducing a minimum set of nonlinear algebraic equations that ensure the rigidity of the rims, axles, and possibly the chassis of the vehicle. A continuum-based air pressure tire model that allows for accounting for the change of the inner surface area of the tire due to the contact forces is developed. In this continuum-based air pressure model, Nanson's formula is used to define the area in the current deformed configuration in terms of the area in the reference configuration. This continuum-based air pressure model can be used as an alternative to the discrete spring models often used in the literature to model the tire pressure forces. Because general and more accurate tire models require the use of composite materials, it is shown how an ANCF composite tire model can be systematically developed and integrated with MBS algorithms. To this end, fully parameterized ANCF plate

elements are used. Numerical results are presented in this thesis in order to demonstrate the implementation of the proposed computational MBS approach.

In this thesis, a method for the integration of localized surface geometry with fully parameterized ANCF elements is proposed as well. ANCF FEs are used to create the global geometry and perform the FE/MBS analysis of the bodies. The surface geometry details can be added without refining the mesh to the scale of the detailed features. The localized surface may be represented by NURBS and can accurately describe complex geometric shapes such as a conic surface and freeform surface. The basic idea lies in the integration of the localized surface with the global surface by augmenting the geometry during the numerical integration process. Two methods for including the localized geometry in the ANCF elements are proposed. The overlapping method simply changes the thickness of the element using a function that is dependent on the lateral and longitudinal coordinates of the element. The domain trimming method takes advantage of the powerful NURBS geometry as a tool to trim the domain of original ANCF element according to the shape of the localized geometry. While using NURBS to define the localized geometry, a mapping between ANCF local coordinates and NURBS localized geometric parameters is used in both geometric integration methods. Furthermore, a comparison of two numerical integration methods, the global domain and the subdomain methods is presented in this thesis. The results show that the subdomain method is better suited for integrating complex geometry in ANCF elements since it has more flexibility in the distribution of the Gauss integration points. Using the subdomain method, any kind of geometry can be superimposed in the case of fully parameterized ANCF elements without the need for further mesh refinement during dynamic simulations. A cantilever plate example with localized surface geometry is provided to validate the proposed method by comparing the simulation results obtained with the proposed method against a

commercial FE code. A model of a flexible ANCF plate contacting with rigid ground is used to study the effect of the number of subdomains and the number of integration points per subdomain used in accounting for the localized geometry. Finally, a tire model meshed with ANCF plate elements and described by a hyperelastic incompressible Mooney-Rivlin material with four grooves integrated as localized surface geometry is considered. The results from the tire simulation that capture the effect of the grooves in the tire contact patch show the effectiveness of the proposed method whereas the convergence study performed with the tire model helps support the basis of the proposed concepts by demonstrating that the model can achieve convergence with mesh refinement and reduced integration techniques which help alleviate locking. In summary, the proposed method does a good job of capturing surface geometry without significantly increasing the computational cost that comes from mesh refinement. Future studies can be focused on eliminating the limitations of the method that include the fact that very localized deformations of the more intricate geometry cannot be easily captured since the element deformation field is still governed by its basis functions, and that the method will be challenging to use with very complex three-dimensional changes in the structure's geometry.

ANCF beam element locking was another subject studied in this thesis, which also presented a literature review of classical FE and ANCF locking alleviation techniques. This literature review shows the significant contributions reported in the FE literature and clearly demonstrates that, while locking is a common problem in most FEs, it can be dealt with relatively easily and effectively. ANCF locking alleviation techniques can be broadly classified into two distinct categories: kinematics- and kinetics-based methods. Kinematics-based locking alleviation techniques alter the kinematic description of the element in order to improve its performance. Such methods include improvement in the displacement polynomials or improvement of the strain

measures. Kinetics-based methods operate at the elastic force level by modifying the stresses without directly affecting the basic element kinematics. Such methods include different formulations of the strain energy function and reduced integration. The locking alleviation techniques investigated and compared in this thesis can be categorized in the aforementioned two types. These include the new method that is proposed in this thesis to solve the ANCF beam and plate locking problems, known as the strain split method (SSM). A new higher-order two-dimensional ANCF beam element was also developed for the purpose of comparison with other locking alleviation methods. Implementation of the enhanced assumed strain method in ANCF beams using one parameter interpolation and using ANCF higher-order beam shape functions was presented and discussed. Three planar static examples that include a slender beam, a thick beam and a curved beam structure undergoing small and large deformations, one planar dynamic pendulum problem and one three-dimensional dynamic cantilever beam problem were presented, and the locking alleviation techniques were compared. The newly proposed SSM concept in curved structures was discussed and its advantages and drawbacks were discussed.

One of the goals of this thesis is to develop a computational framework for complex vehicle systems that consist of components with geometry characterized by structural discontinuities as in the cases of chassis and airless tires. Accurate durability analysis of such systems requires the integration of small- and large-deformation formulations. The thesis proposes a new ANCF approach for modeling structural discontinuities in which a constant velocity transformation matrix is used that allows combining the structural discontinuity constraint equations with other ANCF constraint equations before the application of any coordinate transformation. The ANCF linear constraint equations are used to eliminate dependent variables at a preprocessing stage. The thesis also proposes a new radial damping model for the tires and demonstrates its use in MBS vehicle

system applications. The use of the new computational framework proposed in this thesis is demonstrated by developing and performing the simulation of a detailed wheeled vehicle model that consists of rigid body, FFR, and ANCF components. The vehicle components undergoing small deformations are modeled using the FFR approach, whereas the components undergoing large deformations and finite rotations are modeled using the ANCF approach. Three types of tire models that include a rigid brush-type tire model, an ANCF airless tire model, and an ANCF pneumatic tire model are compared as the vehicle traverses a series of bumps. The airless tire is modeled for the first time using ANCF fully parameterized plate/shell elements, which is one of the main contributions of this thesis.

6.2 Future Work

Some future work that can improve the concepts and methodologies proposed in this thesis include the following:

1. Consideration of the physics that occurs at the rim-tire interface by relaxation of some of the rim reference node to tire-rim interface node constraints.
2. Improvement of the pressure force model by considering the effect of the change in the volume of the air cavity on the air pressure value, in order to avoid the simplification of constant air pressure. Incorporation of thermodynamics will also improve the pressure force fidelity.
3. Consideration of viscoelastic effects in the ANCF tire material model.
4. Extension of the proposed SSM method in order to fully alleviate the locking seen in ANCF beams in response to pure torsion and twisting deformations.
5. Study of the effects of reduced integration within the subdomain integration scheme can also be considered as a topic of future investigations.

APPENDIX A

Permission for use of journal article:

Patel, M., Orzechowski, G., Tian, Q., and Shabana A.A., 2016, "A New Multibody System Approach for Tire Modeling using ANCF Finite Elements," *Proceedings of Institution of Mechanical Engineers Part K: Journal of Multibody Dynamics*, 230(1), pp. 69-84. Copyright © 2016 SAGE Publications. Reprinted by the permission of SAGE Publications. DOI: <https://doi.org/10.1177%2F1464419315574641>.



RightsLink®

[Home](#)
[Create Account](#)
[Help](#)




Title: A new multibody system approach for tire modeling using ANCF finite elements

Author: Mohil Patel, Grzegorz Orzechowski, Qiang Tian, et al

Publication: Proceedings of the Institution of Mechanical Engineers, Part K: Journal of Multi-body Dynamics

Publisher: SAGE Publications

Date: 03/01/2016

Copyright © 2016, © SAGE Publications

LOGIN

If you're a copyright.com user, you can login to RightsLink using your copyright.com credentials. Already a RightsLink user or want to [learn more?](#)

If you are a SAGE journal author requesting permission to reuse material from your journal article, please note you may be able to reuse your content without requiring permission from SAGE. Please review SAGE's author re-use and archiving policies at <https://us.sagepub.com/en-us/nam/journal-author-archiving-policies-and-re-use> for more information.

If your request does not fall within SAGE's reuse guidelines, please proceed with submitting your request by selecting one of the other reuse categories that describes your use. Please note, a fee may be charged for reuse of content requiring permission. Please contact permissions@sagepub.co.uk if you have questions.

BACK

CLOSE WINDOW

Copyright © 2017 Copyright Clearance Center, Inc. All Rights Reserved. [Privacy statement](#). [Terms and Conditions](#). Comments? We would like to hear from you. E-mail us at customer@copyright.com

When posting or reusing your Contribution under this policy, appropriate credit must be given to the SAGE journal where the Contribution has been published, as the original source of the content, as follows: **Author(s), Article Title, Journal Title (Journal Volume Number and Issue Number) pp. xx-xx. Copyright © [year] (Copyright Holder). Reprinted by permission of SAGE Publications.** Additionally, please provide a link to the appropriate DOI for the published version of the Contribution on the SAGE Journals website (<http://journals.sagepub.com>).

The chart below includes common requests and an explanation of which 'version' of the article can be used in each circumstance. If the table below indicates that permission is required, please see the instructions for requesting permission at Journals Permissions.

I WANT TO:	CLEARED PERMISSION	REQUIRES PERMISSION
include up to one full article in my unpublished dissertation or thesis	Version 3	

Permission for use of journal article:

He, G., Patel, M., and Shabana, A.A., 2017, "Integration of Localized Surface Geometry in Fully Parameterized ANCF Finite Elements," *Computer Methods in Applied Mechanics and Engineering*, 313, pp. 966-985.

FW: Use of article in thesis [171023-007522]



Inbox x



oxfordcopyrights (ELS) <oxfordcopyrights@elsevier.com>

to me, Computer



Dear Dr Patel,

Thank you for your email.

Please note that, as one of the Authors of this article, you retain the right to reuse it in a thesis/dissertation. You do not require formal permission to do so. For full details of your rights as a Journal Author, please visit:

<https://www.elsevier.com/about/our-business/policies/copyright>

Please feel free to contact me if you have any queries.

Kind regards

Laura

Laura Pritchard

Permissions Supervisor | ELSEVIER | The Boulevard | Langford Lane | Kidlington | Oxford OX5 1GB |

Tel: +44 1865 843517 Fax: +44 1865 853333

lpritchard@elsevier.com



Q SEARCH CART MENU

Personal use

Authors can use their articles, in full or in part, for a wide range of scholarly, non-commercial purposes as outlined below:

- Use by an author in the author's classroom teaching (including distribution of copies, paper or electronic)
- Distribution of copies (including through e-mail) to known research colleagues for their personal use (but not for Commercial Use)
- Inclusion in a thesis or dissertation (provided that this is not to be published commercially)
- Use in a subsequent compilation of the author's works
- Extending the Article to book-length form
- Preparation of other derivative works (but not for Commercial Use)
- Otherwise using or re-using portions or excerpts in other works

These rights apply for all Elsevier authors who publish their article as either a subscription article or an open access article. In all cases we require that all Elsevier authors always include a full acknowledgement and, if appropriate, a link to the final published version hosted on Science Direct.

APPENDIX B

B.1 Higher-Order ANCF Planar Element Shape Functions

The shape functions for the new higher-order two-dimensional element proposed in Section 4.3.3 are given as:

$$\left. \begin{aligned} s_1 &= 1 - 3\xi^2 + 2\xi^3, & s_2 &= l(\xi - 2\xi^2 + \xi^3), & s_3 &= l(\eta - \eta\xi), \\ s_4 &= \frac{l^2}{2}(\eta^2 - \eta^2\xi), & s_5 &= 3\xi^2 - 2\xi^3, & s_6 &= l(-\xi^2 + \xi^3), \\ s_7 &= l\eta\xi, & s_8 &= \frac{l^2}{2}\eta^2\xi \end{aligned} \right\} \quad (\text{B.1})$$

where $\xi = x/l$, $\eta = y/l$ are the dimensionless element parameters and l is the element length.

The matrix of shape functions can be written as $\mathbf{S} = [s_1\mathbf{I} \ s_2\mathbf{I} \ s_3\mathbf{I} \ s_4\mathbf{I} \ s_5\mathbf{I} \ s_6\mathbf{I} \ s_7\mathbf{I} \ s_8\mathbf{I}]$.

B.2 Enhanced Strain Submatrices

The submatrices used in Eq. 40 are given as follows:

$$\left. \begin{aligned} \mathbf{K} &= \frac{\partial \mathbf{f}}{\partial \mathbf{e}} = \int_{V_0} \left(\frac{\partial \boldsymbol{\varepsilon}^{com}}{\partial \mathbf{e}} \right)^T \frac{\partial^2 U}{\partial \boldsymbol{\varepsilon}^2} \left(\frac{\partial \boldsymbol{\varepsilon}^{com}}{\partial \mathbf{e}} \right) dV_0 + \int_{V_0} \left(\frac{\partial^2 \boldsymbol{\varepsilon}^{com}}{\partial \mathbf{e}^2} \right)^T \frac{\partial U}{\partial \boldsymbol{\varepsilon}} dV_0, \\ \mathbf{P} &= \frac{\partial \mathbf{f}}{\partial \mathbf{a}} = \int_{V_0} \left(\frac{\partial \boldsymbol{\varepsilon}^{com}}{\partial \mathbf{e}} \right)^T \frac{\partial^2 U}{\partial \boldsymbol{\varepsilon}^2} \left(\frac{\partial \boldsymbol{\varepsilon}^{enh}}{\partial \mathbf{a}} \right) dV_0, & \mathbf{S} &= \frac{\partial \mathbf{g}}{\partial \mathbf{e}} = \int_{V_0} \left(\frac{\partial \boldsymbol{\varepsilon}^{enh}}{\partial \mathbf{a}} \right)^T \frac{\partial^2 U}{\partial \boldsymbol{\varepsilon}^2} \left(\frac{\partial \boldsymbol{\varepsilon}^{com}}{\partial \mathbf{e}} \right) dV_0, \\ \mathbf{G} &= \frac{\partial \mathbf{g}}{\partial \mathbf{a}} = \int_{V_0} \left(\frac{\partial \boldsymbol{\varepsilon}^{enh}}{\partial \mathbf{a}} \right)^T \frac{\partial^2 U}{\partial \boldsymbol{\varepsilon}^2} \left(\frac{\partial \boldsymbol{\varepsilon}^{enh}}{\partial \mathbf{a}} \right) dV_0 \end{aligned} \right\} \quad (\text{B.2})$$

B.3 Design of Enhanced Strain Field

In a state of constant stress or a patch test, $\int_{V_0} \boldsymbol{\sigma}_{P2} : \boldsymbol{\varepsilon}^{enh} dV_0 = 0$ must be satisfied. This leads to the

following expression

$$\int_{\Omega} \bar{\mathbf{M}} d\Omega = \mathbf{0}, \quad \int_{V_0} \mathbf{M}_s dV_0 = \mathbf{0} \quad (\text{B.3})$$

where Ω is the element parametric domain, $\bar{\mathbf{M}}$ and \mathbf{M}_s is the matrix of enhanced strain interpolation functions defined in the parametric domain and physical reference domain respectively. Satisfying Eq. B.3 is important for the stability and convergence properties of the enhanced strain-based element. Furthermore, another condition required for element stability is that the intersection of the subspaces spanned by the compatible and enhanced strain fields must be a null set. Finally, in order to ensure that the objectivity of the strain tensor is ensured, the enhanced strain interpolation functions must demonstrate frame invariance in the parametric domain (Simo and Armero, 1992). The enhanced strain field interpolation functions defined in the parametric domain can be transformed into the reference domain using the following operation $\mathbf{M}_s = (|\mathbf{J}_c|/|\mathbf{J}|)\mathbf{T}_c^T\bar{\mathbf{M}}$ where \mathbf{J} is the matrix of position vector gradients at the integration point in the reference configuration (Simo and Rifai, 1990), c represents element coordinates corresponding to the center of the element and the transformation matrix \mathbf{T} is given as (Andelfinger and Ramm, 1993)

$$\mathbf{T} = \begin{bmatrix} J_{11}J_{11} & J_{12}J_{12} & 2J_{11}J_{12} \\ J_{21}J_{21} & J_{22}J_{22} & 2J_{21}J_{22} \\ J_{11}J_{21} & J_{12}J_{22} & J_{11}J_{22} + J_{12}J_{21} \end{bmatrix} \quad (\text{B.4})$$

where J_{ij} is the ij^{th} element of the matrix of position vector gradients defined in the reference configuration.

APPENDIX C

C.1 FE/FFR Beam Element Shape Function Matrix

The shape function matrix for the non-isoparametric beam element used with the FE/FFR model in this thesis is given as

$$\mathbf{S}^{ijT} = \begin{bmatrix} 1-\xi & 0 & 0 \\ 6(\xi-\xi^2)\eta & 1-3\xi^2+2\xi^3 & 0 \\ 6(\xi-\xi^2)\zeta & 0 & 1-3\xi^2+2\xi^3 \\ 0 & -(1-\xi)l\zeta & (1-\xi)l\eta \\ (1-4\xi+3\xi^2)l\zeta & 0 & (-\xi+2\xi^2-\xi^3)l \\ (-1+4\xi-3\xi^2)l\eta & (\xi-2\xi^2+\xi^3)l & 0 \\ \xi & 0 & 0 \\ 6(-\xi+\xi^2)\eta & 3\xi^2-2\xi^3 & 0 \\ 6(-\xi+\xi^2)\zeta & 0 & 3\xi^2-2\xi^3 \\ 0 & -l\xi\zeta & l\xi\eta \\ (-2\xi+3\xi^2)l\zeta & 0 & (\xi^2-\xi^3)l \\ (2\xi-3\xi^2)l\eta & (-\xi^2+\xi^3)l & 0 \end{bmatrix} \quad (\text{C.1})$$

C.2 ANCF Plate/Shell Element Shape Functions

The shape function matrix and the shape functions of the ANCF fully-parameterized plate/shell element with gradient conformity at element edges are given, respectively, as

$$\mathbf{S} = [\mathbf{S}_1 \mathbf{I} \quad \mathbf{S}_2 \mathbf{I} \quad \mathbf{S}_3 \mathbf{I} \quad \mathbf{S}_4 \mathbf{I} \quad \mathbf{S}_5 \mathbf{I} \quad \mathbf{S}_6 \mathbf{I} \quad \mathbf{S}_7 \mathbf{I} \quad \mathbf{S}_8 \mathbf{I} \quad \mathbf{S}_9 \mathbf{I} \quad \mathbf{S}_{10} \mathbf{I} \quad \mathbf{S}_{11} \mathbf{I} \quad \mathbf{S}_{12} \mathbf{I} \quad \mathbf{S}_{13} \mathbf{I} \quad \mathbf{S}_{14} \mathbf{I} \quad \mathbf{S}_{15} \mathbf{I} \quad \mathbf{S}_{16} \mathbf{I}] \quad (\text{C.2})$$

and

$$\left. \begin{aligned}
S_1 &= (2\xi + 1)(\xi - 1)^2(2\eta + 1)(\eta - 1)^2 \quad ; \quad S_2 = l\xi(\xi - 1)^2(2\eta + 1)(\eta - 1)^2 \\
S_3 &= w\eta(\xi - 1)^2(2\xi + 1)(\eta - 1)^2 \quad ; \quad S_4 = t\xi(\xi - 1)(\eta - 1) \\
S_5 &= -\xi^2(2\xi - 3)(2\eta + 1)(\eta - 1)^2 \quad ; \quad S_6 = l\xi^2(\xi - 1)(2\eta + 1)(\eta - 1)^2 \\
S_7 &= -w\eta\xi^2(2\xi - 3)(\eta - 1)^2 \quad ; \quad S_8 = -t\xi\xi(\eta - 1) \\
S_9 &= \eta^2\xi^2(2\xi - 3)(2\eta - 3) \quad ; \quad S_{10} = -l\eta^2\xi^2(\xi - 1)(2\eta - 3) \\
S_{11} &= -w\eta^2\xi^2(\eta - 1)(2\xi - 3) \quad ; \quad S_{12} = t\xi\xi\eta \\
S_{13} &= -\eta^2(2\xi + 1)(\xi - 1)^2(2\eta - 3) \quad ; \quad S_{14} = -l\xi\eta^2(\xi - 1)^2(2\eta - 3) \\
S_{15} &= w\eta^2(\xi - 1)^2(2\xi + 1)(\eta - 1) \quad ; \quad S_{16} = -t\xi\eta(\xi - 1)
\end{aligned} \right\} \quad (C.3)$$

where $\xi = x/l$, $\eta = y/w$, and $\zeta = z/t$ in which l , w , and t are, respectively, the length, width, and thickness of the plate.

CITED LITERATURES

1. Aboubakr, A.K., and Shabana, A.A., 2015, “Efficient and Robust Implementation of the TLISMNI Method”, *Journal of Sound and Vibration*, 353, pp. 220-242.
2. Agrawal, O.P., and Shabana, A.A., 1986, “Application of Deformable-Body Mean Axis to Flexible Multibody System Dynamics”, *Computer Methods in Applied Mechanics and Engineering*, 56, pp. 217-245.
3. Alvarez, L, Yi, J., Horowitz, R., and Olmos, L., 2005, “Dynamic Friction Model-Based Tire-Road Friction Estimation and Emergency Braking Control”, *ASME Dynamic Systems, Measurement and Control*, 127, pp. 22-32.
4. Ambrosio, J.A.C, and Goncalves, J.P.C., 2001, “Complex Flexible Multibody Systems with Application to Vehicle Dynamics”, *Multibody System Dynamics*, 6, pp. 163-182.
5. Andelfinger, U., and Ramm, E., 1993, “EAS-elements for Two-Dimensional, Three-Dimensional, Plate and Shell Structures and their Equivalence to HR-Elements”, *International Journal for Numerical Methods in Engineering*, 36(8), pp. 1311-1337.
6. ANSYS® Academic Research Mechanical APDL Documentation, ANSYS Inc. Release 15.0, 2013.
7. Armero, F., 2000, “On the Locking and Stability of Finite Elements in Finite Deformation Plane Strain Problems”, *Computer & Structures*, 75(3), pp. 261-290.
8. Babuska, I., and Suri, M., 1992A, “Locking Effects in the Finite Element Approximation of Elasticity Problems”, *Numerische Mathematik*, 62(1), pp. 439-463.
9. Babuska, I., and Suri, M., 1992B, “On Locking and Robustness in the Finite Element Method”, *SIAM Journal for Numerical Analysis*, 29(5), pp. 1261-1293.

10. Bathe, K.J., 2001, “The Inf-Sup Condition and its Evaluation for Mixed Finite Element Methods”, *Computers & Structures*, 79(2), pp. 243-252.
11. Bazeley, G.P., Cheung, Y.K., Irons, B.M., and Zienkiewicz, O.C, 1965, “Triangular Elements in Plate Bending – Conforming and Nonconforming Solutions”, *Proc. First Conference on Matrix Methods in Structural Mechanics*, Wright-Patterson ATBFB, Ohio.
12. Belytschko, T., Stolarski, H., Liu, W.K., Carpenter, N., and Ong, J.S.J, 1985, “Stress Projection for Membrane and Shear Locking in Shell Finite Elements”, *Computer Methods in Applied Mechanics & Engineering*, 51(1-3), pp. 221-258.
13. Bergan, P.G., and Nygard, M.K., 1984, “Finite Elements with Increased Freedom in Choosing Shape Functions”, *International Journal for Numerical Methods in Engineering*, 20(4), pp. 643-663.
14. Bischoff, M., and Ramm, E., 1997, “Shear Deformable Shell Elements for Large Strains and Rotations”, *International Journal for Numerical Methods in Engineering*, 40(23), pp. 4427-4449.
15. Bischoff, M., and Romero, I., 2007, “A Generalization of the Method of Incompatible Modes”, *International Journal for Numerical Methods in Engineering*, 69(9), pp. 1851-1868.
16. Blundell, M., and Harty, D., 2004, *Multibody Systems Approach to Vehicle Dynamics*, Elsevier, New York.
17. Bonet, J., and Wood, R.D., 1997, *Nonlinear Continuum Mechanics for Finite Element Analysis*, Cambridge University Press, Cambridge.
18. Bornemann, P. B., and Cirak, F., 2013, “A Subdivision-based Implementation of the Hierarchical B-spline Finite Element Method”, *Computer Methods in Applied Mechanics & Engineering*, 253, pp. 584–598.

19. Bouclier, R., Passieux, J. C., and Salaün, M., 2016, “Local Enrichment of NURBS Patches using a Non-intrusive Coupling Strategy: Geometric Details, Local Refinement, Inclusion, Fracture”, *Computer Methods in Applied Mechanics & Engineering*, 300, pp. 1–26.
20. Canudas-de-Wit, C., Tsiotras, P., Velenis, E., Basset, M., and Gissinger, G., 2003, “Dynamic Friction Models for Road/Tire Longitudinal Interaction”, *Vehicle System Dynamics*, 39, pp.189-226.
21. Carpenter, N., Belytschko, T., and Stolarski, H., 1986, “Locking and Shear Scaling Factors in C^0 Bending Elements”, *Computers & Structures*, 22(1), pp. 39-52.
22. Carpinelli, M., Mundo, D., Tamarozzi, T., Gubitosa, M., Donders, S., and Desmet, W., 2012, “Integrating Vehicle Body Concept Modelling and Flexible Multibody Techniques for Ride and Handling Simulation”, *Proc. Of ASME 11th Biennial Conference on Engineering Systems Design and Analysis*, Nantes, France, July 2-4.
23. Caterpillar. *834K Wheel Dozer*. Caterpillar, 2013. Print.
24. Chemin, A., Elguedj, T., and Gravouil, A., 2015, “Isogeometric Local H-refinement Strategy Based on Multigrids”, *Finite Elements in Analysis & Design*, 100, pp. 77–90.
25. Cho, J. R., Kim, K. W., Yoo, W. S., and Hong, S. I., 2004, “Mesh Generation Considering Detailed Tread Blocks for Reliable 3D Tire Analysis”, *Advances in Engineering Software*, 35(2), pp. 105–113.
26. Choi, J., and Lim, J., 1995, “General Curved Beam Elements Based on the Assumed Strain Fields”, *Computers & Structures*, 55(3), pp. 379-386.
27. Clover, C. L., and Bernard, J. E., 1998, “Longitudinal Tire Dynamics”, *Vehicle System Dynamics*, 29, pp. 231–260.

28. Das, M., Barut, A., and Madenci, E., 2010, “Analysis of Multibody Systems Experiencing Large Elastic Deformations”, *Multibody System Dynamics*, 23(1), pp. 1-31.
29. Deur, J., Asgari, J., and Hrovat, D., 2004, “A 3D Brush-Type Dynamic Tire Friction Model”, *Vehicle System Dynamics*, 42, pp. 133-173.
30. Deur, J., Ivanović, V., Pavković, D., Hrovat, D., Asgari, J., Troulis, M., and Miano, C., 2005, “Experimental Analysis and Modelling of Longitudinal Tyre Friction Dynamics for Abrupt Transients”, *Vehicle System Dynamics*, 43, pp. 525-539.
31. De Souza Neto, E.A., Peric, D., and Owen, D.R.J., 2008, *Computational Methods For Plasticity: Theory And Applications*, John Wiley and Sons, West Sussex.
32. Dmitrochenko, O., Hussein, B.A., and Shabana, A.A., 2009, “Coupled Deformation Modes in the Large Deformation Finite Element Analysis: Generalization”, *ASME Journal of Computational & Nonlinear Dynamics*, 4(2), pp. 021002-1 – 021002-8.
33. Dong, S.B., Alpdogan, C., and Taciroglu, E., 2010, “Much Ado about Shear Correction Factors in Timoshenko Beam Theory”, *International Journal of Solids & Structures*, 47(13), pp. 1651-1665.
34. Dorfi, H.R., and Busby, H.R., 1994, “An Effective Curved Composite Beam Finite Element based on the Hybrid-Mixed Formulation”, *Computers & Structures*, 53(1), pp. 43-52.
35. Dufva, K.E., Sopanen, J.T., and Mikkola, A.M., 2005, “A Two-Dimensional Shear Deformable Beam Element based on Absolute Nodal Coordinate Formulation”, *Journal of Sound & Vibration*, 280(3-5), pp. 719-738.
36. Dufva, K., Kerkkanen, K., Maqueda, L.G., and Shabana, A.A., 2007, “Nonlinear Dynamics of Three-Dimensional Belt Drives Using the Finite Element Method”, *Nonlinear Dynamics*, 48, pp. 449-466.

37. Ebel, H., Matikainen, M.K., Hurskainen, V., and Mikkola, A., 2016A, “Higher-Order Beam Elements based on the Absolute Nodal Coordinate Formulation for Three-Dimensional Elasticity”, *Nonlinear Dynamics*, 88(2), pp. 1075-1091.
38. Ebel, H., Matikainen, M.K., Hurskainen, V., and Mikkola, A., 2016B, “Higher-Order Plate Elements for Large Deformation Analysis in Multibody Applications”, *Proceedings of the ASME 2016 International Design Engineering Technical Conferences & Computers and Information in Engineering Conference*, Charlotte, North Carolina, USA, August 21-24.
39. Felippa, C.A., 1989, “The Extended Free Formulation of Finite Elements in Linear Elasticity”, *ASME Journal of Applied Mechanics*, 56(3), pp. 609-616.
40. Forsey, D. R., and Bartels, R. H., 1988, “Hierarchical B-Spline Refinement”, *ACM SIGGRAPH Computer Graphics*, 22(4), pp. 205-212.
41. Friedman, Z., and Kosmatka, J.B., 1993, “An Improved Two-Node Timoshenko Beam Finite Element”, *Computers & Structures*, 47(3), pp. 473-481.
42. Gantoi, F.M., Brown, M.A., and Shabana, A.A., 2013, “Finite Element Modeling of the Contact Geometry and Deformation in Biomechanics Applications”, *ASME Journal of Computational and Nonlinear Dynamics*, 8 (4), pp. 041013-1 – 041013-11.
43. Garcia-Vallejo, D., Mikkola, A., and Escalona, J.L., 2007, “A New Locking-Free Shear Deformable Finite Element based on Absolute Nodal Coordinates”, *Nonlinear Dynamics*, 50(1), pp. 249-264.
44. Gerstmayr, J., and Matikainen, M., 2006, “Analysis of Stress and Strain in the Absolute Nodal Coordinate Formulation”, *Mechanics Based Design of Structures and Machines: An International Journal*, 34(4), pp. 409-430.

45. Gerstmayr, J., and Irschik, H., 2008, “On the Correct Representation of Bending and Axial Deformation in the Absolute Nodal Coordinate Formulation with an Elastic Line Approach”, *Journal of Sound & Vibration*, 318(3), pp. 461-487.
46. Gerstmayr, J., Matikainen, M.K., and Mikkola, A.M., 2008, “A Geometrically Exact Beam Element based on the Absolute Nodal Coordinate Formulation”, *Multibody System Dynamics*, 20, pp. 359-384.
47. Gerstmayr, J., Sugiyama, H., and Mikkola, A., 2013, “Review on the Absolute Nodal Coordinate Formulation for Large Deformation Analysis of Multibody Systems”, *ASME Journal of Computational & Nonlinear Dynamics*, 8(3), pp. 031016-1 – 031016-12.
48. Gilewski, W., and Sitek, M., 2011, “The Inf-Sup Condition Tests for Shell/Plate Finite Elements”, *Archives of Civil Engineering*, 57(4), pp. 425-447.
49. Gim, G. H., and Nikraves, P. E., 1990, “An Analytical Model of Pneumatic Tires for Vehicle Dynamic Simulations. Part 1: Pure Slips”, *International Journal of Vehicle Design*, 11, pp. 589-618.
50. Gipser, M., 2005, “FTire: A Physically Based Application-Oriented Tyre Model for Use with Detailed MBS and Finite-Element Suspension Models”, *Vehicle System Dynamics*, 43, pp. 76-91.
51. Goncalves, J.P.C., and Ambrosio, J.A.C., 2003, “Optimization of Vehicle Suspension Systems for Improved Comfort of Road Vehicles using Flexible Multibody Dynamics”, *Nonlinear Dynamics*, 34, pp. 113-131.
52. Gruber, P., Sharp, R. S., and Crocombe, A. D., 2012, “Normal and Shear Forces in the Contact Patch of a Braked Racing Tyre. Part 2: Development of a Physical Tyre Model”, *Vehicle System Dynamics*, 50, pp. 339-356.

53. Hamed, A.M., Jayakumar, P., Letherwood, M.D., Gorsich, D.J., Recuero, A.M., Shabana, A.A., 2015, “Ideal Compliant Joints and Integration of Computer Aided Design and Analysis”, *ASME Journal of Computational and Nonlinear Dynamics*, 10(2), pp. 021015-1 – 021015-14.
54. Haug, E.J., Wehage, R.A., Barman, N.C., and Beck, R.R., 1981, “Dynamic Analysis and Design of Constrained Mechanical Systems”, Technical Report No. 50, Contract No. DAAK30-78-C-0096.
55. He, G., Patel, M., and Shabana, A.A., 2017, “Integration of Localized Surface Geometry in Fully Parameterized ANCF Finite Elements”, *Computer Methods in Applied Mechanics and Engineering*, 313, pp. 966-985.
56. Heyliger, P.R., and Reddy, J.N., 1988, “A Higher-order Beam Finite Element for Bending and Vibration Problems”, *Journal of Sound & Vibration*, 126(2), pp. 309-326.
57. Hughes, T.J.R., Taylor, R., and Kanoknukulchai, W., 1977, “A Simple and Efficient Finite Element for Plate Bending”, *International Journal for Numerical Methods in Engineering*, 11(10), pp. 1529-1543.
58. Hughes, T.J.R., Cohen, M., and Haroun, M., 1978, “Reduced and Selective Integration Techniques in the Finite Element Analysis of Plates”, *Nuclear Engineering and Design*, 46(1), pp. 203-222.
59. Hughes, T.J.R., 1987, *The Finite Element Method: Linear Static and Dynamic Finite Element Analysis*, Prentice Hall, New Jersey.
60. Hurskainen, V.T., Matikainen, M.K., Wang, J., and Mikkola, A.M., 2017, “A Planar Beam Finite-Element Formulation with Individually Interpolated Shear Deformation”, *ASME Journal of Computational & Nonlinear Dynamics*, 12(4), pp. 041007-1 – 041007-8.
61. Hussein, B.A., Sugiyama, H., and Shabana, A.A., 2007, “Coupled Deformation Modes in the Large Deformation Finite-element Analysis: Problem Definition”, *ASME Journal of Computational & Nonlinear Dynamics*, 2(2), pp. 146-154.

62. Ibrahimbegovic, A., and Wilson, E.L., 1991, “A Modified Method of Incompatible Modes”, *International Journal for Numerical Methods in Biomedical Engineering*, 7(3), pp. 187-194.
63. Ito, Y., Shih, A., Koomullil, R., Kasmai, N., Jankun-Kelly, M., and Thompson, D., 2009, “Solution Adaptive Mesh Generation using Feature-aligned Embedded Surface Meshes”, *AIAA Journal*, 47(8), pp. 1879–1888.
64. Kagan, P., Fischer, A., and Bar-Yoseph, P. Z., 2003, “Mechanically Based Models: Adaptive Refinement for B-spline Finite Element”, *International Journal for Numerical Methods in Engineering*, 57(8), pp. 1145–1175.
65. Kerkkanen, K.S., Sopanen, J.T., and Mikkola, A.M., 2005, “A Linear Beam Finite Element based on the Absolute Nodal Coordinate Formulation”, *ASME Journal of Mechanical Design*, 127(4), pp. 621-630.
66. Kim, J.G., and Kim, Y.Y., 1998, “A New Higher-Order Hybrid-Mixed Curved Beam Element”, *International Journal for Numerical Methods in Engineering*, 43(5), pp. 925-940.
67. Kim, S., Nikraves, P. E., and Gim, G., 2008, “A Two-Dimensional Tire Model on Uneven Roads for Vehicle Dynamic Simulation”, *Vehicle System Dynamics*, 46, pp. 913-930.
68. Kleiss, S. K., Juttler, B., and Zulehner, W., 2012, “Enhancing Isogeometric Analysis by a Finite Element-based Local Refinement Strategy”, *Computer Methods in Applied Mechanics & Engineering*, 213-216, pp. 168–182.
69. Kollar, L.P. and Springer, G.S., 2003, *Mechanics of Composite Structures*, Cambridge University Press, Cambridge.
70. Koishi, M., Kabe, K., and Shiratori, M., 1998, “Tire Cornering Simulation Using an Explicit Finite Element Analysis Code”, *Tire Science and Technology*, 26, pp. 109-119.

71. Kulkarni, S., Pappalardo, C.M., and Shabana, A.A., 2017, “Pantograph/Catenary Contact Formulations”, *ASME Journal of Vibrations & Acoustics*, 139(1), pp. 011010-1-011010-12.
72. Lan, P., and Shabana, A. A., 2010, “Integration of B-spline Geometry and ANCF Finite Element Analysis”, *Nonlinear Dynamics*, 61(1-2), pp. 193–206.
73. Lee, C.R., Kim, J.W., Hallquist, J.O., Zhang, Y., and Farahani, A.D., 1997, “Validation of a FEA Tire Model for Vehicle Dynamic Analysis and Full Vehicle Real Time Proving Ground Simulations”, *SAE Technical Paper 971100*.
74. Lee, P., and Sin, H., 1994, “Locking-Free Curved Beam Element based on Curvature”, *International Journal for Numerical Methods in Engineering*, 37(6), pp. 989-1007.
75. Li, J., and Ke, Y., 2000, “Feature-based Surface Modeling of Complex Surface in Reverse Engineering”, *Chinese Journal of Mechanical Engineering*, 36(5), pp. 18–22.
76. Liu, C., Tian, Q., Hu, H.Y., 2011, “Dynamics of Large Scale Rigid-Flexible Multibody System Composed of Composite Laminated Plates”, *Multibody System Dynamics*, 26, pp. 283-305.
77. Liu, W.K., Belytschko, T., and Chen, J., 1988, “Nonlinear Versions of Flexurally Superconvergent Elements”, *Computer Methods in Applied Mechanics & Engineering*, 71(3), pp. 241-258.
78. Lugner, P., Pacejka, H., and Plochl, M., 2005, “Recent Advances in Tyre Models and Testing Procedures”, *Vehicle System Dynamics*, 43, pp. 413-436.
79. Malkus, D., and Hughes, T.J.R., 1978, “Mixed Finite Element Methods – Reduced and Selective Integration Techniques: A Unification of Concepts”, *Computer Methods in Applied Mechanics and Engineering*, 15(1), pp. 63-81.
80. Maqueda, L.G., Mohamed, A.A., and Shabana, A.A., 2010, “Use of General Nonlinear Material Models in Beam Problems: Application to Belts and Rubber Chains”, *ASME Journal of Computational and Nonlinear Dynamics*, 5, pp. 021003-1 – 021003-10.

81. Matikainen, M.K., Dmitrochenko, O., and Mikkola, A., 2010, “Beam Elements with Trapezoidal Cross Section Deformation Modes based on the Absolute Nodal Coordinate Formulation”, *International Conference on Numerical Analysis and Applied Mathematics*, Rhodes, Greece, September 19-25.
82. Mikkola, A.M., and Shabana, A.A., 2003, “A Non-Incremental Finite Element Procedure for the Analysis of Large Deformation of Plates and Shells in Mechanical System Applications”, *Multibody System Dynamics*, 9(3), pp. 283-309.
83. Mikkola, A.M., and Matikainen, M.K., 2006, “Development of Elastic Forces for a Large Deformation Plate Element based on the Absolute Nodal Coordinate Formulation”, *ASME Journal of Computational & Nonlinear Dynamics*, 1(2), pp. 103-108.
84. Mohamed, A.N.A., and Liu, J, 2014, “The Three-Dimensional Gradient Deficient Beam Element (Beam9) using the Absolute Nodal Coordinate Formulation”, *Proceedings of the ASME 2014 International Design Engineering Technical Conferences & Computers and Information in Engineering Conference*, Buffalo, New York, USA, August 17-20.
85. Nachbagauer, K., Pechstein, A.S., Irschik, H., and Gerstmayr, J., 2011, “A New Locking-Free Formulation for Planar, Shear Deformable, Linear and Quadratic Beam Finite Elements based on the Absolute Nodal Coordinate Formulation”, *Multibody System Dynamics*, 26(3), pp. 245-263.
86. Nachbagauer, K., Gruber, P., and Gerstmayr, J., 2013A, “Structural and Continuum Mechanics Approaches for a 3D Shear Deformable ANCF Beam Finite Element: Application to Static and Linearized Dynamic Examples”, *ASME Journal of Computational & Nonlinear Dynamics*, 8(2), pp. 021004-1 – 021004-7.

87. Nachbagauer, K., Gruber, P., and Gerstmayr, J., 2013B, “A 3D shear deformable finite element based on absolute nodal coordinate formulation”, *Multibody Dynamics: Computational Methods in Applied Sciences*, 28, pp. 77-96, Springer, Amsterdam.
88. Nachbagauer, K., 2014, “State of the Art of ANCF Elements Regarding Geometric Description, Interpolation Strategies, Definition of Elastic Forces, Validation and Locking Phenomenon in Comparison with Proposed Beam Finite Elements”, *Archives of Computational Methods in Engineering*, 21(3), pp. 293-319.
89. Neto, M. A., Ambrosio, J. A. C., and Leal, R. P., 2004, “Flexible Multibody Systems Models using Composite Materials Components”, *Multibody System Dynamics*, 12(4), pp. 385–405.
90. Nicolas, G., and Fouquet, T., 2013, “Adaptive Mesh Refinement for Conformal Hexahedral Meshes”, *Finite Elements in Analysis & Design*, 67, pp. 1–12.
91. Noor, A., and Peters, J., 1981, “Mixed Models and Reduced/Selective Integration Displacement Models for Nonlinear Analysis of Curved Beams”, *International Journal for Numerical Methods in Engineering*, 17(4), pp. 615-631.
92. Ogden, R.W., 1984, *Nonlinear Elastic Deformations*, Ellis Harwood Ltd., Chichester.
93. Olshevskiy, A., Dmitrochenko, O., and Kim, C.W., 2014, “Three-Dimensional Solid Brick Element using Slopes in the Absolute Nodal Coordinate Formulation”, *ASME Journal of Computational & Nonlinear Dynamics*, 9(2), pp. 021001-1-021001-10.
94. Omar, M.A., and Shabana, A.A., 2001, “A Two-Dimensional Shear Deformable Beam for Large Rotation and Deformation Problems”, *Journal of Sound & Vibration*, 243(3), pp. 565-576.
95. Orlandea, N., 1973, “Node-analogous, Sparsity-oriented Methods for Simulation of Mechanical Dynamic Systems”, Ph.D. Thesis, University of Michigan, Ann Arbor.

96. Orzechowski, G., and Fraczek, J., 2015, “Nearly Incompressible Nonlinear Material Models in the Large Deformation Analysis of Beams using ANCF”, *Nonlinear Dynamics*, 82, pp. 451-464.
97. Orzechowski, G., and Shabana, A.A., 2016, “Analysis of Warping Deformation Modes using Higher-Order ANCF Beam Element”, *Journal of Sound and Vibration*, 363, pp. 428-445.
98. Pacejka, H. B., 2002, *Tire and Vehicle Dynamics*, First Edition, Society of Automotive Engineers (SAE), Warrendale, PA.
99. Pacejka, H. B., 2006, *Tire and Vehicle Dynamics*, Third Edition, Society of Automotive Engineers (SAE), Warrendale, PA.
100. Pappalardo, C.M., Yu, Z., Zhang, X., and Shabana, A.A., 2016A, “Rational ANCF Thin Plate Finite Element”, *ASME Journal of Computational & Nonlinear Dynamics*, 11(5), pp. 051009-1 – 051009-15.
101. Pappalardo, C. M., Wallin, M., and Shabana, A. A., 2016B, “A New ANCF/CRBF Fully Parametrized Plate Finite Element”, *ASME Journal of Computational and Nonlinear Dynamics*, 12(3), pp. 031008-1-031008-13.
102. Pappalardo, C. M., Wang, T., and Shabana, A. A., 2017A, “On the Formulation of the Planar ANCF Triangular Finite Elements”, *Nonlinear Dynamics*, 89(2), pp. 1019-1045.
103. Pappalardo, C. M., Wang, T., and Shabana, A. A., 2017B, “Development of ANCF Tetrahedral Finite Elements for the Nonlinear Dynamics of Flexible Structures”, *Nonlinear Dynamics*, 89(4) pp. 2905-2932.
104. Patel, M., Orzechowski, G., Tian, Q., and Shabana A.A., 2016, “A New Multibody System Approach for Tire Modeling using ANCF Finite Elements”, *Proceedings of Institution of Mechanical Engineers Part K: Journal of Multibody Dynamics*, 230(1), pp. 69-84.

105. Patel, M., and Shabana, A.A., 2017, "Locking Alleviation in the Large Displacement Analysis of Beam Elements: The Strain Split Method", *submitted to Acta Mechanica*.
106. Patel, M., Pappalardo, C.M., Wang, G., and Shabana, A.A., 2017, "Integration of Geometry and Small and Large Deformation Analysis for Vehicle Modelling: Chassis, and Airless and Pneumatic Tire Flexibility", *submitted to International Journal of Vehicle Performance*.
107. Pian, T.H.H., 1985, "Finite Elements based on Consistently Assumed Stresses and Displacements", *Finite Elements in Analysis and Design*, 1(2), pp. 131-140.
108. Pian, T.H.H., and Sumihara, K., 1984, "Rational Approach for Assumed Stress Finite Elements", *International Journal for Numerical Methods in Engineering*, 20(9), pp. 1685-1695.
109. Piegl, L. and Tiller, W., 1997, *The NURBS Book*, Second Edition, Springer-Verlag, Berlin Heidelberg.
110. Prathap, G. and Babu, R., 1986A, "Field-Consistent Strain Interpolations for the Quadratic Shear Flexible Beam Element", *International Journal for Numerical Methods in Engineering*, 23(11), pp. 1973-1984.
111. Prathap, G., and Babu, R., 1986B, "An Isoparametric Quadratic Thick Curved Beam Element", *International Journal for Numerical Methods in Engineering*, 23(9), pp. 1583-1600.
112. Prathap, G., and Bhashyam, G.R., 1982, "Reduced Integration and the Shear-Flexible Beam Element", *International Journal for Numerical Methods in Engineering*, 18(2), pp. 195-210.
113. Rakowski, J., 1990, "The Interpretation of the Shear Locking in Beam Elements", *Computers & Structures*, 37(5), pp. 769-776.
114. Rakowski, J., 1991, "A Critical Analysis of Quadratic Beam Finite Elements", *International Journal for Numerical Methods in Engineering*, 31(5), pp. 949-966.

115. Raveendranath, P., Singh, G., and Pradhan, B., 1999, “A Two-Noded Locking-Free Shear Flexible Curved Beam Element”, *International Journal for Numerical Methods in Engineering*, 44(2), pp. 265-280.
116. Recuero, A.M., Aceituno, J.F., Escalona, J.L., and Shabana, A.A., 2016A, “A Nonlinear Approach for Modeling Rail Flexibility Using ANCF Finite Elements”, *Nonlinear Dynamics*, 83(1-2), pp. 463-481.
117. Recuero, A., Contreras, U., Patel, M., and Shabana, A.A., 2016B, “ANCF Continuum-based Soil Plasticity for Wheeled Vehicle Off-road Mobility”, *ASME Journal of Computational and Nonlinear Dynamics*, 11, pp. 044504-1 – 044504-5.
118. Recuero, A., Serban, R., Peterson, B., Sugiyama, H., Jayakumar, P., and Negrut, D., 2017, “A High-fidelity Approach for Vehicle Mobility Simulation: Nonlinear Finite Element Tires Operating on Granular Material”, *Journal of Terramechanics*, 72, pp. 39-54.
119. Reddy, J.N., 1997, “On Locking-Free Shear Deformable Beam Finite Elements”, *Computers Methods in Applied Mechanics & Engineering*, 149(1-4), pp. 113-132.
120. Reddy, J.N., Wang, C.M., and Lee, K.H., 1997, “Relationships Between Bending Solutions of Classical and Shear Deformation Beam Theories”, *International Journal of Solids & Structures*, 34(26), pp. 3373-3384.
121. Sampo, E., 2011, “Modelling Chassis Flexibility in Vehicle Dynamics Simulation”, Ph.D. Thesis, University of Surrey, Surrey.
122. Sanborn, G. G., and Shabana, A. A., 2009, “A Rational Finite Element Method Based on the Absolute Nodal Coordinate Formulation”, *Nonlinear Dynamics*, 58(3), pp. 565–572.

123. Sanborn, G.G., Choi, J., and Choi, J.H., 2011, “Curve-Induced Distortion of Polynomial Space Curves, Flat-Mapped Extension Modeling, and their Impact on ANCF Thin-plate Elements”, *Multibody System Dynamics*, 26(2), pp. 191-211.
124. Schillinger, D., Dedè, L., Scott, M. A., Evans, J. A., Borden, M. J., Rank, E., and Hughes, T. J. R., 2012, “An Isogeometric Design-Through-Analysis Methodology Based on Adaptive Hierarchical Refinement of NURBS, Immersed Boundary Methods, and T-spline CAD Surfaces”, *Computer Methods in Applied Mechanics & Engineering*, 249-252, pp. 116–150.
125. Schmidt, R., Wuchner, R., and Bletzinger, K.-U., 2012, “Isogeometric Analysis of Trimmed NURBS Geometries”, *Computer Methods in Applied Mechanics & Engineering*, 241-244, pp. 93–111.
126. Schwab, A.L., and Meijaard, J.P., 2005, “Comparison of Three-Dimensional Flexible Beam Elements for Dynamic Analysis: Finite Element Method and Absolute Nodal Coordinate Formulation”, *Proceedings of ASME International Design Engineering Technical Conferences and Computer and Information in Engineering Conference*, Long Beach, CA, September 24-28.
127. Schwarze, M., and Reese, S., 2009, “A Reduced Integration Solid-Shell Finite Element based on the EAS and ANS Concept – Geometrically Linear Problems”, *International Journal for Numerical Methods in Engineering*, 80(10), pp. 1322-1355.
128. Shabana, A.A., 1985, “Substructure Synthesis Methods for Dynamic Analysis of Multibody Systems”, *Computers and Structures*, 20(4), pp. 737-744.
129. Shabana, A.A., 1997, “Definition of the Slopes and the Finite Element Absolute Nodal Coordinate Formulation”, *Multibody System Dynamics*, 1(3), pp. 339-348.
130. Shabana, A.A., 2012, *Computational Continuum Mechanics*, Second Edition, Cambridge University Press, Cambridge.

131. Shabana, A.A., 2013, *Dynamics of Multibody Systems*, Fourth Edition, Cambridge University Press, Cambridge.
132. Shabana, A.A., 2015A, “ANCF Reference Node for Multibody System Applications”, *Proc. of Institute of Mechanical Engineers Part K: Journal of Multibody Dynamics*, 229(1), pp. 109-112.
133. Shabana, A.A., 2015B, “ANCF Tire Assembly Model for Multibody System Applications”, *ASME Journal of Computational and Nonlinear Dynamics*, 10(2), pp. 024504-1 – 024504-4.
134. Shabana, A.A., and Maqueda, L.G., 2008, “Slope Discontinuities in the Finite Element Absolute Nodal Coordinate Formulation: Gradient Deficient Elements”, *Multibody System Dynamics*, 20(3), pp. 239-249.
135. Shabana, A.A., and Mikkola, A., 2003, “Use of Finite Element Absolute Nodal Coordinate Formulation in Modeling Slope Discontinuity”, *ASME Journal of Mechanical Design*, 125(2), pp. 342-350.
136. Shen, Z., Li, P., Liu, C., and Hu, G., 2014, “A Finite Element Beam Model Including Cross-Section Distortion in the Absolute Nodal Coordinate Formulation”, *Nonlinear Dynamics*, 77(3), pp. 1019-1033.
137. Shiiba, T., Fehr, J., and Eberhard, P., 2012, “Flexible Multibody Simulation of Automotive Systems with Non-modal Model Reduction Techniques”, *Vehicle System Dynamics*, 50(12), pp. 1905-1922.
138. Simo, J.C., and Rifai, M.S., 1990, “A Class of Mixed Assumed Strain Methods and the Method of Incompatible Modes”, *International Journal for Numerical Methods in Engineering*, 29(8), pp. 1595-1638.

139. Simo, J.C., and Armero, F., 1992, “Geometrically Non-Linear Enhanced Strain Mixed Methods and the Method of Incompatible Modes”, *International Journal for Numerical Methods in Engineering*, 33(7), pp. 1413-1449.
140. Simo, J.C., Armero, F., and Taylor, R.L., 1993, “Improved Versions of Assumed Enhanced Strain Tri-linear Elements for 3D Finite Deformation Problems”, *Computer Methods in Applied Mechanics and Engineering*, 110(3-4), pp. 359-386.
141. Sopanen, J., and Mikkola, A., 2003, “Studies on the Stiffness Properties of the Absolute Nodal Coordinate Formulation for Three-Dimensional Beams”, *Proceedings Of Design Engineering Technical Conferences & Computers & Information in Engineering Conference*, Chicago, Illinois, USA, September 2-6.
142. Stolarski, H., and Belytschko, T., 1983, “Shear and Membrane Locking in Curved C^0 Elements”, *Computer Methods in Applied Mechanics & Engineering*, 41(3), pp. 279-296.
143. Stolarski, H, and Belytschko, T., 1986A, “On the Equivalence of Mode Decomposition and Mixed Finite Elements based on the Hellinger-Reissner Principle. Part 1: Theory”, *Computer Methods in Applied Mechanics & Engineering*, 58(3), pp. 249-263.
144. Stolarski, H, and Belytschko, T., 1986B, “On the Equivalence of Mode Decomposition and Mixed Finite Elements based on the Hellinger-Reissner Principle. Part 2: Applications”, *Computer Methods in Applied Mechanics & Engineering*, 58(3), pp. 265-284.
145. Stolarski, H., and Chen, Y, 1995, “Assumed Strain Formulation for the Four-Node Quadrilateral with Improved In-Plane Bending Behavior”, *International Journal for Numerical Methods in Engineering*, 38(8), pp. 1287-1305.

146. Sugiyama, H., and Suda, Y., 2007, “A Curved Beam Element in the Analysis of Flexible Multi-body Systems using the Absolute Nodal Coordinates”, *Proc. of Institute of Mechanical Engineers Part K: Journal of Multibody Dynamics*, 221(2), pp. 219-231.
147. Sugiyama, H., Gerstmayr, J., and Shabana, A.A., 2006, “Deformation Modes in the Finite Element Absolute Nodal Coordinate Formulation”, *Journal of Sound and Vibration*, 298(4-5), pp. 1129-1149.
148. Sugiyama, H., and Suda, Y., 2009, “Nonlinear Elastic Ring Tire Model Using the Absolute Nodal Coordinate Formulation”, *Proc. of Institute of Mechanical Engineers Part K: Journal of Multibody Dynamics*, 223(3), pp. 211-219.
149. Sugiyama, H., Koyama, H., and Yamashita, H., 2010, “Gradient Deficient Curved Beam Element using Absolute Nodal Coordinate Formulation”, *ASME Journal of Computational & Nonlinear Dynamics*, 5(2), pp. 021001-1 – 021001-8.
150. Sussman, T., and Bathe, K.J., 1987, “A Finite Element Formulation for Nonlinear Incompressible Elastic and Inelastic Analysis”, *Computers & Structures*, 26(1-2), pp. 357-409.
151. Sussman, T., and Bathe, K.J., 2014, “Spurious Modes in Geometrically Nonlinear Small Displacement Finite Elements with Incompatible Modes”, *Computers & Structures*, 140, pp. 14-22.
152. Taylor, R.L., Beresford, P.J., and Wilson, E.L., 1976, “A Non-Conforming Element for Stress Analysis”, *International Journal for Numerical Methods in Engineering*, 10(6), pp. 1211-1219.
153. Taylor, R.L., Filippou, F.C., Saritas, A., and Auricchio, F., 2003, “A Mixed Finite Element Method for Beam and Frame Problems”, *Computational Mechanics*, 31(1), pp. 192-203.

154. Tessler, A., and Hughes, T.J.R., 1983, “An Improved Treatment of Transverse Shear in the Mindlin-Type Four Node Quadrilateral Element”, *Computer Methods in Applied Mechanics & Engineering*, 39(3), pp. 311-335.
155. Timoshenko, S.P., 1921, “On the Correction for Shear of the Differential Equation for Transverse Vibrations of Prismatic Beams”, *Philosophical Magazine*, 41, pp. 744-746.
156. Uhm, T.-K., and Youn, S.-K., 2009, “T-spline Finite Element Method for the Analysis of Shell Structures”, *International Journal for Numerical Methods in Engineering*, 80(4), pp. 507–536.
157. Valkeapää, A.I., Yamashita, H., Jayakumar, P., and Sugiyama, H., 2015, “On the Use of Elastic Middle Surface Approach in the Large Deformation Analysis of Moderately Thick Shell Structures using Absolute Nodal Coordinate Formulation”, *Nonlinear Dynamics*, 80(3), pp. 1133-1146.
158. Von Dombrowski, S., 1997, “Modellierung von Balken bei grossen Verformungen für ein kraftreflektierendes Eingabegerät”, Diploma thesis, University Stuttgart & DLR.
159. Wang, P., Xu, J., Deng, J., and Chen, F., 2011, “Adaptive Isogeometric Analysis using Rational PHT-splines”, *Computer Aided Design*, 43(11), pp. 1438–1448.
160. Wang, W., 2000, “Special Quadratic Quadrilateral Finite Elements for Local Refinement with Irregular Nodes”, *Computer Methods in Applied Mechanics & Engineering*, 182, pp. 109–134.
161. Wilson, E.L., Taylor, R.L., Doherty, W.P., and Ghaboussi, J., 1973, “Incompatible Displacement Models”, *Numerical and Computer Models in Structural Mechanics*, pp. 43-57.
162. Wriggers, P., and Reese, S., 1996, “A Note on Enhanced Strain Methods for Large Deformations”, *Computer Methods in Applied Mechanics & Engineering*, 135(3-4), pp. 201-209.
163. Yakoub, R.Y., and Shabana, A.A., 2001, “Three-Dimensional Absolute Nodal Coordinate Formulation for Beam Elements: Implementation and Applications”, *ASME Journal of Mechanical Design*, 123(4), pp. 614-621.

164. Yamashita, H., Valkeapää, A.I., Jayakumar, P., and Sugiyama. H., 2015, “Continuum Mechanics based Bilinear Shear Deformable Shell Element Using the Absolute Nodal Coordinate Formulation”, *ASME Journal of Computational & Nonlinear Dynamics*, 10(5), pp. 051012-1 - 051012-9.
165. Yamashita, H., Jayakumar, P. and Sugiyama, H., 2016, “Physics-based Flexible Tire Model Integrated with LuGre Tire Friction for Transient Braking and Cornering Analysis”, *ASME Journal of Computational and Nonlinear Dynamics*, 11(3), pp. 031017-1 – 031017-17.
166. Yang, X., 2011, “Finite Element Analysis and Experimental Investigation of Tyre Characteristics for Developing Strain-based Intelligent Tire System”, PhD Thesis, College of Engineering and Physical Sciences, University of Birmingham.
167. Yu, Z., and Shabana, A.A., 2015, “Mixed-Coordinate ANCF Rectangular Plate Finite Element”, *ASME Journal of Computational and Nonlinear Dynamics*, 10(6), pp. 061003-1 – 061003-14.
168. Yu, Z., Liu, Y., Tinsley, B., and Shabana, A. A., 2016, “Integration of Geometry and Analysis for Vehicle System Applications: Continuum-based Leaf Spring and Tire Assembly”, *ASME Journal of Computational and Nonlinear Dynamics*, 11, pp. 031011-1- 031011-11.
169. Yunhua, L., 1998, “Explanation and Elimination of Shear Locking and Membrane Locking with Field Consistence Approach”, *Computer Methods in Applied Mechanics and Engineering*, 162(1-4), pp. 249-269.
170. Zegelaar, P.W.A., Gong, S., and Pacejka, H.B., 2008, “Tyre Models for the Study of In- Plane Dynamics”, *Vehicle System Dynamics, Supplement*, 23, pp. 578-590.
171. Zheng, Y., and Shabana, A.A., 2017, “A Two-Dimensional Shear Deformable ANCF Consistent Rotation-based Formulation Beam Element”, *Nonlinear Dynamics*, 87(2), pp. 1031-1043.

172. Zienkiewicz, O.C., Taylor, R., and Too, J.M., 1971, "Reduced Integration Technique in General Analysis of Plates and Shells", *International Journal for Numerical Methods in Engineering*, 3(2), pp. 275-290.
173. Zienkiewicz, O.C., Owen, D.R.J, and Lee, K.N., 1974, "Least Square-Finite Element for Elastostatic Problems. Use of 'Reduced' Integration", *International Journal for Numerical Methods in Engineering*, 8(2), pp. 341-358.

VITA

MOHIL PATEL

EDUCATION

Doctor of Philosophy, Mechanical Engineering, May 2018, University of Illinois at Chicago, Focus in Dynamic Analysis of Multi-body Systems, GPA 3.91/4.00

Bachelor of Science, Mechanical Engineering, May 2014, University of Illinois at Chicago, GPA 3.71/4.00

PROFESSIONAL EXPERIENCE

Research and Teaching Assistant, University of Illinois at Chicago, Department of Mechanical and Industrial Engineering, 2014-2017

Associate Mechanical Engineer, Alion Science & Technology, Warren, MI, May 2016 – August 2016

Consultant, Computational Dynamics Inc., Berwyn, IL, August 2015 – April, 2016

JOURNAL PUBLICATIONS

1. **Patel, M.**, Orzechowski, G., Tian, Q., and Shabana A.A., 2016, “A New Multibody System Approach for Tire Modeling using ANCF Finite Elements”, *Proceedings of Institution of Mechanical Engineers Part K: Journal of Multibody Dynamics*, 230(1), pp. 69-84.
2. Pappalardo, C.M., **Patel, M.**, Tinsley, B., and Shabana, A.A., 2016, “Contact Force Control in Multibody Pantograph/Catenary Systems”, *Proceedings of Institution of Mechanical Engineers Part K: Journal of Multibody Dynamics*, 230(4), pp. 307-328.
3. Recuero, A., Contreras, U., **Patel, M.**, and Shabana, A.A., 2016, “ANCF Continuum-based Soil Plasticity for Wheeled Vehicle Off-road Mobility”, *ASME Journal of Computational and Nonlinear Dynamics*, 11, pp. 044504-1 – 044504-5.
4. He, G., **Patel, M.**, and Shabana, A.A., 2017, “Integration of Localized Surface Geometry in Fully Parameterized ANCF Finite Elements”, *Computer Methods in Applied Mechanics and Engineering*, 313, pp. 966-985.

5. **Patel, M.**, and Shabana A.A., 2017, “Locking Alleviation in the Large Displacement Analysis of Beam Elements: The Strain Split Method”, Submitted to *Acta Mechanica*.
6. **Patel, M.**, Pappalardo, C.M., Wang, G., and Shabana A.A., 2017, “Integration of Geometry and Small and Large Deformation Analysis for Vehicle Modelling: Chassis and Airless and Pneumatic Tire Flexibility”, Submitted to *International Journal of Vehicle Performance*.
7. Shabana, A.A., and **Patel, M.**, 2017, “Coupling Between Shear and Bending in the Analysis of Beam Problems: Planar Case”, Accepted in *Journal of Sound and Vibration*.

CONFERENCE PUBLICATIONS

1. **Patel, M.**, Orzechowski, G., Tian, Q., Shabana, A. A., “A novel method for modeling ANCF based finite element tire assemblies”, *Proceedings of the ASME 2015 International Design Engineering Technical Conference & Computers and Information in Engineering Conference*. August 2-5, 2015, Boston, MA, USA.
2. Pappalardo, C. M., **Patel, M.**, Tinsley, B., Shabana, A. A., “Pantograph/Catenary contact force control”, *Proceedings of the ASME 2015 International Design Engineering Technical Conference & Computers and Information in Engineering Conference*. August 2-5, 2015, Boston, MA, USA.

PROFESSIONAL SERVICE

Journal Reviewer:

- Proceedings of Institution of Mechanical Engineers Part K: Journal of Multibody Dynamics
- ASME Journal of Computational and Nonlinear Dynamics

Conference Reviewer:

- ASME IDETC/CIE 2015

Other:

- Mentored a team of undergraduate seniors for their senior design project
- Guided senior mechanical engineering students to acquire jobs in the industry

PROFESSIONAL AFFILIATIONS

- American Society of Mechanical Engineers
- Society of Automotive Engineers

RESEARCH PROJECTS AND COLLABORATIONS

Development of a high fidelity off-road vehicle model

- Developed a multibody model of the HMMWV vehicle in the general purpose flexible multibody dynamics code SIGMA/SAMS
- Integrated FFR chassis, ANCF pneumatic and ANCF airless tires with the vehicle model
- Implemented rack and pinion joint using a position level based formulation

Locking in ANCF finite elements

- Investigated locking effects in fully parameterized ANCF finite elements with emphasis on improving element performance

Development of new tire modeling techniques in a multibody dynamics framework

- Demonstrated a new technique for modeling tires using a nonlinear finite element formulation (ANCF) suitable for modeling large deformation and rotation
- Implemented an algorithm in MATLAB to mesh tires using ANCF plate elements
- Tested the new tire modeling technique on a bulldozer vehicle model with a simplified composite material model
- Developed a new method of including tire tread details in the ANCF tire mesh using NURBS geometry
- Implemented the hyperelastic incompressible Mooney-Rivlin material in order to model the rubber in tires

Tire-soil interaction

- Implemented a ‘flex-to-flex’ contact algorithm for the tire-soil interaction problem
- Soil was modeled using ANCF solid elements and the Drucker-Prager plasticity model

Control of pantograph/catenary systems on high speed trains

- Developed a detailed flexible multibody model of pantograph/catenary system operating at a speed of 200km/hr
- Analyzed the deformation and wave propagation characteristics of the catenary at varying train speeds
- Implemented three types of controllers in order to reduce the contact force standard deviation in the pantograph/catenary system

RESEARCH INTERESTS

Flexible multibody dynamics, Computational methods, Vehicle dynamics, Large deformation theory, Nonlinear finite element analysis, Contact mechanics, Computational geometry